Spring 2018

Atomic layer deposition prepared nanostructured materials for various catalytic reactions

Xiaofeng Wang

Department: Chemical and Biochemical Engineering

ATOMIC LAYER DEPOSITION PREPARED NANOSTRUCTURED MATERIALS FOR VARIOUS CATALYTIC REACTIONS

by

XIAOFENG WANG

A DISSERTATION

Presented to the Faculty of the Graduate School of the

MISSOURI UNIVERSITY OF SCIENCE AND TECHNOLOGY

In Partial Fulfillment of the Requirements for the Degree

DOCTOR OF PHILOSOPHY

in

CHEMICAL ENGINEERING

2018

Approved by:

Dr. Xinhua Liang, Advisor
Dr. Douglas K. Ludlow
Dr. Fateme Rezaei
Dr. Jee-Ching Wang
Dr. Honglan Shi

PUBLICATION DISSERTATION OPTION

This dissertation consists of the following eight articles that have been published or pending submission for publication as follows:

Paper I: Pages 13-39 have been published in ***Journal of Nanoparticle Research***.

Paper II: Pages 40-86 have been submitted to ***ACS Catalysis***.

Paper III: Pages 87-116 have been submitted to ***Green Chemistry***.

Paper IV: Pages 117-142 have been published in ***Catalysis Letters***.

Paper V: Pages 143-169 have been published in ***Nanotechnology***.

Paper VI: Pages 170-189 have been submitted in ***ChemCatChem***.

Paper VII: Pages 190-209 are intended for submission to ***ACS Catalysis***.

Paper VIII: Pages 210-237 are intended for submission to ***Nano Letters***.

ABSTRACT

Atomic layer deposition (ALD) has been widely used for thin film coating and metal nanoparticles (NPs) preparation. In this report, the applications of ALD prepared nanostructured materials in catalysis were examined.

Highly dispersed Pt monometallic catalysts with different substrates and multi-walled carbon nanotubes (MWCNTs) supported Pt-Co bimetallic catalysts were synthesized by ALD for selective hydrogenation of α, β-unsaturated aldehydes to unsaturated alcohols (UA). Pt/MWCNTs showed the highest selectivity of UA in selective hydrogenation of citral, as compared to Pt/SiO_2, $Pt/ALD\text{-}Al_2O_3$, and $Pt/\gamma\text{-}Al_2O_3$. After adding Co, the highest selectivity was achieved with high conversion in hydrogenation of both cinnamaldehyde and citral over an optimized Pt-Co/MWCNTs catalyst.

Highly dispersed Pt-Co/MWCNTs bimetallic catalysts were also used for hydrogenolysis of 5-hydroxymethylfurfural (HMF) to 2,5-dimethylfuran (DMF) reaction. High yield of DMF (> 90%) was achieved in hydrogenolysis of HMF over an optimized Pt-Co/MWCNTs catalyst after 8 hr of reaction time under mild conditions.

Fe NPs and single atoms were deposited on various substrates via ALD. Fe/SiO_2 NPs showed a high activity in CO oxidation reaction with a long-term stability at high temperature. The TiO_2 NPs deposited with Fe single atoms showed the highest activity and had an up to six-fold photocatalytic activity enhancement over pure TiO_2. CeO_2 ALD and ZrO_2 ALD were also applied on TiO_2 to boost the photocatalytic activity of TiO_2, and both two methods improved the photocatalytic efficiency of TiO_2 significantly.

ACKNOWLEDGMENTS

This study was conceived and completed from August 2014 to May 2018 in the Department of Chemical and Biochemical Engineering (ChBE) at Missouri S&T. I would like to express my appreciation to the people who helped me during my graduate studies.

In particular, I would like to express my deep gratitude to my advisor, Dr. Xinhua Liang, for his willingness to share his experience, precious and tireless advice, encouragement, and endless patience all throughout my graduate studies.

I also want to express my thanks to Dr. Douglas K. Ludlow, Dr. Fateme Rezaei and Dr. Jee-Ching Wang in the ChBE Department, and Dr. Honglan Shi in the Chemistry Department for being my graduation thesis committee. Their constructive suggestions for my research were vital.

In addition, I would like to thank technicians in the Materials Research Center (Dr. Eric Bohannan for XRD analysis, Dr. Jessica Terbush and Dr. Jingjing Qing for TEM analysis, and Dr. Clarissa Weisner for SEM analysis), and technician (Dean Lenz) and staff (Marlene Albrecht, Emily Kost, and Dawn Schacht) in the ChBE Department. I am also grateful to Dr. Rajankumar Patel, Dr. Zeyu Shang, and all of my colleagues in Dr. Liang's group for their willingness to share ideas and their help with experiments.

This work was supported in part by the National Science Foundation (NSF-CBET 1402122) and American Chemical Society Petroleum Research Fund.

Last but not least, I would like to convey a special thanks to my parents for their understanding, caring, and endless love. Without their encouragement and support, I would not be able to accomplish my study.

TABLE OF CONTENTS

LIST OF ILLUSTRATIONS

PAPER II

PAPER III

PAPER IV

PAPER V

PAPER VI

PAPER VII

PAPER VIII

LIST OF TABLES

SECTION

1. INTRODUCTION

1.1. ATOMIC LAYER DEPOSITION

Atomic layer deposition (ALD) is a layer-by-layer process with the capability of growing films with precise atomic layer control.[1-4] It is able to meet the needs for atomic layer control and conformal deposition using sequential, self-limiting surface reactions. Most ALD processes are based on binary reaction sequences where two surface reactions occur and deposit a binary compound film. Because there are only a finite number of surface sites, the reactions can only deposit a finite number of surface species. If each of the two surface reactions is self-limiting, then the two reactions may proceed in a sequential fashion to deposit a thin film with atomic level control. Under favorable conditions, deposition can be limited by the number of functional groups on the surface. Depending on the properties of substrate and coating material, and process conditions, one ALD cycle deposits a ~0.05-0.3 nm thick film. The final film thickness is simply determined by the growth rate per cycle and the number of cycles completed. ALD can prepare pin hole free and conformal films. For example, Al_2O_3 ALD can be divided into the following two half-reactions:

$AlOH^* + Al(CH_3)_3 \rightarrow Al\text{-}O\text{-}Al(CH_3)_2^* + CH_4$

$Al\text{-}O\text{-}Al(CH_3)_2^* + 2H_2O \rightarrow Al\text{-}O\text{-}Al(OH)_2^* + 2CH_4$

where an asterisk (*) indicates the surface species.[5] Figure 1.1 schematically shows the Al_2O_3 ALD process. In the first half-reaction, the first precursor, trimethylaluminum (TMA), will react with the surface -OH groups and $-CH_3$ surface groups will form. In the

second half-reaction, the surface -CH_3 groups will react with the second precursor, H_2O, and one atomic layer of Al_2O_3 would form and the surface -OH groups will be regenerated.

ALD has been utilized to deposit metal oxide films, metal films, and metal nanoparticles with subnanometer-sized control of film thickness and well controlled particle size. Consequently, ALD shows many advantages compared to some traditional thin film coating methods. Using the ALD method, it is possible to prepare coated core particles of different sizes with uniform distribution of composite as well as controllable thickness.

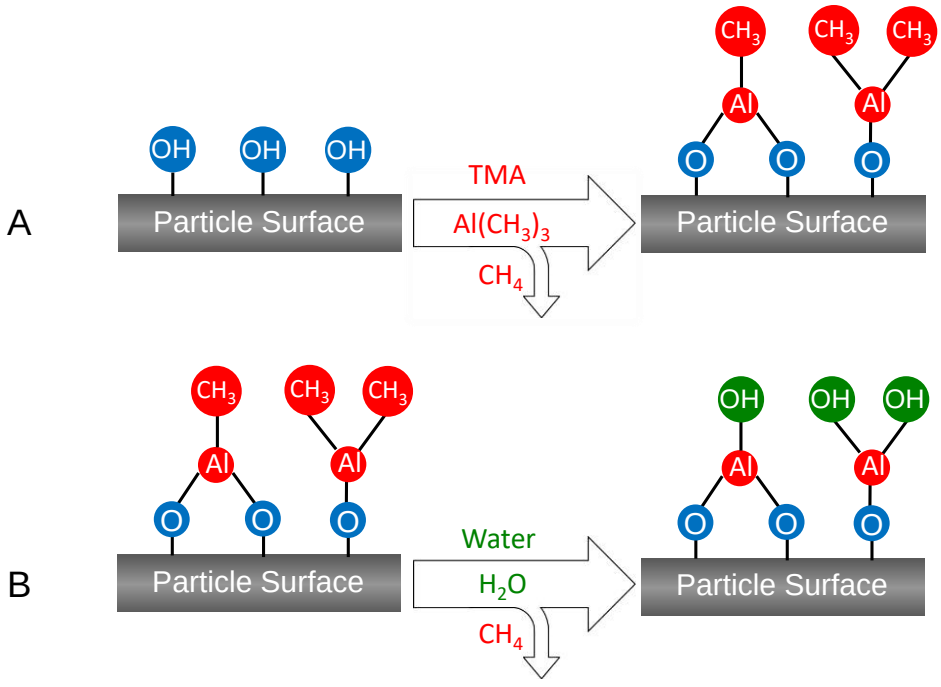

Figure 1.1. Scheme of one cycle of Al_2O_3 ALD using TMA and water as precursors.

1.2. SELECTIVE HYDROGENATION OF A, B-UNSATURATED ALDEHYDES TO UNSATURATED ALCOHOLS

The selective hydrogenation of unsaturated carbonyls is a key step in the manufacture of pharmaceuticals, flavors, and fragrances. The hydrogenation of the C=C bond to yield saturated carbonyls is thermodynamically favored and can be readily achieved with high selectivity. The selective hydrogenation of the C=O bond to yield unsaturated alcohols is much more difficult to achieve, and as a result it has been the focus of much research. This is due to the fact that the difference in negative free reaction enthalpy of ~35 KJ/mol favors the hydrogenation of C=C rather than C=O.[6] Cinnamaldehyde, an example of unsaturated aldehyde, is of great practical importance in perfume industries, fine chemicals,[7] and pharmaceutical drugs.[8, 9] Cinnamic alcohol, an unsaturated alcohol hydrogenated from cinnamaldehyde, is an important building block in organic synthesis. Cinnamic alcohol and cinnamic aldehyde are generally considered to be the most prominent example of a prohapten–hapten pair. Therefore, cinnamic alcohol has been the preferred prohapten in numerous experimental studies on skin metabolism over the years.[10, 11] Giroir-Fendler et al.[12] studied the hydrogenation of cinnamaldehyde with various noble metal catalysts supported on carbon and graphite, and found that the selectivity towards the unsaturated alcohol followed the series of Pd < Rh < Ru < Pt < Ir. The best results were obtained with a carbon supported iridium catalyst. Ruthenium and rhodium catalysts were active for the reduction of the carbonyl group, but also for the reduction of the C=C bond; palladium catalysts gave very high selectivity for the production of the saturated alcohol.[13] Platinum tends to be less selective than iridium for hydrogenation to the unsaturated alcohol, but it can be improved by the addition of a metallic salt, such as $FeCl_3$.[14, 15]

Over the past decade, a lot of studies have been carried out over a variety of bimetallic catalysts.[16-19] Bimetallic catalysts usually showed a higher activity due to the synergetic effect of two metal elements and a higher selectivity to unsaturated alcohols due to electronic and geometric effects, when compared to monometallic catalysts. Among them, platinum (Pt) – cobalt (Co) bimetallic catalysts attracted increasing interest and high unsaturated alcohols yields were gained over Pt-Co catalysts by some studies.[19-22] However, the studies on synergetic effect between Pt and Co and the interaction between Pt-Co bimetallic NPs and support are lack. Thus, it is essential and important to reveal the effect of interaction between Pt-Co and substrates on selective hydrogenation reactions.

1.3. HYDROGENOLYSIS OF 5-HYDROXYMETHYLFURFURAL TO 2,5-DIMETHYLFURAN

Nowadays, fossil fuels, such as petrol, coal, and natural gas play principal roles as source of energy and chemicals.[23] However, due to the gradual exhaust of fossil resource and greenhouse effect for the consumption of fossil fuels, the transformation of renewable biomass into biofuel has become a hotspot research area to replace oil-based energy. With the advances in conversion technology, abundant biomass resources have the potential as feedstock to be converted to biofuels.

Currently, ethanol is the only biofuel produced at commercial scale available to meet advanced non-cellulosic renewable fuel targets.[24] Though it comes from renewable resource and burns more cleanly in air than petroleum, a great deal of arable land is required to produce the crops to obtain ethanol, leading to various problems, such as soil erosion, deforestation, and salinity. Besides, its high oxygen content (O/C=0.5) and low

energy density (23.4 MJL^{-1} vs. 34 MJL^{-1} for gasoline) are seen as disadvantages. While the lower energy density of ethanol is largely offset by its higher research octane number (RON =110), as compared to gasoline (RON =89-96), the average fuel economy of E15 (15% ethanol, 85% gasoline) fuel is still about 5% lower than that of regular gasoline. Therefore, researchers in both industry and academia are developing technologies for the next-generation advanced liquid fuels based on biorenewable platform chemicals, including 5-hydroxymethylfurfural (HMF) and furfural (Ff).[25, 26] The platform molecular, HMF, a hexose dehydration product, will be a key player in the biobased renaissance, because it can be converted into 5-ethoxymethylfurfural (EMF), levulinic acid (LA), ethyl levulinate (EL), 2,5-diformlfuran (DFF), and 2,5-dimethylfuran (DMF).[27-33] DMF processes a high energy density (30 $KJcm^{-3}$), a high research octane number (RON=119), and a low volatility (boiling point= 92-94 ℃), which are close to the values of gasoline (which possesses 34 MJL^{-1}, RON=89-96, and boiling point= 96.3 ℃). Besides, a low solubility in water (2.3 gL^{-1}) is superior to miscible ethanol, which makes DMF more suitable than ethanol as the blend fuel.[34] These excellent performances make DMF a more appropriate, ideal, and promising biomass-derived liquid biofuel for transportation.

HMF, containing an aldehyde group, a hydroxyl group, and a furan ring, is very reactive, and its hydrogenation products are kind of complicated.[35] Therefore, how to ensure the hydrogenation priorities of an aldehyde group and a hydroxyl group and avoid further hydrogenation of a furan ring are the principal issues in the selective hydrogenation of HMF into DMF. Nishimura et al. prepared Pd_{50}/C, Au_{50}/C, Pt_{50}/C, Ru_{50}/C, and Pd_xAu_y/C catalysts with various Pd/Au molar ratio (x/y) by $NaBH_4$ reduction method with some modification to examine hydrogenation of HMF to DMF in the

presence of hydrochloric acid (HCl) under an atmospheric hydrogen pressure.[34] The highest conversion of HMF (99%) and yield of DMF (96%) were achieved over $Pd_{50}Au_{50}$/C for 12 hours. However, corrosive hydrochloric acid was used in this process and their prepared catalysts were not very reactive.

Pd/C and Ru/C catalysts were also adopted by some researchers to perform the hydrogenation of HMF to DMF under various conditions.[36-42] In 2010, Thananatthanachon and Rauchfuss proposed a mild catalytic system, in which formic acid (FA) was first used as a hydrogen donor for the selective hydrogenation of HMF. [43] When the reaction was carried out in tetrahydrofuran (THF) over the catalysts of sulfuric acid (H_2SO_4) and Pd/C, more than 95% DMF yield with 100% HMF conversion was observed at 70 °C for 15 h under atmospheric pressure. Besides, some novel catalysts were prepared for the hydrogenation of HMF to DMF. Wang et al. fabricated PtCo bimetallic NPs and 98% DMF yield with 100% HMF conversion was observed at 180 ºC after 2 h under 10 bar H_2.[44] However, for the third cycle, the yield of DMF decreased significantly to 72% and 13% of 2,5-di(hydroxymethyl)furan and 9% of 2-methyl-5-hydroxymethylfuran were left.

While high HMF conversion and DMF yield were reported over the Pd/C[43] and PdAu/C[34] catalysts, it took more than 12 hours to achieve the results in a small scale. High HMF conversion and high DMF selectivity also were obtained over Ru/C in a short reaction time,[37, 38, 41] but it required high pressure or high temperature, and could only obtain such good results in a small scale. Thus, these catalysts were not very reactive. Compared with these catalysts, Pt/C[45] showed a high reactivity and the HMF conversion was higher than 95% under high H_2 pressure, but the DMF selectivity was about only

70% due to its high reactivity and the generation of more byproducts. The low DMF yield was also reported over $CuCrO_4$[27], CuRu/C,[46] and Pd/Fe_2O_3[47] catalysts. For the PtCo NPs,[44] they were not recyclable and unstable because of the leaching of the catalysts.

Over all, the above-mentioned recent research advancements have shown some exciting results: it presented high HMF conversion and selectivity of DMF over $Pd_{50}Au_{50}/C$ and many other catalysts were also fabricated and used in the hydrogenation of HMF and so on. However, so far, no one catalyst can keep high activity, high stability, and high selectivity in a large scale of HMF hydrogenation. This is the big barrier to accomplish the large-scale production of DMF.

1.4. PHOTOCATALYTIC DEGRADATION OF ORGANIC POLLUTANTS BY TIO_2-BASED PHOTOCATALYSTS

Nowadays, organic pollutants have become one of the most important environmental concerns in fast growing society. As a potential and promising technology, photocatalytic degradation of organic pollutants on TiO_2 has been studied for decades because of the TiO_2 properties of remarkable incident photon-to-electron conversion efficiencies, chemical stability, and low cost.[48-50] However, the photocatalytic efficiency of TiO_2 is not high enough in practical applications because the photo-generated electrons (e^-) and holes (h^+) recombine easily, which limits the efficiency greatly.[51] Hence, it is necessary to reduce the e^-/h^+ recombination rate and thereby boost the photocatalytic efficiency.

There are several methods to improve the photocatalytic activity of TiO_2 and one effective method is to dope metal oxides when preparing TiO_2-based photocatalysts. Among various metal oxides, CeO_2 and ZrO_2 are two popular oxides used to improve the

activity of TiO_2. CeO_2 doping has been considered as an effective way for several reasons. Firstly, CeO_2 can play a role as e^-/h^+ pair trap centers, since the energy level of Ce^{3+}/Ce^{4+} lies close to that of Ti^{3+}/Ti^{4+}, favoring the separation of photo-generated e^-/h^+ pair, and consequently reducing e^-/h^+ pair recombination rate.[52] Secondly, there are many oxygen vacancies and Ce^{3+} defects in CeO_2,[53] which can store/release oxygen for photo-degradation process. With ZrO_2 doping, the band gap of TiO_2 photocatalysts increases and subsequently the e^-/h^+ pair recombination rate decreases, which also leads to the improvement of photocatalytic activity. But almost all studies adopted sol-gel[52, 54-57] or hydrothermal[58] methods to prepare CeO_2/TiO_2 and ZrO_2/TiO_2 catalysts, and thereby the physical properties between pure TiO_2 and doped TiO_2 were remarkably different, including the crystal structure and phase composition. High CeO_2/ZrO_2 content would lead to poor anatase crystallinity and decrease the photocatalytic efficiency; in contrast, too low ZrO_2 loading does not ensure the obvious change of the band gap and thereby the e^-/h^+ recombination rate cannot be reduced effectively. Thus, it is necessary to adopt a new strategy for CeO_2/TiO_2 and ZrO_2/TiO_2 preparation to further promote the photoactivity of TiO_2.

1.5. SUPPORTED FE SINGLE ATOMS

Recently, metal single-atom materials have become a new hot spot due to their unique properties and great potential in various applications, especially in catalysis.[59-65] For example, Ding et al. demonstrated that infrared spectroscopy could be a fast and convenient characterization method with which to directly distinguish and quantify Pt single atoms from nanoparticles; in addition, they directly observed that only Pt

nanoparticles showed activity for carbon monoxide (CO) oxidation and water-gas shift reaction at low temperatures, whereas Pt single atoms behaved as spectators.[62] However, single atoms are too mobile on supports, since the surface free energy of metal increases dramatically when the metal particle size reduces to single-atom level.[59] Thus, the metal single atoms are easy to sinter and aggregate during drying or calcination in the synthesis process. There is a challenge to prepare single-atom materials by traditional methods, including sol-gel and coprecipitation methods.

During the past few years, some studies have focused on the synthesis of single-atom materials and several new methods have been reported; these include taking advantage of the unique properties of supports (e.g., photocatalysis of TiO_2 and defects of graphene),[63, 65-68] and enhancing the metal-support interactions (e.g., Pt-CeO_2, Pd-C_3N_4, and Au-zeolite).[64, 69, 70] In these methods, specific substrates were needed, since strong interaction between metal single atoms and substrates was needed to prevent moving of single atoms on the substrates during preparation. Thereby, though most of these single-atom catalysts presented excellent catalytic performance in various applications, the specific supports used in these methods became a limitation to expand their applications. Moreover, although some reports have been published, few of them focused on synthesis and applications of transition metal (e.g., Fe, Co and Ni) single-atom materials.[61, 68, 71, 72]

1.6. DISSERTATION SUMMARY

In Paper I, the effect of support on selective hydrogenation of citral over supported Pt catalysts was investigated. The Pt catalysts supported on MWCNTs, silica gel, γ-Al_2O_3, and porous ALD-Al_2O_3 were prepared by ALD in a scalable fluidized bed

reactor. The acid-base property of supports was the dominating factor that determined the activity of all catalysts. On the other hand, the electronic effect and geometric structure influenced the product distribution of citral hydrogenation greatly for Pt/MWCNTs.

In Paper II, Pt-Co bimetallic catalysts were prepared by ALD for selective hydrogenation of α, β-unsaturated aldehydes to unsaturated alcohols. Both the HRTEM images and STEM/EDS results confirmed the formation of Pt-Co bimetallic particles on MWCNTs. After optimization, a desired catalyst showed high selectivity to unsaturated alcohols (> 90%) with high conversion in all selective hydrogenation reactions due to the synergistic effect between Pt and Co NPs.

In Paper III, highly dispersed Pt-Co bimetallic catalysts were deposited on MWCNTs by ALD for hydrogenolysis of HMF to DMF. High yield of DMF (> 90%) was achieved in hydrogenolysis of HMF over an optimized Pt-Co/MWCNTs catalyst after 8 hr of reaction time under mild conditions.

In Paper IV, highly dispersed and highly stable supported Au-Pt bimetallic catalysts were prepared using a two-step process. Pt NPs were first deposited on porous γ-Al_2O_3 particles by ALD. Au NPs were synthesized by NaOH reduction method using gold(III) chloride as the Au precursor, and then immobilized on ALD Pt/γ-Al_2O_3 particles. The Au-Pt bimetallic catalysts were highly active and highly stable in a vigorously stirred liquid phase reaction of glucose oxidation.

In Paper V, different cycles of CeO_2 deposited TiO_2 powders were prepared via ALD. With an increase in the number of ALD coating cycles, the amount of e^-/h^+ pair trap centers increased. The 40 cycles CeO_2 ALD deposited TiO_2 catalyst showed the highest photocatalytic activity and had a more than three-fold photocatalytic activity

enhancement over pure TiO_2 for the degradation of MB due to the fact that CeO_2 played a role as e^-/h^+ pair trap centers and consequently reduced the recombination rate of e^-/h^+ pairs.

In Paper VI, 5-90 cycles of ZrO_2 were deposited on TiO_2 NPs by ALD to improve their photocatalytic activity under UV light. TiO_2 sample deposited with 45 cycles of ZrO_2 ALD was proved to be the most efficient catalyst with degradation kinetic constant 10 times larger than that of the pure TiO_2 sample.

In Paper VII, highly dispersed Fe NPs were deposited on SiO_2 NPs by ALD at 400 ºC. In CO oxidation reactions over Fe/SiO_2 catalyst, the temperatures for 100% conversion were 550 ºC, 470 ºC, and 410 ^{o}C with the $CO:O_2$ ratio of 1:1, 1:5, and 1:10, respectively. Compared with reported iron oxide catalysts, the efficiency of Fe/SiO_2 for CO oxidation was more than 2 orders of magnitude higher than the reported values. Fe/SiO_2 was very stable after 4 reaction cycles. In a long-term stability test, there was almost no activity loss of Fe/SiO_2 at 550 ºC for more than 300 hrs of CO oxidation reaction.

In Paper VIII, a general strategy was reported to synthesize Fe single-atom materials on various substrates (e.g., multi-walled carbon nanotubes, SiO_2, and TiO_2) by ALD through optimization of ferrocene (Fe precursor) dose time and the number of ALD cycles. The formation of Fe single atoms was verified by HAADF-STEM and XAS analysis. One application of Fe single atoms is used as catalysts. The photocatalytic activity of Fe/TiO_2 catalysts was evaluated based on the degradation of MB solution under UV light. The photocatalysis experiment demonstrated that TiO_2 nanoparticles

deposited with 2 cycles of Fe ALD showed the highest activity and had a more than six-fold photocatalytic activity enhancement over pure TiO_2 for the degradation of MB.

In Section 2, the findings of this dissertation are summarized and future work directions are discussed.

PAPER

I. SELECTIVE HYDROGENATION OF CITRAL OVER SUPPORTED PT CATALYSTS: INSIGHT INTO SUPPORT EFFECTS

Xiaofeng Wang [a], Weiming Hu [b], Baolin Deng [b], and Xinhua Liang [a,*]

[a] Department of Chemical and Biochemical Engineering, Missouri University of Science and Technology, Rolla, MO 65409, United States

[b] Department of Civil and Environmental Engineering, University of Missouri, Columbia, MO 65211, United States

[*] Corresponding author, Email: liangxin@mst.edu

This paper has been published in *Journal of Nanoparticle Research*, 19(4), article No. 153, 2017.

ABSTRACT

Highly dispersed platinum (Pt) nanoparticles (NPs) were deposited on various substrates by atomic layer deposition (ALD) in a fluidized bed reactor at 300 ºC. The substrates included multi-walled carbon nanotubes (MWCNTs), silica gel (SiO_2), commercial γ-Al_2O_3, and ALD-prepared porous Al_2O_3 particles (ALD-Al_2O_3). The results of TEM analysis showed that ~1.3 nm Pt NPs were highly dispersed on all different supports. All catalysts were used for the reaction of selective hydrogenation of citral to unsaturated alcohols (UA), geraniol and nerol. Both the structure and acidity of supports affected the activity and selectivity of Pt catalysts. Pt/SiO_2 showed the highest activity due to the strong acidity of SiO_2 and the conversion of citral reached 82% after

12 hr with a selectivity of 58% of UA. Pt/MWCNTs showed the highest selectivity of UA, which reached 65% with a conversion of 38% due to its unique structure and electronic effect. The cycling experiments indicated that Pt/MWCNTs and Pt/ALD-Al_2O_3 catalysts were more stable than Pt/SiO_2, as a result of the different interactions between the Pt nanoparticles and the supports.

Keywords: Atomic layer deposition (ALD), Platinum (Pt), Citral hydrogenation, Unsaturated alcohols (UA), Supports, Stability

1. INTRODUCTION

Selective hydrogenation of α,β-unsaturated aldehydes to corresponding allylic alcohols over metal-supported catalysts is attractive for both economic and scientific reasons (Hájek et al. 2005; Vu et al. 2006; Lordi et al. 2001). As one of such selective reactions, hydrogenation of citral (3,7-dimethyl-2,6-octadienal) to unsaturated alcohols (UA), geraniol and nerol, is a critical step in the industrial production of many fine chemicals, especially perfumes, and pharmaceutical intermediates. However, the hydrogenation of a carbonyl group is thermodynamically less favorable than that of a C=C double bond conjugate to the carbonyl present in citral, since the bond energy of C=C (615 KJ/mol) is lower than that of C=O (715 KJ/mol) (Vilella et al. 2007; Noller and Lin 1984). Therefore, the principal issue in these selective reactions is ensuring the hydrogenation priority of the C=O bond, but avoiding the hydrogenation of the C=C bond.

It has been reported that catalytic performance (activity and selectivity) depends on many factors, such as type of metal and promoter. Among them, the nature of supports shows a critical influence on the activity of catalysts and product distribution during a selective hydrogenation reaction. Several reports focusing on this topic have been published (Gallezot and Richard 1998; Claus 1998; Santiago-Pedro et al. 2013). For example, Santiago-Pedro et al. (2013) reported that basic materials were the most active catalysts and that the formation of unsaturated alcohols was related to the strength and density of the acid sites of the catalyst. In addition, the stability of catalysts is also related to the properties of supports since the interactions between metal and various supports are different. Recycling and reusing catalysts are key factors in practical applications. This is especially important for noble metal catalysts because of their high cost. However, to the best of our knowledge, the effects of supports on the stability of catalysts have been scarcely addressed in the open literature. Herein, the aim of this work was to investigate and determine the influence of support on the activity, selectivity, and stability of different supported Pt catalysts prepared systematically by atomic layer deposition (ALD) in the chemoselective hydrogenation of citral.

Over the past decade, ALD has been used to prepare supported catalysts for gas and liquid phase reactions (King et al. 2008; Feng et al. 2010; Li et al. 2010; Lu et al. 2012; Jiang et al. 2015; Christensen et al. 2010). ALD is a surface-controlled process based on self-limiting reactions and has been demonstrated to deposit highly dispersed metal nanoparticles (NPs) on support surfaces (Leskelä and Ritala 2003; Suntola 1992). Since ALD leads to perfect 3D conformality, excellent step coverage, and reproducibility of high aspect ratio structures, the metal particles are very uniform in size at nanometer

scale, and can be homogeneously dispersed on supports. Therefore, in this study, Pt NPs deposited on different supports, were prepared by ALD to investigate and determine the influence of supports on the selective hydrogenation of citral to UA. Multi-walled carbon nanotubes (MWCNTs), silica gel (SiO_2), commercial γ–alumina (γ-Al_2O_3), and porous ALD-Al_2O_3 particles, prepared by a template-directed synthesis approach (Liang et al. 2012), were used as the catalyst supports.

2. EXPERIMENTAL

2.1. MATERIALS

(Methylcyclopentadienyl) trimethylplatinum [(MeCp)$PtMe_3$] was purchased from Strem Chemicals, Inc. MWCNTs (>95%, outside diameter: 10-20 nm) were purchased from US Research Nanomaterials, Inc. Silica gel, γ-Al_2O_3 (40 μm), citral, and 2-propanol were received from Sigma, Inc. All of the chemicals were used as received without any treatment. Porous Al_2O_3 was prepared by ALD in our lab, following the procedure we reported earlier (Liang et al. 2012). Briefly, highly porous Al_2O_3 particles, with precise wall thickness control, were synthesized by ALD of Al_2O_3 on highly porous poly(styrene–divinylbenzene) (PS–DVB) particle templates. 25 cycles of Al_2O_3 ALD were carried out using alternating reactions of trimethylaluminum (TMA, 97%, Sigma-Aldrich) and water at 33 ºC. Then, the Al_2O_3 coated PS–DVB particles were heated in air at 400 °C for 24 h to remove organic constituents after ALD and the porous Al_2O_3 particles (ALD-Al_2O_3) were produced.

2.2. CATALYST PREPARATION

Pt was deposited on MWCNTs, SiO_2, commercial γ-Al_2O_3, and porous ALD-Al_2O_3 substrates by ALD using (MeCp)$PtMe_3$ as the Pt precursor and oxygen (O_2) as the reactant gas in a fluidized bed reactor, as described in detail elsewhere (Liang et al. 2011). For a typical run, 1-5 g of substrates were loaded into the reactor. The reaction temperature was 300 ºC. Before the reaction, the substrates were degassed at 300 ºC for 5 hr. The solid (MeCp)$PtMe_3$ was heated and carried by N_2 to enter the reactor through a distributor plate. N_2 was also used as flush gas to remove unreacted precursors and any byproducts during the reaction. A typical coating cycle used the following steps: (MeCp)$PtMe_3$ dose, N_2 purge, evacuation; O_2 dose, N_2 purge, evacuation. The Pt loading was controlled by Pt precursor dose time and the number of ALD cycles. All these ALD-deposited Pt catalysts were directly used in the following catalytic tests without any further treatment.

2.3. CATALYST CHARACTERIZATION

The Pt mass fraction of the catalysts was measured by inductively coupled plasma atomic emission spectroscopy (ICP-AES). The Pt NPs were visualized with a FEI Tecnai F20 field emission gun high-resolution transmission electron microscope (TEM)/scanning transmission electron microscope (STEM). A Quantachrome Autosorb-1 was used to obtain nitrogen adsorption and desorption isotherms of the substrates at -196 ºC. The surface areas of the particles were calculated using the Brunauer–Emmett–Teller (BET) method in a relative pressure range of 0.05 - 0.25. The total pore volumes were calculated from the adsorption quantities at a relative pressure of $P/P_0 = 0.99$. The pore

size distribution curves were derived from the adsorption branches of the isotherms using the Barrett–Joyner–Halenda (BJH) method.

The pH at the point of zero charge, pH_{PZC}, is the pH at which the net surface charge is zero. The pH_{PZC} values of all supports (MWCNTs, silica gel, ALD-Al_2O_3, and γ-Al_2O_3) were measured by potentiometric titrations, which were carried out using an auto-titrator (798 MPT Titino from Metrohm), with a Metrohm electrode (6.0259.100) calibrated before each titration. Specifically, for each sample, solid loading of 0.05 g was added in 50.0 mL Milli-Q water with a pre-determined NaCl concentration. The solution was purged with high purity N_2 gas for 12 hr before titration and during the experiment. The pH value was brought down to around 3 or 4 by adding 0.10 M HCl before titration, then 0.05 g of support material was added to the solution, followed by automatic titration using 0.10 M NaOH solution. pH_{PZC} values were calculated from titration data using a traditional 2-pk model (Christl and Kretzschmar 1999).

CO-chemisorption was carried out using a Micromeritics Autochem Ⅱ 2920 to investigate and determine the Pt particle size and Pt dispersion. All four catalysts were reduced at 350 °C for 0.5 h and degassed at the same temperature in pure He for 1.5 h. The CO adsorption isotherms were obtained at 50 °C and the stoichiometry of Pt:CO was assumed to be 1:1.

2.4. CATALYTIC PERFORMANCE

The citral hydrogenation was performed in a stainless steel Parr reactor (50 mL) with an external temperature and stirring controllers. In a typical run, 0.5 g citral and 30 mL 2-propanol were introduced into the reactor. 25 mg of a Pt/MWCNTs catalyst were

added. For the hydrogenation reactions over other catalysts, 32.3 mg Pt/SiO_2, or 56.1 mg Pt/ALD-Al_2O_3, or 53.5 mg Pt/γ-Al_2O_3, were separately added in the reactor, in order to ensure an identical Pt loading (1.28 mg). The reactor was first pressurized to 10 bar with hydrogen and depressurized to atmospheric pressure. This process was repeated 10 times. Then, the reactor was filled with H_2 at 10 bar and the temperature was increased to 70 °C. A small volume of sample (1 mL) was periodically withdrawn and analyzed by using a gas chromatography (GC, Agilent 6890) equipped with a capillary column (DB-5) and a flame ionization detector (FID). Toluene was used as an internal standard. After reaction, Pt/MWCNTs, Pt/SiO_2, and Pt/ALD-Al_2O_3 catalysts were washed with 2-propanol and collected by centrifugation for cycling tests. In addition, 25 mg supports (MWCNTs, silica gel, ALD-Al_2O_3, or γ-Al_2O_3) were also used in citral hydrogenation reactions following identical procedures (mentioned above) to investigate and determine the catalytic properties of the supports. The dissolution of Pt from Pt/SiO_2 and Pt/ALD-Al_2O_3 was studied separately, by placing 0.5 g Pt/SiO_2 or Pt/ALD-Al_2O_3 particles in a 100 mL solution (2-propanol or water). Liquid samples were taken at regular periods, and the amounts of Pt NPs leached to the 2-propanol and water were analyzed by ICP-AES.

3. RESULTS AND DISCUSSION

3.1. CHARACTERIZATION OF SUPPORTS AND CATALYSTS

Figure 1 shows the nitrogen adsorption-desorption curves and pore size distributions (PSD) of MWCNTs, silica gel, porous ALD-Al_2O_3, and γ-Al_2O_3. A hysteresis loop was observed at high relative pressures in all isotherms, suggesting that

all supports had porous structures. The characteristics of the adsorption-desorption isotherms at different ranges of relative pressures, which reflected the properties of the surface area, were summarized as follows: (1) The amount of N_2 adsorbed was in the decreasing order of MWCNTs > silica gel > ALD-Al_2O_3 > γ-Al_2O_3; (2) The amount of N_2 adsorbed on all particles (at relative pressures less than 0.1) was very small, suggesting that micropores in the particles were insignificant (Li et al. 2004) and could not affect the catalytic performance of supports very much. From the PSD given in

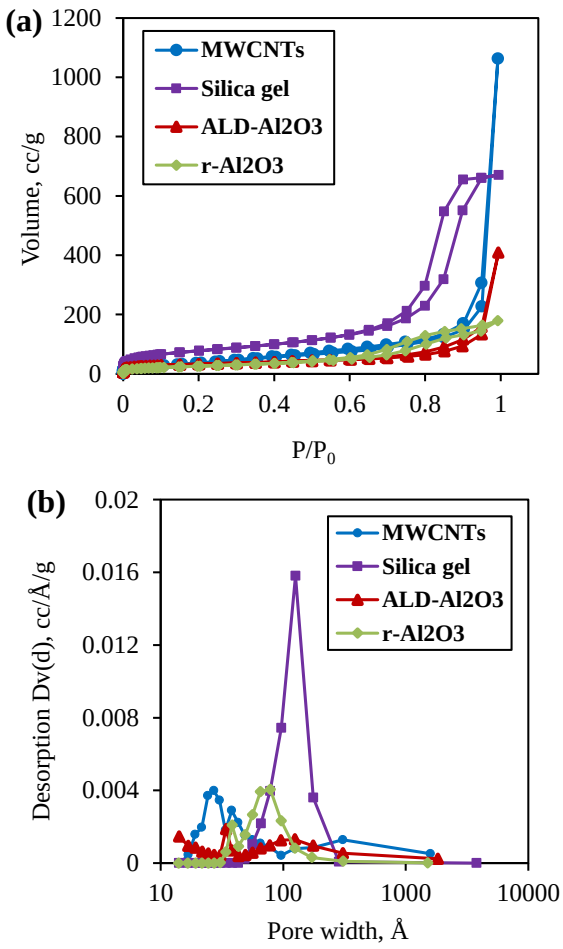

Figure 1. (a) Nitrogen adsorption and desorption isotherms, and (b) pore size distributions of MWCNTs, silica gel, ALD-Al_2O_3, and γ-Al_2O_3.

Figure 1b, these materials were eminently mesoporous in structure. MWCNTs showed two broad peaks around 2-10 nm and 10-120 nm, as shown in Figure 1b. Silica gel presented a total porosity higher than all other supports, but a narrow PSD. To the contrary, ALD-Al_2O_3 presented a wide PSD. γ-Al_2O_3 showed a sharp peak centered around 3.8 nm, and a broad peak around about 4.3-17.0 nm.

As Table 1 shows, the BET surface areas of MWCNTs, silica gel, ALD-Al_2O_3 and γ-Al_2O_3 were 144.6, 279.9, 114.6, and 95.5 m^2/g, respectively. From the calculated pore volumes listed in Table 1, the MWCNTs showed the highest total pore volume of about 1.65 cm^3g^{-1}, while γ-Al_2O_3 had a lower value of 0.28 cm^3g^{-1}. The measured pH_{PZC} values of the supports are also included in Table 1, which shows that pH_{PZC} was related to a strong acidity. SiO_2 and ALD-Al_2O_3 were acidic, and normally had Lewis and Brönsted acid sites. γ-Al_2O_3 presented a neutral surface, and MWCNTs was a basic material. Based on ICP-AES analysis, the Pt mass fractions on MWCNTs, silica gel, porous ALD-Al_2O_3, and γ-Al_2O_3 were 5.14 wt.%, 3.98 wt.%, 2.29 wt.%, and 2.40 wt.%, respectively. In order to determine Pt particle size and Pt dispersion on the supports, CO-chemisorption analysis was performed. As shown in Table 1, Pt/MWCNTs, Pt/ALD-Al_2O_3, and Pt/γ-Al_2O_3 showed similar Pt particle sizes (1.3-1.4 nm) and dispersion (75%-85%). However, the Pt particle size was larger on silica gel and the dispersion was lower. We believed that when Pt/SiO_2 was reduced by H_2 at 350 ºC in CO-chemisorption analysis, some Pt particles aggregated because of the weak interaction between Pt and silica gel, which resulted in the large Pt particle size and relatively low dispersion.

In order to verify the Pt particle size on supports, TEM/STEM was performed. Figure 2 shows that the ALD Pt NPs were highly dispersed on the surfaces of MWCNTs,

silica gel, and porous ALD-Al_2O_3. After one cycle of Pt ALD, the average Pt particle size was 1.2 nm, 1.3 nm, and 1.2 nm on MWCNTs, silica gel, and porous ALD-Al_2O_3, respectively. This was consistent with the Chemisorption results; and all of the size distributions of Pt particles were narrow. We believe that the average size of Pt NPs deposited on γ-Al_2O_3 particles, with one cycle of Pt ALD, should be around ~1.3 nm as well. Accordingly, all catalysts had similar Pt-particle sizes, as we expected.

Table 1. The properties of different supports.

	MWCNTs	Silica gel	ALD-Al_2O_3	γ-Al_2O_3
BET surface area (m^2g^{-1})	144.6	279.9	114.6	95.5
Total pore volume (cm^3g^{-1})	1.65	1.04	0.63	0.28
pH_{PZC}	7.9	4.0	6.5	7.0
Pt mass fraction (wt.%)	5.14	3.98	2.29	2.40
Pt particle size (nm)[a]	1.3	1.8	1.4	1.3
Pt dispersion (%)	82.4	62.5	76.2	83.3

[a] Pt particle size was determined in accordance with CO-chemisorption results.

3.2. CATALYTIC PERFORMANCE

The hydrogenation of citral is a parallel and consecutive reduction of different functional groups, i.e., a carbonyl group (C=O), a double bond (C=C) conjugated to the carbonyl, and an isolated double bond (C=C), from the same starting substrate. The general pathways for the hydrogenation of citral are shown in Figure 3.

As shown in Figure 4, the reaction was performed at various stirring rates between 300 rpm and 700 rpm for the Pt/MWCNTs catalyst in order to determine the

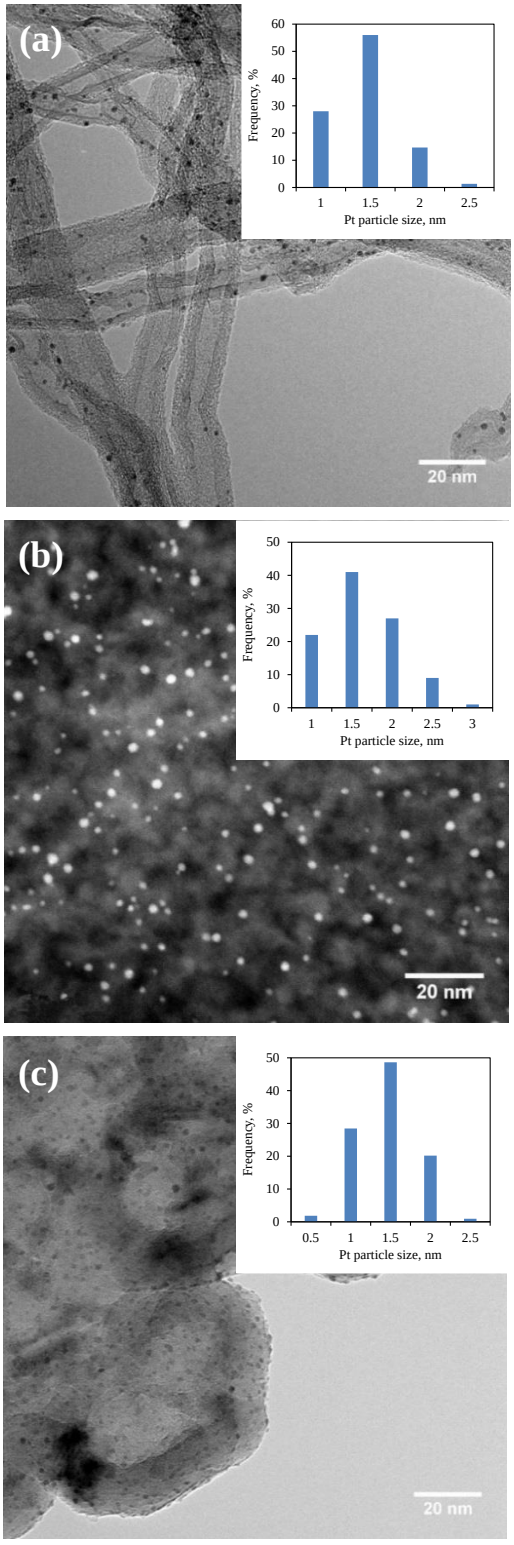

Figure 2. TEM/STEM images of Pt nanoparticles deposited on various substrates: (a) MWCNTs, (b) silica gel, and (c) ALD-Al_2O_3. The *inset* figures show the size distributions of Pt nanoparticles.

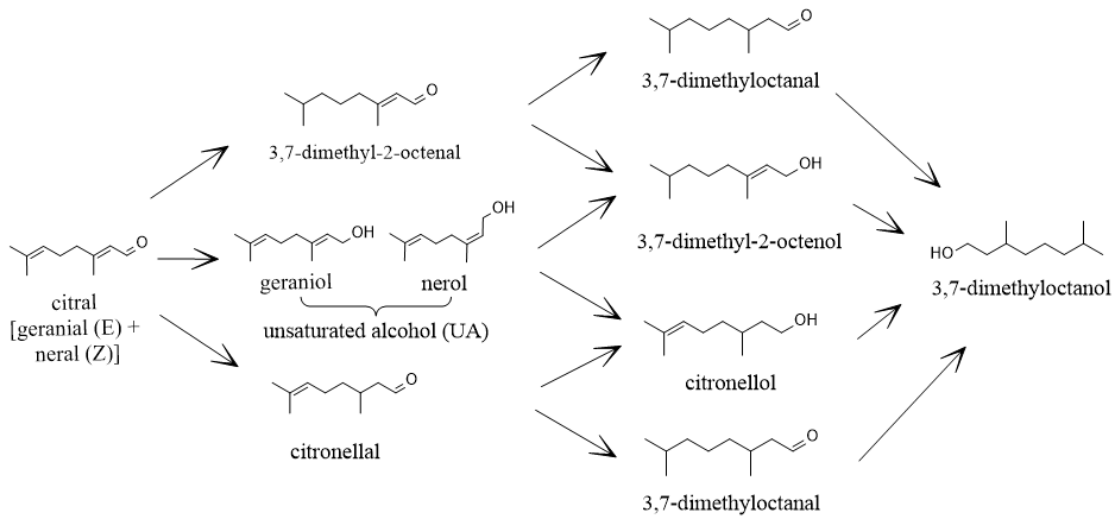

Figure 3. Reaction routes of citral hydrogenation.

slowest stirring rate that prevented diffusion limitations. The 500 rpm and 700 rpm provided similar reaction rates, indicating that a stirring rate of 500 rpm was sufficient for mass transfer. It was also anticipated that 500 rpm was the sufficient stirring rate required to minimize diffusion limitations for the other three catalysts since they had larger pores than Pt/MWCNTs (Figure1b), which are helpful for mass transfer. Thus, 500 rpm was adopted for the following experiments. The catalytic performance of the hydrogenation of citral over Pt catalysts is provided in Figure 5. Pt/SiO_2 showed the highest activity and the conversion of citral reached 82.3% after 12 hr of reaction time. The conversion of citral at 12 hr was in a decreasing order of Pt/SiO_2, $Pt/ALD\text{-}Al_2O_3$, $Pt/\gamma\text{-}Al_2O_3$, and Pt/MWCNTs. The results indicated that the characteristics of catalyst supports strongly influenced the activities of the Pt catalysts, since all catalysts were prepared using the same method, and had similar Pt particle sizes and dispersion. It seems that the acid-base properties of the supports played a significant role in the catalytic performance, but the geometric structures of the supports did not affect the activities of the catalysts very

much. For instance, MWCNTs had the largest pore volume and second highest surface area, but Pt/MWCNTs showed the lowest activity. Thus, the acid characteristics of supports are the dominate parameter that determine the activity of Pt catalysts. Since both the Lewis and Brönsted acid sites favored the catalytic activity (Bailón-García et al. 2014), silica gel showed the highest activity with its strong acid sites, while the weak acidic ALD-Al_2O_3 was the second highest active support. In contrast, the Pt/MWCNTs was not highly active. This could be due to the absence of acidic sites and the inert properties of MWCNTs. As shown in Table 2, the conversion of citral reached 18.2% over silica gel, but was much higher than that over MWCNTs. In addition, the activity of Pt/MWCNTs was also partly affected by the curvature of the MWCNTs channel (Bailón-García et al. 2013). It induced an extra modification of molecular adsorption on the Pt phase that affected the catalytic activity of citral hydrogenation. It is noted that the reaction rates over all Pt catalysts decreased, apparently after 1 hr of reaction time, indicating the deactivation of the catalysts with increasing reaction times (Figure 5). The deactivation could be caused by the adsorption of reaction products on the active Pt surface. Similarly, the reported Pt catalysts, prepared by the conventional method, were also deactivated by product poisoning and over-oxidation (Prati and Porta 2005). Since there was no oxygen in this reaction, the Pt NPs on the supports could be covered by reaction products. This indicated that supports did not improve resistance to the deactivation of catalysts.

The selectivity of the main products (UA, citronellol and citronellal), as a function of reaction time over different Pt catalysts, is shown in Figure 6. For all catalysts, the selectivity of UA and citronellol increased with increased reaction time. In contrast, the

selectivity of citronellal kept decreasing after a few hours of reaction. This observation could be explained since citral was adsorbed on the Pt particles through both C=C and C=O groups at the beginning of the reaction. Then, the adsorption occurred through C=O,

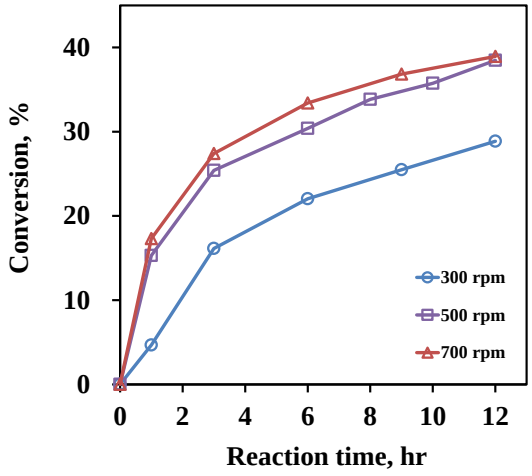

Figure 4. Effect of stirring speed on citral hydrogenation over Pt/MWCNTs. Reaction conditions: 1.28 mg of Pt, 0.5 g citral, 30 mL 2- propanol, P_{H2} = 10 bar, 70 ºC.

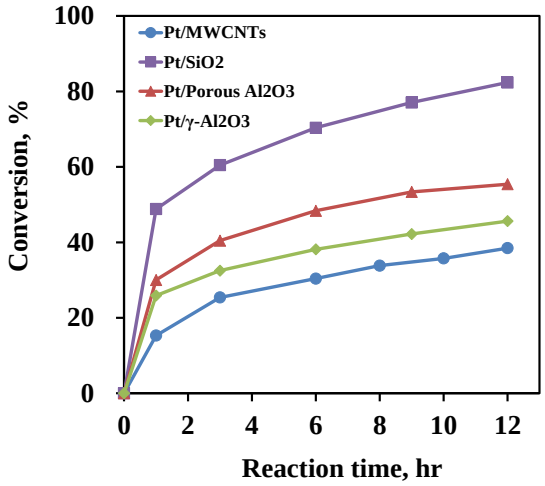

Figure 5. Conversion of citral as function of reaction time over different Pt catalysts. Reaction conditions: 1.28 mg of Pt, 0.5 g citral, 30 mL 2- propanol, P_{H2} = 10 bar, 70 ºC, 500 rpm.

Table 2. Conversion and products distribution after 12 hr of reaction using different supports as catalysts.

Catalyst	Conversion, %	Selectivity distribution, %			
		UA	Citronellal	Citronellol	Others
MWCNTs	3.0	43.7	35.4	3.1	17.8
Silica gel	18.9	30.1	45.2	10.7	14.0
ALD-Al_2O_3	11.3	24.3	43.2	4.5	28.0
γ-Al_2O_3	10.5	23.7	42.7	5.2	28.4

Reaction conditions: 25 mg of support, 500 rpm, 0.5 g citral, 30 mL 2- propanol, P_{H2} = 10 bar, 70 ºC.

mostly after citronellal reached a certain concentration (Daly et al. 2014). According to results reported by Daly et al., the selectivity of C=O reached more than 90% after the formation of citronellal at the beginning of the reaction (Daly et al. 2014). Though Pt/MWCNTs was not highly active, it showed the highest selectivity of UA, due to a transfer of the π-electrons from the graphene layer to the Pt particles (Ma et al. 2007). In this way, the charge density on the metal increased, thus decreasing the probability of C=C bond activation (Toebes et al. 2003). This could affect the properties of the metallic phase and their catalytic behavior (Bailón-García et al. 2013; Bligaard 2009). The selectivity of UA for Pt/MWCNTs were close to that reported previously by Qin et al. (Qin et al. 2008), showing a selectivity of 59.2% in the hydrogenation of citral using Pt/MWCNTs. Santiago-Pedro et al. (2013) applied acid solids (Pt/SiO_2, Pt/SiO_2-TiO_2, and Pt/SiO_2-ZrO_2) and basic materials (Pt/MgAl-c) as Pt supports for the hydrogenation of UA. They reported that the formation of UA was directly related to the acidity of the support. The trend of selectivity was found to be Pt/SiO_2-ZrO_2> Pt/SiO_2-TiO_2> Pt/SiO_2>

Pt/MgAl-c in their study. However, when compared to the favored adsorption of citral through the carbonyl group on Lewis acid sites (Santiago-Pedro et al. 2013), Brönsted acid sites favored the cracking of citral molecules and/or their hydrogenated products (Bailón-García et al. 2014), which would reduce the selectivity to UA for Pt/SiO_2. In addition, it was easier to induce further hydrogenation of UA and citronellal to citronellol over Pt/SiO_2 due to its high activity (Figure 6b), but decrease the selectivity to UA. Moreover, when compared with other supports, SiO_2 was the most active substrate in

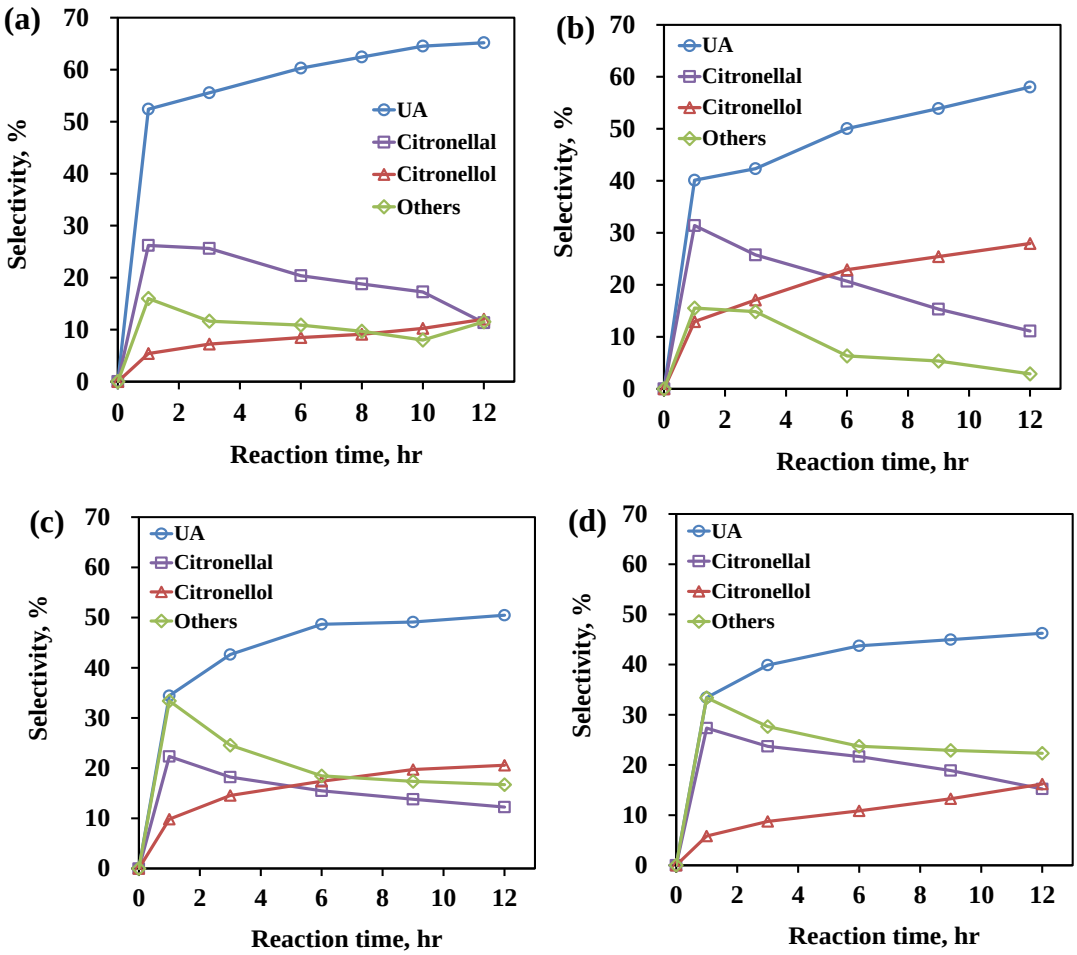

Figure 6. Product selectivity as a function of reaction time over (a) Pt/MWCNTs, (b) Pt/SiO_2, (c) $Pt/ALD\text{-}Al_2O_3$, and (d) $Pt/\gamma\text{-}Al_2O_3$.

citral hydrogenation. As shown in Table 2, the selectivity to UA over SiO_2 was not high (less than 35%) and it would affect the catalytic performance of Pt/SiO_2.

In comparison, ALD-Al_2O_3 and γ-Al_2O_3 had lower selectivity to UA than Pt/MWCNTs and Pt/SiO_2. There was an electronic charge transfer from Al_2O_3 to Pt particle that provided a basic character (δ-) that increased its electronic density (Álvarez-Rodríguez et al. 2011). Thus, due to the electronic repulsion, the adsorption of citral molecules through carbonyl bond was hindered, resulting in preferential hydrogenation of C=C, which was consistent with previous reports (Santiago-Pedro et al. 2013). Moreover, both ALD-Al_2O_3 and γ-Al_2O_3 showed a lower selectivity to UA than MWCNTs and silica gel (Table 2). Though the activities of ALD-Al_2O_3 and γ-Al_2O_3 were not high, the performance of Pt catalysts could still be affected. When compared with Pt/γ-Al_2O_3, Pt/ALD-Al_2O_3 showed slightly higher selectivity to UA at 12 hr of reaction time, which could be attributed to the higher conversion. Both catalysts showed similar UA selectivity at the same conversion. For example, the UA selectivity was 42.6% and 43.1% over Pt/ALD-Al_2O_3 and Pt/γ-Al_2O_3 at the conversion of 40%, respectively. Bailón-García et al. (2014) employed SiO_2, TiO_2, Al_2O_3, and carbon xerogel as Pt supports to catalyze the hydrogenation of citral, and found that Pt/Al_2O_3 showed both higher conversion (~50%) and selectivity (~40%) than Pt/SiO_2. This result was not consistent with what we have seen in this work. The difference might result from different pH_{PZC} values and methods of catalyst preparation. In their report, the pH_{PZC} of Al_2O_3 and SiO_2 was 4.39 and 7.58, respectively. On the contrary, Al_2O_3 was neutral and SiO_2 was acid in our study. An acid-base property affects the activity and selectivity of catalysts greatly; thus, the results are different.

The recycle and reuse ability of catalysts is one of the key factors in practical applications, and this is especially important for noble metal catalysts due to their high cost. During the cycling experiments, 5% of a fresh catalyst was added each time to make up for the loss during the filtration process. The results of the successive experiments of citral hydrogenation catalyzed by Pt/MWCNTs, Pt/SiO_2, and Pt/porous ALD-Al_2O_3 are shown in Figure 7, Figure 8, and Figure 9, respectively. For the Pt/SiO_2 catalyst, three cycles were applied and a noticeable decrease in conversion was observed with an increase in the number of reaction cycles, as shown in Figure 8a. In contrast, a total of six cycles were used for the Pt/MWCNTs and Pt/ALD-Al_2O_3 catalysts, and no noticeable difference in catalytic activity was observed, as shown in Figure 7a and Figure 9a, respectively. The results indicated that the Pt/MWCNTs and Pt/ALD-Al_2O_3 catalysts showed higher stability than Pt/SiO_2. Figure 8b showed that the selectivity of UA for Pt/SiO_2 decreased during the cycling tests, which could be attributed to the decrease in citral conversion. It indicated that the selectivity of UA was related to the activity of Pt/SiO_2. Figure 7b and Figure 9b showed that the selectivity of UA for Pt/MWCNTs and Pt/ALD-Al_2O_3 remained constant in the cycling reactions. This implied that the properties and the particle sizes of Pt NPs on MWCNTs and ALD-Al_2O_3 changed very little. Thus, the stability of Pt/MWCNTs and Pt/ALD-Al_2O_3 catalysts was better than that of Pt/SiO_2.

Since the stability of Pt/MWCNTs was investigated in our previous study (Liang and Jiang 2013; Jiang and Liang 2014), we only focused on the stability of Pt/SiO_2 and Pt/ALD-Al_2O_3 catalysts in this work. In order to gain more insight into the loss of Pt present in the SiO_2 and porous ALD-Al_2O_3 supports during citral hydrogenation,

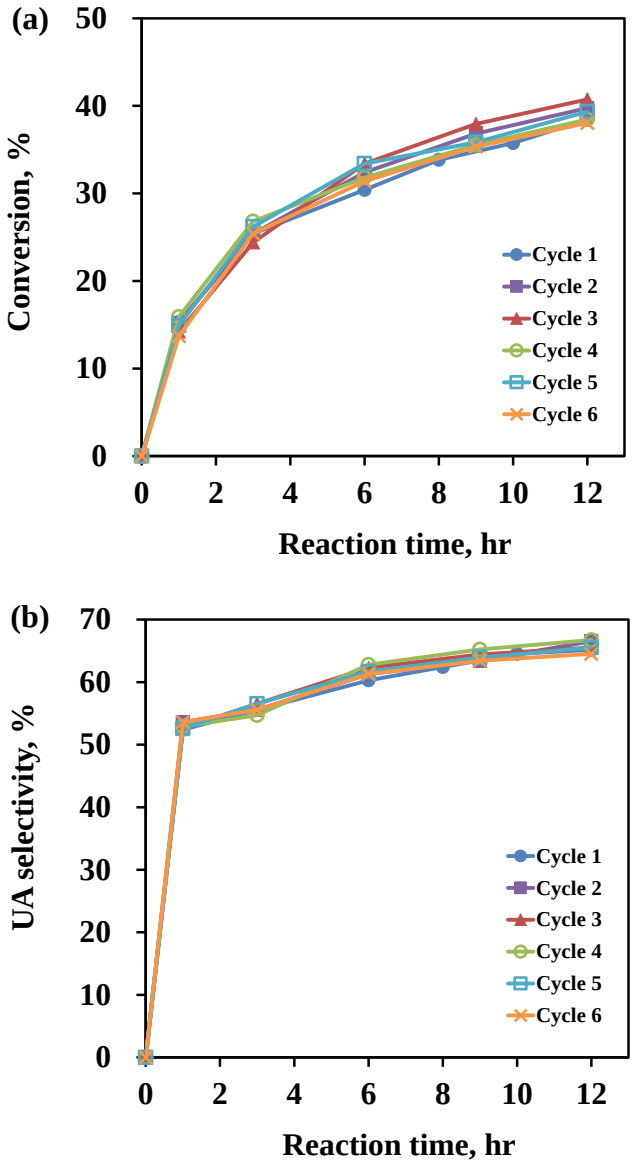

Figure 7. (a) Conversion of citral and (b) selectivity of UA in the cycling tests over Pt/MWCNTs catalyst. Reaction conditions: 1.28 mg of Pt, 0.5 g citral, 30 mL 2-propanol, P_{H2} = 10 bar, 70 ºC, 500 rpm.

dissolution experiments with the two catalysts in 2-propanol or water were carried out. A mass fraction of Pt leached in liquid was tested by ICP-AES. As shown in Figure 10, for the Pt/porous ALD-Al_2O_3, only 0.27 wt.% Pt leached in the 2-propanol, while no Pt leached in water after 72 hr of leaching time. For the Pt/SiO_2, the Pt mass fraction was

reduced by 20 wt.% after 33 hr, and the loss reached 30 wt.% after 72 hr in 2-propanol. The Pt mass fraction also was reduced by 0.23 wt.% after 33 hr and 0.24 wt.% after 72 hr

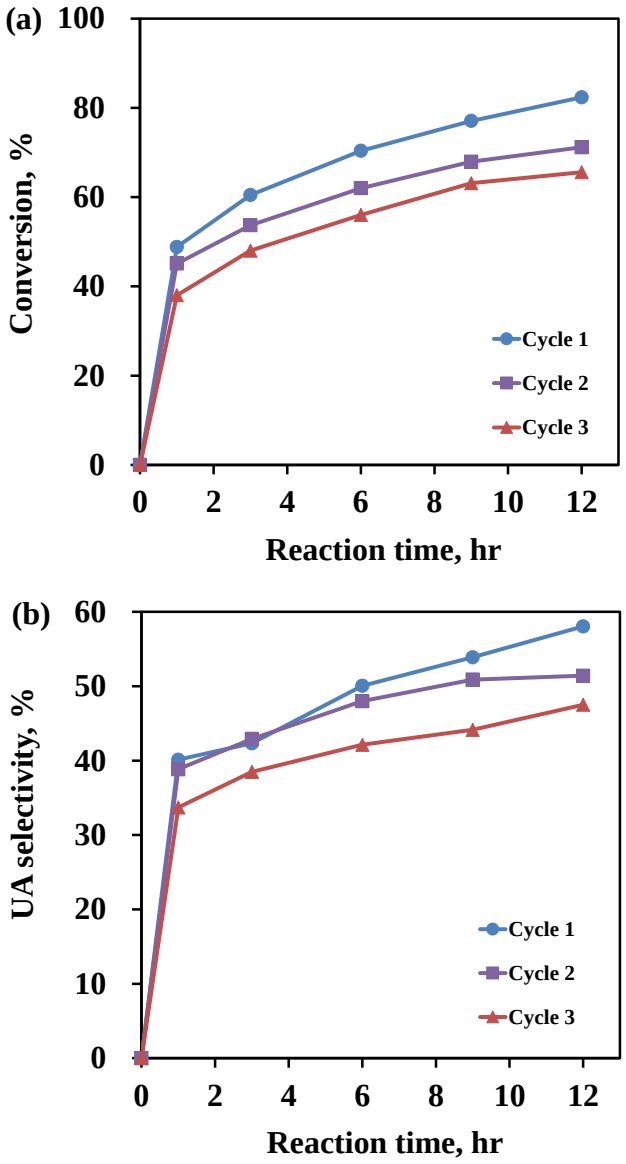

Figure 8. (a) Conversion of citral and (b) selectivity of UA in the cycling tests over Pt/SiO_2 catalyst. Reaction conditions: 1.28 mg of Pt, 0.5 g citral, 30 mL 2- propanol, P_{H2} = 10 bar, 70 ºC, 500 rpm.

in water. Clearly, the interaction between Pt/Al_2O_3 and Pt/SiO_2 was different in different liquids. In our previous work (Liang and Jiang 2013; Jiang and Liang 2014), ALD-prepared Pt/MWCNTs was used for the reactions of hydrogen transfer of acetophenone and xylose hydrogenation in 2-propanol and water. There was no noticeable decrease in

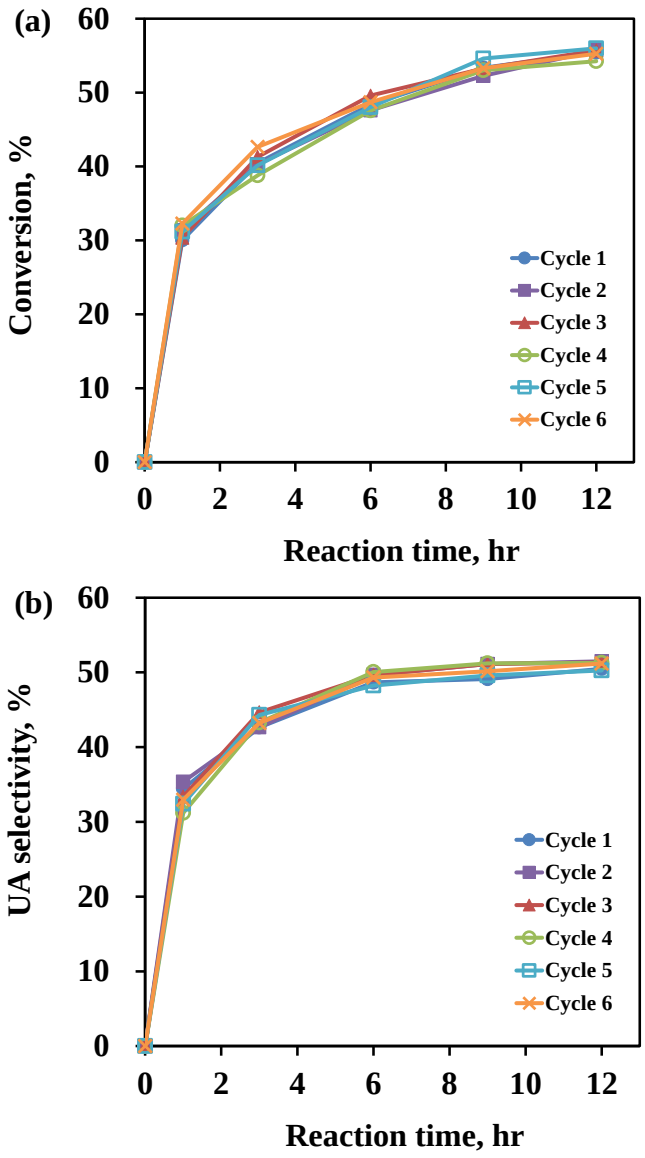

Figure 9. (a) Conversion of citral and (b) selectivity of UA in the cycling tests over $Pt/ALD\text{-}Al_2O_3$ catalyst. Reaction conditions: 1.28 mg of Pt, 0.5 g citral, 30 mL 2-propanol, P_{H2} = 10 bar, 70 ºC, 500 rpm.

catalytic activity after 10 and 20 cycles of cycling tests of the two reactions using Pt/MWCNTs as the catalyst. The stability property of ALD-prepared Pt/MWCNTs was similar to that of the Pt/ALD-Al_2O_3 sample in this study, but Pt/SiO_2 was not that stable when compared with other catalysts prepared by ALD. Interactions between Pt and supports determine the stability of catalysts. It appeared that the strong acidic sites on the surface of SiO_2 may have affected the chemical bonding between Pt and SiO_2 and, thereby, the interaction between Pt and SiO_2 was weak. This was consistent with the CO-chemisorption results. In comparison, ALD-Al_2O_3 was a weak acid and MWCNTs was a

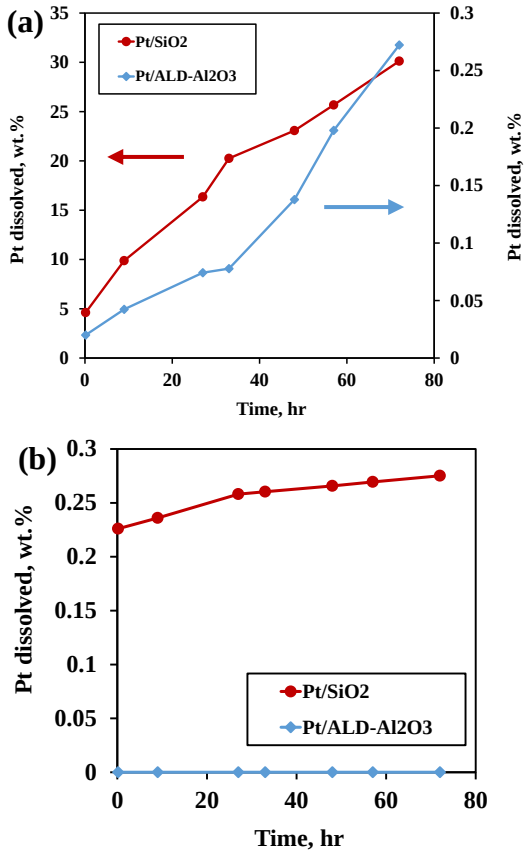

Figure 10. Pt loss of Pt/SiO_2 and Pt/ALD-Al_2O_3 catalysts in (a) 2-propanol and (b) water versus soaking time.

basic material. Moreover, in this work, Pt/SiO_2 was found to be much more stable in water than in 2-propanol, indicating that different solvents also affected the stability of catalysts. Thus, both catalytic support and solvent needed to be considered in selecting an appropriate catalyst. The detailed mechanisms of the different interactions between Pt/Al_2O_3 and Pt/SiO_2 is being pursued by this group.

4. CONCLUSIONS

Pt NPs were deposited on MWCNTs, silica gel, γ-Al_2O_3, and porous ALD-Al_2O_3 supports with similar Pt particle sizes and uniform Pt dispersion by ALD. TEM observation indicated that the diameters of Pt NPs were around 1.2-1.3 nm on all supports and Pt NPs were highly dispersed on the supports. The catalytic activity and selectivity of the Pt catalysts were evaluated by selective hydrogenation of citral to UA. Pt/SiO_2 showed the highest activity, with 82% conversion of citral and a selectivity of 58%. Pt/MWCNTs showed the highest selectivity, with 65% selectivity to UA. The order of catalytic activity and selectivity to UA was observed to be Pt/SiO_2 > Pt/ALD-Al_2O_3 > Pt/γ-Al_2O_3 > Pt/MWCNTs and Pt/MWCNTs > Pt/SiO_2 > Pt/ALD-Al_2O_3 > Pt/γ-Al_2O_3, respectively. The acid-base property of supports was the dominating factor that determined the activity of all catalysts. On the other hand, the electronic effect and geometric structure influenced the product distribution of citral hydrogenation greatly for Pt/MWCNTs. The cycling experiments indicated that the Pt/ALD-Al_2O_3 had better stability than Pt/SiO_2 due to the different interactions between Pt-SiO_2 and Pt-Al_2O_3 in the solvent.

CONFLICT OF INTEREST

The authors declare no competing financial interest.

ACKNOWLEDGEMENTS

Acknowledgment is made to the donors of the American Chemical Society Petroleum Research Fund for partial support of this research. The authors also thank Jessica TerBush at the Materials Research Center at Missouri University of Science and Technology for TEM analysis.

REFERENCES

Álvarez-Rodríguez J., Rodríguez-Ramos I., Guerrero-Ruiz A., and Arcoya A. (2011) Selective hydrogenation of citral over Pt/KL type catalysts doped with Sr, La, Nd and Sm. Appl. Catal., A 401:56-64

Bailón-García E., Carrasco-Marín F., Pérez-Cadenas A. F., and Maldonado-Hodar F. (2014) Microspheres of carbon xerogel: An alternative Pt-support for the selective hydrogenation of citral. Appl. Catal., A 482:318-326

Bailón-García E., Maldonado-Hódar F. J., Pérez-Cadenas A. F., and Carrasco-Marín F. (2013) Catalysts supported on carbon materials for the selective hydrogenation of citral. Catalysts 3:853-877

Bligaard T. (2009) Linear energy relations and the computational design of selective hydrogenation/dehydrogenation catalysts. Angew. Chem. Int. Ed. 48:9782-9784

Christensen S. T., Feng H., Libera J. L., Guo N., Miller J. T., Stair P. C., and Elam J. W. (2010) Supported Ru− Pt bimetallic nanoparticle catalysts prepared by atomic layer deposition. Nano Lett. 10:3047-3051

Christl I., and Kretzschmar R. (1999) Competitive sorption of copper and lead at the oxide-water interface: Implications for surface site density. Geochim. Cosmochim. Acta 63:2929-2938

Claus P. (1998) Selective hydrogenation of ά, β-unsaturated aldehydes and other C=O and C= C bonds containing compounds. Top. Catal. 5:51-62

Daly H., Manyar H., Morgan R., Thompson J. M., Delgado J.-J., Burch R., and Hardacre C. (2014) Use of Short Time-on-Stream Attenuated Total Internal Reflection Infrared Spectroscopy To Probe Changes in Adsorption Geometry for Determination of Selectivity in the Hydrogenation of Citral. ACS Catal. 4:2470-2478

Feng H., Elam J. W., Libera J. A., Setthapun W., and Stair P. C. (2010) Palladium catalysts synthesized by atomic layer deposition for methanol decomposition. Chem. Mater. 22:3133-3142

Gallezot á., and Richard D. (1998) Selective hydrogenation of α, β-unsaturated aldehydes. Cat. Rev. 40:81-126

Hájek J., Kumar N., Salmi T., and Murzin D. Y. (2005) Short overview on the application of metal-modified molecular sieves in selective hydrogenation of cinnamaldehyde. Catal. Today 100:349-353

Jiang C., and Liang X. (2014) Catalytic hydrogen transfer of ketones over atomic layer deposited highly-dispersed platinum nanoparticles supported on multi-walled carbon nanotubes. Catal. Commun. 46:41-45

Jiang C., Shang Z., and Liang X. (2015) Chemoselective Transfer Hydrogenation of Nitroarenes Catalyzed by Highly Dispersed, Supported Nickel Nanoparticles. ACS Catal. 5:4814-4818

King J. S., Wittstock A., Biener J., Kucheyev S. O., Wang Y. M., Baumann T. F., Giri S. K., Hamza A. V., Baeumer M., and Bent S. F. (2008) Ultralow loading Pt nanocatalysts prepared by atomic layer deposition on carbon aerogels. Nano Lett. 8:2405-2409

Leskelä M., and Ritala M. (2003) Atomic layer deposition chemistry: recent developments and future challenges. Angew. Chem. Int. Ed. 42:5548-5554

Li J., Liang X., King D. M., Jiang Y.-B., and Weimer A. W. (2010) Highly dispersed Pt nanoparticle catalyst prepared by atomic layer deposition. Appl. Catal., B 97:220-226

Li Z., Pan Z., and Dai S. (2004) Nitrogen adsorption characterization of aligned multiwalled carbon nanotubes and their acid modification. J. Colloid Interface Sci. 277:35-42

Liang X., and Jiang C. (2013) Atomic layer deposited highly dispersed platinum nanoparticles supported on non-functionalized multiwalled carbon nanotubes for the hydrogenation of xylose to xylitol. J. Nanopart. Res. 15:article No. 1890

Liang X., Li N.-H., and Weimer A. W. (2012) Template-directed synthesis of porous alumina particles with precise wall thickness control via atomic layer deposition. Microporous Mesoporous Mater. 149:106-110

Liang X., Zhou Y., Li J., and Weimer A. W. (2011) Reaction mechanism studies for platinum nanoparticle growth by atomic layer deposition. J. Nanopart. Res. 13:3781-3788

Lordi V., Yao N., and Wei J. (2001) Method for supporting platinum on single-walled carbon nanotubes for a selective hydrogenation catalyst. Chem. Mater. 13:733-737

Lu J., Fu B., Kung M. C., Xiao G., Elam J. W., Kung H. H., and Stair P. C. (2012) Coking-and sintering-resistant palladium catalysts achieved through atomic layer deposition. Science 335:1205-1208

Ma H., Wang L., Chen L., Dong C., Yu W., Huang T., and Qian Y. (2007) Pt nanoparticles deposited over carbon nanotubes for selective hydrogenation of cinnamaldehyde. 8:452-456

Noller H., and Lin W. (1984) Activity and selectivity of $NiCuAl_2O_3$ catalysts for hydrogenation of crotonaldehyde and mechanism of hydrogenation. J. Catal. 85:25-30

Prati L., and Porta F. (2005) Oxidation of alcohols and sugars using Au/C catalysts: Part 1. Alcohols. Appl. Catal., A 291:199-203

Qin F., Shen W., Wang C., and Xu H. (2008) Selective hydrogenation of citral over a novel platinum/MWNTs nanocomposites. Catal. Commun. 9:2095-2098

Santiago-Pedro S., Tamayo-Galván V., and Viveros-García T. (2013) Effect of the acid–base properties of the support on the performance of Pt catalysts in the partial hydrogenation of citral. Catal. Today 213:101-108

Suntola T. (1992) Atomic layer epitaxy. Thin Solid Films 216:84-89

Toebes M. L., Prinsloo F. F., Bitter J. H., van Dillen A. J., and de Jong K. P. (2003) Influence of oxygen-containing surface groups on the activity and selectivity of carbon nanofiber-supported ruthenium catalysts in the hydrogenation of cinnamaldehyde. 214:78-87

Vilella I., Borbáth I., Margitfalvi J., Lázár K., de Miguel S., and Scelza O. (2007) $PtSn/SiO_2$ catalysts prepared by controlled surface reactions for citral hydrogenation in liquid phase. Appl. Catal., A 326:37-47

Vu H., Gonçalves F., Philippe R., Lamouroux E., Corrias M., Kihn Y., Plee D., Kalck P., and Serp P. (2006) Bimetallic catalysis on carbon nanotubes for the selective hydrogenation of cinnamaldehyde. J. Catal. 240:18-22

II. ATOMIC LAYER DEPOSITED PT-CO BIMETALLIC CATALYSTS FOR SELECTIVE HYDROGENATION OF A, B-UNSATURATED ALDEHYDES TO UNSATURATED ALCOHOLS

Xiaofeng Wang, † Yuzi Liu, ‡ and Xinhua Liang †,*

† Department of Chemical and Biochemical Engineering, Missouri University of Science and Technology, Rolla, MO 65409, United States

‡ Center for Nanoscale Materials, Argonne National Laboratory, 9700 S. Cass Ave., Argonne, IL 60439, United States

KEYWORDS Platinum (Pt), Cobalt (Co), Al_2O_3, Atomic layer deposition (ALD), Cinnamaldehyde (CAL), Bimetallic catalyst

ABSTRACT

Highly dispersed Pt-Co bimetallic catalysts were deposited on multi-walled carbon nanotubes (MWCNTs) by atomic layer deposition (ALD). Both high-resolution TEM and STEM/EDS analysis verified the formation of Pt-Co bimetallic particles. High selectivity to cinnamic alcohol (> 90%) was achieved with high conversion (> 90%) in hydrogenation of cinnamaldehyde over an optimized Pt-Co/MWCNTs catalyst. The catalyst also showed both high activity and high selectivity in C=O activation (> 90%) in selective hydrogenation reactions of other α, β-unsaturated aldehydes, which indicates that the bimetallic catalyst was a universal and highly efficient catalyst for these kinds of reactions. Through a series of experiments and comparisons, the synergistic effects of Pt, Co, and MWCNTs were investigated. The results revealed that the interaction between Pt and Co NPs played a vital role in the high selectivity in C=O activation, and the

synergistic effect between Pt-Co and MWCNTs boosted greatly the activity of Pt-Co bimetallic catalysts.

1. INTRODUCTION

Selective hydrogenation of α, β-unsaturated aldehydes to unsaturated alcohols is of great importance due to numerous applications of these alcohols in fine chemical industries, such as the production of chemicals, perfume, fragrances, and pharmaceutical intermediates.[1-3] Among various α, β-unsaturated aldehydes, cinnamaldehyde (CAL) and citral are two important representatives, and the selective hydrogenation of CAL and citral are good models for investigating catalytic performance. Selective hydrogenation is a rather complex reaction network involving several parallel and consecutive reductions of different functional groups, i.e., a carbonyl group (C=O), a double bond (C=C) conjugated to the carbonyl group, and an isolated double bond (C=C) in a citral molecule. Since the hydrogenation of C=C bond is thermodynamically more favorable than that of the C=O group, it is essential that a high selective hydrogenation of C=O bond is achieved.[4]

During the past decade, a number of studies have been made of a variety of bimetallic catalysts.[5-8] Bimetallic catalysts usually showed a high catalytic activity due to the synergetic effects of two metal elements and a high selectivity to unsaturated alcohols due to electronic and geometric effects, when compared to monometallic catalysts. The synergistic effect is connected to an intimate contact between two metal elements on substrates,[9-10] and refers to the electron transfer between these two metal elements, which

results in improved activity and selectivity in C=O activation. Among them, platinum (Pt) – cobalt (Co) bimetallic catalysts attracted increasing interest, while high unsaturated alcohol yields gained over Pt-Co catalysts in some studies. [8, 11-13] Though the interaction between Pt and Co has been widely investigated,[8, 12] the role of interaction between Pt-Co bimetallic nanoparticles (NPs) and substrates on catalytic performance has not been reported. Studies of the synergistic effects of Pt, Co, and substrates on selective hydrogenation reactions are lacking and the mechanisms as to how they work collectively to improve the activity and selectivity of C=O activation are not clear. For these reactions, it is essential that these synergistic effects be systematically investigated in order to further optimize bimetallic catalysts.

Our previous report explored the effects of Pt monometallic catalyst support (including multi-walled carbon nanotubes (MWCNTs), SiO_2, and γ-Al_2O_3) on hydrogenation of citral.[14] Compared to Pt/SiO_2 and Pt/γ-Al_2O_3 catalysts, Pt/MWCNTs showed a higher selectivity (62%) to that of unsaturated alcohol (UA).[14] Thus, MWCNTs were chosen as the support for this work. First, different amounts of Pt and Co were deposited on MWCNTs, via atomic layer deposition (ALD), to obtain various mass ratios of Pt to Co for Pt-Co bimetallic catalysts. ALD has been utilized to deposit metal oxide films and metal nanoparticles with sub-nanometer-size control of film thickness and well controlled particle size.[15-16] The catalytic performance of the bimetallic catalysts was evaluated for selective hydrogenation of CAL and citral reaction, and the Pt-Co catalysts were optimized. Then, the optimized catalyst was used in other selective hydrogenation reactions of α, β-unsaturated aldehydes to verify its universality. Al_2O_3 ALD was applied for preparation of Pt-Co/Al_2O_3/MWCNTs catalysts to separate Pt-Co and MWCNTs, as

schematically shown in Figure 1. The synergetic effects between Pt-Co and MWCNTs on the catalytic performance of Pt-Co bimetallic catalysts were investigated through a series of CAL hydrogenation reactions. Moreover, in order to study the interaction and synergetic effect between Pt and Co NPs, a mixture of Pt/MWCNTs and Co/MWCNTs monometallic catalysts was used for a CAL hydrogenation reaction, so that the contact between Pt and Co NPs could be avoided. By comparing the CAL hydrogenation reaction results, the role of interaction between Pt and Co NPs was identified.

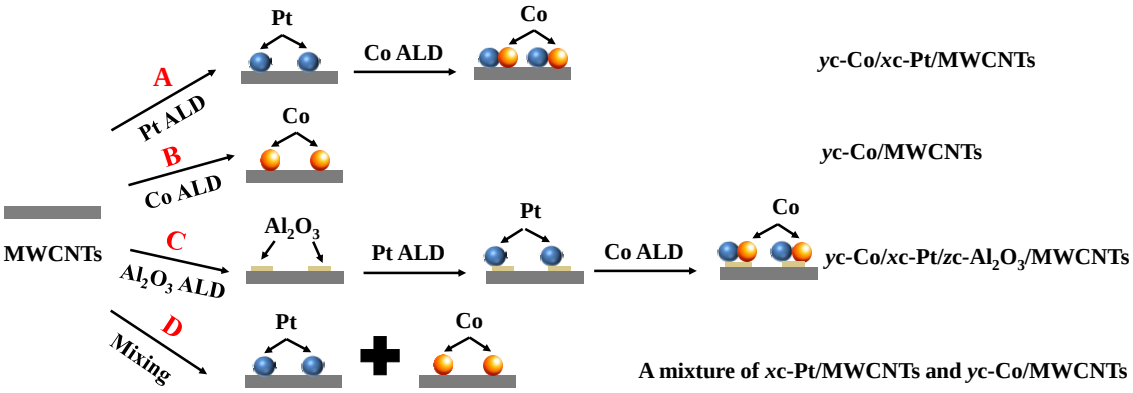

Figure 1. Scheme for the synthesis of Pt and Co monometallic and bimetallic catalysts (*x*, *y*, and *z* are the number of Pt, Co, and Al_2O_3 ALD cycles, respectively, and the order of *x*, *y*, and *z* represents the order of deposition).

2. EXPERIMENTAL SECTION

2.1. CATALYST PREPARATION

All catalysts were synthesized as schematically presented in Figure 1. MWCNTs supported Pt and Pt-Co catalysts were obtained via path A, while Co/MWCNTs was prepared through path B. The Pt and Pt-Co bimetallic NPs were isolated from MWCNTs

via coating five cycles of Al_2O_3 ALD on MWCNTs (path C), and a mixture of Pt/MWCNTs and Co/MWCNTs catalysts was prepared, as shown in path D. *x*, *y*, and *z* are the number of cycles of Pt, Co, and Al_2O_3 ALD, respectively. The order of *x*, *y*, and *z* represents the order of ALD deposition. The ALD coating process was carried out in a fluidized bed reactor, as described in detail elsewhere.[17-18] All catalysts were directly used in the following catalytic tests without any further treatment. The details of Pt ALD, Co ALD, and Al_2O_3 ALD are described in the Supporting Information (SI).

2.2. CATALYST CHARACTERIZATION

A Quantachrome Autosorb-1 was used to obtain nitrogen adsorption and desorption isotherms of MWCNTs and all catalysts at -196 ºC. The surface areas of the samples were calculated using the Brunauer–Emmett–Teller (BET) method in a relative pressure range of 0.05-0.25. The total pore volumes were calculated from the adsorption quantity at a relative pressure of P/P_0 = 0.99. The pore size distribution curves of mesopores and micropores were derived from the adsorption branches of the isotherms using the Barrett–Joyner–Halenda (BJH) method and the Horvath–Kawazoe (HK) method, respectively. The Pt, Co, and Al mass fractions of all catalysts were measured by inductively coupled plasma atomic emission spectroscopy (ICP-AES). The catalysts were visualized with a FEI Tecnai F20 field emission gun high-resolution transmission electron microscope (TEM)/scanning transmission electron microscope (STEM). At least 200 particles were randomly measured to determine the average diameter of the metal NPs. The high-resolution TEM (HRTEM) images of Pt-Co/MWCNTs were obtained by a JEOL JEM-2100F TEM operated at 200 kV.

The reduction properties of the supported Pt, Pt-Co, Co, Pt/Al_2O_3 and $Pt-Co/Al_2O_3$-based catalysts were measured by hydrogen temperature programmed reduction (H_2-TPR). H_2-TPR was performed in a quartz tube using Micromeritics Autochem Ⅱ 2920 and the reduction of the samples was performed using 10 mol% H_2/Ar flowing at a heating rate of 10 ºC/min. CO-chemisorption was performed using Micromeritics Autochem Ⅱ 2920 to determine the Pt dispersion. 2c-Pt/MWCNTs and 2c-Pt/5c-Al_2O_3/MWCNTs catalysts were reduced at 350 ºC for 0.5 hr and degassed at the same temperature in pure He for 1.5 hr. The CO adsorption isotherms were obtained at 50 ºC and the stoichiometry of Pt:CO was assumed to be 1:1.

2.3. HYDROGENATION OF UNSATURATED ALDEHYDES

The hydrogenation of unsaturated aldehydes was performed in a stainless steel Parr reactor (50 mL) with an external temperature and stirring controller. In a typical run of CAL hydrogenation, 0.5 g CAL and 30 mL 2-propanol were first introduced into the reactor, and then 25 mg of 10c-Co/2c-Pt/MWCNTs catalyst were added. All catalysts had an identical total metal loading (Pt and Co), even though the total mass of each catalyst was different due to the different contents of Pt and Co on the MWCNTs (see details in Table S1). All catalysts were used directly without any pretreatment. The reactor was first pressurized to 10 bar with hydrogen and depressurized to atmosphere pressure. This process was repeated 10 times. Then the reactor was filled with H_2 at 10 bar and the temperature was increased to 80 °C. The gas replacement was done at room temperature, which did not change the state of any Pt, Pt-Co, and Co-based catalysts. The slurry was stirred at a rate of 500 rpm to eliminate the external diffusion limitations based on our

previous results.[14] A small volume of the sample (1 mL) was periodically withdrawn and analyzed by using a gas chromatography (GC, Agilent 6890) equipped with a capillary column (DB-5) and a flame ionization detector (FID). Toluene was used as an internal standard. After reaction, the catalysts were washed with 2-propanol and collected by centrifugation for cycling tests. The hydrogenation of other unsaturated aldehydes (citral, 2-furfural, and α-amylcinnamaldehyde) was also carried out following identical procedures but using different reaction temperatures. More details are described in SI.

3. RESULTS AND DISCUSSION

3.1. CATALYST CHARACTERIZATION

Some of the physical-chemical properties of the MWCNTs and of the prepared Pt, Pt-Co, and Co-based catalysts are summarized in Table 1. After Pt and Co ALD, the BET surface area and total pore volume of all catalysts decreased slightly as compared to those of MWCNTs, but the pore size distribution of all catalysts remained almost the same (Figure S1). The Co content of *y*c-Co/*x*c-Pt/MWCNTs catalysts (based on ICP-AES analysis) increased almost linearly with the increase in the number of Co ALD cycles (Figure S2), as expected. It was also noted that the increase in total metal loading (Pt and Co) resulted in a reduction in total pore volume for all samples.

Pt, Co, and Al loadings in the Al_2O_3 coated Pt and Pt-Co catalysts are summarized in Table 2. After two cycles of Pt ALD, the Pt loadings in all catalysts were similar (around 5 wt.%). It was also noted that, after Al_2O_3 ALD coating, the Co content increased rapidly with the increase in the number of Co ALD cycles, as compared to that

Table 1. Physical properties of MWCNTs and MWCNTs-supported Pt and Co catalysts (Path A and B).

Sample	BET surface area, m^2/g	Pore volume, cm^3/g [a]	Pt, wt.% [b]	Co, wt.% [b]	Average particle size, nm [c]
MWCNTs	144	2.1	0	0	-
2c-Pt/MWCNTs	136	1.8	4.8	0	1.2
5c-Co/2c-Pt/MWCNTs	137	1.7	4.7	1.1	1.5
10c-Co/2c-Pt//MWCNTs	132	1.7	4.6	2.8	1.6
30c-Co/1c-Pt/MWCNTs	128	1.6	2.8	7.3	1.7
15c-Co/MWCNTs	142	1.9	0	3.5	1.3

[a] Pore volume was obtained from the desorption curve of the N_2 isotherm. [b] Pt and Co loadings were obtained from ICP-AES. [c] The average metal particle size was obtained from TEM images.

of the MWCNTs. According to previous results, the growth rate of Al_2O_3 film was 0.10-0.15 nm/cycle via ALD.[19] So the Al_2O_3 film thickness, after five cycles Al_2O_3 ALD, was around 0.6 nm in this study. Although a calculation of a 0.6 nm Al_2O_3 layer (3.95 g/cm^3) on a ~140 m^2/g MWCNTs could lead to 24.9 wt.% Al_2O_3 loading (13.2 wt.% Al), the actual Al loading in this study was less than 5 wt.%. Thus, only ~35% of the surface area (4.7% / 13.2%) of MWCNTs was covered by Al_2O_3, and the film was not uniform. This could be attributed to the fact that Al_2O_3 only grew on specific defective sites rather than forming a uniform film on the MWCNTs through ALD, since the surface of MWCNTs lacked hydroxyl groups. A similar phenomenon has been previously reported.[16] In

addition, because of the low Al_2O_3 ALD reaction temperature (177 ºC), the Al_2O_3 film should be amorphous.

Table 2. Physical properties of MWCNTs-supported Pt and Co catalysts with Al_2O_3 coating (Path C).

Sample	BET surface area, m^2/g	Pt, wt.% [a]	Co, wt.% [a]	Al, wt.% [a]	Average particle size, nm [b]
2c-Pt/5c-Al_2O_3/MWCNTs	95	5.5	0	4.8	1.3
3c-Co/2c-Pt/5c-Al_2O_3/MWCNTs	92	5.3	3.4	4.7	1.5
5c-Co/2c-Pt/5c-Al_2O_3/MWCNTs	98	5.2	5.5	4.6	1.7
8c-Co/2c-Pt/5c-Al_2O_3/MWCNTs	94	5.2	6.4	4.5	1.7

[a] Pt, Co and Al loading were obtained from ICP-AES. [b] The average metal particle size was obtained from TEM images.

The TEM images of Pt/MWCNTs, Pt-Co/MWCNTs, and Co/MWCNTs catalysts, along with their size distributions are shown in Figure S3. The NPs were highly dispersed on the surface of the MWCNTs in all catalysts. The average sizes of the Pt NPs and Co NPs were 1.2 nm and 1.3 nm, respectively (Table 1). Compared with Pt and Co NPs, the sizes of Pt-Co bimetallic NPs were larger (1.5-1.7 nm) and their size distribution was broader (Figure S3). The elemental composition of catalyst 10c-Co/2c-Pt/MWCNTs was analyzed via STEM/EDS (Figures S4–S5) and the results indicated that the molar ratio of Pt to Co was around 1:1 for most of the NPs on the MWCNTs (Table S2). This indicates

that most particles on the MWCNTs were Pt-Co bimetallic particles, rather than Pt or Co monometallic NPs, even though the Pt to Co ratio was not identical. To further verify the formation of Pt-Co bimetallic NPs, HRTEM was performed. As shown in Figure 2, some metal NPs stuck together (red circle). The crystal fringes are clearly displayed (inset from Figure 2) and the *d*-spacing was determined to be 0.228 nm and 0.205 nm, corresponding to the (111) planes of the face-centered cubic (fcc) Pt crystals and the (111) planes of Co crystals.[20-21] Thus, the formation of Pt-Co bimetallic NPs was confirmed and the "twinned" Pt-Co NPs were defined as bimetallic NPs in this study. They were not alloy or core-shell structures.

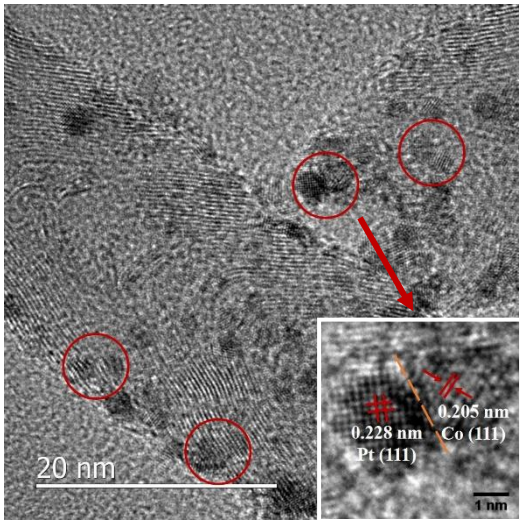

Figure 2. HRTEM image of 10c-Co/2c-Pt/MWCNTs catalyst.

As shown in Table 2 and Figure S6, the average particle sizes of Pt and Pt-Co NPs on Al_2O_3-coated MWCNTs were close to those of Pt and Pt-Co on MWCNTs, respectively. No Al_2O_3 films were observed in the TEM images, although EDS spectra verified the existence of Al on MWCNTs (Figure S7), which could have been due to the

ultrathin Al_2O_3 films (< 1 nm thick). The BET surface areas of all Al_2O_3-coated catalysts were around 95 m^2/g, which was lower than those of catalysts without Al_2O_3 ALD coating. This was due to the fact that some pores, especially micro-pores, were blocked by Al_2O_3. Based on TEM images, the metal particle sizes did not increase on the Al_2O_3-coated MWCNTs. In addition, the Pt dispersion of 2c-Pt/5c-Al_2O_3/MWCNTs (79.3%) was similar to that of 2c-Pt/MWCNTs (81.4%), which was consistent with TEM analysis. Thus, the change in surface area would not have affected the catalytic performance of catalysts very much.

The reducibility of supported catalysts is an important factor that influences their catalytic property. H_2-TPR profiles of the MWCNTs-supported Pt, Pt-Co, and Co catalysts are shown in Figure 3. No obvious peak was observed for 2c-Pt/MWCNTs and 2c-Pt/5c-Al_2O_3/MWCNTs catalysts, which indicated that Pt NPs were metallic and did no t oxidize in air after the ALD process. This was consistent with the previous report.[22] While the 15c-Co/MWCNTs catalyst presented a large peak of H_2 consumption, appearing at 422 ºC (Table 3), which implied that Co NPs were partly oxidized in air after Co ALD. The TPR profile of 10c-Co/2c-Pt/MWCNTs showed a two-stage reduction at 290 ºC and 405 ºC, which were assigned to the reduction of CoO_x that were in contact with Pt and the isolated CoO_x, respectively. It has been reported that Pt was found to significantly promote the reduction of Co.[23] Influenced by hydrogen spillover, the reduction of CoO_x shifted to lower temperatures, as the reduced Pt atoms were able to dissociate hydrogen molecules into hydrogen atoms, leading to the accelerated reduction rate of CoO_x.[24-25] This TPR analysis further verified the formation of Pt-Co bimetallic NPs, which was consistent with the results of TEM and STEM/EDS analysis. For the 5c-

Co/2c-Pt/5c-Al_2O_3/MWCNTs catalyst, two-stage reduction also showed at 388 ºC and 480 ºC. Compared with that of 10c-Co/2c-Pt/MWCNTs, the reduction temperature of 5c-Co/2c-Pt/5c-Al_2O_3/MWCNTs had obviously increased, which indicated that there was a stronger interaction between Co and Al_2O_3 than there was between Co and MWCNTs. In addition, for the 5c-Co/2c-Pt/5c-Al_2O_3/MWCNTs catalyst, the amount of H_2 consumption was smaller than that for the 10c-Co/2c-Pt/MWCNTs catalyst (Table 3), although 5c-Co/2c-Pt/5c-Al_2O_3/MWCNTs had a higher loading of Co (Table 2), which implied that 5c-Co/2c-Pt/5c-Al_2O_3/MWCNTs was more difficult to be reduced.

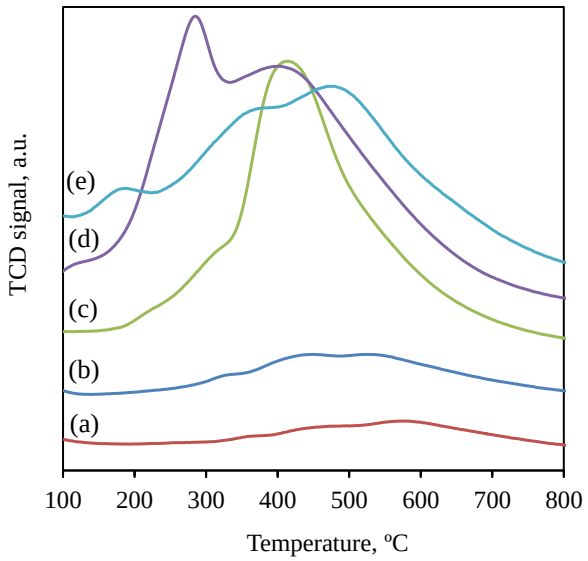

Figure 3. TPR profiles of the catalysts: (a) 2c-Pt/MWCNTs, (b) 2c-Pt/5c-Al_2O_3/MWCNTs, (c) 15c-Co/MWCNTs, (d) 10c-Co/2c-Pt/MWCNTs, and (e) 5c-Co/2c-Pt/5c-Al_2O_3/MWCNTs.

3.2. CATALYTIC PERFORMANCE

Hydrogenation of CAL is a representative reaction of selective hydrogenation of α,β-unsaturated aldehydes. The general pathways for the reaction network are shown in Figure S8. Table 4 displays the results of CAL hydrogenation catalyzed by Pt/MWCNTs, Pt-Co/MWCNTs, and Co/MWCNTs catalysts. Among all monometallic and bimetallic catalysts, the 10c-Co/2c-Pt/MWCNTs catalyst showed the highest conversion and loading; most NPs formed on the MWCNTs were Co NPs. It is also noted that the reaction rate decreased along with the reaction time (Figure S9), which was due to the fact that the reaction was performed in a batch reactor.

Table 3. H_2 consumption and temperature of TPR peaks for catalysts.

Catalyst	H_2 consumption, mmol/g_{cat}	Peak temperature, ºC
2c-Pt/MWCNTs	-	-
2c-Pt/5c-Al_2O_3/MWCNTs	-	-
15c-Co/MWCNTs	6.22	422
10c-Co/2c-Pt/MWCNTs	3.84	290, 405
5c-Co/2c-Pt/5c-Al_2O_3/MWCNTs	2.91	388, 480

As shown in Table 4, COL was the main product in the reaction of either Pt or Co catalysts; this is consistent with previous reports.[26-27] According to theoretical calculations by Delbecq and Sautet,[28] the selectivity to the unsaturated alcohol can be

Table 4. Hydrogenation of cinnamaldehyde to cinnamic alcohol catalyzed by various Pt, Co, and Pt-Co catalysts.

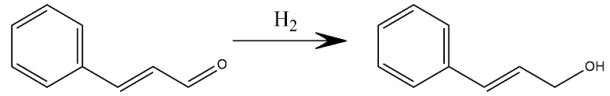

Cinnamaldehyde (CAL) Cinnamic alcohol (COL)

Entry	Catalyst	Con. (%)	Sel. (%)
1	2c-Pt/MWCNTs	46.0	62.2
2	5c-Co/2c-Pt/MWCNTs	74.3	75.4
3	10c-Co/2c-Pt/MWCNTs	93.3	93.4
4	30c-Co/1c-Pt/MWCNTs	27.3	80.1
5	15c-Co/MWCNTs	11.2	76.6

Reaction conditions: 1.87 mg of metal (Pt and Co), 0.5 g CAL, 30 mL 2-propanol, P_{H2} = 10 bar, 80 ºC, 500 rpm, and 12 hr.

correlated with the metal d-band width. Generally, flat surfaces, such as Pt(111) and Co(111), adsorb the unsaturated aldehyde in a terminal di-σ_{co} mode.[28] Therefore, Pt and Co can provide good selectivity to unsaturated alcohol, since they have a relatively large radial expansion of the d orbitals and the (111) planes of crystals.[29] In contrast, low coordination sites (such as corners, kinks, adatoms, and defective sites) favor π interactions with C=C, which account for unselective products.[8] The selectivities to the main products (COL, hydrocinnamaldehyde (HCAL), and 3-phenyl-1-propanol (HCOL)), as a function of reaction time over catalysts are shown in Figure S10. For 2c-Pt/MWCNTs and 5c-Co/2c-Pt/MWCNTs catalysts, both COL and HCOL selectivities

increased with increasing reaction time. In contrast, the selectivity to HCAL kept decreasing after a few hours of reaction. This observation could be explained by the fact that CAL was adsorbed on the Pt NPs through both C=C and C=O groups at the beginning of the reaction; then the adsorption occurred through C=O, mainly after HCAL reached a certain concentration. With further increases of Co loading in the catalysts, the selectivity to COL reached a plateau and almost remained constant, along with the reaction time, over the 10c-Co/2c-Pt/MWCNTs catalyst (Figure S10c). When the ratio of Pt to Co was small and more monometallic Co NPs existed on the MWCNTs, both the conversion of CAL and the selectivity to COL decreased, especially for the conversion.

The increase of selectivity to COL could have been due to the fact that the deposition of Co on Pt NPs modified the electronic structure of Pt atoms, and destabilized the adsorption of the C=C bond.[8] Thereby, the selectivity for C=O activation improved greatly. Figure 4a shows the CAL adsorption mode for Co/Pt/MWCNTs catalysts. The contact between Pt and Co favored the electronic transfer from Co^0 toward Pt^0,[12] which led to a positive charge density in the Co atoms and a negative charge density in the Pt atoms. The increased charge density on the metal NPs helped the $C^{\delta+}$-$O^{\delta-}$ adsorb over a Pt $^{\delta-}$-Co $^{\delta+}$ site and decrease the probability of adsorption via the C=C bond, so the selectivity to COL was higher over Pt-Co catalysts. The electron can be transferred from Co to Pt directly or through MWCNTs. The excellent electrical conductivity of MWCNTs enhanced the electronic transfer and thereby improved the charge density of the metal NPs, which promoted the adsorption and desorption rates of C=O for Pt $^{\delta-}$-Co $^{\delta+}$ sites. Thus, the activity of Pt-Co bimetallic catalysts and the conversion of CAL were higher when compared to Pt or Co monometallic catalysts. The proposed hypothesis will

be discussed and verified later. Similar phenomena was reported by Bertero et al. for hydrogenation of citral over for the Pt-Co/C catalyst.[12]

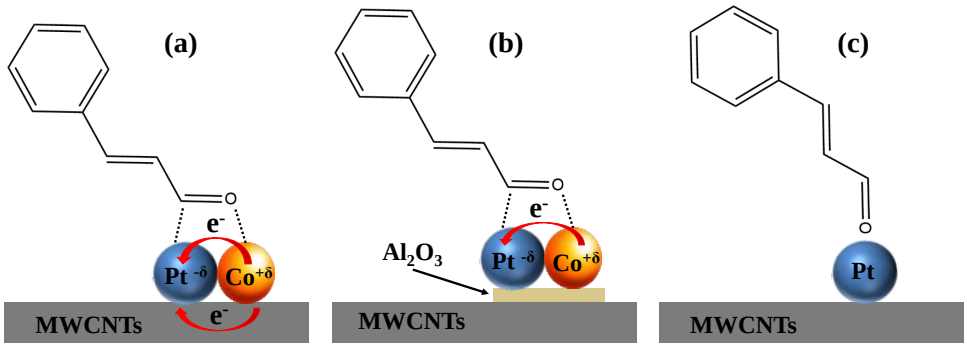

Figure 4. CAL adsorption modes for different catalysts: (a) *y*c-Co/*x*c-Pt/MWCNTs; (b) *y*c-Co/*x*c-Pt/*z*c-Al_2O_3/MWCNTs; (c) a mixture of *x*c-Pt/MWCNTs and *y*c-Co/MWCNTs.

Compared to selective hydrogenation of CAL, the reaction network of citral hydrogenation is more complicated (Figure S11), since citral contains one isolated double bond (C=C), besides a carbonyl group (C=O), and a double bond (C=C) conjugated to the carbonyl group. As shown in Table 5, 10c-Co/2c-Pt/MWCNTs still showed the highest selectivity to UA (90.5%) with a conversion of 94.5 %. In addition, the trends of citral conversions, along with reaction times for all catalysts (Figure S12), were similar to that of a CAL conversion. It is also noted that the main byproducts were citronellal and citronellol, and the catalysts produced almost no 3,6-dimethyl-2-octen-1-ol for this reaction (Figure S13). This implies that the isolated C=C was more stable than the C=C conjugated to the carbonyl in the reaction. In addition to citral, a 10c-Co/2c-Pt/MWCNTs catalyst was applied to selective hydrogenation of 2-furfural and α-amylcinnamaldehyde as well. The results are demonstrated in Figure 5. The selectivity to

the corresponding unsaturated alcohols was more than 90% for both reactions. Though high unsaturated alcohols yields (> 80%) have been achieved for Pt-Co bimetallic catalysts in some studies, only one model reaction was used in these reports.[8, 12-13] In this study, through these four selective hydrogenation reactions, our 10c-Co/2c-Pt/MWCNTs catalyst was proved to be a universally suitable catalyst with high activity and high selective for C=O for all hydrogenation of α, β-unsaturated aldehydes to unsaturated alcohols reactions, rather than for a specific one.

Table 5. Hydrogenation of citral to unsaturated alcohol catalyzed by various Pt, Co, and Pt-Co catalysts

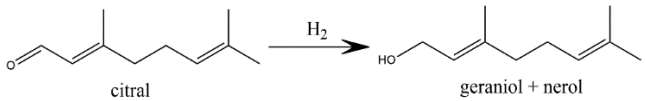

citral geraniol + nerol (UA)

Entry	Catalyst	Con. (%)	Sel. (%)
1	2c-Pt/MWCNTs	44.1	60.1
2	5c-Co/2c-Pt/MWCNTs	71.0	75.8
3	10c-Co/2c-Pt/MWCNTs	94.5	90.5
4	30c-Co/1c-Pt/MWCNTs	16.0	81.7
5	15c-Co/MWCNTs	11.1	77.1

Reaction conditions: 1.87 mg of metal (Pt and Co), 0.5 g citral, 30 mL 2-propanol, P_{H2} = 10 bar, 70 ºC, 500 rpm, and 12 hr.

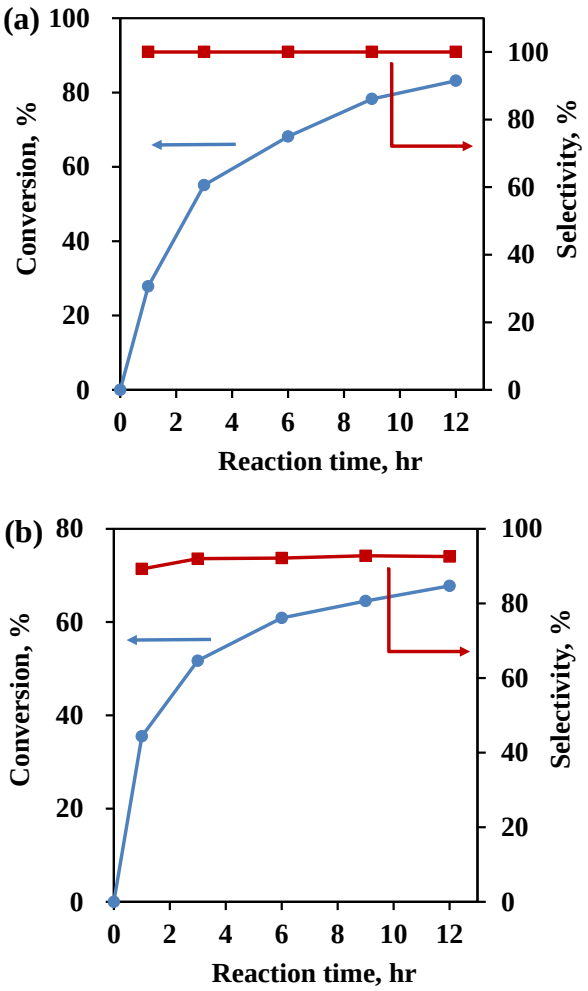

Figure 5. Conversion of (a) 2-furfural and (b) α-amylcinnamaldehyde, and selectivity to the corresponding unsaturated alcohols versus reaction time over the 10c-Co/2c-Pt/MWCNTs catalyst. Reaction conditions: 25 mg catalyst, 0.5 g reactant, 30 mL 2-propanol, P_{H2} = 10 bar, 80 ºC, and 500 rpm.

In order to verify the proposed synergistic effect among Pt, Co, and MWCNTs, an ultra-thin Al_2O_3 film (~0.6 nm thick), deposited by five cycles of Al_2O_3 ALD, was used to tune the interfaces of the catalysts. The Al_2O_3 coated catalysts were used for the reaction of CAL hydrogenation; results are presented in Table 6 and Figures S14-S15. Compared to that for the 2c-Pt/MWCNTs catalyst, the selectivity to COL for the 2c-Pt/5c-

Al_2O_3/MWCNTs catalyst decreased to 57.1%, which was consistent with our previous results.[14] After depositing Co on 2c-Pt/5c-Al_2O_3/MWCNTs, both 3c-Co/2c-Pt/5c-Al_2O_3/MWCNTs and 5c-Co/2c-Pt/5c-Al_2O_3/MWCNTs presented a much lower activity than the 10c-Co/2c-Pt/MWCNTs catalyst, since the CAL conversion reached 93.3% for 10c-Co/2c-Pt/MWCNTs. This was much higher than those for 3c-Co/2c-Pt/5c-Al_2O_3/MWCNTs and 5c-Co/2c-Pt/5c-Al_2O_3/MWCNTs, although all three catalysts have similar selectivities for C=O activation. As schematically demonstrated in Figure 4b, due to the existence of Al_2O_3 film, the electronic transfer can only occur from Co to Pt

Table 6. Hydrogenation of CAL to COL catalyzed by various catalysts

Entry	Catalyst	Con. (%)	Sel. (%)
1	2c-Pt/5c-Al_2O_3/MWCNTs	45.2	57.1
2	3c-Co/2c-Pt/5c-Al_2O_3/MWCNTs	32.6	88.3
3	5c-Co/2c-Pt/5c-Al_2O_3/MWCNTs	52.7	85.7
4	8c-Co/2c-Pt/5c-Al_2O_3/MWCNTs	33.1	87.3
5	A mixture of 2c-Pt/MWCNTs and 15c-Co/MWCNTs	43.4	53.1

Reaction conditions: 1.87 mg of metal (Pt and Co), 0.5 g CAL, 30 mL 2-propanol, P_{H2} = 10 bar, 80 ºC, 500 rpm, and 12 hr.

directly, instead of through MWCNTs in 3c-Co/2c-Pt/5c-Al_2O_3/MWCNTs and 5c-Co/2c-Pt/5c-Al_2O_3/MWCNTs catalysts. The increased charge density on the bimetallic Pt-Co NPs would promote selectivity to COL. Thus, the interaction between Pt and Co NPs played an important role in the selectivity to C=O. In other words, the formation of Pt-Co bimetallic NPs was the dominate factor in the high selectivity to COL in the hydrogenation of the CAL reaction, no matter what support materials were used.

However, the synergistic effect among Pt, Co, and MWCNTs greatly affected the activity of Pt-Co bimetallic catalysts. After an ultra-thin layer of Al_2O_3 film was used to isolate Pt-Co bimetallic NPs from MWCNTs (Figure 4b), the conversion of CAL decreased significantly for the 3c-Co/2c-Pt/5c-Al_2O_3/MWCNTs and 5c-Co/2c-Pt/5c-Al_2O_3/MWCNTs catalysts. This indicated that the interaction between Pt-Co bimetallic NPs and MWCNTs had a great influence on the activity of bimetallic catalysts. It helps explain that MWCNTs worked as a “bridge”, connected Pt with Co, and helped electronic transfer from Co to Pt, which enhanced the charge density on metal NPs (Pt and Co), and boosted the adsorption and dissociation rate of C=O over $Pt^{\delta-}$-$Co^{\delta+}$ sites for reactions of CAL hydrogenation. In addition, Co was more preferentially deposited on Al_2O_3 by ALD based on ICP-AES results, and thus had less contact with Pt. This also resulted in a low activity of Al_2O_3-coated Pt-Co bimetallic catalysts. The synergistic effect between Pt-Co bimetallic NPs and MWCNTs promoted the activity of Pt-Co bimetallic catalysts.

To further verify the interaction between Pt and Co NPs, a mixture of Pt and Co NPs was used for CAL hydrogenation. As shown in Table 6 and Figure S15e, the CAL conversion and selectivity to COL were 43.4% and 53.1% over a mixture of the 2c-Pt/MWCNTs and 15c-Co/MWCNTs catalysts, respectively. Both of them were much

lower than that for the 10c-Co/2c-Pt/MWCNTs catalyst, although the Pt and Co masses of the mixed catalysts added to the reaction were the same as the Pt and Co masses of the 10c-Co/2c-Pt/MWCNTs catalyst, respectively. As schematically shown in Figure 4c, the reactant, CAL, was mainly adsorbed on the 2c-Pt/MWCNTs for a hydrogenation reaction since the activity of the 2c-Pt/MWCNTs catalyst was much higher than that of the 15c-Co/MWCNTs catalyst (Table 4). Thus, this proved that the interaction between Pt and Co NPs had played an important role in the activity of Pt-Co bimetallic catalysts and the selectivity in C=O activation. It was also noted that in all of these hydrogenation reactions, no hydrogen transfers or etherification reactions were observed in the hydrogenation reactions based on GC-FID results; this was consistent with our previous study and others.[14, 30-32]

Although Pt-Co bimetallic catalysts have been proved to be suitable catalysts for selective hydrogenation of α, β-unsaturated aldehydes for unsaturated alcohol reactions,[29] no previous studies have reported the effect of support on hydrogenation reaction for Pt-Co bimetallic catalysts. In this study, we first revealed the mechanism as to how the support worked collectively with Pt-Co NPs to improve activity and selectivity through controlling samples and experiments.

Stability, another crucial property of catalysts for practical applications, is especially vital for noble metal catalysts. During the cycling experiments, about 5% fresh catalyst was added every time to make up for the loss during the filtration process. The results of the successive experiments of CAL hydrogenation catalyzed by 2c-Pt/MWCNTs, 10c-Co/2c-Pt/MWCNTs, and 5c-Co/2c-Pt/5c-Al_2O_3/MWCNTs are shown in Figure S16. Three cycling tests were applied for the 10c-Co/2c-Pt/MWCNTs catalyst,

and a noticeable decrease in the conversion of CAL and selectivity in COL activation was observed when the number of reaction cycles increased (Figure S16b). In contrast, the conversion and selectivity for 2c-Pt/MWCNTs remained almost the same after three cycling tests (Figure S16a); this was consistent with our previous results.[14, 33] Thus, this study indicated that some Co NPs were leached out during the cycling reactions, which led to the decreases in activity and selectivity of the catalyst. This implied that the interaction between Co and MWCNTs was weak. A total of fiv cycling tests were also applied for the 5c-Co/2c-Pt/5c-Al_2O_3/MWCNTs catalyst, with no noticeable difference in catalytic activity and selectivity, as shown in Figure S16c. These results indicated that the 5c-Co/2c-Pt/5c-Al_2O_3/MWCNTs catalyst showed a higher stability than the 10c-Co/2c-Pt/MWCNTs catalyst did, and that the interaction between Co and Al_2O_3 was stronger than that between Co and MWCNTs; this was consistent with the TPR results. Improvement in the cycling stability of the Pt-Co/MWCNTs catalyst is being addressed by this group.

4. CONCLUSIONS

Highly dispersed Pt-Co bimetallic NPs were deposited on MWCNTs for selective hydrogenation of α, β-unsaturated aldehydes to unsaturated alcohols. Both HRTEM and STEM/EDS analysis confirmed the formation of Pt-Co bimetallic particles on MWCNTs. The 10c-Co/2c-Pt/MWCNTs catalyst showed high selectivity to unsaturated alcohols (> 90%), with high conversion in various selective hydrogenation reactions due to the synergistic effect between Pt, Co, and MWCNTs, and proved its universality. A series of

experiments revealed that the interaction between Pt and Co NPs improved the selectivity in C=O activation of the selective hydrogenation reactions, and the synergistic effect between Pt-Co bimetallic NPs and MWCNTs dramatically enhanced the activity of the catalysts. This research produced the essential foundation knowledge needed to solve the "activity-selectivity" dilemma.

ACKNOWLEDGMENT

Acknowledgment is made to the donors of the American Chemical Society Petroleum Research Fund for partial support of this research. The authors thank Jessica TerBush at the Materials Research Center at Missouri University of Science and Technology for TEM and STEM/EDS analysis. Use of the Center for Nanoscale Materials, an Office of Science user facility, was supported by the U.S. Department of Energy, Office of Science, Office of Basic Energy Sciences, under Contract No. DE-AC02-06CH11357.

REFERENCES

(1) Mäki-Arvela, P.; Hajek, J.; Salmi, T.; Murzin, D. Y. Chemoselective hydrogenation of carbonyl compounds over heterogeneous catalysts. *Applied Catalysis A: General* **2005,** *292*, 1-49.

(2) Manyar, H. G.; Yang, B.; Daly, H.; Moor, H.; McMonagle, S.; Tao, Y.; Yadav, G. D.; Goguet, A.; Hu, P.; Hardacre, C. Selective hydrogenation of α, β-unsaturated aldehydes and ketones using novel manganese oxide and platinum supported on manganese oxide octahedral molecular sieves as catalysts. *ChemCatChem* **2013,** *5*, 506-512.

(3) Tian, Z.; Li, Q.; Hou, J.; Li, Y.; Ai, S. Highly selective hydrogenation of α, β-unsaturated aldehydes by Pt catalysts supported on Fe-based layered double hydroxides and derived mixed metal oxides. *Catalysis Science & Technology* **2016,** *6*, 703-707.

(4) Bachiller-Baeza, B.; Rodrıguez-Ramos, I.; Guerrero-Ruiz, A. Influence of Mg and Ce addition to ruthenium based catalysts used in the selective hydrogenation of α, β-unsaturated aldehydes. *Applied Catalysis A: General* **2001,** *205*, 227-237.

(5) Mahata, N.; Gonçalves, F.; Pereira, M. F. R.; Figueiredo, J. L. Selective hydrogenation of cinnamaldehyde to cinnamyl alcohol over mesoporous carbon supported Fe and Zn promoted Pt catalyst. *Applied Catalysis A: General* **2008,** *339*, 159-168.

(6) Plomp, A.; Van Asten, D.; Van der Eerden, A.; Mäki-Arvela, P.; Murzin, D. Y.; de Jong, K.; Bitter, J. Catalysts based on platinum–tin and platinum–gallium in close contact for the selective hydrogenation of cinnamaldehyde. *Journal of Catalysis* **2009,** *263*, 146-154.

(7) Zgolicz, P. D.; Stassi, J. P.; Yañez, M. J.; Scelza, O. A.; de Miguel, S. R. Influence of the support and the preparation methods on the performance in citral hydrogenation of Pt-based catalysts supported on carbon nanotubes. *Journal of Catalysis* **2012,** *290*, 37-54.

(8) Tsang, S. C.; Cailuo, N.; Oduro, W.; Kong, A. T.; Clifton, L.; Yu, K. K.; Thiebaut, B.; Cookson, J.; Bishop, P. Engineering preformed cobalt-doped platinum nanocatalysts for ultraselective hydrogenation. *ACS Nano* **2008,** *2*, 2547-2553.

(9) Wang, D.; Villa, A.; Porta, F.; Prati, L.; Su, D. Bimetallic gold/palladium catalysts: Correlation between nanostructure and synergistic effects. *The Journal of Physical Chemistry C* **2008,** *112*, 8617-8622.

(10) Prati, L.; Villa, A.; Porta, F.; Wang, D.; Su, D. Single-phase gold/palladium catalyst: The nature of synergistic effect. *Catalysis Today* **2007,** *122*, 386-390.

(11) Li, Y.; Li, Z.-G.; Zhou, R.-X. Bimetallic Pt-Co catalysis on carbon nanotubes for the selective hydrogenation of cinnamaldehyde to cinnamyl alcohol: Preparation and characterization. *Journal of Molecular Catalysis A: Chemical* **2008,** *279*, 140-146.

(12) Bertero, N. M.; Trasarti, A. F.; Moraweck, B.; Borgna, A.; Marchi, A. J. Selective liquid-phase hydrogenation of citral over supported bimetallic Pt–Co catalysts. *Applied Catalysis A: General* **2009,** *358*, 32-41.

(13) Wu, B.; Huang, H.; Yang, J.; Zheng, N.; Fu, G. Selective hydrogenation of α, β-unsaturated aldehydes catalyzed by amine-capped platinum-cobalt nanocrystals. *Angewandte Chemie International Edition* **2012,** *51*, 3496-3499.

(14) Wang, X.; Hu, W.; Deng, B.; Liang, X. Selective hydrogenation of citral over supported Pt catalysts: insight into support effects. *Journal of Nanoparticle Research* **2017,** *19*, Article No. 153.

(15) Puurunen, R. L. Surface chemistry of atomic layer deposition: a case study for the trimethylaluminum/water process. *Journal of Applied Physics* **2005,** *97*, Article No. 121301.

(16) George, S. M. Atomic layer deposition: An overview. *Chemical Reviews* **2010,** *110*, 111-131.

(17) Shang, Z.; Patel, R. L.; Evanko, B. W.; Liang, X. Encapsulation of supported metal nanoparticles with an ultra-thin porous shell for size-selective reactions. *Chemical Communications* **2013,** *49*, 10067-10069.

(18) Wang, X.; Zhao, H.; Wu, T.; Liu, Y.; Liang, X. Synthesis of highly dispersed and highly stable supported Au–Pt bimetallic catalysts by a two-step method. *Catalysis Letters* **2016,** *146*, 2606-2613.

(19) Groner, M.; Fabreguette, F.; Elam, J.; George, S. Low-temperature Al_2O_3 atomic layer deposition. *Chemistry of Materials* **2004,** *16*, 639-645.

(20) Su, Y.; Zhu, Y.; Jiang, H.; Shen, J.; Yang, X.; Zou, W.; Chen, J.; Li, C. Cobalt nanoparticles embedded in N-doped carbon as an efficient bifunctional electrocatalyst for oxygen reduction and evolution reactions. *Nanoscale* **2014,** *6*, 15080-15089.

(21) Xin, L.; Yang, F.; Rasouli, S.; Qiu, Y.; Li, Z.-F.; Uzunoglu, A.; Sun, C.-J.; Liu, Y.; Ferreira, P.; Li, W. Understanding Pt nanoparticle anchoring on graphene supports through surface functionalization. *ACS Catalysis* **2016,** *6*, 2642-2653.

(22) Aaltonen, T.; Ritala, M.; Sajavaara, T.; Keinonen, J.; Leskelä, M. Atomic layer deposition of platinum thin films. *Chemistry of Materials* **2003,** *15*, 1924-1928.

(23) Silva, D. O.; Luza, L.; Gual, A.; Baptista, D. L.; Bernardi, F.; Zapata, M. J.; Morais, J.; Dupont, J. Straightforward synthesis of bimetallic Co/Pt nanoparticles in ionic liquid: atomic rearrangement driven by reduction–sulfidation processes and Fischer–Tropsch catalysis. *Nanoscale* **2014,** *6*, 9085-9092.

(24) Jacobs, G.; Das, T. K.; Patterson, P. M.; Li, J.; Sanchez, L.; Davis, B. H. Fischer–Tropsch synthesis XAFS: XAFS studies of the effect of water on a Pt-promoted Co/Al_2O_3 catalyst. *Applied Catalysis A: General* **2003,** *247*, 335-343.

(25) Vada, S.; Hoff, A.; Ådnanes, E.; Schanke, D.; Holmen, A. Fischer-Tropsch synthesis on supported cobalt catalysts promoted by platinum and rhenium. *Topics in Catalysis* **1995,** *2*, 155-162.

(26) Ji, X.; Niu, X.; Li, B.; Han, Q.; Yuan, F.; Zaera, F.; Zhu, Y.; Fu, H. Selective hydrogenation of cinnamaldehyde to cinnamal alcohol over platinum/graphene catalysts. *ChemCatChem* **2014,** *6*, 3246-3253.

(27) Mo, M.; Zheng, M.; Tang, J.; Lu, Q.; Xun, Y. Highly active Co–B, Co–Mo (W)–B amorphous nanotube catalysts for the selective hydrogenation of cinnamaldehyde. *Journal of Materials Science* **2014,** *49*, 877-885.

(28) Delbecq, F.; Sautet, P. Competitive C=C and C=O adsorption of α-β-unsaturated aldehydes on Pt and Pd surfaces in relation with the selectivity of hydrogenation reactions: A theoretical approach. *Journal of Catalysis* **1995,** *152*, 217-236.

(29) Bailón-García, E.; Maldonado-Hódar, F. J.; Pérez-Cadenas, A. F.; Carrasco-Marín, F. Catalysts supported on carbon materials for the selective hydrogenation of citral. *Catalysts* **2013,** *3*, 853-877.

(30) Gutierrez, V.; Alvarez, M.; Volpe, M. A. Liquid phase selective hydrogenation of cinnamaldehyde over copper supported catalysts. *Applied Catalysis A: General* **2012,** *413*, 358-365.

(31) Handjani, S.; Marceau, E.; Blanchard, J.; Krafft, J.-M.; Che, M.; Mäki-Arvela, P.; Kumar, N.; Wärnå, J.; Murzin, D. Y. Influence of the support composition and acidity on the catalytic properties of mesoporous SBA-15, Al-SBA-15, and Al 2 O 3-supported Pt catalysts for cinnamaldehyde hydrogenation. *Journal of Catalysis* **2011,** *282*, 228-236.

(32) Kahsar, K. R.; Schwartz, D. K.; Medlin, J. W. Control of metal catalyst selectivity through specific noncovalent molecular interactions. *Journal of the American Chemical Society* **2013,** *136*, 520-526.

(33) Liang, X.; Jiang, C. Atomic layer deposited highly dispersed platinum nanoparticles supported on non-functionalized multiwalled carbon nanotubes for the hydrogenation of xylose to xylitol. *Journal of Nanoparticle Research* 2013, *15*, Article No. 1890.

SUPPORTING INFORMATION

This file includes catalyst preparation experimental details, TEM images of Pt, Pt-Co, and Co catalysts, STEM image, EDS data and spectra, data of Co loading, and details of CAL and citral hydrogenation reactions over different catalysts.

Experimental details

Catalyst preparation. Platinum (Pt) nanoparticles (NPs) were deposited by ALD using (methylcyclopentadienyl)trimethyl platinum [(MeCp)$PtMe_3$] as the Pt precursor and oxygen (O_2) as the other reactant at 300 °C in a fluidized bed reactor, as described previously.[1-2] In a typical run, 5 g of substrates were loaded into the reactor. Before the reaction, the substrates were degassed at 300 °C for 5 hr. During the ALD process, the solid (MeCp)$PtMe_3$ was heated and carried by nitrogen (N_2) to enter the reactor. (MeCp)$PtMe_3$ and O_2 were fed separately into the reactor. The particle substrates were fully fluidized with the gas flow rate controlled by mass flow controllers. The reactor was also subjected to vibration via vibrators to improve the quality of particle fluidization during the ALD process.[3] N_2 was used as a flush gas to remove unreacted precursors and any byproducts during the reaction. A typical coating cycle used the following steps: (MeCp)$PtMe_3$ dose, N_2 purge, evacuation; O_2 dose, N_2 purge, evacuation.

Co ALD was carried out following similar procedures using cobaltocene ($CoCp_2$) and hydrogen (H_2) as precursors at 300 °C. The solid $CoCp_2$ was loaded in a heated bubbler and carried by N_2. A typical Co depositing cycle used the following steps: $CoCp_2$ dose, N_2 purge, evacuation; H_2 dose, N_2 purge, evacuation.

Al_2O_3 ALD was performed following similar procedures (as mentioned above) using trimethylaluminium (TMA) and deionized water (H_2O) as precursors at 177 ºC. A typical coating cycle used the following steps: TMA dose, N_2 purge, evacuation; H_2O dose, N_2 purge, evacuation.

Hydrogenation of unsaturated aldehydes. The hydrogenation of unsaturated aldehydes was performed in a stainless steel Parr reactor (50 mL) with an external

temperature and stirring controller. In a typical run of cinnamaldehyde (CAL) hydrogenation, 0.5 g of CAL, 0.1 g of toluene, and 30 mL of 2-propanol were first introduced into the reactor, and then 25 mg of 10c-Co/2c-Pt/MWCNTs catalyst were added. All catalysts had an identical total metal loading (Pt and Co), even though the total mass of each catalyst could have been different due to the various content of Pt and Co on the MWCNTs (see Table S1). All catalysts were used directly without any pretreatment. The reactor was first pressurized to 10 bar with hydrogen and depressurized to atmospheric pressure. This process was repeated 10 times. Then the reactor was filled with H2 at 10 bar and the temperature was increased to 80 °C. The slurry was stirred at a rate of 500 rpm to eliminate the external diffusion limitations based on our previous results.[4] A small volume of sample (1 mL) was periodically withdrawn and analyzed by using a gas chromatography (GC, Agilent 6890) equipped with a capillary column (DB-5) and a flame ionization detector (FID). After a reaction, the catalysts were washed with 2-propanol and collected by centrifugation for cycling tests. The hydrogenation of other unsaturated aldehydes (citral, 2-furfural, and α-amylcinnamaldehyde) was also carried out following the identical procedures, but with different reaction temperatures.

In each hydrogenation reaction, 0.1 g of toluene was added in the reactor and worked as an internal standard for GC-FID analysis. The individual components were separated, using a 30 meter DB-5 capillary column (250 μm i.d. x 0.25 μm film thickness). The initial column temperature was set at 70 ºC (for 3 min) and programmed to 250 ºC at 10.0 ºC/min. The injector temperature was set at 250 ºC, and the FID temperature was set at 280 ºC.

Retention times in GC-FID were determined by injections of commercially available chemicals in the cinnamaldehyde (CAL) hydrogenation reaction, in the following order: 2-propanol (2.85 min), toluene (3.95 min), hydrocinnamaldehyde (HCAL, 8.76 min), 3-phenyl-1-propanol (HCOL, 9.51 min), CAL (10.03 min), and cinnamic alcohol (COL, 10.26 min).

Retention times for the citral hydrogenation reaction are as follows: 2-propanol (2.85 min), toluene (3.95 min), citronellal (7.41 min), citronellol (8.07 min), nerol (8.11 min), (Z)-citral (neral, 8.24 min), geraniol (8.31 min), and (E)-citral (geranial, 8.48 min).

Retention times for the 2-furfural hydrogenation reaction are as follows: 2-propanol (2.85 min), toluene (3.95 min), 2-furfural (4.68 min), furfural alcohol (4.97 min).

Retention times for the α-Amylcinnamaldehyde hydrogenation reaction are as follows: 2-propanol (2.85 min), toluene (3.95 min), 2-benzyl heptanol (12.02 min), 2-benzylheptan-1-ol (12.41 min), α-Amylcinnamaldehyde (13.50 min), and α-amylcinnamyl alcohol (13.61 min).

References

(1) Shang, Z.; Patel, R. L.; Evanko, B. W.; Liang, X. Encapsulation of supported metal nanoparticles with an ultra-thin porous shell for size-selective reactions. *Chemical Communications* 2013, *49*, 10067-10069.

(2) Wang, X.; Zhao, H.; Wu, T.; Liu, Y.; Liang, X. Synthesis of highly dispersed and highly stable supported Au–Pt bimetallic catalysts by a two-step method. *Catalysis Letters* 2016, *146*, 2606-2613.

(3) Patel, R. L.; Jiang, Y.-B.; Liang, X. Highly porous titania films coated on sub-micron particles with tunable thickness by molecular layer deposition in a fluidized bed reactor. *Ceramics International* 2015, *41*, 2240-2246.

(4) Wang, X.; Hu, W.; Deng, B.; Liang, X. Selective hydrogenation of citral over supported Pt catalysts: insight into support effects. *Journal of Nanoparticle Research* 2017, *19*, Article No. 153.

Table S1. List of total mass of each catalyst added in hydrogenation reactions

Catalyst	Mass, mg
2c-Pt/MWCNTs	38.5
5c-Co/2c-Pt/MWCNTs	31.9
10c-Co/2c-Pt/MWCNTs	25.0
30c-Co/1c-Pt/MWCNTs	18.3
15c-Co/MWCNTs	52.9
2c-Pt/5c-Al_2O_3/MWCNTs	33.6
3c-Co/2c-Pt/5c-Al_2O_3/MWCNTs	21.3
5c-Co/2c-Pt/5c-Al_2O_3/MWCNTs	17.3
8c-Co/2c-Pt/5c-Al_2O_3/MWCNTs	15.9
A mixture of 2c-Pt/MWCNTs and 15c-Co/MWCNTs [a]	24.0 mg 2c-Pt/MWCNTs and 20.0 mg 15c-Co/MWCNTs

[a] The Pt and Co masses of the mixed catalyst were the same as the Pt and Co masses of 10c-Co/2c-Pt/MWCNTs catalyst, respectively.

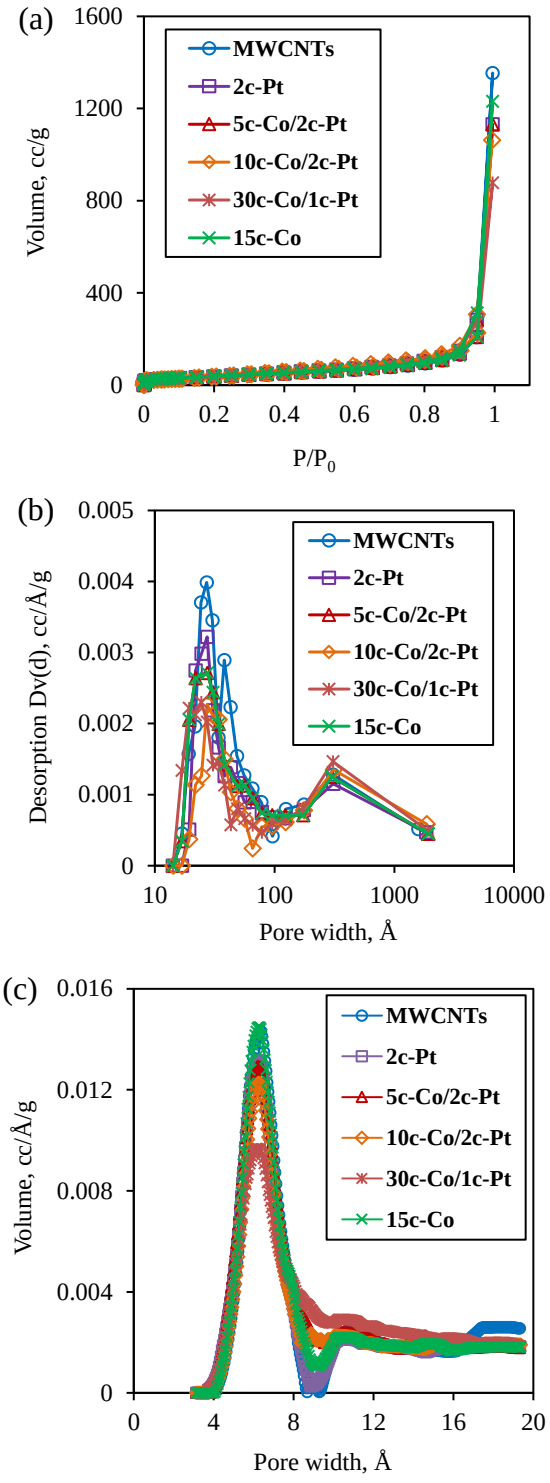

Figure S1. (a) Nitrogen adsorption and desorption isotherms, (b) mesopore pore size distribution, and (c) micropore pore size distribution of MWCNTs and MWCNTs-supported Pt and Co catalysts.

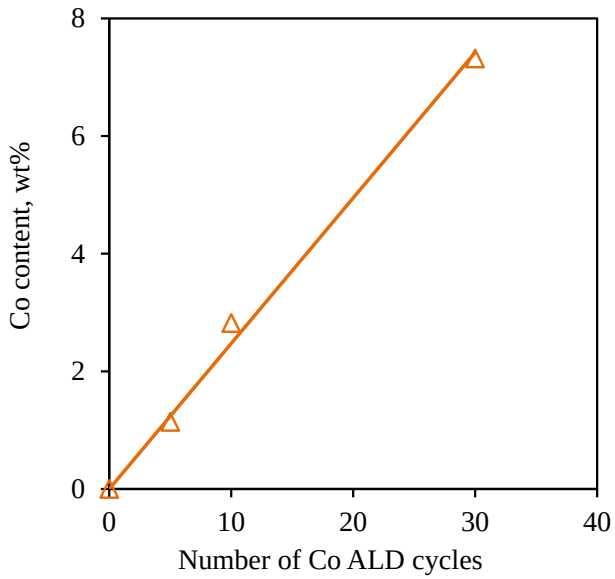

Figure S2. Co content (based on ICP-AES) of Pt-Co/MWCNTs bimetallic catalysts versus the number of Co ALD cycles.

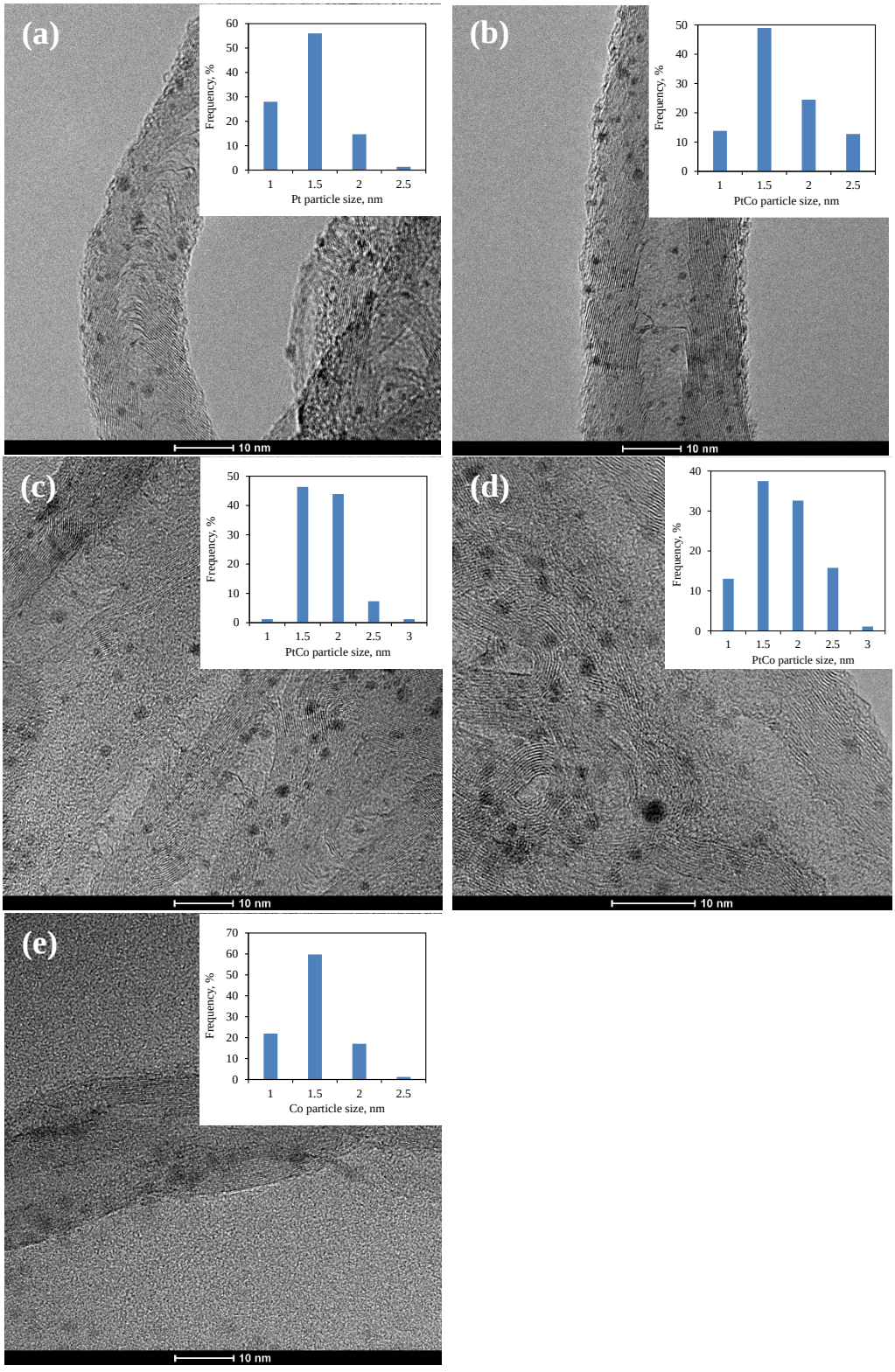

Figure S3. TEM images of (a) 2c-Pt/MWCNTs, (b) 5c-Co/2c-Pt/MWCNTs, (c) 10c-Co/2c-Pt/MWCNTs, (d) 30c-Co/1c-Pt/MWCNTs, and (e) 15c-Co/MWCNTs. The inset figures show the size distribution of Pt, Pt-Co, or Co particles.

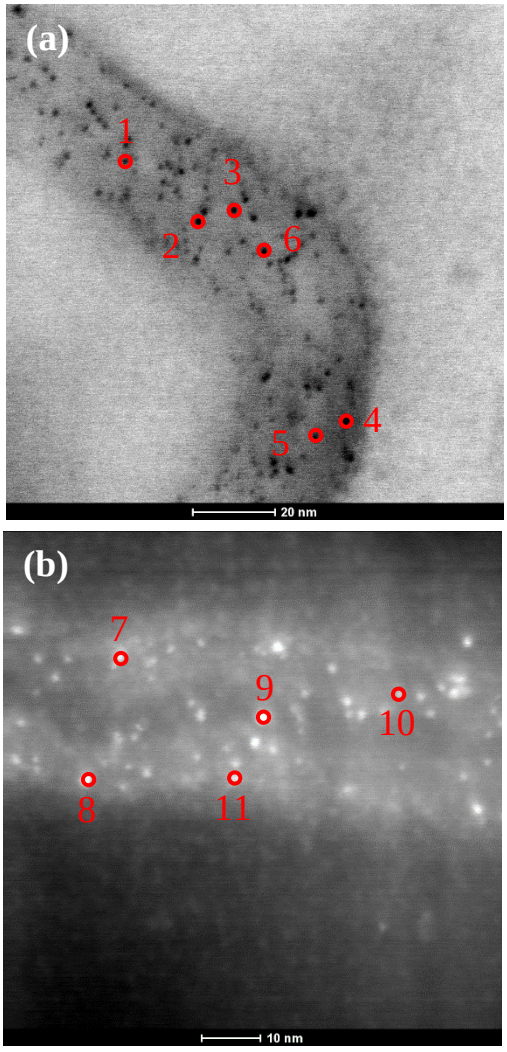

Figure S4. STEM images of 10c-Co/2c-Pt/MWCNTs (a and b). The labeled 11 points were analyzed by EDS. The results are listed in Table S2.

Table S2. Pt and Co weight percentages and molar percentages of the 11 points in Figure S4.

	Element Wt.%		Element Atom %	
	Pt	Co	Pt	Co
Point 1	78	22	51	49
Point 2	76	24	48	52
Point 3	76	24	49	51
Point 4	76	24	49	51
Point 5	90	10	73	27
Point 6	24	76	9	91
Point 7	77	23	50	50
Point 8	74	26	46	54
Point 9	81	19	56	44
Point 10	87	13	67	33
Point 11	65	25	44	56

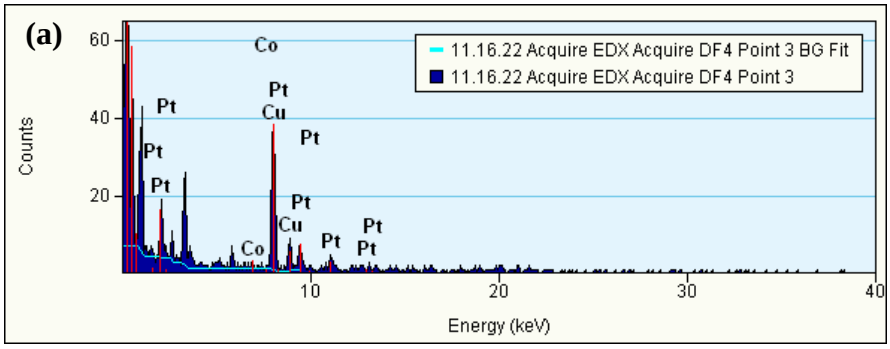

Figure S5. EDS spectra of 11 points in Figure S4: (a) point 1, (b) point 2, (c) point 3, (d) point 4, (e) point 5, (f) point 6, (g) point 7, (h) point 8, (i) point 9, (j) point 10, and (k) point 11.

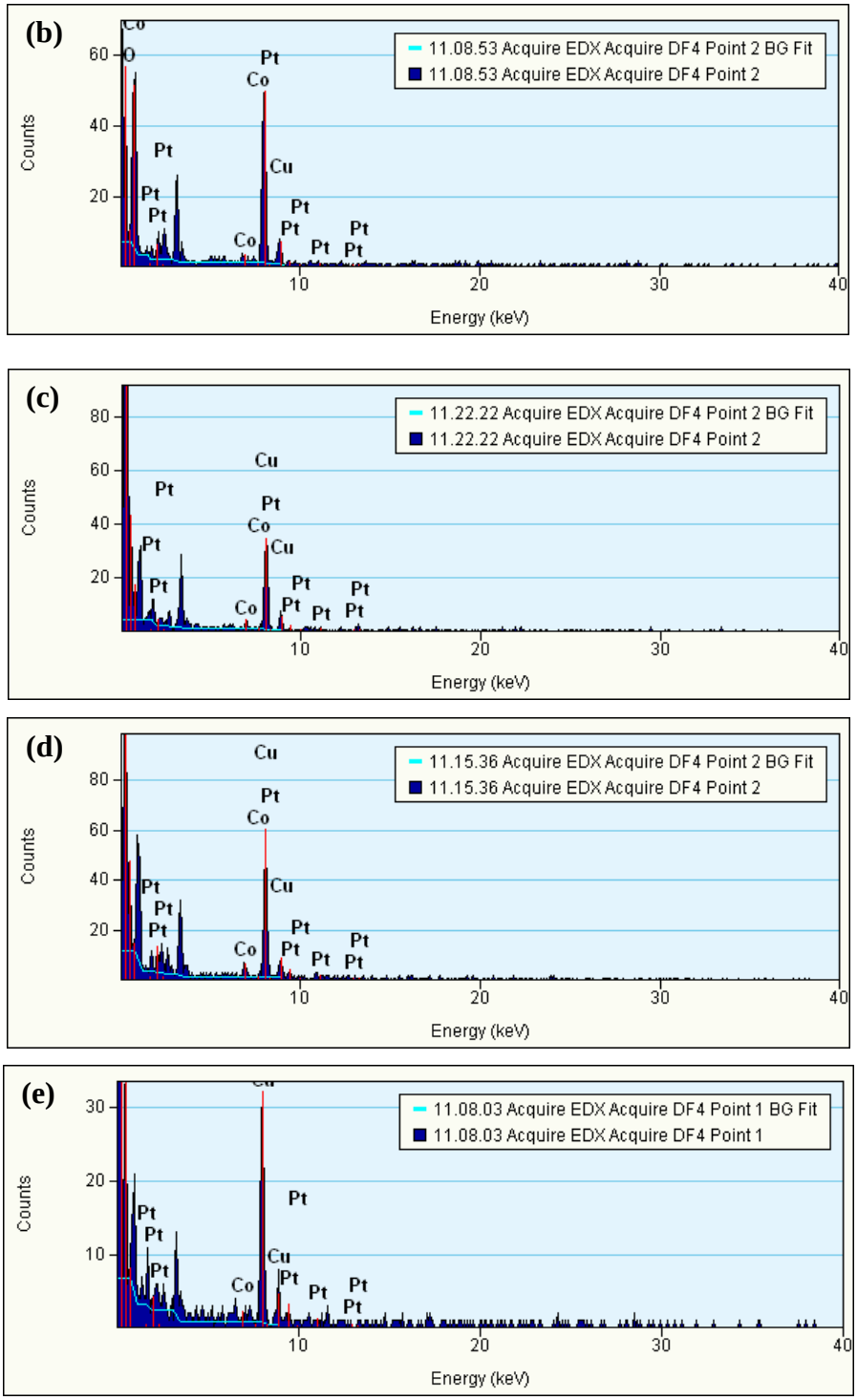

Figure S5. EDS spectra of 11 points in Figure S4: (a) point 1, (b) point 2, (c) point 3, (d) point 4, (e) point 5, (f) point 6, (g) point 7, (h) point 8, (i) point 9, (j) point 10, and (k) point 11. (Cont.)

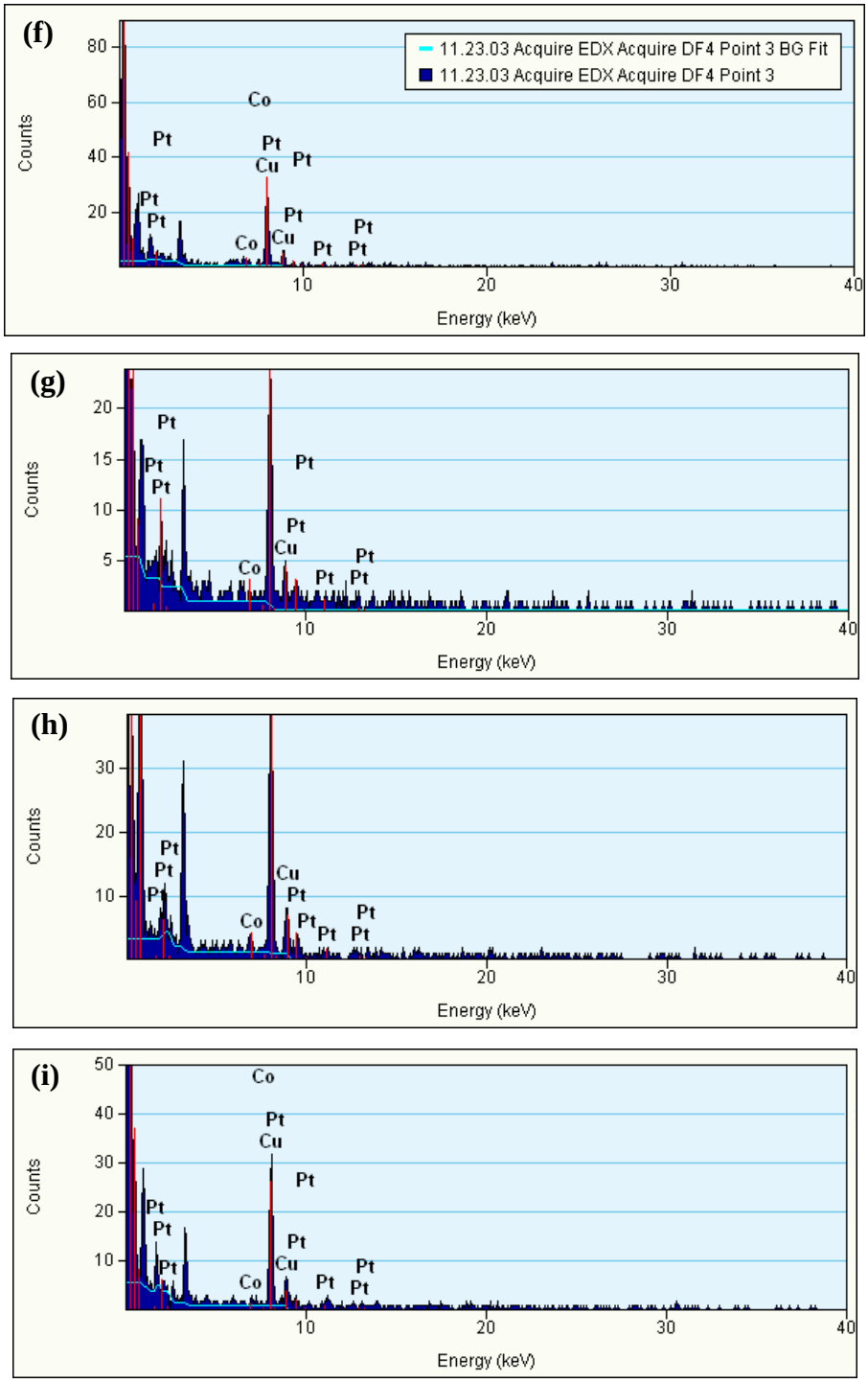

Figure S5. EDS spectra of 11 points in Figure S4: (a) point 1, (b) point 2, (c) point 3, (d) point 4, (e) point 5, (f) point 6, (g) point 7, (h) point 8, (i) point 9, (j) point 10, and (k) point 11. (Cont.)

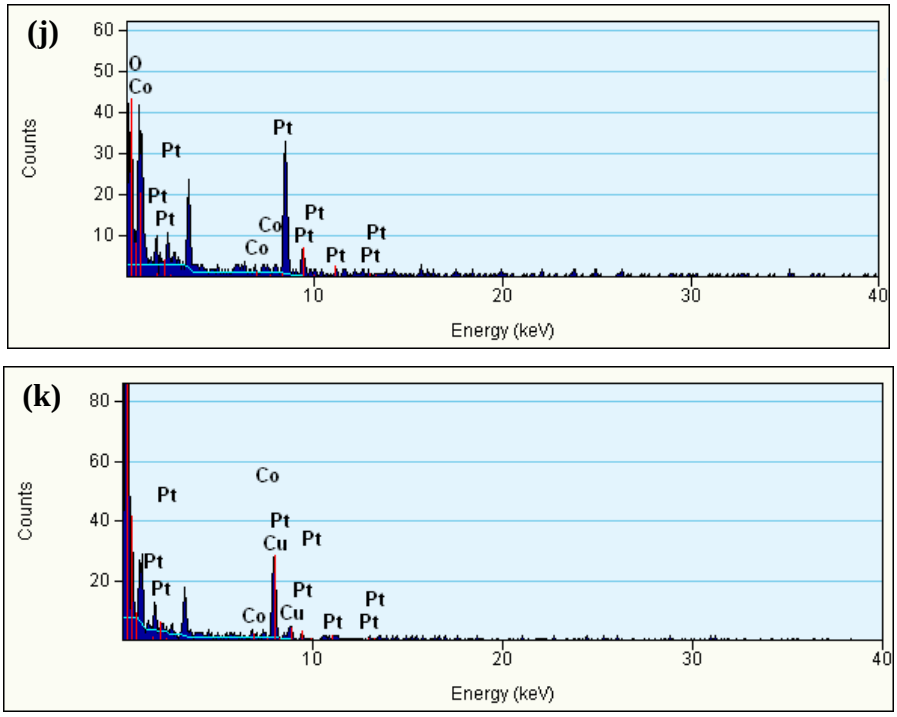

Figure S5. EDS spectra of 11 points in Figure S4: (a) point 1, (b) point 2, (c) point 3, (d) point 4, (e) point 5, (f) point 6, (g) point 7, (h) point 8, (i) point 9, (j) point 10, and (k) point 11. (Cont.)

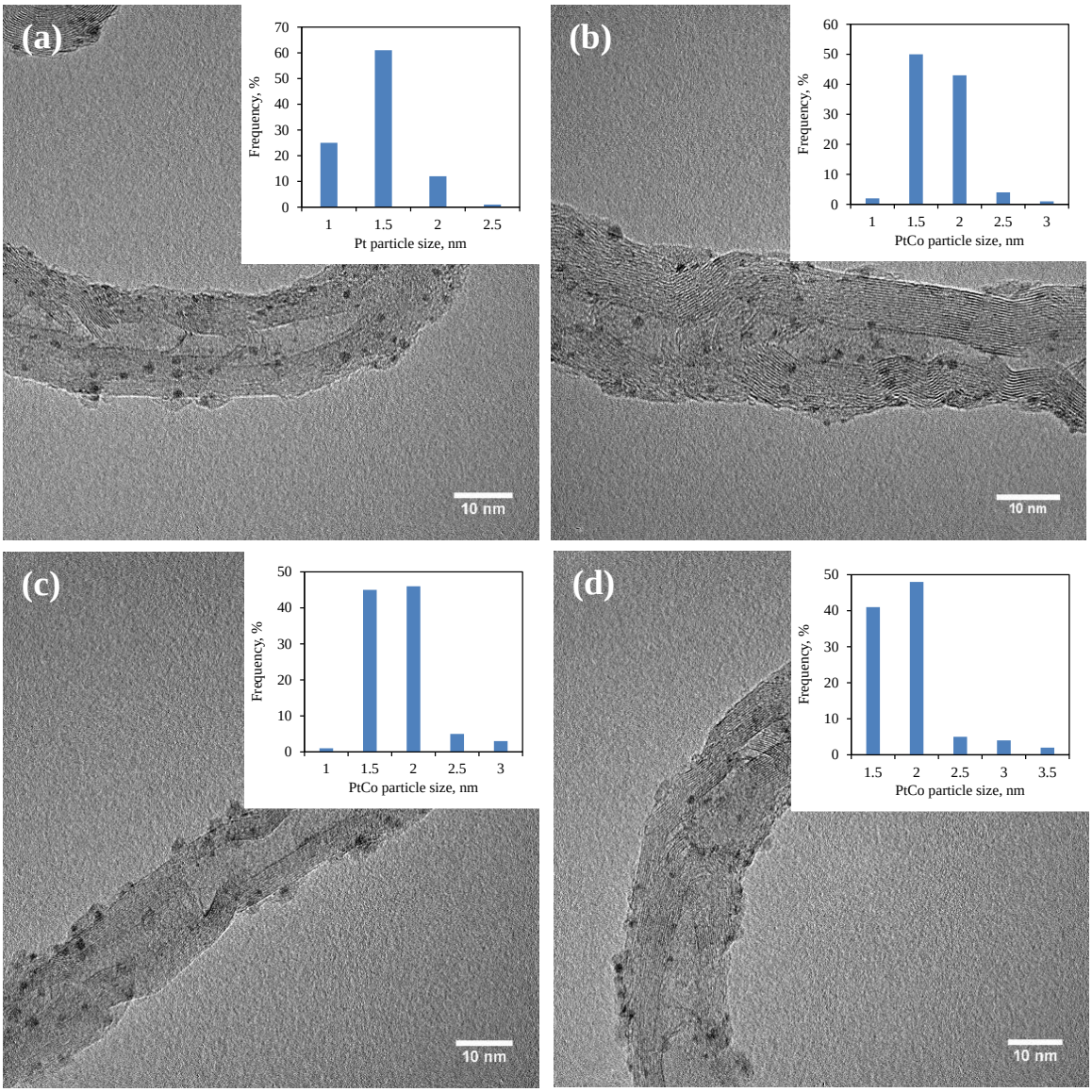

Figure S6. TEM images of (a) 2c-Pt/5c-Al_2O_3/MWCNTs, (b) 3c-Co/2c-Pt/5c-Al_2O_3/MWCNTs, (c) 5c-Co/2c-Pt/5c-Al_2O_3/MWCNTs, and (d) 8c-Co/2c-Pt/5c-Al_2O_3/MWCNTs. The inset figures show the size distribution of Pt or Pt-Co particles.

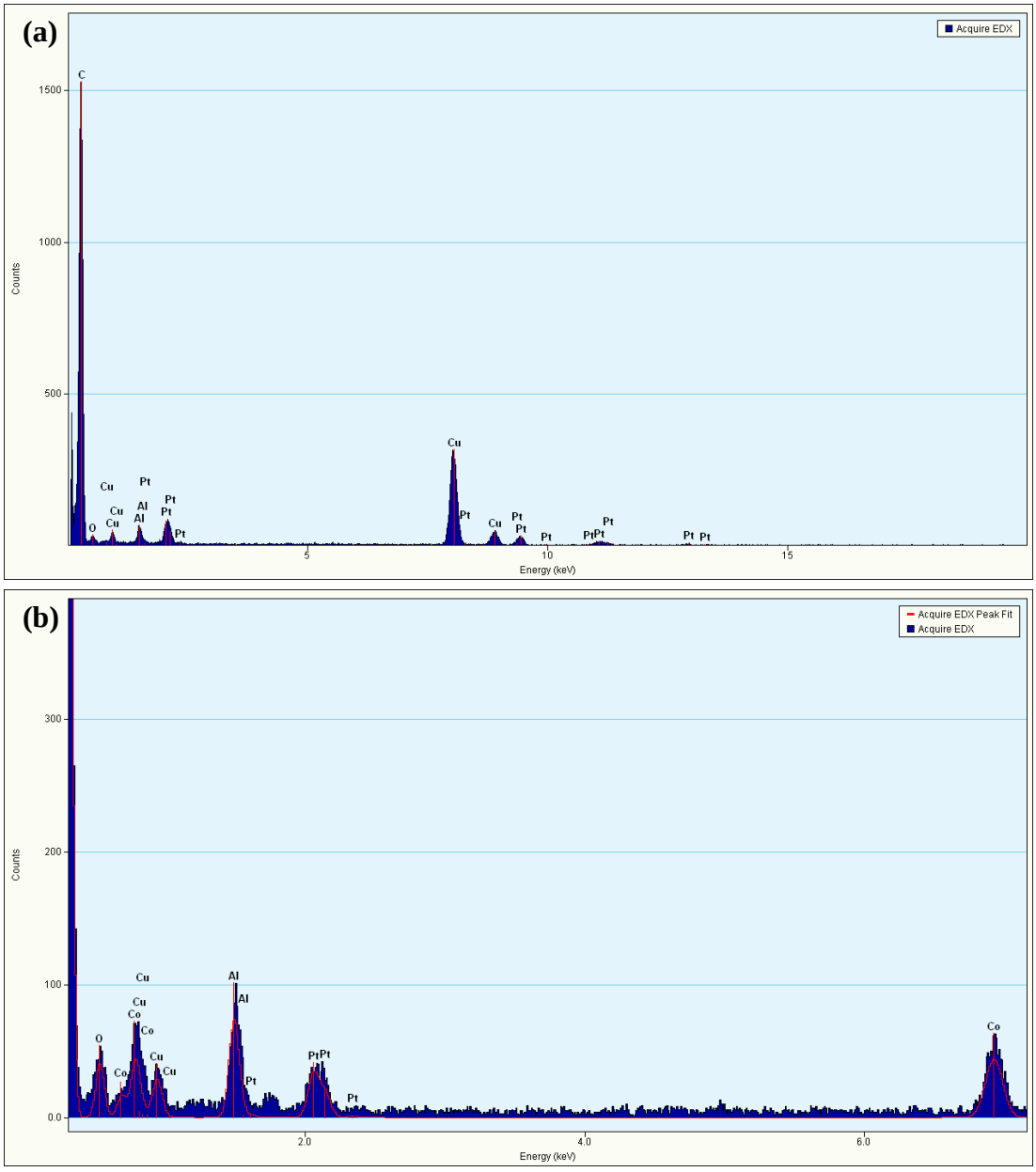

Figure S7. EDS spectra of (a) 2c-Pt/5c-Al_2O_3/MWCNTs catalyst in Figure S6a, and (b) 5c-Co/2c-Pt/5c-Al_2O_3/MWCNTs catalyst in Figure S6c.

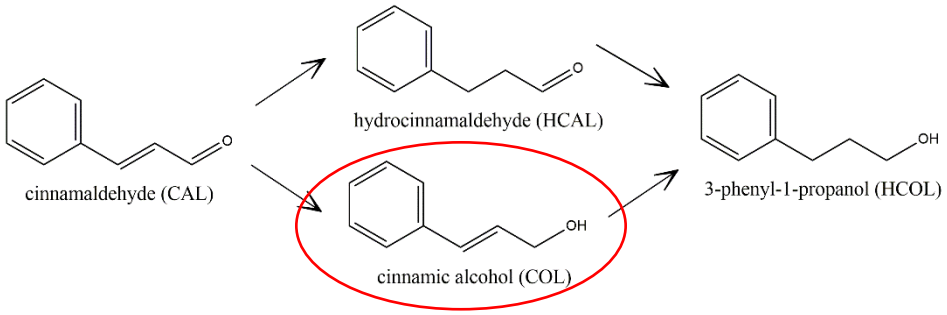

Figure S8. Reaction routes of cinnamaldehyde (CAL) hydrogenation; the desired product is circled.

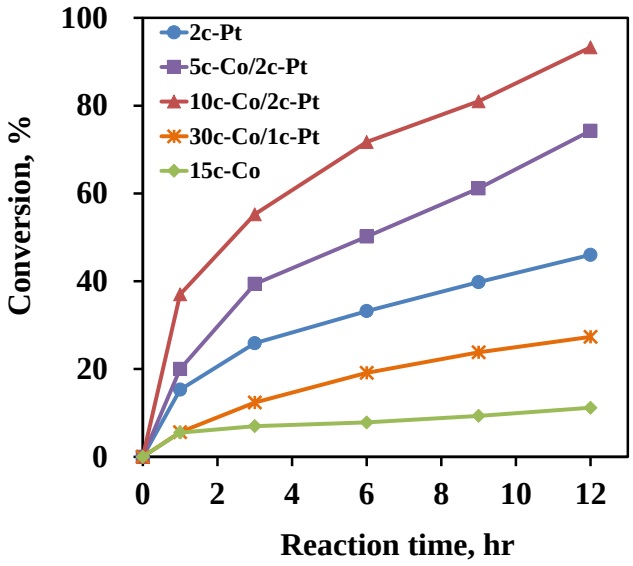

Figure S9. Conversion of CAL versus reaction times for different Pt, Pt-Co, and Co-based catalysts. Reaction conditions: 1.87 mg of metal (Pt and Co), 0.5 g CAL, 30 mL 2-propanol, P_{H2} = 10 bar, 80 ºC, and 500 rpm.

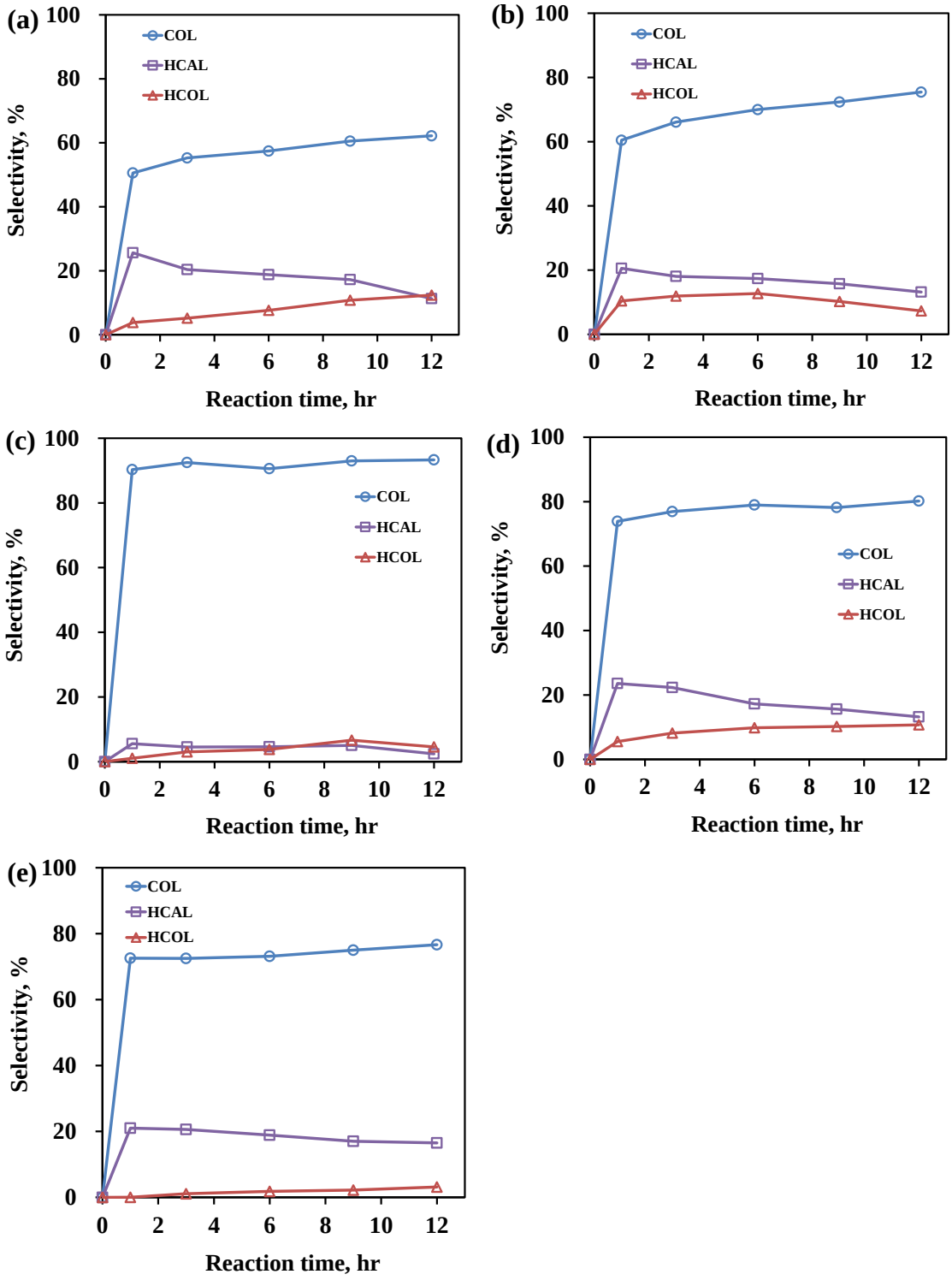

Figure S10. Product selectivity of CAL hydrogenation for (a) 2c-Pt/MWCNTs, (b) 5c-Co/2c-Pt/MWCNTs, (c) 10c-Co/2c-Pt/MWCNTs, (d) 30c-Co/1c-Pt/MWCNTs, and (e) 15c-Co/MWCNTs.

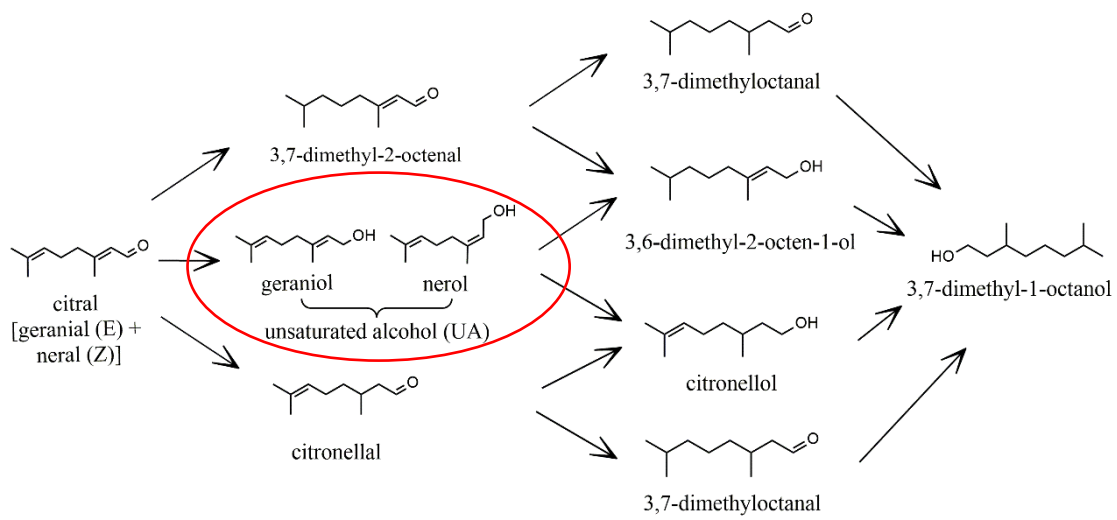

Figure S11. Reaction routes of citral hydrogenation; the desired product is circled.

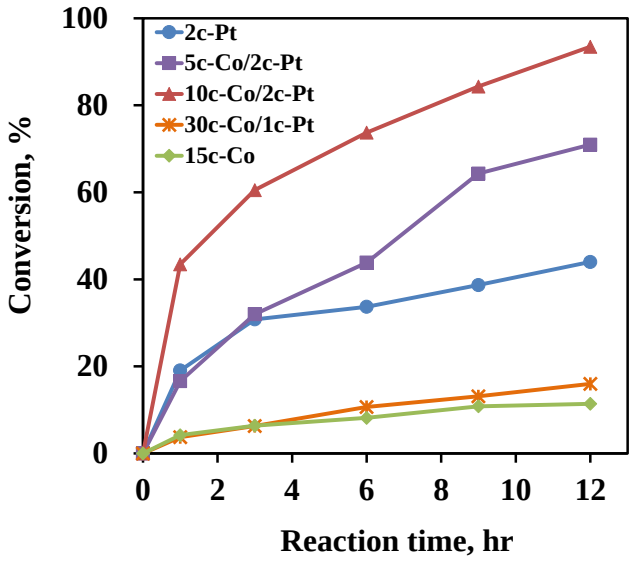

Figure S12. Conversion of citral versus reaction times for different Pt, Pt-Co, and Co-based catalysts. Reaction conditions: 1.87 mg of metal (Pt and Co), 0.5 g citral, 30 mL 2-propanol, P_{H2} = 10 bar, 70 ºC, and 500 rpm.

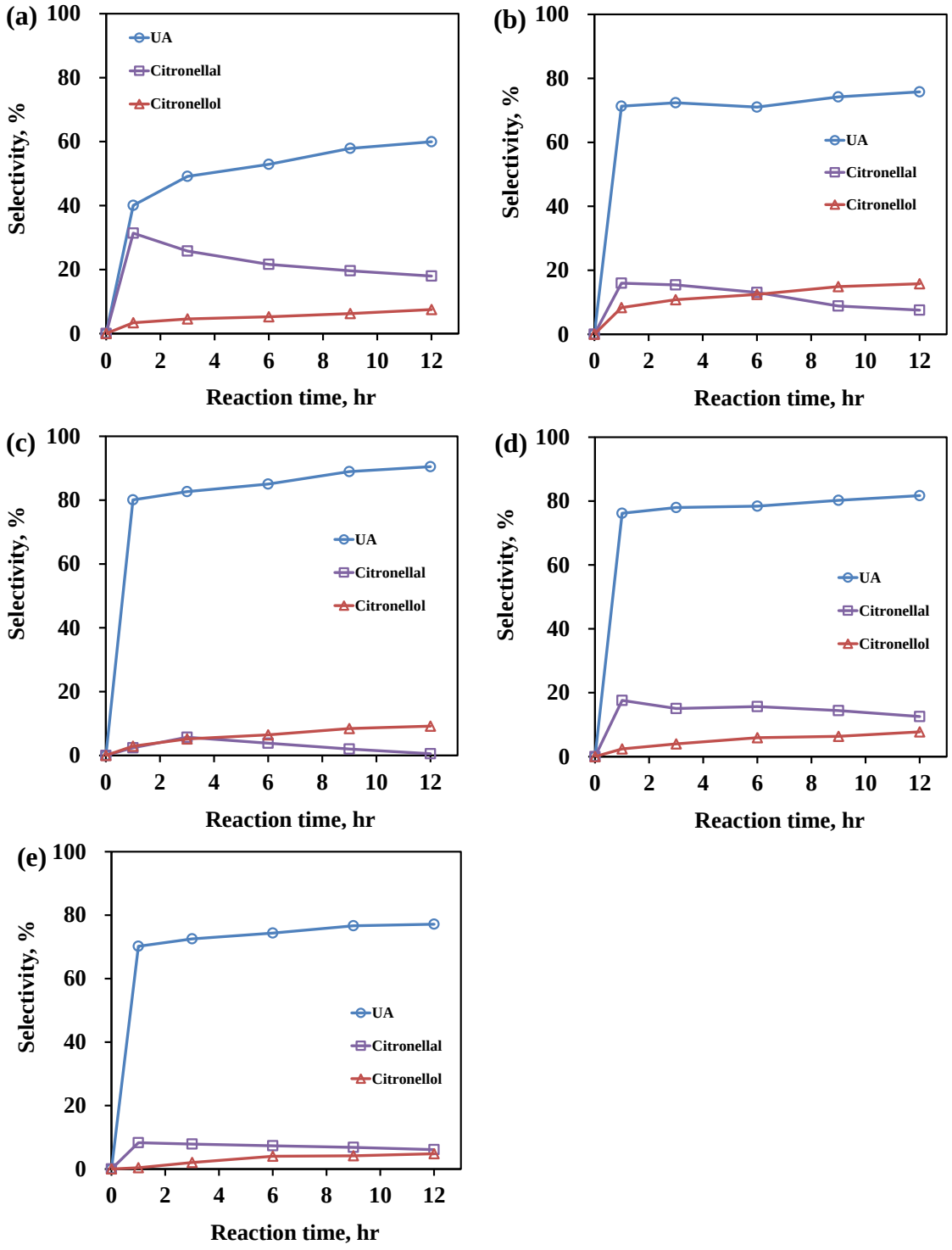

Figure S13. Product selectivity of citral hydrogenation for (a) 2c-Pt/MWCNTs, (b) 5c-Co/2c-Pt/MWCNTs, (c) 10c-Co/2c-Pt/MWCNTs, (d) 30c-Co/1c-Pt/MWCNTs, and (e) 15c-Co/MWCNTs.

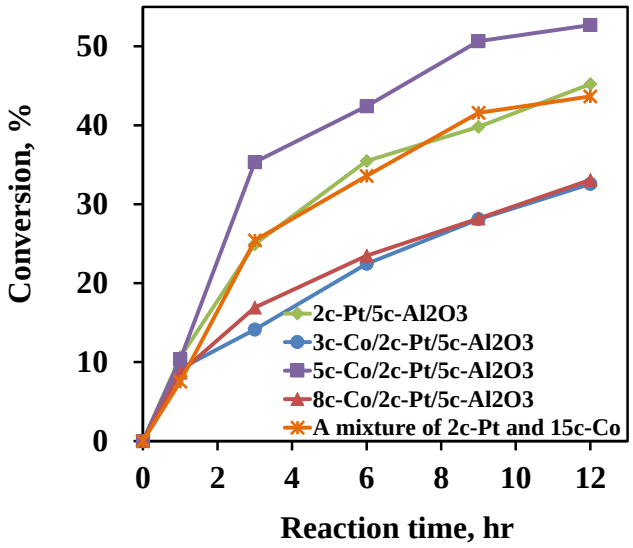

Figure S14. Conversion of CAL versus reaction times for different catalysts. Reaction conditions: 1.87 mg of metal (Pt and Co), 0.5 g CAL, 30 mL 2-propanol, P_{H2} = 10 bar, 70 ºC, and 500 rpm.

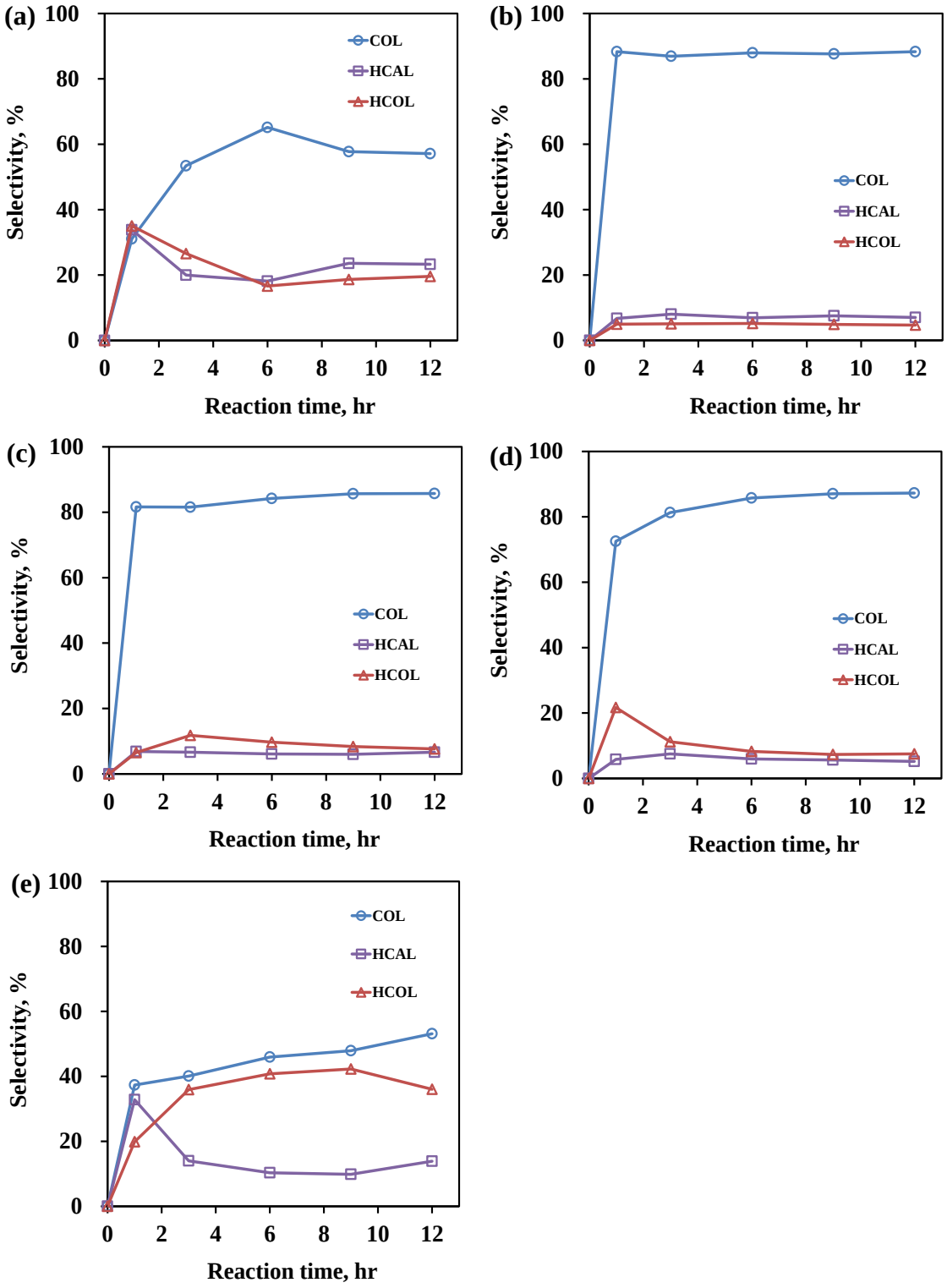

Figure S15. Product selectivity of CAL hydrogenation for (a) 2c-Pt/5c-Al_2O_3/MWCNTs, (b) 3c-Co/2c-Pt/5c-Al_2O_3/MWCNTs, (c) 5c-Co/2c-Pt/5c-Al_2O_3/MWCNTs, (d) 8c-Co/2c-Pt/5c-Al_2O_3/MWCNTs, and (e) a mixture of 2c-Pt/MWCNTs and 15c-Co/MWCNTs.

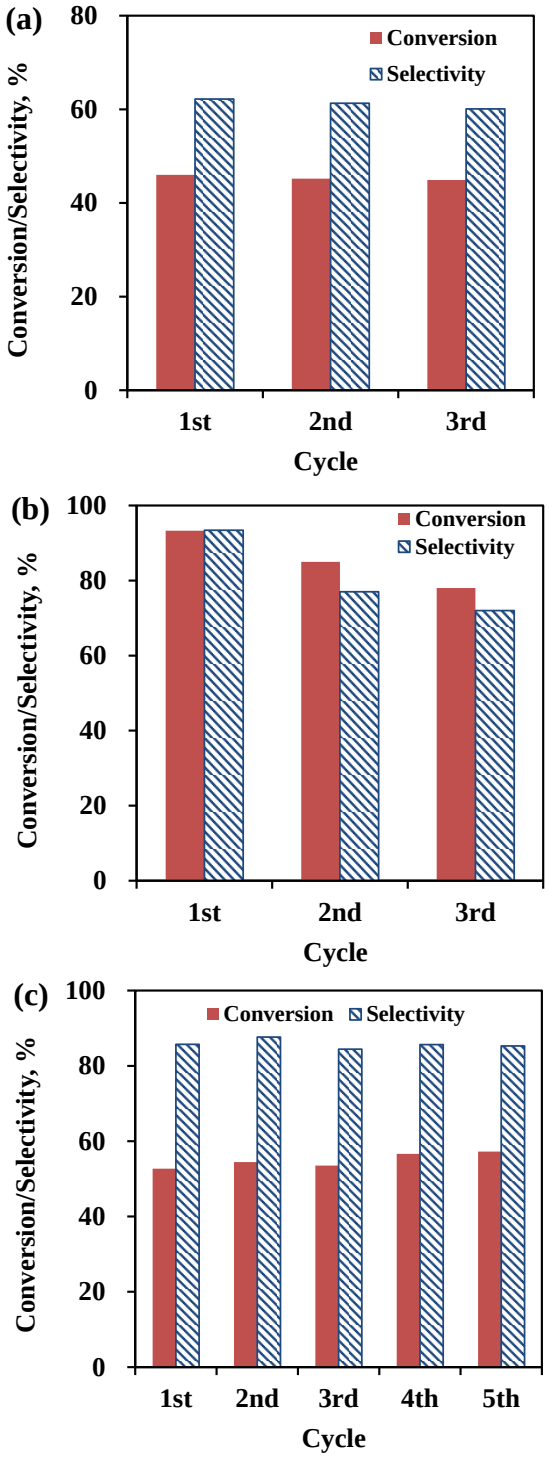

Figure S16. The conversion of CAL and the selectivity to COL in the cycling tests of CAL hydrogenation for (a) 2c-Pt/MWCNTs, (b) 10c-Co/2c-Pt/MWCNTs and (c) 5c-Co/2c-Pt/5c-Al_2O_3/MWCNTs catalysts. Reaction conditions: 1.87 mg of metal (Pt and Co), 0.5 g CAL, 30 mL 2-propanol, P_{H2} = 10 bar, 80 ºC, 500 rpm, 12 hr.

III. HYDROGENOLYSIS OF 5-HYDROXYMETHYLFURFURAL TO 2,5-DIMETHYLFURAN OVER SUPPORTED PT-CO BIMETALLIC CATALYST UNDER MILD CONDITIONS

Xiaofeng Wang,[a] Yuzi Liu [b] and Xinhua Liang *[a]

[a] Department of Chemical and Biochemical Engineering, Missouri University of Science and Technology, Rolla, MO 65409, United States

[b] Center for Nanoscale Materials, Argonne National Laboratory, 9700 S. Cass Ave., Argonne, IL 60439, United States

ABSTRACT

Highly dispersed Pt-Co bimetallic catalysts were deposited on multi-walled carbon nanotubes (MWCNTs) by atomic layer deposition. High-resolution TEM and TPR analysis verified the formation of Pt-Co bimetallic particles. Catalysts were applied for hydrogenolysis of 5-hydroxymethyfurfural (HMF) to 2,5-dimethyfuran (DMF). High yield of DMF (> 90%) was achieved in hydrogenolysis of HMF over the optimized Pt-Co/MWCNTs catalyst after 8 hr of reaction time under 10 bar H2 at 160 ºC. Through a series of experiments and comparison, the synergistic effect among Pt, Co, and MWCNTs was investigated. The results revealed that the synergistic effect between Pt-Co and MWCNTs played an important role in the improvement of selectivity to DMF for Pt-Co/MWCNTs bimetallic catalysts. In addition, steric hindrance appeared when the Co loading in Pt-Co/MWCNTs was high and it affected the activity of Pt-Co bimetallic catalysts. However, the moderate activity can inhibit the production of byprodct and thereby improve the yield of DMF.

1. INTRODUCTION

Nowadays, fossil fuels such as petrol, coal, and natural gas, play principal roles as source of energy and chemicals.[1] However, due to the gradual exhaust of fossil resource and greenhouse effect for the consumption of fossil fuels, the transformation of renewable biomass into biofuel has become a hotspot research area to replace oil-based energy. With the advances in conversion technology, abundant biomass resources have the potential to convert biofuel as feedstock. 2,5-dimethylfuran (DMF), a product from hydrogenolysis of biomass-derived 5-hydroxymethylfurfural (HMF), has a high energy density (30 MJL^{-1}), a high research octane number (RON=119), and a lower volatility (boiling point= 92-94 ℃), which are close to the values of gasoline, which possesses 34 MJL^{-1}, RON=89-96, and boiling point= 96.3 ℃, respectively.[2] Besides, a low solubility in water (2.3 gL^{-1}) is superior to miscible ethanol, which makes DMF more suitable than ethanol as the blend fuel.[3] These excellent performances make DMF a more appropriate, ideal, and promising biomass-derived liquid biofuel for transportation.

It is a possible and reliable approach to obtain DMF from the hydrogenolysis of HMF. HMF, containing an aldehyde group, a hydroxyl group, and a furan ring, is very reactive, and its hydrogenation and hydrogenolysis products are kind of complicated, as shown in Scheme 1.[4] Therefore, how to ensure the hydrogenation priorities of an aldehyde group and a hydroxyl group, but to avoid the further hydrogenation of a furan ring, are the principal issue in the selective hydrogenolysis of HMF to DMF. So far, many researchers have focused on the improvement of the hydrogenolysis process and some heterogeneous catalysts have been used for this reaction.[3, 5] For example, Nishimura et al.

prepared Pd_xAu_y/C catalysts with various Pd/Au molar ratios (x/y) to examine the hydrogenolysis of HMF to DMF in the presence of hydrochloric acid (HCl) under an atmospheric hydrogen pressure.[3] The highest conversion of HMF (99%) and yield of DMF (96%) was obtained for $Pd_{50}Au_{50}/C$ after a reaction time of 12 hr. Wang et al. prepared PtCo bimetallic nanoparticles (NPs), and 98% DMF yield with 100% HMF conversion was observed at 180 ℃ after 2 hr under 10 bar H_2.[5b]

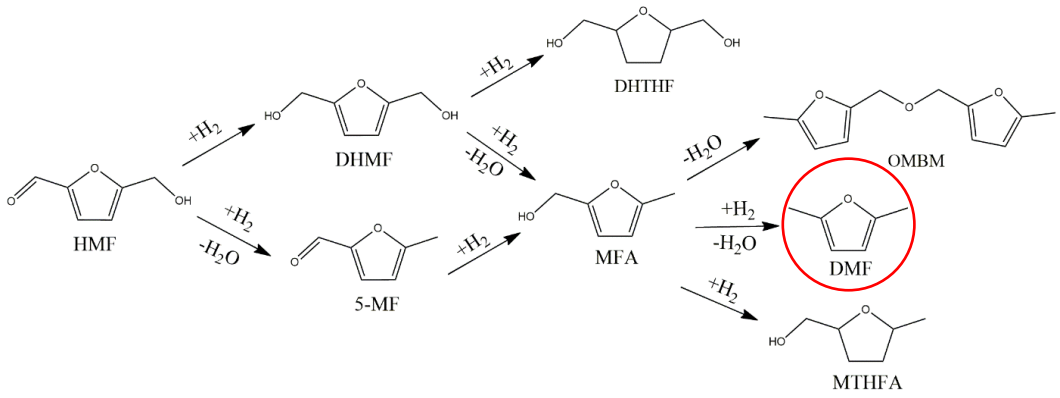

Scheme 1. Proposed reaction pathways for the conversion of HMF, and the desired product is encircled. Compounds: 5-(hydroxymethyl)furfural (HMF); 2,5-dimethylfuran (DMF); 2,5-bis(hydroxymethyl)furan (DHMF); 5-mmethyl furfural (5-MF); 5-methyl furfuryl alcohol (MFA); 5-bis(hydroxymethyl)tetrahydrofuran (DHTHF); 5,5-(oxybis(methylene))bis(2-methylfuran) (OMBM); Tetrahydro-5-methyl 2-furammethanol (MTHFA).

Although excellent DMF yields (as high as 98%) were gained by some studies, these catalytic systems required strict reaction conditions, including a higher reaction temperature (200-300 ºC),[5e, 5g] a higher hydrogen pressure (20-40 bar),[5a, 5d-g] or corrosive hydrochloric acid (HCl or H_2SO_4),[3] which is unfavorable for the practical production of DMF. Thus, it is necessary to prepare a catalyst with high activity and high selectivity under mild conditions. In addition, the role of interface between bimetallic NPs (e.g., Pt-

Co) and substrates on catalytic performance is not explored. There is no study on the synergistic effect between metal NPs and substrates on the hydrogenolysis of HMF and the mechanism is not clear that how they work collectively to improve the activity and selectivity to DMF. It is vital to investigate the synergistic effect systematically in order to further optimize the bimetallic catalysts and improve the yield of DMF.

In this study, supported Pt-Co bimetallic NPs were prepared and studied for HMF hydrogenolysis. First, Pt NPs was deposited on different substrates (i.e., multi-walled carbon nanotubes (MWCNTs), silica gel particles, and γ-Al_2O_3 NPs) using atomic layer deposition (ALD). After screening examination in HMF hydrogenolysis reactions, MWCNTs were chosen as the support to prepare Pt-Co bimetallic catalysts, since Pt/MWCNTs showed excellent catalytic performance. Then, 10 and 25 cycles of Co were deposited on Pt/MWCNTs via ALD to obtain different mass ratios of Pt to Co for Pt-Co/MWCNTs bimetallic catalysts (Figure 1, Path A), and these two Pt-Co bimetallic catalysts were used in hydrogenolysis of HMF to DMF with different reaction temperatures to further improve the yield of DMF. In order to investigate the synergetic effect among Pt, Co, and MWCNTs on the catalytic performance of Pt-Co/MWCNTs bimetallic catalysts, Al_2O_3 ALD was applied for preparation of Pt-Co/Al_2O_3/MWCNTs catalysts to separate Pt-Co from MWCNTs, as schematically shown in Figure 1 (Path B). In addition, a mixture of Pt/MWCNTs and Co/MWCNTs monometallic catalysts was prepared to avoid the contact between Pt NPs and Co NPs (Figure 1, Path C), and it was also used in HMF hydrogenolysis reactions to investigate the synergetic effect between Pt and Co NPs through comparing with Pt-Co/MWCNTs bimetallic catalysts.

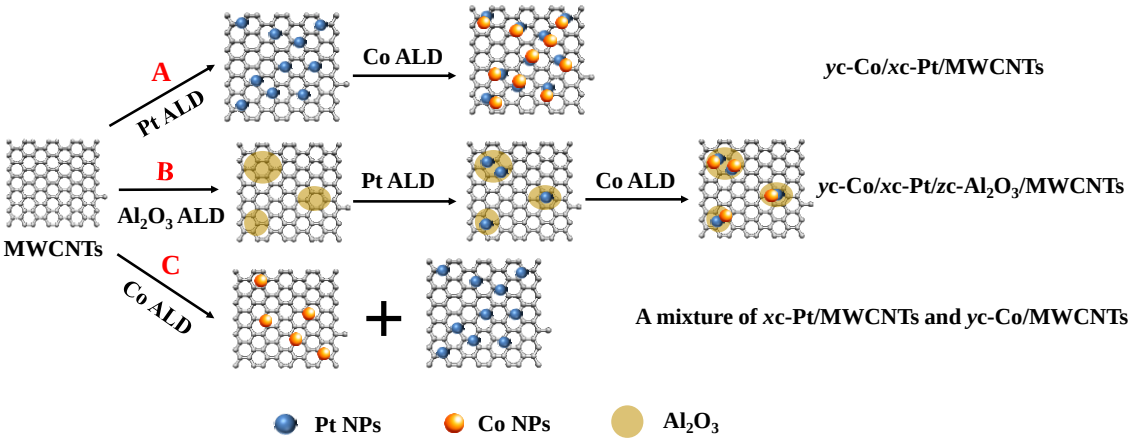

Figure 1. Scheme for the synthesis of catalysts (*x*, *y* and *z* are the number of Pt, Co, and Al_2O_3 ALD cycles, respectively, and the order of *x*, *y*, and *z* represents the order of deposition).

2. EXPERIMENTAL SECTION

2.1. CATALYST PREPARATION

All MWCNTs supported catalysts were synthesized as presented in Figure 1. MWCNTs supported Pt and Pt-Co catalysts were obtained via path A. The Pt-Co bimetallic NPs were isolated from MWCNTs via coating 5 cycles of Al_2O_3 ALD on MWCNTs (path B), and Pt NPs were separated from Co NPs via Al_2O_3 ALD, as shown in path C. *x*, *y* and *z* are the number of Pt, Co, and Al_2O_3 ALD cycles, respectively. 1 cycle of Pt ALD was also deposited on silica gel and porous γ-Al_2O_3 particles to obtain Pt/SiO_2 and Pt/γ-Al_2O_3 catalysts. In addition, 15 cycles of Co ALD was applied on MWCNTs directly to get 15c-Co/MWCNTs sample for hydrogen temperature programmed reduction (H_2-TPR) analysis and hydrogenolysis of HMF reaction. The ALD deposition process was performed in a fluidized bed reactor, as reported in detail previously.[6] All

catalysts were directly used in the following catalytic experiments without any further treatment. The details of Pt ALD, Co ALD, and Al_2O_3 ALD are described in the Electronic Supplementary Information (ESI).

2.2. CATALYST CHARACTERIZATION

Pt, Co and Al mass fractions of all catalysts were analyzed by inductively coupled plasma atomic emission spectroscopy (ICP-AES). The Brunauer–Emmett–Teller (BET) surface area and pore size distribution of substrates and catalysts were measured by Quantachrome Autosorb-1. The Pt and Pt-Co NPs were visualized with transmission electron microscopy/Energy Dispersive Spectroscopy (TEM/EDS) and high-resolution TEM (HRTEM). The reduction properties of the MWNCTs supported Pt, Pt-Co, Co, and Pt-Co/Al_2O_3 catalysts were analyzed by H_2-temperature programmed reduction (TPR). CO-chemisorption was used to determine the Pt dispersion of Pt monometallic catalysts. The details of characterization are described in ESI.

2.3. CATALYST PERFORMANCE

Hydrogenolysis of HMF was performed in a stainless steel Parr reactor (50 mL) with an external temperature and stirring controller, as described in detail elsewhere.[7] Briefly, 0.5 g HMF and 30 mL 1-butanol were added into the reactor. Then certain amount of catalyst was added. Due to the different contents of Pt on the catalyst supports, the mass of catalysts added in the reactor was different in order to ensure an identical Pt loading (4.35 mg) added in the reaction. The reactor was first pressurized to 10 bar with H_2 and the valve was opened to air to depressurize the reactor to atmospheric pressure.

This process was repeated 10 times to make sure 99.99% of the air in the reactor was replaced by H_2. Then the reactor was pressurized with H_2 at 10 bar and the temperature increased to certain temperature (140, 160 or 180 °C). The slurry was stirred at a rate of 500 rpm to eliminate the external diffusion limitations. A small volume of sample (1 mL) was periodically collected and analyzed by using a gas chromatography with flame ionization detector system (GC-FID, Agilent 6890) according to internal standard (toluene).

3. RESULTS AND DISCUSSION

3.1. CATALYST CHARACTERIZATION

Some physical-chemical properties of different substrates (MWCNTs, silica gel, and γ-Al_2O_3) are shown in Tables 1 and S1. The BET surface areas of MWCNTs, silica gel, and γ-Al_2O_3 were 144, 272, and 91 m^2/g, respectively. The pore volume of MWCNTs was the highest and reached 2.1 cm^3/g. As shown in Figure S1, the structure of all substrates were mesoporous. MWCNTs showed two broad peaks between 2 to 100 nm, and silica gel presented a sharp peak centered on 15 nm with a narrow pore size distribution. The size of most pores for γ-Al_2O_3 was between 5 to 30 nm. Based on ICP-AES results, the Pt loadings on silica gel and γ-Al_2O_3 were 4.0 and 2.4 wt.%, respectively. The average Pt particle size and Pt dispersion on γ-Al_2O_3 were 1.3 nm and 83% through CO-chemisorption analysis, respectively, and the Pt dispersion on silica gel was lower than that on γ-Al_2O_3, as shown in Table S1. These results were consistent with our previous report.[7]

Table 1. Properties of the MWCNTs and MWCNTs supported Pt and Pt-Co catalysts (Path A and Path C).

Sample	BET surface area, m^2/g	Pore volume, cm^3/g [a]	Pt, wt.% [b]	Co, wt.% [b]	Average particle size, nm [c]
MWCNTs	144	2.1	0	0	-
3c-Pt/MWCNTs	133	1.6	8.7	0	1.5
10c-Co/3c-Pt/MWCNTs	130	1.4	8.5	2.4	1.6
25c-Co/3c-Pt/MWCNTs	125	1.3	8.2	6.3	1.6
15c-Co/MWCNTs	140	1.9	0	3.5	1.3

[a] Pore volume was obtained from the desorption curve of the N_2 isotherm. [b] Pt and Co loadings were obtained from ICP-AES. [c] The average metal particle size was obtained from TEM images.

The physical-chemical properties of the MWCNTs and MWCNTs-supported catalysts are summarized in Table 1. After Pt and Co ALD, the BET surface areas and total pore volume of all catalysts decreased slightly as compared to those of MWCNTs, but the pore size distribution of all catalysts almost did not change (Figure S2). Thus, the effect of catalysts structure on the following HMF hydrogenolysis reactions was not considered when we studied the catalytic performance of MWCNTs supported catalysts. The ICP−AES results in Table 1 showed the Pt and Co contents on MWCNTs. After 3 cycles of Pt ALD, the Pt content was 8.7 wt.% for 3c-Pt/MWCNTs sample. Then the Pt content decreased slightly with the increase of the number of Co ALD. The TEM images

of MWCNTs supported Pt and Pt-Co catalysts, along with their particle size distribution were shown in Figure S3. The NPs were highly dispersed on the surface of MWCNTs for all catalysts. The average size of the Pt NPs were 1.5 nm for 3c-Pt/MWCNTs catalyst (Table 1). Compared with Pt NPs, the NPs sizes of Pt-Co samples were slight larger and their particle size distribution changed broad (Figure S3). Compared to that of Pt NPs, the average particle size of Co was smaller and it was 1.5 nm. To further demonstrate the structure of Pt-Co bimetallic NPs, HRTEM was carried out. As presented in Figure 2, some metal NPs stuck to each other (red circle). The crystal fringes are clearly displayed (the inset from Figure 2) and the *d*-spacing was determined to be 0.230 nm and 0.206 nm, corresponding to the (111) planes of the face centered cubic (fcc) Pt crystals and the (111) planes of Co crystals, respectively.[8] Thus, the formation of Pt-Co bimetallic NPs was confirmed and the "twinned" Pt-Co NPs were defined as bimetallic NPs in this study.

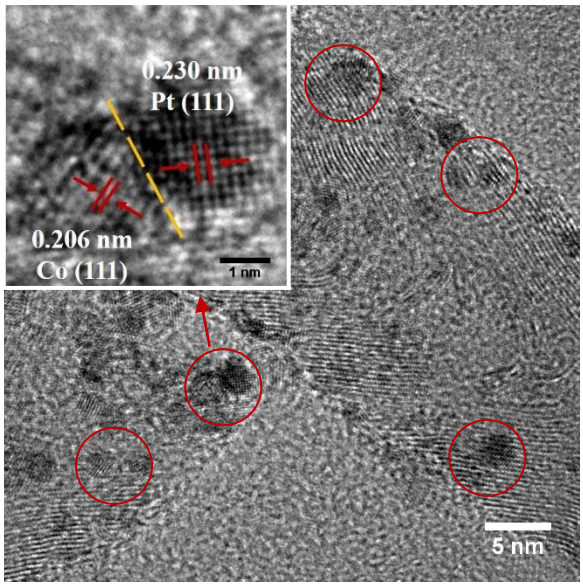

Figure 2. HRTEM image of 25c-Co/3c-Pt/MWCNTs catalyst.

Pt, Co, and Al contents in the Al_2O_3 coated Pt and Pt-Co catalysts are summarized in Table 2. After 5 cycles of Al_2O_3 ALD and 2 cycles of Pt ALD, the Al and Pt loadings in all catalysts were similar and they were about 4.7 and 5.0 wt.%, respectively. It is noted that after Al_2O_3 ALD coating, the Co content increased fast on 5c-Al_2O_3/MWCNTs with the increasing number of Co ALD cycles in comparison to that on MWCNTs, as shown in Figure S4, which could be due to the near-perfect structure and inert property of MWCNTs. According to previous report, the growth rate of Al_2O_3 film was 0.10-0.15 nm/cycle via ALD.[9] Thus, the Al_2O_3 film thickness, after five cycles Al_2O_3 ALD, was ~0.6 nm in this work. Based on theoretical calculation, 1 g of 5c-Al_2O_3/MWCNTs contained about 0.089 g Al_2O_3 (8.9 wt.%, and density of 3.95 g/cm^3), and the thickness of Al_2O_3 should be around 0.16 nm (0.089/3.95/140*1000 nm) if Al_2O_3 formed as a uniform film on the MWCNTs (~ 140 m^2/g). This number was much lower than 0.6 nm, which indicates that the Al_2O_3 film covered on MWNCTs was not uniform. This could be attributed to the fact that Al_2O_3 only grew on specific defective sites rather than forming a uniform film on the MWCNTs through ALD, since the surface of MWCNTs lacked hydroxyl groups and the structure was near-perfect. A similar phenomenon has been observed previously.[10]

As shown in Table 2, the BET surface areas of all Al_2O_3 coated samples decreased from ~140 to ~95 m^2/g, which could be attributed to the fact that some pores were blocked by Al_2O_3. However, the Pt and Pt-Co NPs were still highly dispersed on the MWCNTs, and the average particle sizes of Pt and Pt-Co NPs were ~1.3 and ~1.6 nm, respectively, as shown in Figure S5. They were close to the average particle sizes of Pt and Pt-Co NPs on MWCNTs, which implied that the decrease of surface area did not

Table 2. Pt, Co, and Al loading of Al_2O_3-coated catalysts (Path B).

Sample	BET surface area, m^2/g	Pt, wt.%[a]	Co, wt.%[a]	Al, wt.%[a]	Average particle size, nm[b]
2c-Pt/5c-Al_2O_3/MWCNTs	95	5.5	0	4.8	1.3
3c-Co/2c-Pt/5c-Al_2O_3/MWCNTs	92	5.3	3.4	4.7	1.5
5c-Co/2c-Pt/5c-Al_2O_3/MWCNTs	98	5.2	5.5	4.6	1.7
8c-Co/2c-Pt/5c-Al_2O_3/MWCNTs	94	5.2	6.4	4.5	1.7

[a] Pt, Co and Al loading were obtained from ICP-AES. [b] The average metal particle size was obtained from TEM images.

affect the Pt dispersion. In order to verify it, the Pt dispersion of 3c-Pt/MWCNTs and 2c-Pt/5c-Al_2O_3/MWCNTs catalysts was measured via CO-chemisorption and they were 77.5% and 79.3%, respectively, which were similar and consistent with TEM analysis. In addition, since the Al_2O_3 film was ultrathin, no Al_2O_3 films were observed in the TEM images (Figure S5), although the EDS spectra verified the existence of Al_2O_3 on the samples (Figure S6).

In order to study the reducibility of MWCNTs supported catalysts, TPR analysis was performed. As shown in Figure 3, there is no H_2 consumption peak observed for 3c-Pt/MWCNTs and 2c-Pt/5c-Al_2O_3/MWCNTs catalysts, which indicates that Pt NPs kept metallic in the air after ALD process. This was consistent with the previous publication.[11] While a peak at around 422 ºC appeared in Figure 3c, which could be attributed to the reduction of CoO_x. It implies that Co NPs were partly oxidized in the air after Co ALD for 15c-Co/MWCNTs sample. The TPR profile of 25c-Co/3c-Pt/MWCNTs shows two intense peaks observed at 285 and 401 ºC, (Figure 3d) which are attributed to the reduction of CoO_x that was in contact with Pt and the isolated CoO_x, respectively.[12]

Affected by hydrogen spillover, the reduction of CoO_x shifted to lower temperatures, as the reduced Pt atoms were able to dissociate hydrogen molecules into hydrogen atoms, resulting in the accelerated reduction rate of CoO_x.[13] Thus, it indicates the electron transfer between Pt and Co in Pt-Co bimetallic NPs. This H_2-TPR analysis further proved the formation of Pt-Co "twinned" NPs, which was consistent with the HRTEM result. For the 5c-Co/2c-Pt/5c-Al_2O_3/MWCNTs catalyst, two-stage reduction also showed at 388 ºC and 480 ºC. Compared with that of 25c-Co/3c-Pt/MWCNTs, the reduction temperatures of 5c-Co/2c-Pt/5c-Al_2O_3/MWCNTs increased (Figure 3e), which implied that Pt-Co NPs were deposited on Al_2O_3 instead of MWCNTs and there was a stronger interaction between Co and Al_2O_3 in comparison with that between Co and MWCNTs.

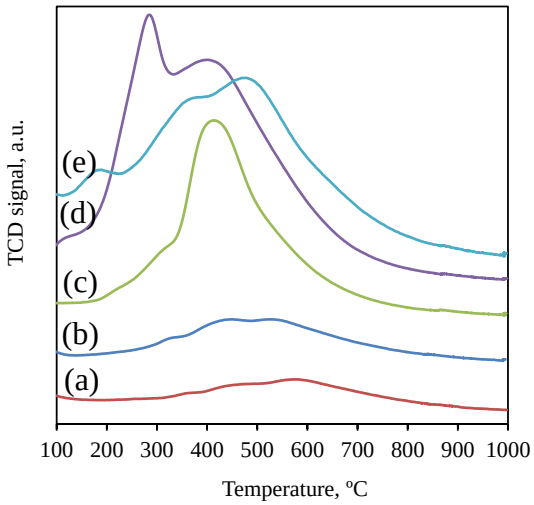

Figure 3. TPR profiles of the catalysts: (a) 3c-Pt/MWCNTs, (b) 2c-Pt/5c-Al_2O_3/MWCNTs, (c) 15c-Co/MWCNTs, (d) 25c-Co/3c-Pt/MWCNTs, and (e) 5c-Co/2c-Pt/5c- Al_2O_3/MWCNTs.

3.2. CATALYST PERFORMANCE

The performance of all Pt catalysts supported on different substrates at 180 ºC and 10 bar H_2 for the hydrogenolysis of HMF to DMF reactions were presented in Table 3. No reaction happened without catalyst (entry 1), and the conversion of HMF over MWCNTs was quite low (entry 2). When using 3c-Pt/MWCNTs as a catalyst, the conversion of HMF was 100% within 6 hr (Figure S7a) and the yield of DMF was 59.6%, with an amount of 5,5-(oxybis(methylene))bis(2-methylfuran) (OMBM) (28%) (entry 3), indicating the effectiveness of Pt/MWCNTs for the selective hydrogenation of the formyl group in HMF. In contrast, the selectivity to DMF was very low over both Pt/SiO_2 and Pt/γ-Al_2O_3 catalysts (entries 4 and 5). It demonstrates that MWCNTs played an important role in enhancing the activity and selectivity to DMF for Pt catalysts in the HMF hydrogenolysis reaction. It can be due to a transfer of the π-electrons from the graphene layer of MWCNTs to the Pt NPs.[14] In this way the charge density on the Pt increases, thus improving the probability for the C=O bond activation.[15] MWCNTs are the material with excellent electrical conductivity, but silica gel and γ-Al_2O_3 are semiconductor and insulated substrate, respectively. Hence, they cannot enhance the charge density of Pt NPs, and thereby MWCNTs were chosen as the support to prepare Pt-Co bimetallic catalysts.

In search of the desired catalyst, first the reaction was conducted over 10c-Co/3c-Pt/MWCNTs and 25c-Co/3c-Pt/MWCNTs catalysts supported on MWCNTs at 180 ºC. As shown in Table 4, with the increase of Co loading in the bimetallic catalysts, the selectivity to DMF increased greatly (entries 1 and 2), and 84.2% yield of DMF was obtained over 25c-Co/3c-Pt/MWCNTs catalyst, indicating the presence of Co can

Table 3. Hydrogenolysis of HMF to DMF over Pt monometallic catalysts with different supports. [a]

Entry	Catalyst	Temperature/time (ºC/hr)	Conversion (%)	Selectivity distribution (%)				
				DMF	DHMF	MFA	OMBM	Others[b]
1	Blank [c]	180/10	0	-	-	-	-	-
2	MWCNTs [d]	180/8	7.3	17.4	-	-	trace	-
3	3c-Pt/MWCNTs	180/8	100	59.6	-	-	28.1	10.7
4	Pt/SiO_2	180/8	68.6	8.3	-	-	-	91.7
5	$Pt/\gamma\text{-}Al_2O_3$	180/8	84.6	12.8	trace	-	trace	97.2

[a] Reaction conditions: 0.5 g HMF, 30 mL 1-butanol, 4.35 mg Pt, 10 bar H_2. [b] Other byproducts include 5-MF, DHTHF, and MTHFA. [c] No catalyst was added in the reaction. [d] 50 mg MWCNTs was added in the reaction.

promote the selectivity of HMF hydrogenolysis to DMF and hinder the production of OMBM. The increase of selectivity to DMF could be due to the fact that the deposition of Co on Pt NPs modified the electronic structure of Pt atoms, and destabilized the adsorption of the C=C bond.[16] Thereby, the selectivity to C=O improved greatly. Figure 4a shows the reactant adsorption mode over Pt-Co/MWCNTs catalysts. The contact between Pt and Co favors the electronic transfer from Co^0 towards Pt^0,[17] which results in a positive charge density in the Co atoms and a negative charge density in the Pt atoms. The increased charge density on the metal NPs would help $C^{\delta+}$-$O^{\delta-}$ adsorb over a $Pt^{\delta-}$-$Co^{\delta+}$ site and decrease the probability of adsorption via the furan group, so the selectivity to DMF was higher over 25c-Co/3c-Pt/MWCNTs catalyst. The electron can be transferred from Co to Pt directly or through MWCNTs. Since MWCNTs are a kind of material with

excellent electrical conductivity, they could enhance the electronic transfer and thereby improve the charge density on metal NPs, as mentioned above, which would further promote the yield of DMF. Thus, the synergistic effect among Pt, Co and MWCNTs improved the yield of DMF over Pt-Co/MWCNTs bimetallic catalysts compared to 3c-Pt/MWCNTs catalyst. The proposed hypothesis will be discussed later.

Table 4. Hydrogenolysis of HMF to DMF over MWCNTs-supported Pt-Co bimetallic catalysts. [a]

Entry	Catalyst	Temperature/time (°C/hr)	Conversion (%)	Selectivity distribution (%)				
				DMF	DHMF	MFA	OMBM	Others [a]
1	10c-Co/3c-Pt/MWCNTs	180/8	100	69.0	-	-	20.2	10.0
2	25c-Co/3c-Pt/MWCNTs	180/8	100	84.2	trace	-	12.3	3.2
3	25c-Co/3c-Pt/MWCNTs	160/8	100	92.3	trace	-	5.7	2.0
4	25c-Co/3c-Pt/MWCNTs	140/10	79.3	77.2	10..1	trace	4.1	17.1
5	3c-Co/2c-Pt/5c-Al_2O_3/MWCNTs	160/8	41.7	14.2	trace	-	7.2	78.6
6	5c-Co/2c-Pt/5c-Al_2O_3/MWCNTs	160/8	56.9	13.5	-	-	10.2	76.3
7	8c-Co/2c-Pt/5c-Al_2O_3/MWCNTs	160/8	39.8	13.1	trace	-	9.3	77.6
8	A mixture of 3c-Pt/MWCNTs and 15c-Co/MWCNTs [b]	160/8	100	65.3	-	-	22.1	12.6

[a] Reaction conditions: 0.5 g HMF, 30 mL 1-butanol, 4.35 mg Pt, 10 bar H_2. [a] Other byproducts include 5-MF, DHTHF, and MTHFA. [b] 53 mg 3c-Pt/MWCNTs and 95 mg 15c-Co/MWCNTs were used in hydrogenolysis of HMF reaction, which were the same as the Pt and Co masses of 25c-Co/3c-Pt/MWCNTs catalyst, respectively.

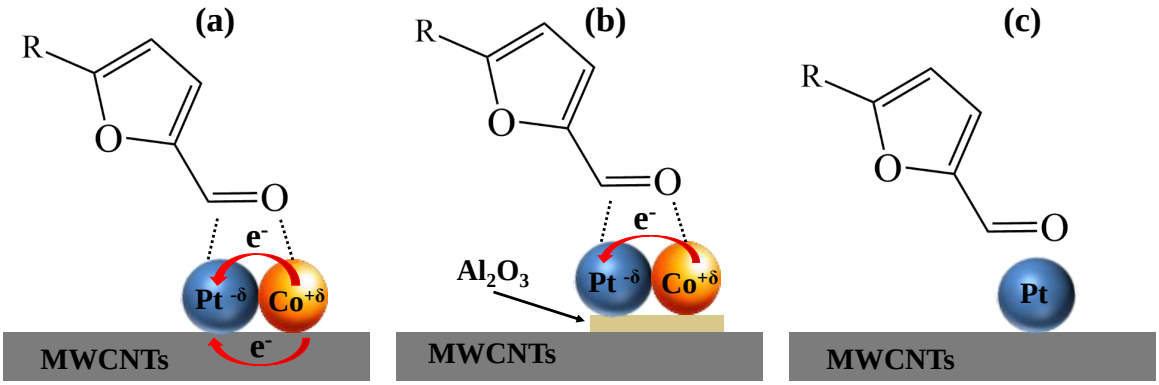

Figure 4. Adsorption models of reactant on different catalysts: (a) *y*c-Co/*x*c-Pt/MWCNTs; (b) *y*c-Co/*x*c-Pt/*z*c-Al_2O_3/MWCNTs; (c) a mixture of *x*c-Pt/MWCNTs and *y*c-Co/MWCNTs.

It is quite interesting to note that 10c-Co/3c-Pt/MWCNTs catalyst showed the highest activity, followed by 3c-Pt/MWCNTs and 25c-Co/3c-Pt/MWCNTs samples, since the conversion of HMF over 10c-Co/3c-Pt/MWCNTs reached 100% in a shortest time (Figure S7a). As reported in previous work, the presence of Co can improve the activity of Pt-Co catalysts due to the synergistic effect of Pt-Co bimetallic NPs.[16] However, compared with 3c-Pt/MWCNTs and 10c-Co/3c-Pt/MWCNTs catalysts, the low activity of 25c-Co/3c-Pt/MWCNTs should be attributed to the fact that too many Co NPs attached to Pt NPs and it leaded to steric hindrance. It would hinder the adsorption of reactant onto 25c-Co/3c-Pt/MWCNTs catalyst due to lack of enough space and thereby affect the catalytic activity of the catalyst. But the moderate activity is good for improving the selectivity to DMF since OMBM is relatively easy to be produced over catalysts with very high activity. It is also noted that the selectivity to DMF kept same between 8 hr to 10 hr of reaction time over all three catalysts (Figure S7b), indicating that there was no intermediate byproducts (DHMF, 5-MF and MFA) produced in the solution after 8 hr. In

addition, DMF was stable in this catalytic system and further hydrogenation of furan ring did not occur, which is crucial in the large-scale production of DMF in industry. In order to obtain a higher selectivity to DMF, the reaction of HMF hydrogenolysis carried out at different temperatures over 25c-Co/3c-Pt/MWCNTs catalyst (entries 2-4). The highest yield of DMF (92.3%) achieved at 160 ºC (entry 3). With the reaction temperature decreasing the selectivity to OMBM decreased, indicating that the reaction of OMBM production occurred easier at high temperature. Though the selectivity to OMBM was lower at 140 ºC than that at 160 ºC, the selectivity to DMF was not high, since HMF did not react completely (Figure S8) and other byproducts, especially intermediate byproducts, formed (entry 4). Thus, high yield of DMF (>90%) was obtained over 25c-Co/3c-Pt/MWCNTs under mild conditions.

In order to verify the proposed synergistic effect among Pt, Co, and MWCNTs, an ultra-thin Al_2O_3 film (~0.6 nm thick) deposited by 5 cycles of Al_2O_3 ALD was used to modify the interfaces of catalysts. All Al_2O_3 coated catalysts were used for the reaction of HMF hydrogenolysis and the results are presented in Table 4 (entries 5-7). After depositing Co on 2c-Pt/5c-Al_2O_3/MWCNTs, all Pt-Co/5c-Al_2O_3/MWCNTs catalysts presented a much lower selectivity to DMF than 25c-Co/3c-Pt/MWCNTs catalyst. As schematically demonstrated in Figure 4b, since Pt-Co NPs were isolated from MWCNTs via Al_2O_3 film, the electronic transfer can only occur from Co to Pt directly, instead of through MWCNTs in Pt-Co/5c-Al_2O_3MWCNTs catalysts. Thus, the charge density on the bimetallic Pt-Co NPs was not strong enough to hinder hydrogenation of furan ring though the density increased slightly. Thus, the selectivity to DMF decreased greatly and more byproducts produced. The increased charge density on the bimetallic Pt-Co NPs would

promote the selectivity to C=O. In other words, the interaction between Pt-Co bimetallic NPs and MWCNTs plays an important role in the selectivity to DMF. It can be explained that MWCNTs worked as a “bridge”, connected Pt with Co, and helped electronic transfer from Co to Pt, which enhanced the charge density on metal NPs (Pt and Co). At the same time, the conversion of HMF over Pt-Co/5c-Al_2O_3/MWCNTs catalysts decreased as well compared with that over 25c-Co/3c-Pt/MWCNTs catalysts. It could be attributed to the fact that the enhanced charge density of bimetallic NPs would boost the adsorption and dissociation rate of C=O over $Pt^{\delta-}$-$Co^{\delta+}$ sites in the reaction of HMF hydrogenolysis. Thus, the synergistic effect between Pt-Co bimetallic NPs and MWCNTs promoted both the selectivity to DMF and activity of Pt-Co bimetallic catalysts greatly.

A mixture of 3c-Pt/MWCNTs and 15c-Co/MWCNTs monometallic catalysts was also used in hydrogenolysis of HMF reaction to investigate the synergistic effect between Pt and Co NPs. As shown in Table 4 (entry 8), the HMF conversion and selectivity to DMF were 100% and 65.3%, respectively. Compared with that over 25c-Co/3c-Pt/MWCNTs, the selectivity to DMF was lower over the mixture catalyst though the conversion of HMF reached 100% over both of them. As schematically presented in Figure 4c, the reactant was mainly adsorbed on the 3c-Pt/MWCNTs instead of 15c-Co/MWCNTs because the activity of the 2c-Pt/MWCNTs catalyst was much higher than that of the 15c-Co/MWCNTs catalyst. Thus, this revealed that the interaction between Pt and Co in the Pt-Co bimetallic NPs had played an important role in the hydrogenolysis of HMF reaction and improved the selectivity to DMF.

4. CONCLUSIONS

Highly dispersed Pt-Co bimetallic NPs were deposited on MWCNTs for hydrogenolysis of HMF to DMF. Both the HRTEM and H2-TPR analysis confirmed the formation of Pt-Co bimetallic NPs on MWCNTs. High yield of DMF (> 90%) was achieved in hydrogenolysis of HMF over 25c-Co/3c-Pt/MWCNTs catalyst after 8 hr of reaction time under mild conditions. More importantly, through a series of experiments it is revealed that the synergistic effect between Pt-Co bimetallic NPs and MWCNTs dramatically improved the yield of DMF in the HMF hydrogenolysis reactions since MWCNTs with excellent electrical conductivity enhanced the electronic transfer and thereby enhanced the charge density on Pt-Co NPs. The current work has extended the utility of readily available catalyst toward large-scale production of DMF in the future.

ACKNOWLEDGEMENTS

This work was supported in part by the ACS Petroleum Research Fund. The authors thank Dr. Jessica TerBush and Dr. Jingjing Qing at the Materials Research Center at Missouri University of Science and Technology for TEM analysis. Use of the Advanced Photon Source and Center for Nanoscale Materials, Office of Science User Facilities operated for the U.S. Department of Energy (DOE) Office of Science by Argonne National Laboratory, was supported by the U.S. DOE under Contract No. DE-AC02-06CH11357.

NOTES AND REFERENCES

1. Y. Zu, P. Yang, J. Wang, X. Liu, J. Ren, G. Lu and Y. Wang, *Applied Catalysis B: Environmental*, 2014, 146, 244.

2. B. Saha, C. M. Bohn and M. M. Abu-Omar, *ChemSusChem*, 2014, 7, 3095.

3. S. Nishimura, N. Ikeda and K. Ebitani, *Catalysis Today*, 2014, 232, 89.

4. Y. Nakagawa, M. Tamura and K. Tomishige, *ACS Catalysis*, 2013, 3, 2655.

5. (a) J. Luo, L. Arroyo-Ramírez, R. J. Gorte, D. Tzoulaki and D. G. Vlachos, *AIChE Journal*, 2015, 61, 590; (b) G. H. Wang, J. Hilgert, F. H. Richter, F. Wang, H. J. Bongard, B. Spliethoff, C. Weidenthaler and F. Schüth, *Nature Materials*, 2014, 13, 293; (c) D. Scholz, C. Aellig and I. Hermans, *ChemSusChem*, 2014, 7, 268; (d) Y. B. Huang, M. Y. Chen, L. Yan, Q. X. Guo and Y. Fu, *ChemSusChem*, 2014, 7, 1068; (e) L. Hu, X. Tang, J. Xu, Z. Wu, L. Lin and S. Liu, *Industrial and Engineering Chemistry Research*, 2014, 53, 3056; (f) J. Jae, W. Zheng, R. F. Lobo and D. G. Vlachos, *ChemSusChem*, 2013, 6, 1158; (g) J. Zhang, L. Lin and S. Liu, *Energy and Fuels*, 2012, 26, 4560; (h) S. De, S. Dutta and B. Saha, *ChemSusChem*, 2012, 5, 1826; (i) M. Chidambaram and A. T. Bell, *Green Chemistry*, 2010, 12, 1253; (j) J. B. Binder and R. T. Raines, *Journal of the American Chemical Society*, 2009, 131, 1979.

6. (a) Z. Shang, R. L. Patel, B. W. Evanko and X. Liang, *Chemical Communications*, 2013, 49, 10067; (b) X. Wang, H. Zhao, T. Wu, Y. Liu and X. Liang, *Catalysis Letters*, 2016, 146, 2606.

7. X. Wang, W. Hu, B. Deng and X. Liang, *Journal of Nanoparticle Research*, 2017, 19, Article No. 153.

8. (a) L. Xin, F. Yang, S. Rasouli, Y. Qiu, Z.-F. Li, A. Uzunoglu, C.-J. Sun, Y. Liu, P. Ferreira and W. Li, *ACS Catalysis*, 2016, 6, 2642; (b) Y. Su, Y. Zhu, H. Jiang, J. Shen, X. Yang, W. Zou, J. Chen and C. Li, *Nanoscale*, 2014, 6, 15080.

9. M. Groner, F. Fabreguette, J. Elam and S. George, *Chemistry of Materials*, 2004, 16, 639.

10. S. M. George, *Chemical Reviews*, 2010, 110, 111.

11. T. Aaltonen, M. Ritala, T. Sajavaara, J. Keinonen and M. Leskelä, *Chemistry of Materials*, 2003, 15, 1924.

12. D. O. Silva, L. Luza, A. Gual, D. L. Baptista, F. Bernardi, M. J. Zapata, J. Morais and J. Dupont, *Nanoscale*, 2014, 6, 9085.

13. (a) G. Jacobs, T. K. Das, P. M. Patterson, J. Li, L. Sanchez and B. H. Davis, *Applied Catalysis A: General*, 2003, 247, 335; (b) S. Vada, A. Hoff, E. Ådnanes, D. Schanke and A. Holmen, *Topics in Catalysis*, 1995, 2, 155.

14. H. Ma, L. Wang, L. Chen, C. Dong, W. Yu, T. Huang and Y. Qian, *Catalysis Communications*, 2007, 8, 452.

15. M. L. Toebes, F. F. Prinsloo, J. H. Bitter, A. J. van Dillen and K. P. de Jong, *Journal of catalysis*, 2003, 214, 78.

16. S. C. Tsang, N. Cailuo, W. Oduro, A. T. Kong, L. Clifton, K. K. Yu, B. Thiebaut, J. Cookson and P. Bishop, *ACS Nano*, 2008, 2, 2547.

17. N. M. Bertero, A. F. Trasarti, B. Moraweck, A. Borgna and A. J. Marchi, *Applied Catalysis A: General*, 2009, 358, 32

ELECTRONIC SUPPLEMENTARY INFORMATION

This file includes:

Experimental details

1. Catalysts preparation

2. N_2 adsorption-desorption measurements

3. Transmission electron microscopy (TEM) analysis

4. H_2-temperature programmed reduction (TPR) analysis

5. CO-chemisorption

Figures S1-S8

Table S1

*Corresponding authors:

E-mail: liangxin@mst.edu (Xinhua Liang)

Experimental details

1. Catalysts preparation.

Platinum (Pt) atomic layer deposition (ALD) was carried out in the fluidized bed reactor at 300 °C, and the two precursors were (methylcyclopentadienyl)trimethyl platinum [(MeCp)$PtMe_3$] and oxygen (O_2), as described previously [1]. Briefly, in a typical run, certain amount of substrates (multi-walled carbon nanotubes, silica gel, or γ-Al_2O_3) were added in the reactor. The particle substrates were fully fluidized with a gas flow rate controlled by mass flow controllers. N_2 was used as flush gas to remove unreacted precursors and any byproducts during the reaction. A typical half coating cycle used the following sequence: precursor dose, N_2 purge, and evacuation. This sequence was repeated alternatively for both precursors.

Co nanoparticles (NPs) were deposited on substrates via ALD following the similar procedures as Pt ALD using conbaltocene ($CoCp_2$) and hydrogen (H_2) as precursors at 300 °C. The solid precursor $CoCp_2$ was put in a heated bubbler and carried by N_2. A typical Co deposition cycle used the following steps: $CoCp_2$ dose, N_2 purge, and evacuation; H_2 dose, N_2 purge, and evacuation.

Al_2O_3 ALD was performed following the similar procedures as mentioned above using trimethylaluminium (TMA) and deionized water (H_2O) as precursors at 177 ºC. A typical coating cycle contained the following steps: TMA dose, N_2 purge, and evacuation; H_2O dose, N_2 purge, and evacuation again.

2. N_2 adsorption-desorption measurements

Nitrogen adsorption and desorption isotherms of substrates and catalysts were obtained at -196 ºC. The surface area and the total pore volume of the samples was

calculated using the Brunauer–Emmett–Teller (BET) method in a relative pressure range of 0.05-0.25 and the adsorption quantity at a relative pressure of $P/P_0 = 0.99$, respectively. The pore size distributions were derived from the desorption branches of the isotherms using the Barrett–Joyner–Halenda (BJH) method.

3. TEM analysis

The supported Pt, Pt-Co and Co NPs were visualized with a FEI Tecnai F20 field emission gun high-resolution TEM. At least 200 NPs on MWCNTs were measured to get the average particle size. The high-resolution TEM (HRTEM) images of 25c-Co/3c-Pt/MWCNTs catalyst were obtained by a JEOL JEM-2100F TEM operated at 200 kV in Argonne National Laboratory.

4. TPR analysis

The reduction properties of the supported Pt, Pt-Co, Co, and Pt-Co/Al_2O_3-based catalysts were analyzed by H_2-TPR. The reaction temperature was programmed to rise at a heating rate of 10 ºC/min up to 1000 ºC and the flow rate was 20 mL/min of 10 mol% H_2/Ar gas. The consumption amount of H_2 during the H_2-TPR was analyzed and measured by a thermal conductivity detector (TCD, Micromeritics Autochem Ⅱ 2920).

5. CO-chemisorption

CO-chemisorption was performed using a Micromeritics Autochem Ⅱ 2920 to investigate the Pt particle size and dispersion of Pt monometallic catalysts. The catalysts were reduced at 350 ºC for 0.5 h and degassed at the same temperature in pure He for 1.5 h. The CO adsorption isotherms were obtained at 50 °C and the stoichiometry of Pt:CO was assumed to be 1:1.

Reference

[1] Jiang, C. and X. Liang, *Catalysis Communications*, 2014. **46**: p. 41-45.

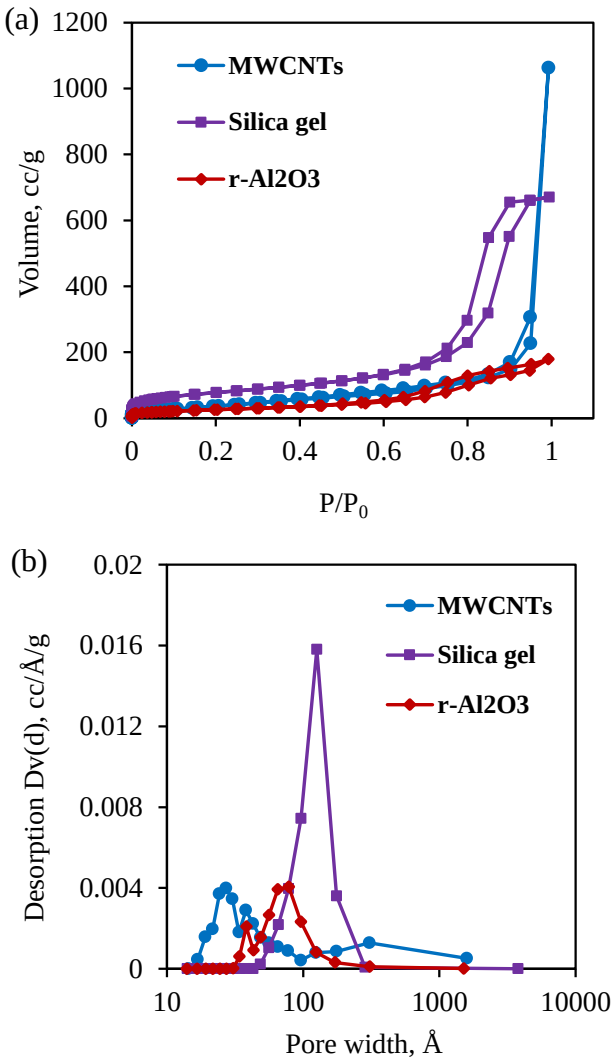

Figure S1. (a) Nitrogen adsorption and desorption isotherms, and (b) pore size distributions of MWCNTs, silica gel, and γ-Al_2O_3.

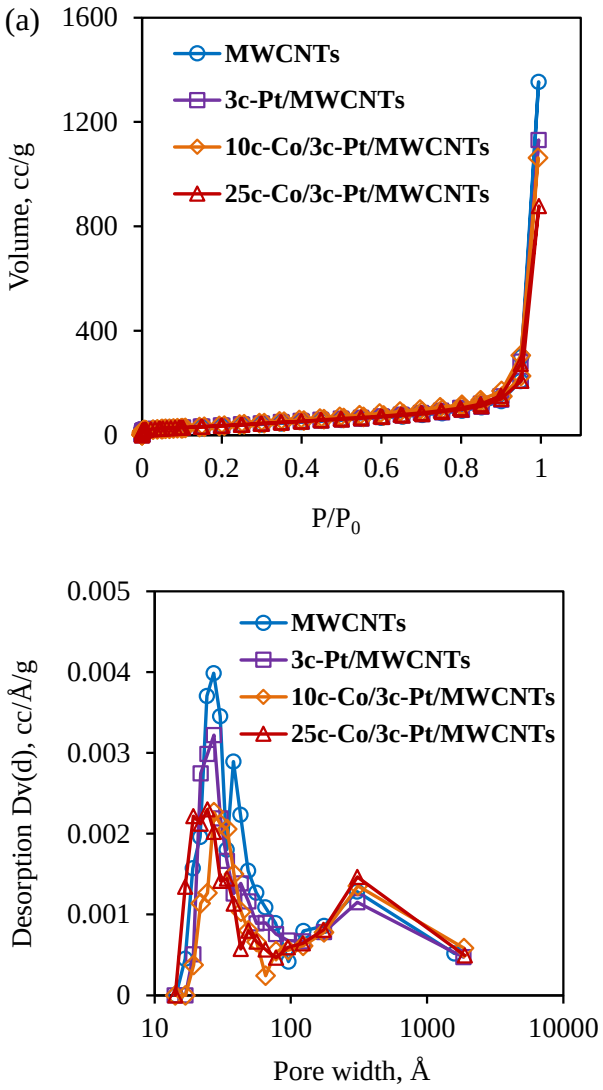

Figure S2. (a) Nitrogen adsorption and desorption isotherms, and (b) pore size distributions of MWCNTs and MWCNTs-supported catalysts.

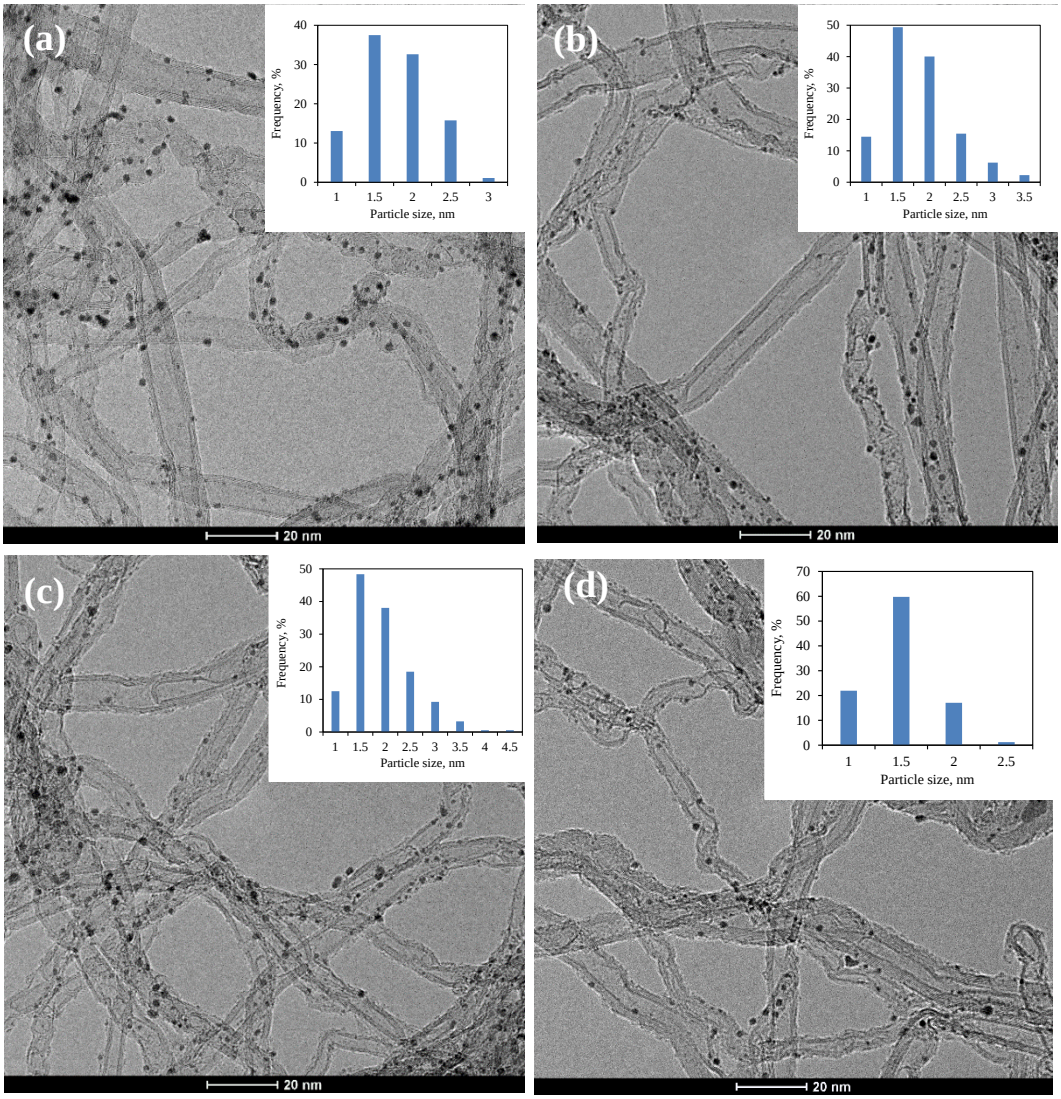

Figure S3. TEM images of (a) 3c-Pt/MWCNTs, (b) 10c-Co/3c-Pt/MWCNTs, (c) 25c-Co/3c-Pt/MWCNTs, and (d) 15c-Co/MWCNTs. The *inset* figures show the size distribution of Pt, Pt-Co, or Co nanoparticles.

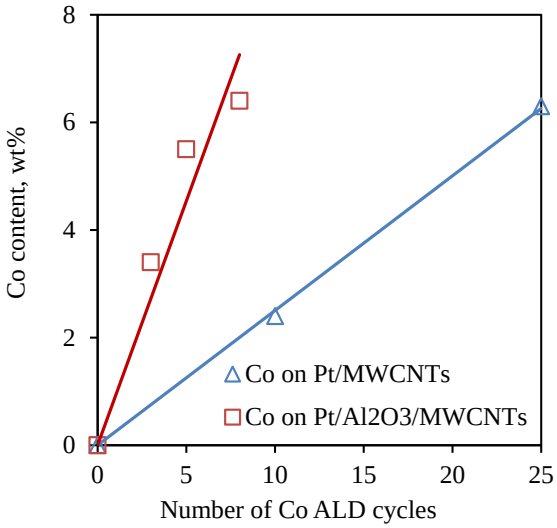

Figure S4. Co content (based on ICP-AES) of Pt-Co bimetallic catalysts versus the number of Co ALD cycles.

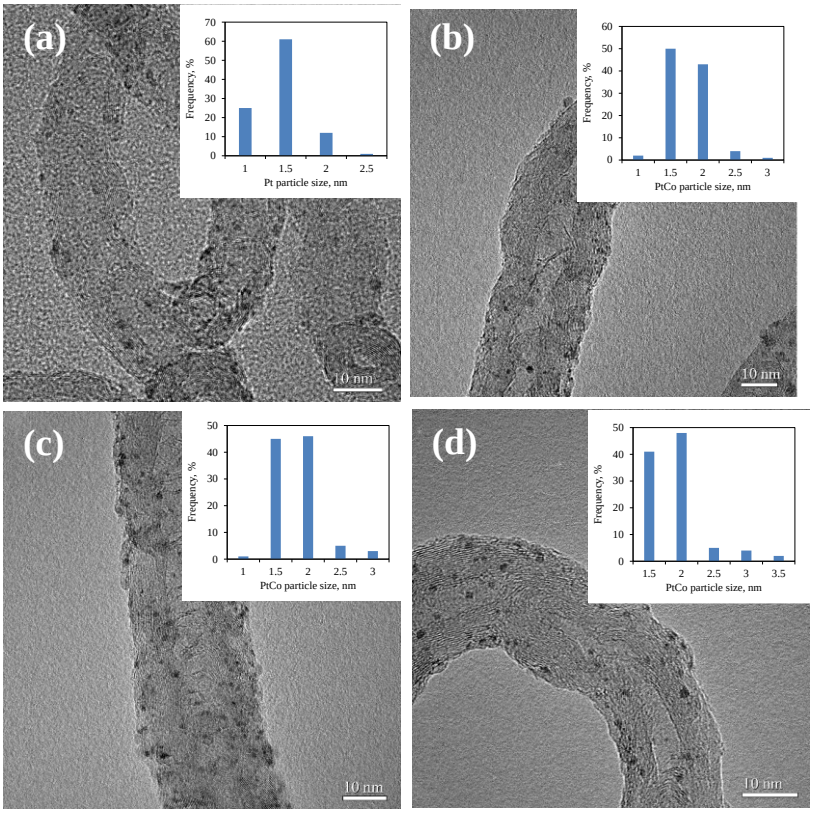

Figure S5. TEM images of (a) 2c-Pt/5c-Al_2O_3/MWCNTs, (b) 3c-Co/2c-Pt/5c-Al_2O_3/MWCNTs, (c) 5c-Co/2c-Pt/5c-Al_2O_3/MWCNTs, and (d) 8c-Co/2c-Pt/5c-Al_2O_3/MWCNTs. The inset figures show the size distribution of Pt or Pt-Co nanoparticles.

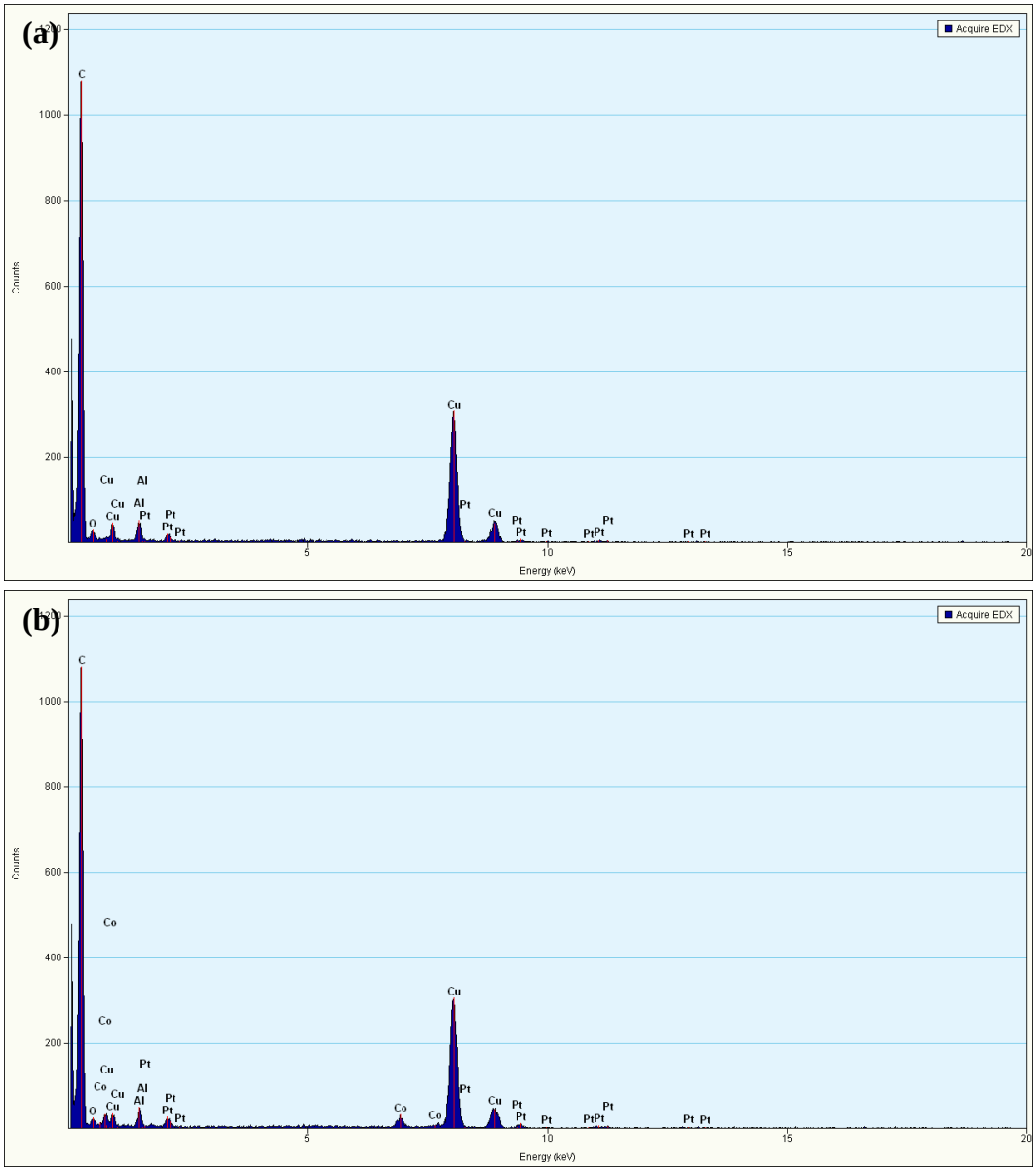

Figure S6. EDS spectra of (a) 2c-Pt/5c-Al_2O_3/MWCNTs catalyst in Figure S5a, and (b) 5c-Co/2c-Pt/5c-Al_2O_3/MWCNTs catalyst in Figure S5c.

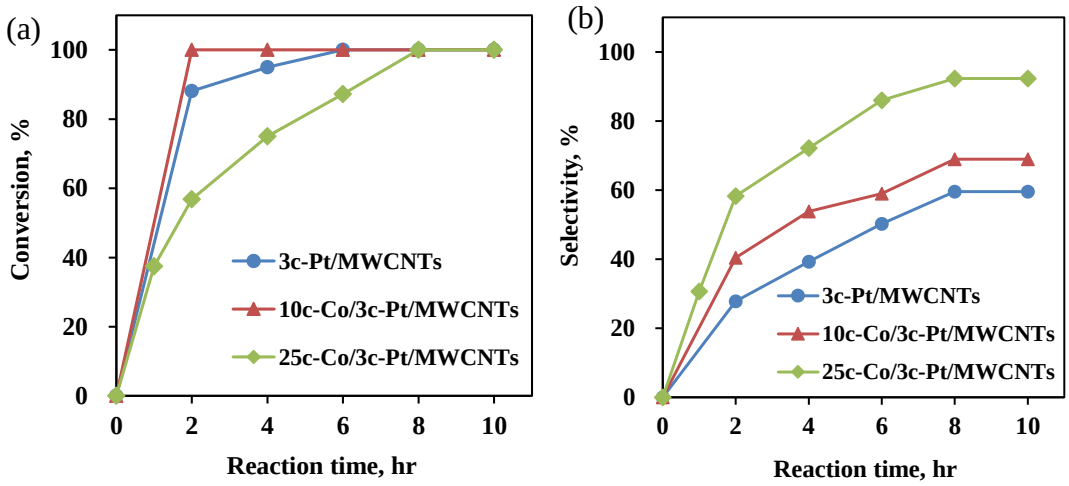

Figure S7. Conversion of HMF (a) and selectivity to DMF (b) versus the reaction time for Pt and Pt-Co catalysts at 180 ºC.

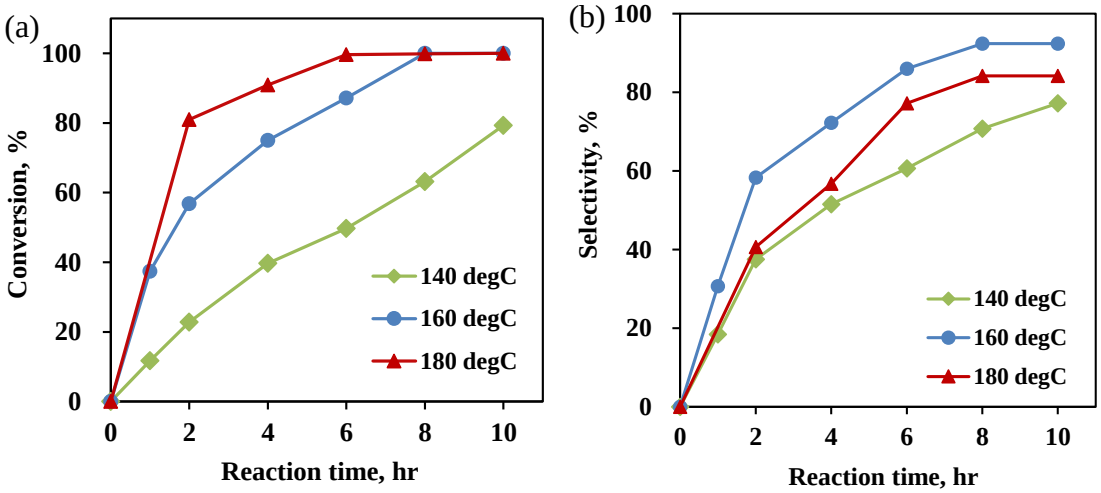

Figure S8. (a) Conversion of HMF and (b) selectivity to DMF versus reaction time for 25c-Co/3c-Pt/MWCNTs catalyst at different reaction temperatures.

Table S1. Properties of silica gel and γ-Al_2O_3.

Sample	BET surface area, m^2/g	Pore volume, cm^3/g	Pt, wt.%	Pt average particle size, nm[a]	Pt dispersion, %
Silica gel	272	0.9	4.0	1.8	62
γ-Al_2O_3	91	0.3	2.4	1.3	83

[a] Pt particle size was obtained according to CO-chemisorption results.

IV. SYNTHESIS OF HIGHLY DISPERSED AND HIGHLY STABLE SUPPORTED AU-PT BIMETALLIC CATALYSTS BY A TWO-STEP METHOD

Highly dispersed and highly stable supported Au-Pt bimetallic catalysts

Xiaofeng Wang [a], Haiyan Zhao [b,#], Tianpin Wu [b], Yuzi Liu [c], and Xinhua Liang [a,*]

[a] Department of Chemical and Biochemical Engineering, Missouri University of Science and Technology, Rolla, Missouri 65409, United States

[b] X-Ray Science Division, Advanced Photon Source, Argonne National Laboratory, 9700 S. Cass Ave., Argonne, Illinois 60439, United States

[c] Center for Nanoscale Materials, Argonne National Laboratory, 9700 S. Cass Ave., Argonne, Illinois 60439, United States

[*] Corresponding author, Email: liangxin@mst.edu

[#] Present address: Department of Chemical & Materials Engineering, University of Idaho, Idaho Falls, Idaho 83401, United States

This paper has been published in *Catalysis Letters*, 146 (12), 2606-2613, 2016.

ABSTRACT

Highly dispersed and highly stable supported bimetallic catalysts were prepared using a two-step process. Pt nanoparticles (NPs) were first deposited on porous γ-Al_2O_3 particles by atomic layer deposition (ALD). Au NPs were synthesized by using gold(III) chloride as the Au precursor, and then immobilized on ALD Pt/γ-Al_2O_3 particles. The Au-Pt bimetallic catalysts were highly active and highly stable in a vigorously stirred liquid phase reaction of glucose oxidation.

Keywords: Gold (Au), Platinum (Pt), Atomic layer deposition (ALD), Glucose oxidation, Bimetallic catalyst, High stability

1. INTRODUCTION

Bimetallic nanoparticles (NPs) have been widely investigated due to their unique properties and great potential in a variety of applications [1-4]. Among them, gold (Au) – platinum (Pt) bimetallic NPs have attracted increasing interest due to their high activity in chemical reactions [5, 6]. However, leaching and the unstable problem of Au-Pt catalysts are barriers to keep their high activity for a long time [6-8]. Over the past decade, numerous studies have focused on this topic and several new preparation methods have been reported to improve the stability of Au-based catalysts [9-11]. For example, Miyamura et al. [10] synthesized Au-Pt catalyst by adding a solution of gold and a secondary metal salt dropwise to a solution of a polymer and sodium borohydride to examine the aerobic glucose oxidation; the activity of the Au-Pt catalyst was maintained after it was recycled for six times. The recycling and reuse of catalysts is one of the key factors for practical applications, since this is especially important for noble metal catalysts because of their high cost.

Herein, we have proposed a two-step approach that combines atomic layer deposition (ALD) and the conventional NaOH reduction method for preparation of Au-Pt bimetallic catalysts in this study. ALD is a surface controlled process, based on self-limiting reactions, that has been demonstrated to deposit highly dispersed metal NPs on a support surface [12, 13]. Recently, ALD has been used to prepare monometallic and

bimetallic catalysts for gas and liquid phase reactions [14-19]. The catalysts prepared by using ALD were much more stable and recyclable due to the strong chemical bonding between the metal NPs and supports, which can prevent leaching in liquid phase reactions [20, 21]. Jiang and Liang [20] reported that there was almost no activity loss for the ALD-prepared Pt catalysts, supported on multi-walled carbon nanotubes (MWCNTs), after recycling the catalysts ten times for a liquid phase hydrogen-transfer reaction of acetophenone. Moreover, the ALD-prepared catalysts usually showed high activity because of the uniform size of the NPs and their high dispersion on the supports [14, 22]. However, it is very difficult to directly prepare Au NPs by ALD, and there has not been any report concerning Au films or the Au NPs ALD process so far.

In this report, a two-step process, using ALD and the NaOH reduction method, was used to prepare Au-Pt bimetallic nanoparticles. Pt was first deposited on an alumina support using ALD in a fluidized bed reactor, and then the NaOH reduction method, modified from literature [23, 24], was used to synthesize the Au NPs and immobilize them onto Pt/γ-Al_2O_3 particles. The synergetic effect between Au and Pt improved both the activity and stability of the catalysts [25]. The catalytic performances of the Au-Pt catalysts were evaluated by selective oxidation of glucose to gluconic acid and compared with the performance of the Au and Pt monometallic catalysts.

2. EXPERIMENTAL

2.1. MATERIALS

(Methylcyclopentadienyl)trimethyl platinum [(MeCp)$PtMe_3$] was purchased from Strem Chemicals, Inc. Alumina (Al_2O_3) NPs (<50 nm), 1.0 wt.% commercial Pt catalyst, gold(III) chloride solution ($HAuCl_4$, ~30 wt.%), tetrakis(hydroxymethyl)-phosphonium chloride (THPC, 80 wt.%), and glucose were received from Sigma-Aldrich, Inc. Porous γ-alumina (γ-Al_2O_3) particles (40 μm) were purchased from Alfa Aesar, Inc. All of the chemicals were used as received without any treatment.

2.2. CATALYSTS PREPARATION

Pt ALD was carried out using (MeCp)$PtMe_3$ as the Pt precursor and oxygen (O_2) as the other reactant at 300 °C in a fluidized bed reactor, as described in detail elsewhere [26]. Both Al_2O_3 NPs and porous γ-Al_2O_3 particles were used as substrates. Four cycles of Pt ALD were applied on Al_2O_3 NPs and different numbers (less than four) of cycles of Pt ALD were deposited on porous γ-Al_2O_3 particles. All ALD Pt/γ-Al_2O_3 particles were directly used in the following catalytic tests without any further treatment. The modified NaOH reduction method [23, 24] was adopted to synthesize Au NPs using $HAuCl_4$ and THPC as precursors, and then the Au NPs were immobilized on γ-Al_2O_3 and ALD Pt/γ-Al_2O_3 particles to fabricate Au/γ-Al_2O_3 and Au-Pt/γ-Al_2O_3 particles. In order to get a better characterization, Au was also deposited on ALD Pt/Al_2O_3 NPs, using the same method, and then the ALD Pt/Al_2O_3 NPs and Au-Pt/Al_2O_3 NPs were used for

transmission electron microscopy (TEM) analysis. The details of Pt, Au, and Au-Pt catalysts preparation are described in the Supplementary Information (SI).

2.3. CATALYSTS CHARACTERIZATION

The Pt and Au mass fractions of prepared catalysts were measured by inductively coupled plasma atomic emission spectroscopy (ICP-AES). The Pt and Au-Pt NPs supported on Al_2O_3 NPs were directly observed by FEI Tecnai F20 TEM. High-resolution TEM (HRTEM) images of Au-Pt/Al_2O_3 NPs were characterized by a JEOL JEM-2100F TEM operated at 200 kV. The composition of the bimetallic NPs was investigated by scanning transmission electron microscopy (STEM)/energy dispersive X-ray spectroscopy (EDS), pair distribution functions (PDF), and X-ray absorption spectroscopy (XAS) analysis. The details of characterization are described in the SI.

2.4. CATALYTIC TEST

The catalytic performances of the Pt, Au, and Au-Pt supported on γ-Al_2O_3 particles were evaluated by glucose oxidation under atmospheric pressure. The reaction was performed in a semi-batch glass reactor (500 mL) equipped with a mechanical propeller stirrer, a gas supply system, a burette containing NaOH solution (0.5 mol/L), and a pH/temperature probe (Mettler Toledo Seven Easy), as previously described in detail [21]. Briefly, 40 mL of distilled water and a certain amount of desired catalyst were loaded into a reactor and the temperature was increased to 50 °C. After the suspension was brought to 50 °C, 50 mL of a glucose solution (0.4 mol/L) were added, and 10 mL of distilled water were used to rinse the remaining glucose into the reactor. During the

reaction, the flow rate of O_2 was 400 sccm and the stirring rate was kept at 600 rpm. NaOH from the burette was added to keep the solution at a constant pH of about 9, and the conversion of glucose to gluconic acid was determined by the amount of NaOH used. Since it is well documented that the selectivity to gluconic acid exceeds 95% for Au-based catalysts [7], the activity of the catalysts was determined by the addition of an aqueous solution of NaOH. This was a simple method that has been reported by several groups [9, 21, 27, 28]. After the reaction, the catalyst particles were filtered from the reaction mixture, washed three times with deionized water, and then air dried for a recycling test. The activity of the Pt catalysts was compared with that of a commercially available Pt catalyst. The stability of the Pt, Au, and Au-Pt catalysts was evaluated by recycling tests.

3. RESULTS AND DISCUSSION

3.1. CATALYSTS CHARACTERIZATION

Figure 1 shows the TEM images of Au NPs, ALD Pt/Al_2O_3 NPs, and Au-Pt/Al_2O_3 NPs, along with their size distributions. The Au NPs on the specimen grid were nearly monodispersed and spherically shaped with an average diameter of 2.2 nm. Figures 1b and 1c show that the Pt NPs and Au-Pt NPs were widely dispersed on the surface of Al_2O_3 NPs. The average sizes of the Pt NPs and Au-Pt NPs were 1.3 nm and 3.0 nm, respectively. Compared with Au and Pt NPs, the Au-Pt bimetallic NPs sizes were larger, but their size distribution still remained narrow. We believe that the average size of the Pt NPs deposited on γ-Al_2O_3 particles, with different cycles of Pt ALD, should be around

1.3 nm or smaller. The elemental composition in Au-Pt/Al_2O_3 NPs was analyzed via STEM/EDS (Figures S1 and S2) and the results were listed in Table S1, which showed that the atomic mass ratio of Au to Pt was around 40:60 for most of the NPs on the Al_2O_3 surface. This indicated that almost all particles on the support were Au-Pt bimetallic particles, rather than Au or Pt monometallic NPs. The ICP−AES results showed that the Au and Pt loadings on Al_2O_3 NPs were 2.9 wt.% and 6.4 wt.%, respectively. The low mass ratio of Au to Pt for a few NPs (Table S1) could be explained by the relatively low

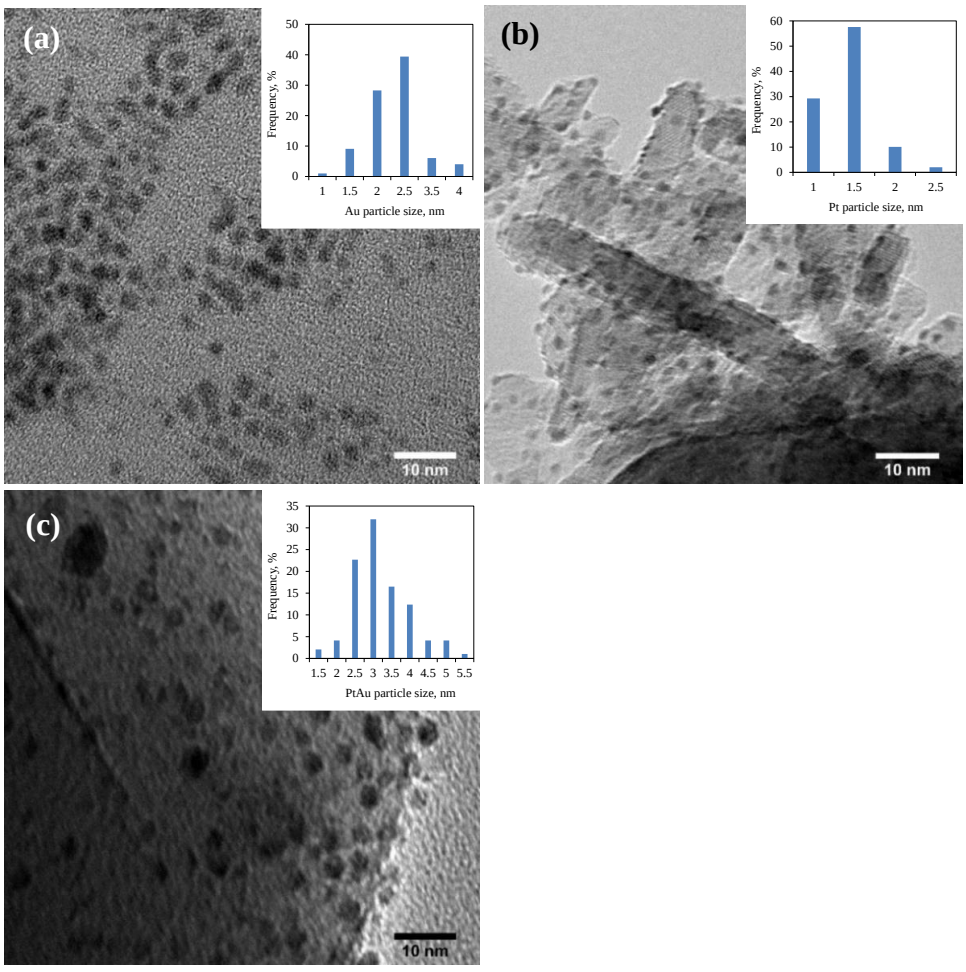

Figure 1. TEM images of (a) Au NPs, (b) 6.4 wt.% ALD Pt/Al_2O_3 NPs, and (c) 2.9 wt.% Au-6.4 wt.% Pt/Al_2O_3 NPs. The *inset* figures show the size distribution of Au, Pt, and Au-Pt NPs.

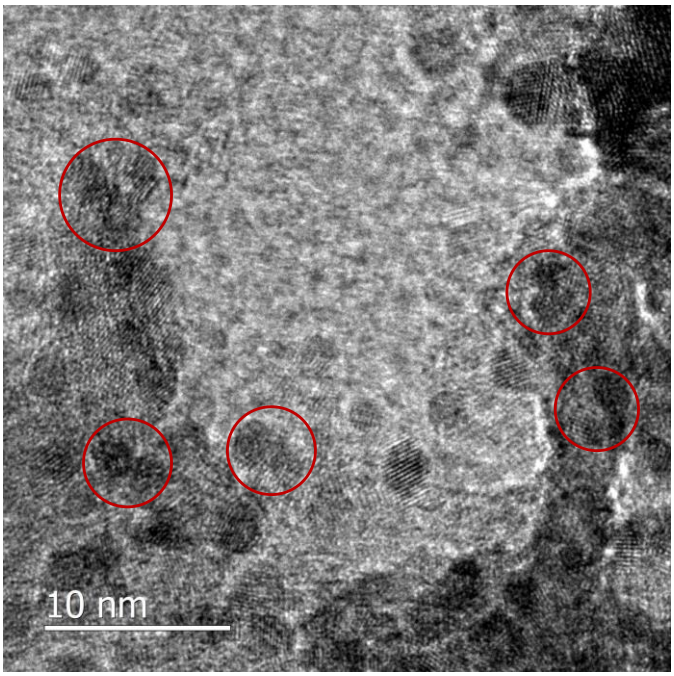

Figure 2. HRTEM image of 2.9 wt.% Au-6.4 wt.% Pt/Al_2O_3 NPs.

Au loading in the Au-Pt/Al_2O_3 particles based on ICP-AES results. The TEM and STEM/EDS analysis indicated that the Au-Pt bimetallic NPs were highly dispersed on Al_2O_3 NPs, and most metal NPs were Au-Pt bimetallic particles for Au-Pt/Al_2O_3 catalysts. As shown in Figure 2, some metal NPs stuck together (red circle). Since Pt NPs were highly dispersed on Al_2O_3 and did not aggregate (Figure 1b), these particles should be Au-Pt bimetallic NPs or Au-Au NPs. The TEM images showed that the metal NPs were crystalline and faceted, but our HRTEM images did not provide sufficient resolution to quantify the lattice fringes in the crystal structure expected for the Au-Pt bimetallic NPs.

To further verify the formation of Pt-Au bimetallic NPs, differential PDFs (d-PDFs) and XAS analysis were performed. As shown in Figure 3, the d-PDF results showed a series of sharp peaks, reflecting the presence of well-defined atomic coordination spheres in the NPs studied here. The Pt-O bond existed in 1.3 wt.% ALD

Pt/γ-Al_2O_3, indicating that the Pt NPs were partially oxidized on the surface [29]. While the d-PDF for 1.0 wt.% Au-1.3 wt.% Pt/γ-Al_2O_3 particles also showed the Pt-O bond, besides the oscillations for the Au NPs. This suggested that the Pt NPs were still around after the Au was deposited on the porous γ-Al_2O_3 support. The longer interatomic distance that was aligned with the Au characteristic peaks suggested the formation of Au NPs [30]. Thus, Pt and Au formed NPs separately, while the Pt NPs were partially oxidized. Though PDF analysis confirmed the formation of Au and Pt NPs, it could not provide direct information on interaction between Au NPs and Pt NPs. Thus, XAS analysis was performed.

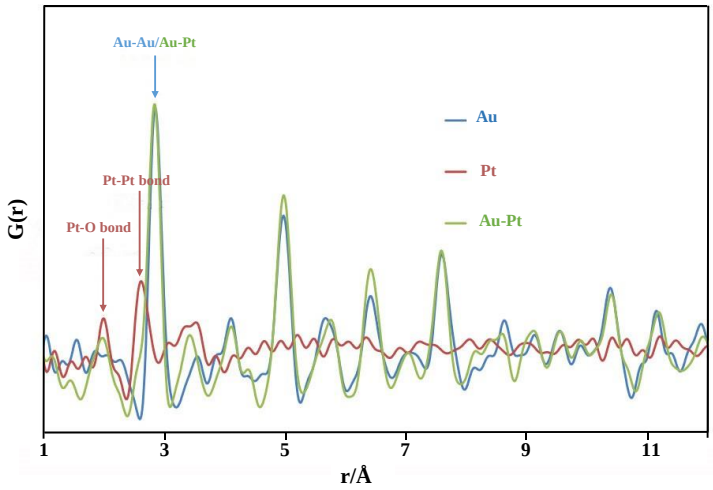

Figure 3. Pair distribution functions of 1.0 wt.% Au/γ-Al_2O_3, 1.3 wt.% ALD Pt/γ- Al_2O_3, and 1.0 wt.% Au-1.3 wt.% Pt/γ-Al_2O_3 particles.

The oxidation states of Au and Pt NPs on Al_2O_3 NPs were determined using X-ray absorption near edge structure spectroscopy (XANES) spectra recorded in an ambient condition. As the Au L_{III} edge XANES spectra showed in Figure 4a, the Au NPs

remained mostly metallic for both Au/Al_2O_3 and $Au\text{-}Pt/Al_2O_3$ samples. In Figure 4b, at the Pt L_{III} edge, Pt/Al_2O_3 and $Au\text{-}Pt/Al_2O_3$ samples exhibited stronger peaks, as compared with the Pt foil, which indicated that the ALD Pt and Au-Pt NPs were partly oxidized upon air exposure because of the small Pt NPs. This was consistent with the PDF results. A similar observation of ALD Pt NPs oxidation was also reported by Lei et al. [31]. Figure 4b also proves that, when the Au NPs were immobilized onto the Pt/Al_2O_3 NPs, there was almost no reaction between Pt and Au^{3+}, since the Pt L_{III} edge of the XANES spectra between the Pt/Al_2O_3 and $Au\text{-}Pt/Al_2O_3$ samples was similar. Figure 5 shows the Fourier transform of Au L_{III} edge extended X-ray absorption fine structure spectroscopy (EXAFS) spectra. Obviously, the new feature in the EXAFS spectrum of the $Au\text{-}Pt/Al_2O_3$ sample at 1.8 Å should be attributed to the interaction between Au and Pt. This indicated

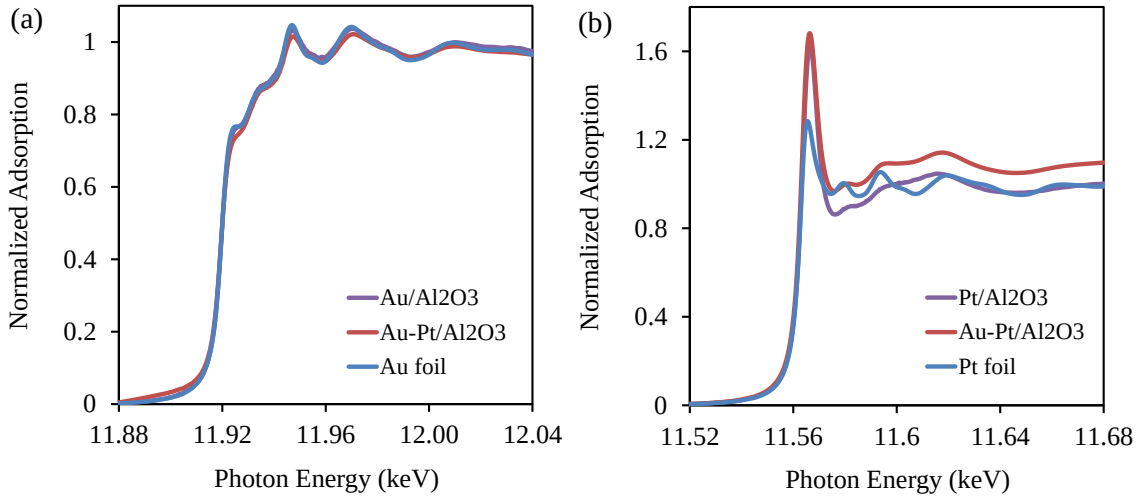

Figure 4. (a) Au L_{III} –edge XANES spectra (11.88-12.04 keV) of 2.9 wt.% Au/Al_2O_3 NPs, 2.9 wt.% Au-6.4 wt.% Pt/Al_2O_3 NPs, and Au foil; (b) Pt L_{III}-edge XANES spectra (11.52-11.68 keV) of 6.4% wt.% ALD Pt/Al_2O_3 NPs, 2.9 wt.% Au-6.4 wt.% Pt/Al_2O_3 NPs, and Pt foil.

that the Au NPs was deposited on Pt NPs, and they stuck together during Au NPs preparation, when the Au-Pt bimetallic NPs formed. As shown in Figure S3, the data taken at Pt L_{III} edge for the Au-Pt/Al_2O_3 sample had fewer data points than the other two, which made the EXAFS (R space) analysis at Pt L_{III} edge for the Au-Pt/Al_2O_3 sample almost impossible. This could have been due to the fact that Au L_{III} edge started to show up after that in the Au-Pt/Al_2O_3 sample, where Pt and Au coexisted.

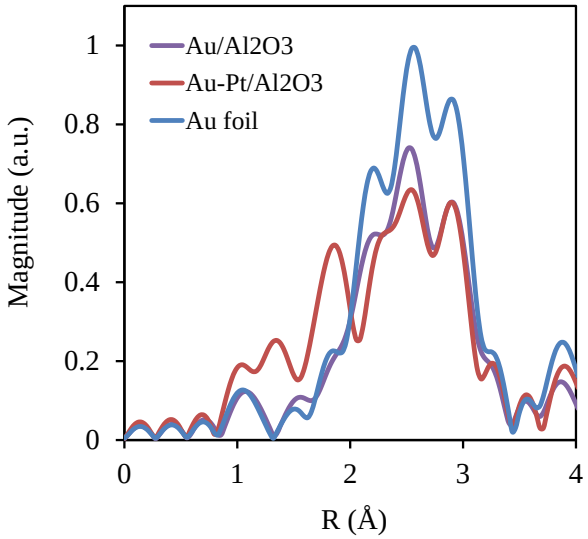

Figure 5. Fourier transform of Au L_{III} edge EXAFS spectra of 2.9 wt.% Au/Al_2O_3 NPs, 2.9 wt.% Au-6.4 wt.% Pt/Al_2O_3 NPs, and Au foil.

3.2. CATALYTIC PERFORMANCE

The catalytic oxidation of glucose to gluconic acid in a liquid phase was studied as a model reaction for the activity and stability of the Pt, Au, and Au-Pt catalysts. The catalytic performance of the glucose oxidation over a 1.3 wt.% ALD Pt/γ-Al_2O_3 and 1.0 wt.% Au/γ-Al_2O_3 catalyst is presented in Figure 6. A total of four cycles of catalytic reactions were applied to the ALD Pt catalyst, but no noticeable difference in catalytic

activity of glucose oxidation was observed during those four cycles. This indicated that there was almost no Pt leaching during the cycling tests due to the strong metal-support interaction of the ALD-prepared Pt catalysts. This evidence supports the premise that chemical bonding between Pt and γ-Al_2O_3 was stable during the vigorously stirred liquid phase reactions. In comparison with a commercial Pt catalyst, the activity of the ALD Pt/γ-Al_2O_3 was much higher with an identical Pt loading (Figure S4). This could have been due to the uniform Pt size and high dispersion of NPs on the support prepared by ALD, which significantly improved the activity of catalysts, as we expected. Au/γ-Al_2O_3 was not stable in the cycling tests, as shown in Figure 6b. The result agrees well with a previous report [7]. The catalytic activity loss of Au/γ-Al_2O_3 was mainly due to the leaching of Au NPs during the reaction. The ICP-AES results showed that the Au content on the Au/γ-Al_2O_3 catalyst decreased about 20% after three cycles of reactions and verified the authenticity of the hypothesis (Figure 7). Though the activity of Au/γ-Al_2O_3 in the second cycle could be competitive with that of the first cycle, the activity decreased greatly during the third cycle, and the conversion only reached 50% after 240 min of reaction. It is noted that the reaction rate obviously decreased after some reaction time, indicating deactivation of the Au catalyst with increasing reaction time. The deactivation could have been caused by the leaching of Au NPs and the adsorption of reaction products on the active Au surface during the reaction. Similarly, the reported Pt catalysts, prepared by a conventional method, were also deactivated by self-poisoning and over-oxidation [32]. Instead, the reaction rate of the ALD Pt/γ-Al_2O_3 particles decreased slightly, along with the reaction time, and the catalyst showed good resistance to any poisoning problem.

Figure 8a shows the activities of the 1.0 wt.% Au/γ-Al_2O_3 catalyst and Au-Pt/γ-Al_2O_3 catalysts with 1.0 wt.% Au and various Pt contents. With an increase in Pt content, the Au-Pt bimetallic catalyst showed higher activity and the conversion reached 100% in a very short time. This indicated that Pt was a promoter for the Au-based catalyst in the reaction of glucose oxidation. The improved activity was generally attributed to the

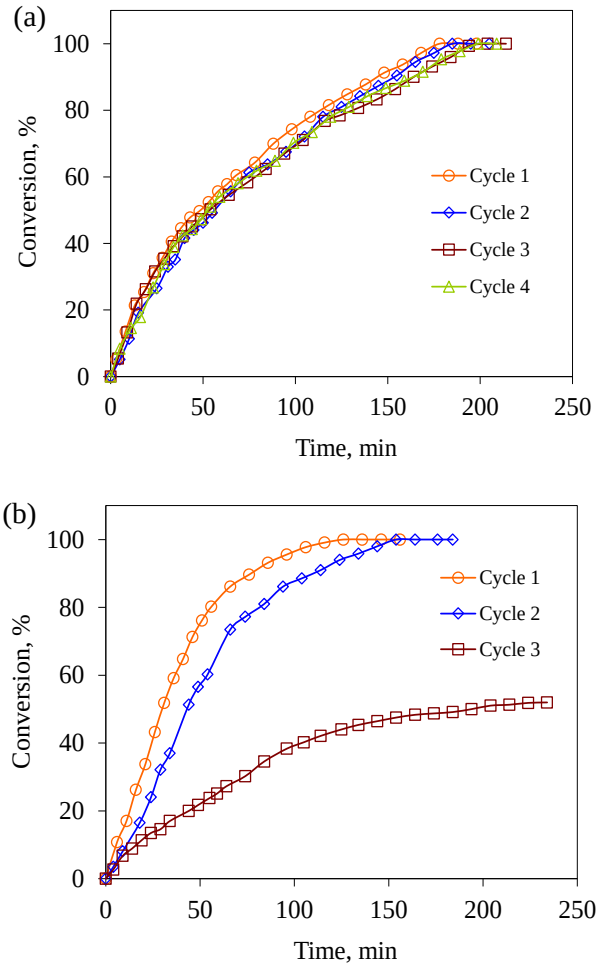

Figure 6. The conversion of glucose in the cycling test for (a) 0.7 g 1.3 wt.% ALD Pt/γ-Al_2O_3 and (b) 0.5 g 1.0 wt.% Au/γ-Al_2O_3 catalysts. Reaction conditions: 50 g water, 50 g 0.4 mol/L glucose, oxygen gas flow rate of 400 mL/min, stirring rate of 600 rpm, 0.5 mol/L NaOH, and pH=9.

synergistic effect that existed between Au and Pt, mainly from an electronic effect and increased Pt content. Since Au has the highest electronegativity (2.54) among transition metals [25], the transfer of electrons from Pt to Au assisted in the activation of oxygen and promoted the oxidation process. According to Tsukuda et al. [33, 34], negatively charged gold clusters were catalytically active sites for alcohol oxidation. In addition, Pt monometallic NPs could catalyze the glucose oxidation, which also partially improved the activity of catalysts. In contrast to the Au catalyst, the reaction rate was almost constant for the 1.0 wt.% Au -0.6 wt.% ALD Pt and 1.0 wt.% Au -1.3 wt.% ALD Pt catalysts. This indicated that the presence of Pt enhanced the resistance of Au-based catalysts to product poisoning, which could be attributed to the higher dispersion of Au-Pt NPs as a result of highly dispersed Pt NPs, strong bonding to the catalyst substrate, and the synergistic effect of Au-Pt bimetallic NPs. In comparison with Au monometallic NPs,

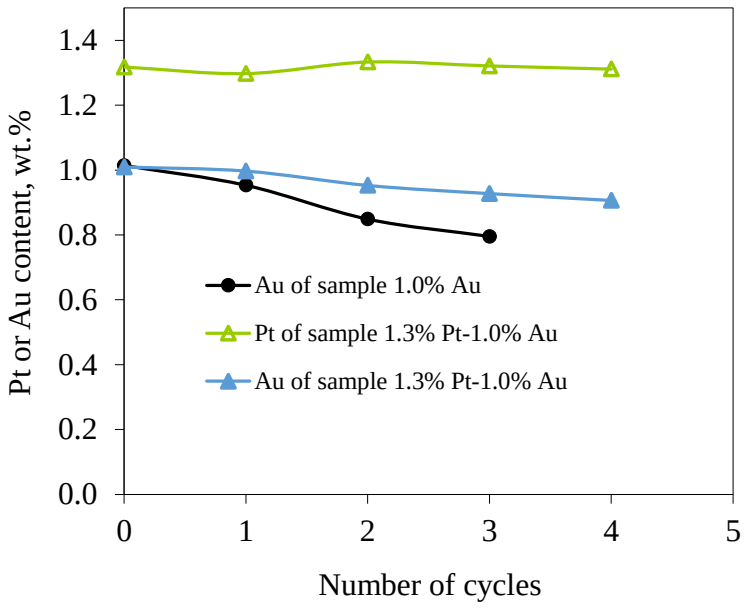

Figure 7. Pt or Au content on catalysts versus the number of reaction cycles.

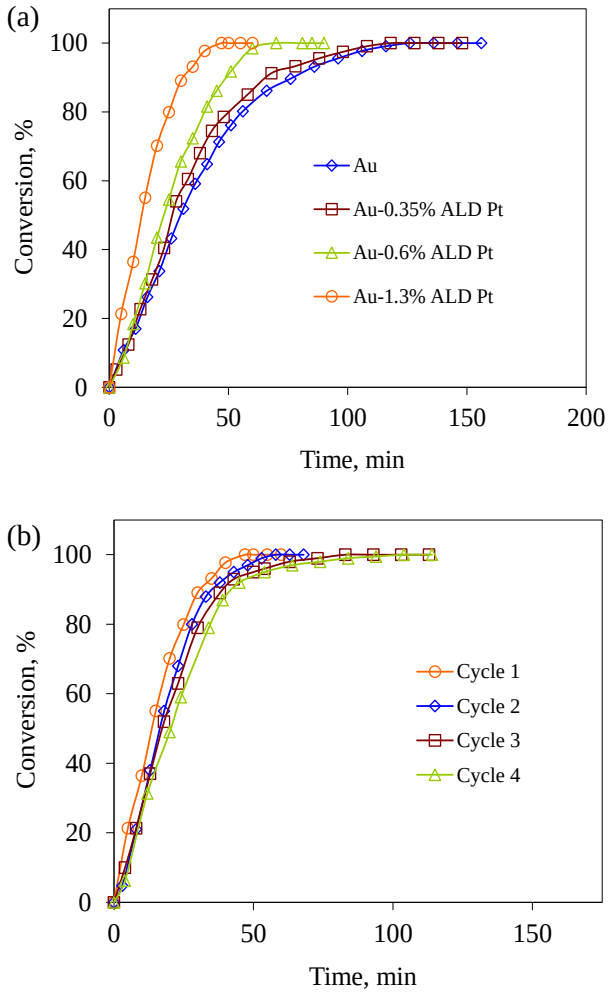

Figure 8. (a) The conversion of glucose versus the reaction time for 1.0 wt.% Au/γ-Al_2O_3 and Au-Pt/γ-Al_2O_3 bimetallic catalysts with 1.0 wt.% Au and various Pt contents (0.35, 0.6 and 1.3 wt.%), and (b) the conversion of glucose in the cycling test for 1.0 wt.% Au-1.3 wt.% Pt/γ-Al_2O_3 bimetallic catalyst. Reaction conditions: 0.5 g catalyst, 50 g water, 50 g 0.4 mol/L glucose, oxygen gas flow rate of 400 mL/min, stirring rate of 600 rpm, 0.5 mol/L NaOH, and pH=9.

the highly dispersed Pt NPs deposited by ALD can help disperse Au NPs on the catalyst support through strong interaction of Pt and Au NPs. The synergistic effect that involves electronic and geometric effects would tune the bimetallic structure and surface composition [25] and, thereby, reduce adsorption of the reaction product during the

reaction. These factors worked collectively and resulted in improved resistance to product poisoning and greater stability.

Results of the successive experiments of glucose oxidation catalyzed by 1.0 wt.% Au-1.3 wt.% Pt bimetallic catalyst are shown in Figure 8b. The activity of this catalyst decreased slightly after four cycles of the reaction and, compared to the Au/γ-Al_2O_3 catalyst, it was much more stable and recyclable. Similar to the Au-Pt/ Al_2O_3 NPs catalyst, almost all NPs supported on the porous γ-Al_2O_3 should be Au-Pt bimetallic NPs. Thus, these catalytic results proved that the interaction between the Au-Pt and γ-Al_2O_3 support was stronger than that between Au and γ-Al_2O_3 support due to the anchoring effect of Pt on γ-Al_2O_3 support and the strong interaction between Au and Pt [25]. The ICP-AES results showed that the Pt mass fraction of the Au-Pt bimetallic catalyst hardly decreased, while the Au content decreased only slightly after four cycles of reactions (Figure 7). The slight decrease in activity could be attributed to the leaching of Au monometallic NPs deposited on γ-Al_2O_3 particles since, normally, not all Au NPs would be stabilized on Pt NPs during the preparation of a catalyst. Other studies of Au-Pt bimetallic NPs [6] and AuPtAg trimetallic catalysts [35], prepared by the NaOH/$NaBH_4$ reduction method, showed a decrease of more than 30% in activity after only three cycles of the reaction of glucose oxidation. In general, the interaction between metal NPs and the substrates of the catalysts synthesized by liquid phase impregnation methods was weak and, thus, leaching could easily occur during a reaction, though the synergetic effect enhanced catalytic activity. In this work, Pt NPs were first highly dispersed on substrates by ALD with strong interaction. The ALD Pt/γ-Al_2O_3 served as a support, and the Au NPs were stabilized on the Pt NPs due to the strong interaction between Au and Pt

NPs. The stable chemical bond between Pt and the support, and the strong interaction between Au and Pt reduced metal leaching and improved the stability of the catalysts.

4. CONCLUSION

Highly dispersed Pt-Au bimetallic NPs were deposited on porous γ-Al_2O_3 particles by a two-step approach. Pt NPs were first deposited on γ-Al_2O_3 particles by ALD, and Au NPs were stabilized on ALD Pt/γ-Al_2O_3 particles from a hydrosol of gold clusters. Both TEM observation and XAS analysis verified the formation of Au-Pt bimetallic NPs with a narrow distribution centered at around 3.0 nm. ALD Pt/γ-Al_2O_3, Au/γ-Al_2O_3, and Au-Pt/γ-Al_2O_3 catalysts were used to study glucose oxidation to gluconic acid under identical reaction conditions. ALD Pt/γ-Al_2O_3 catalysts showed high activity and stability, as compared to a commercial Pt catalyst. Au-Pt bimetallic catalysts showed much higher activity and stability than the Au catalyst. The Au-Pt bimetallic catalysts were synthesized in this work by using the two-step method to overcome the leaching problem and to maintain high activity and stability. The strategy of combining ALD and a conventional method to fabricate a bimetallic catalyst with long-term stability provides an alternative way for preparing other highly dispersed, stable, and recyclable bimetallic catalysts.

ACKNOWLEDGEMENTS

This work was supported in part by the ACS Petroleum Research Fund. The authors thank Jessica TerBush at the Materials Research Center at Missouri University of Science and Technology for TEM analysis. Use of the Advanced Photon Source and Center for Nanoscale Materials, Office of Science User Facilities operated for the U.S. Department of Energy (DOE) Office of Science by Argonne National Laboratory, was supported by the U.S. DOE under Contract No. DE-AC02-06CH11357.

REFERENCES

1. C.J. Serpell, J. Cookson, D. Ozkaya, P.D. Beer (2011) Nature Chem. 3:478-483.

2. A. Habrioux, W. Vogel, M. Guinel, L. Guetaz, K. Servat, B. Kokoh, N. Alonso-Vante (2009) Phys. Chem. Chem. Phys. 11:3573-3579.

3. M. Tang, S. Mao, M. Li, Z. Wei, F. Xu, H. Li, Y. Wang (2015) ACS Catal. 5:3100-3107.

4. S. Nishimura, N. Ikeda, K. Ebitani (2014) Catal. Today 232:89-98.

5. W. Zhang, L. Li, Y. Du, X. Wang, P. Yang (2009) Catal. Lett. 127:429-436.

6. H. Zhang, N. Toshima (2013) J. Colloid Interface Sci. 394:166-176.

7. S. Biella, L. Prati, M. Rossi (2002) J. Catal. 206:242-247.

8. C. Della Pina, E. Falletta, L. Prati, M. Rossi (2008) Chem. Soc. Rev 37:2077-2095.

9. C. Baatz, N. Decker, U. Prüße (2008) J. Catal. 258:165-169.

10. H. Miyamura, R. Matsubara, S. Kobayashi (2008) Chem. Commun. 2031-2033.

11. A. Villa, S. Campisi, K.M. Mohammed, N. Dimitratos, F. Vindigni, M. Manzoli, W. Jones, M. Bowker, G.J. Hutchings, L. Prati (2015) Catal. Sci. Technol. 5:1126-1132.

12. T. Suntola (1992) Thin Solid Films 216:84-89.

13. M. Leskelä, M. Ritala (2003) Angew. Chem. Int. Ed. 42:5548-5554.

14. J.S. King, A. Wittstock, J. Biener, S.O. Kucheyev, Y.M. Wang, T.F. Baumann, S.K. Giri, A.V. Hamza, M. Baeumer, S.F. Bent (2008) Nano Lett. 8:2405-2409.

15. H. Feng, J.W. Elam, J.A. Libera, W. Setthapun, P.C. Stair (2010) Chem. Mater. 22:3133-3142.

16. J. Li, X. Liang, D.M. King, Y.-B. Jiang, A.W. Weimer (2010) Appl. Catal., B 97:220-226.

17. J. Lu, B. Fu, M.C. Kung, G. Xiao, J.W. Elam, H.H. Kung, P.C. Stair (2012) Science 335:1205-1208.

18. C. Jiang, Z. Shang, X. Liang (2015) ACS Catal. 5:4814-4818.

19. S.T. Christensen, H. Feng, J.L. Libera, N. Guo, J.T. Miller, P.C. Stair, J.W. Elam (2010) Nano Lett. 10:3047-3051.

20. C. Jiang, X. Liang (2014) Catal. Commun. 46:41-45.

21. X. Liang, L.B. Lyon, Y.-B. Jiang, A.W. Weimer (2012) J. Nanopart. Res. 14:article No. 943.

22. X. Liang, C. Jiang (2013) J. Nanopart. Res. 15:article No. 1890.

23. D.G. Duff, A. Baiker, P.P. Edwards (1993) Langmuir 9:2301-2309.

24. D.G. Duff, A. Baiker, P.P. Edwards (1993) J. Chem. Soc., Chem. Commun. 96-98.

25. A. Wang, X.Y. Liu, C.-Y. Mou, T. Zhang (2013) J. Catal. 308:258-271.

26. X. Liang, Y. Zhou, J. Li, A.W. Weimer (2011) J. Nanopart. Res. 13:3781-3788.

27. X. Liang, C.-j. Liu, P. Kuai (2008) Green Chem. 10:1318-1322.

28. C. Baatz, U. Prüße (2007) J. Catal. 249:34-40.

29. J.R. Gallagher, T. Li, H. Zhao, J. Liu, Y. Lei, X. Zhang, Y. Ren, J.W. Elam, R.J. Meyer, R.E. Winans (2014) Catal. Sci. Technol. 4:3053-3063.

30. V. Petkov, S. Shastri, B. Wanjala, R. Loukrakpam, J. Luo, C.-J. Zhong (2012) Z. Kristallogr. Cryst. Mater. 227:262-267.

31. Y. Lei, B. Liu, J. Lu, R.J. Lobo-Lapidus, T. Wu, H. Feng, X. Xia, A.U. Mane, J.A. Libera, J.P. Greeley (2012) Chem. Mater. 24:3525-3533.

32. M. Comotti, C. Della Pina, R. Matarrese, M. Rossi, A. Siani (2005) Appl. Catal., A 291:204-209.

33. H. Tsunoyama, H. Sakurai, Y. Negishi, T. Tsukuda (2005) J. Am. Chem. Soc. 127:9374-9375.

34. H. Tsunoyama, N. Ichikuni, H. Sakurai, T. Tsukuda (2009) J. Am. Chem. Soc. 131:7086-7093.

35. N. Toshima, H. Zhang (2012) Macromol. Symp. 317-318:149-159.

ELECTRONIC SUPPLEMENTARY INFORMATION

This file includes:

Experimental details

Catalysts preparation.

Characterization details

1. *Electron microscopy analysis.*
2. *Pair distribution functions (PDF) analysis.*
3. *X-ray absorption spectroscopy (XAS) analysis*

Figures. S1–S4.

Table S1

*Corresponding authors: Xinhua Liang

Experimental details

Catalysts preparation.

Platinum (Pt) nanoparticles (NPs) were deposited by ALD using (methylcyclopentadienyl)trimethyl platinum [(MeCp)$PtMe_3$] as the Pt precursor and oxygen (O_2) as the other reactant at 300 °C in a fluidized bed reactor, as previously described [1]. In a typical run, 5 g of substrates were loaded into a reactor. Before a reaction, the substrates were degassed at 300 °C for 5 hr. During the ALD process, the solid (MeCp)$PtMe_3$ was heated and carried by nitrogen (N_2) into the reactor. (MeCp)$PtMe_3$ and O_2 were fed separately through the reactor's distributor plate. The particle substrates were fully fluidized with the gas flow rate controlled by mass flow controllers. The reactor was also subjected to vibration from vibrators to improve the quality of particle fluidization during the ALD coating process [2]. N_2 was used as flush gas to remove unreacted precursors and any byproducts during the reaction. A typical coating cycle involved the following steps: (MeCp)$PtMe_3$ dose, N_2 purge, evacuation; O_2 dose, N_2 purge, evacuation. The Pt loading was controlled by a dose of Pt precursor and the number of ALD cycles.

The conventional sodium hydroxide (NaOH) reduction method [3, 4] was used to synthesize gold (Au) NPs. Typically, 0.12 g gold(III) chloride solution ($HAuCl_4$, ~30 wt.%) was added to 100 mL of deionized water, at room temperature, while being stirred at 400 rpm. After 3 min, 3 mL of tetrakis(hydroxymethyl)-phosphonium chloride (THPC, 80 wt.%) and 4 mL of 0.2 mol/L NaOH solution were added to the gold solution separately, and the pH was adjusted to 4 using a 0.2 mol/L NaOH or 0.1 mol/L H_2SO_4 solution. After 1 hr, 2.0 g porous γ-alumina (γ-Al_2O_3) or ALD Pt/γ-Al_2O_3 particles were

added to the solution, with stirring for 4 hr. Finally, the solution was centrifuged and dried in an oven at 120 ºC for 2 hr to obtain Au/γ-Al_2O_3 or Au-Pt/γ-Al_2O_3 particles.

Characterization details

1. *Electron microscopy analysis.*

Transmission electron microscopy (TEM) and scanning transmission electron microscopy (STEM)/energy dispersive X-ray spectroscopy (EDS) were carried out with a FEI Tecnai F20 electron microscope that was equipped with a field emission gun operating at an accelerating voltage of 200 kV. The point resolution was 0.24 nm. Samples were directly supported on holey-carbon Cu grids. At least 200 particles were randomly measured to determine the average diameter of Au, Pt, and Au-Pt NPs. The atomic mass ratio of Au to Pt on the Al_2O_3 NPs was determined using EDS.

2. *Pair distribution functions (PDF) analysis.*

PDF analysis of Au, Pt, and Au-Pt supported on porous γ-Al_2O_3 particles was carried out based on X-ray scattering data measured at the 11-ID-B beamline of the Advanced Photon Source at Argonne National Laboratory. High energy X-rays (λ = 0.2128 Å) were used in combination with a large amorphous-silicon based area detector to collect data on high values of momentum transfer (Q ~ 22 $Å^{-1}$) [5]. Diffraction images were integrated within fit2D to obtain one-dimensional diffraction data. Pair distribution functions, G(r), were extracted from the data within PDFgetX2, after correcting for background and Compton scattering [6]. Differential PDFs (d-PDFs), that isolated contributions from the supported Au, Pt, and Au-Pt species, were obtained by direct subtraction of a reference PDF that contained essentially only Al_2O_3 correlations [7].

3. *X-ray absorption spectroscopy (XAS) analysis.*

XAS, including extended X-ray absorption fine structure spectroscopy (EXAFS) and X-ray absorption near edge structure spectroscopy (XANES), was conducted at bending magnet beamline 9-BM at the Advanced Photon Source (APS), Argonne National Laboratory. The XAS spectra were recorded in transmission mode with the ionization chamber optimized for maximum current with a linear response [8]. Spectra at both the Au L_{III} edge (11.918 keV) and Pt L_{III} edge (11.564 keV) were acquired for the Au, Pt, and Au-Pt samples. Au and Pt foils were used to calibrate the monochromator. Standard procedures based on Athena software were used to fit the XAS data.

References

1. Z. Shang, R.L. Patel, B.W. Evanko, X. Liang (2013) Chem. Commun. 49:10067-10069.

2. R.L. Patel, Y.-B. Jiang, X. Liang (2015) Ceram. Int. 41:2240-2246.

3. D.G. Duff, A. Baiker, P.P. Edwards (1993) Langmuir 9:2301-2309.

4. D.G. Duff, A. Baiker, P.P. Edwards (1993) J. Chem. Soc., Chem. Commun. 96-98.

5. P.J. Chupas, X. Qiu, J.C. Hanson, P.L. Lee, C.P. Grey, S.J. Billinge (2003) J. Appl. Crystallogr. 36:1342-1347.

6. X. Qiu, J.W. Thompson, S.J. Billinge (2004) J. Appl. Crystallogr. 37:678-678.

7. K.W. Chapman, P.J. Chupas, C.J. Kepert (2005) J. Am. Chem. Soc. 127:15630-15636.

8. Y. Lei, B. Liu, J. Lu, R.J. Lobo-Lapidus, T. Wu, H. Feng, X. Xia, A.U. Mane, J.A. Libera, J.P. Greeley (2012) Chem. Mater. 24:3525-3533.

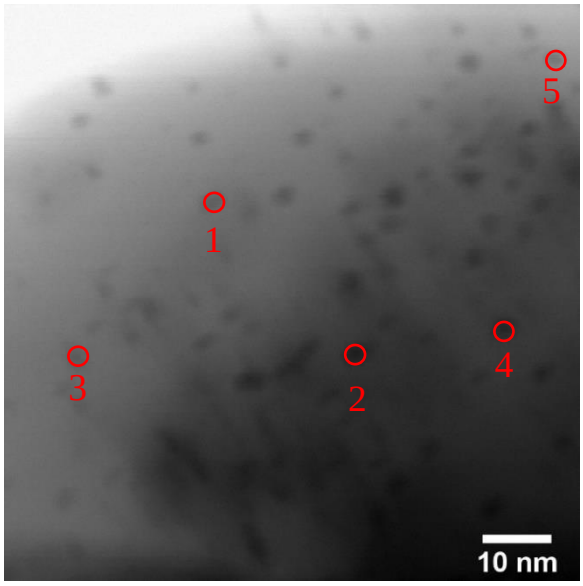

Figure S1. STEM image of 2.9 wt.% Au-6.4 wt.% Pt/Al_2O_3 NPs. The labeled 5 points were analyzed by EDS. The results are listed in Table S1.

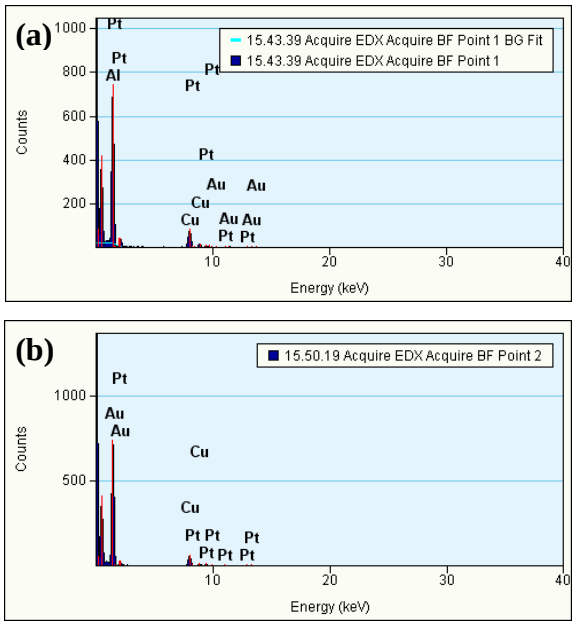

Figure S2. EDS spectra of 5 points in Figure S1: (a) point 1, (b) point 2, (c) point 3, (d) point 4, and (e) point 5.

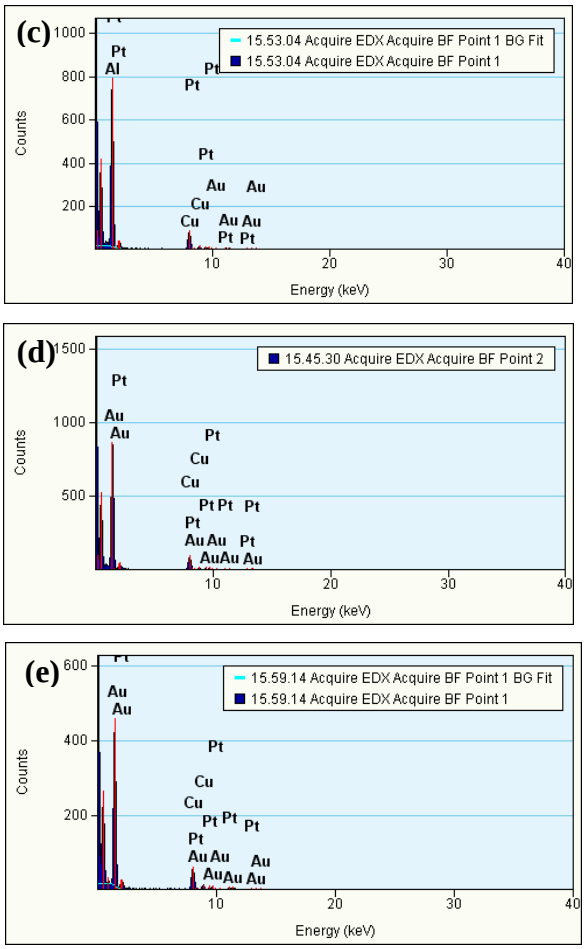

Figure S2. EDS spectra of 5 points in Figure S1: (a) point 1, (b) point 2, (c) point 3, (d) point 4, and (e) point 5. (Cont.)

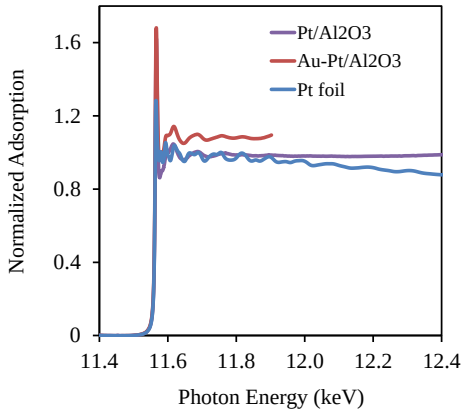

Figure S3. Pt L_{III} edge XANES spectra of 6.4% wt.% ALD Pt/Al_2O_3 NPs, 2.9 wt.% Au-6.4 wt.% Pt/Al_2O_3 NPs, and Pt foil.

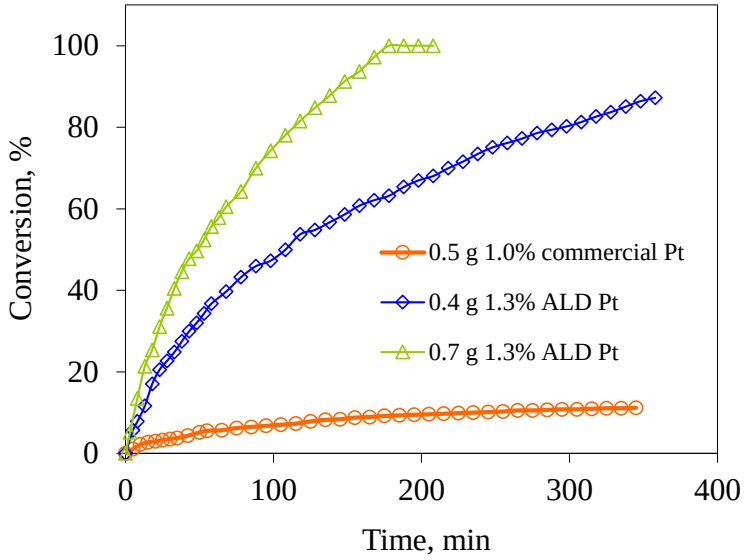

Figure S4. The conversion of glucose versus the reaction time for different Pt catalysts. Reaction conditions: 50 g water, 50 g 0.4 mol/L glucose, oxygen gas flow rate of 400 mL/min, stirring rate of 600 rpm, 0.5 mol/L NaOH, and pH=9

Table S1. Pt and Au weight percentage and molar percentage of the 5 points in Figure S1.

	Element Wt.%		Element Atom %	
	Pt	Au	Pt	Au
Point 1	59.1	40.9	59.3	40.7
Point 2	61.7	38.3	61.9	38.1
Point 3	62.2	37.8	62.4	37.6
Point 4	61.6	38.4	61.8	38.2
Point 5	74.9	25.1	75.1	24.9

V. SIGNIFICANT PHOTOCATALYTIC PERFORMANCE ENHANCEMENT OF TIO_2 BY CEO_2 ATOMIC LAYER DEPOSITION

Xiaofeng Wang, Ye Jin, and Xinhua Liang*

Department of Chemical and Biochemical Engineering, Missouri University of Science and Technology, Rolla, Missouri 65409, United States

*Email: liangxin@mst.edu

This paper has been published in *Nanotechnology*, 28(50), article No. 505709, 2017.

ABSTRACT

Different cycles (10-80) of CeO_2 were coated on TiO_2 nanoparticles by atomic layer deposition (ALD) using tris(ipropylcyclopentadienyl)cerium and de-ionized water as precursors at 250 ºC in a fluidized bed reactor. XRD analysis showed that TiO_2 kept anatase structure after CeO_2 ALD. With an increase in the number of ALD coating cycles, both photoluminescence (PL) intensity and band gap of the samples continuously decreased. The photocatalytic activity was evaluated based on the degradation of methylene blue (MB) solution under UV light. The photocatalysis experiment demonstrated that 40 cycles of CeO_2 deposited TiO_2 sample (40Ce/TiO_2) showed the highest photocatalytic activity and had a more than three-fold activity enhancement over uncoated TiO_2 for the degradation of MB. The enhanced photocatalytic activity was attributed to the fact that CeO_2 played a role as e^-/h^+ pair trap centers and consequently reduced e^-/h^+ pair recombination rate.

Keywords: CeO_2, trap center, atomic layer deposition (ALD), TiO_2, photocatalysis

1. INTRODUCTION

Nowadays, organic pollutants have become one of the most important environmental concerns in fast growing society. As a potential and promising technology, photocatalytic degradation of organic pollutants on TiO_2 has been studied for decades due to the properties of remarkable incident photon-to-electron conversion efficiencies, chemical stability, and low cost [1-5]. TiO_2 is used as catalysts in many areas, including photocatalytic H_2 production [6-9] and degradation of textile [10-12]. However, the photocatalytic efficiency of TiO_2 is not high enough in practical applications [13] because the photo-generated electrons (e^-) and holes (h^+) recombine easily, which limits the efficiency greatly. Hence, it is necessary to reduce the e^-/h^+ recombination rate and thereby boost the photocatalytic efficiency.

It is well known that CeO_2, as one of transition-metal oxides, has been widely applied in various areas because of its unique property to allow storing/releasing oxygen and undergo reversible Ce^{3+}/Ce^{4+} redox cycle. One of important applications is to synthesize CeO_2-modified TiO_2 photocatalysts in order to accelerate the photocatalytic activity of TiO_2 catalysts [14]. It has been considered as an effective way for several reasons. Firstly, CeO_2 can play a role as e^-/h^+ pair trap centers since the energy level of Ce^{3+}/Ce^{4+} lies close to that of Ti^{3+}/Ti^{4+}, favoring the separation of photo-generated e^-/h^+ pair, and consequently reducing e^-/h^+ pair recombination rate [15]. Secondly, there are many oxygen vacancies and Ce^{3+} defects in CeO_2 [16], which can store/release oxygen for photo-degradation process. In fact, some papers reported various kinds of CeO_2/TiO_2 photocatalysts and they were more active than TiO_2. But almost all studies adopted sol-

gel [15, 17-20] or hydrothermal [21] methods to prepare CeO_2/TiO_2, and thereby the physical properties between pure TiO_2 and CeO_2/TiO_2 were remarkably different, including the crystal structure and phase composition. Since the photoactivity of TiO_2-based catalysts is not only related to the existence and property of CeO_2, but also due to the changes of TiO_2 crystal structure, it is difficult to figure out the role of CeO_2 for enhancement of photocatalytic efficiency clearly in these studies. In other words, in order to investigate the role of CeO_2 as trap centers, the crystal structure and phase composition of TiO_2 should be controlled the same as much as possible. Thus, it is necessary to adopt a new strategy for CeO_2/TiO_2 preparation to make clear the effect of CeO_2 and further promote the photoactivity of CeO_2/TiO_2.

In this work, we deposited different cycles (10-80) of CeO_2 on anatase TiO_2 nanoparticles (NPs) via atomic layer deposition (ALD) to investigate the effect of CeO_2 as trap centers in photocatalytic degradation of methylene blue (MB). ALD is a surface controlled layer-by-layer coating process based on self-limiting surface reactions, and it has been utilized to deposit uniform metal oxide films with nanometer-sized control of film thickness and well controlled film compositions [22]. The study was completed with a multitechnique examination of the CeO_2/TiO_2 samples using transmission electron microscopy/energy-dispersive X-ray spectroscopy (TEM/EDS), X-ray diffraction (XRD), Raman analysis, photoluminescence (PL), and diffuse reflectance UV-vis measurement.

2. EXPERIMENTAL SECTION

2.1. PREPARATION OF CEO_2/TIO_2

CeO_2 ALD was carried out using tris(ipropylcyclopentadienyl)cerium ($Ce(^iPrCp)_3$, 99.9%, Strem Chemicals) and de-ionized water (H_2O) as precursors in a fluidized bed reactor, as described in detail elsewhere [23, 24]. For a typical run, 8 g of anatase TiO_2 NPs (99.9%, US Research Nanomaterials, Inc.) were loaded into the reactor. The reaction temperature was 250 ºC. During the ALD process, the solid $Ce(^iPrCp)_3$ was loaded into a heated bubbler and carried by nitrogen (N_2, 99.99% Airgas) into the reactor. $Ce(^iPrCp)_3$ and H_2O were fed separately through the reactor's distributor plate. The particle substrates were fully fluidized with a gas flow rate controlled by mass flow controllers. The reactor was also subjected to vibration from vibrators to improve the quality of particle fluidization during the ALD coating process [25, 26]. N_2 was used as flush gas to remove unreacted precursors and any byproducts during the reaction. A typical coating cycle involved the following steps: $Ce(^iPrCp)_3$ dose, N_2 purge, evacuation; H_2O dose, N_2 purge, evacuation. 10 ($10Ce/TiO_2$), 20 ($20Ce/TiO_2$), 40 ($40Ce/TiO_2$), 60 ($60Ce/TiO_2$), and 80 ($80Ce/TiO_2$) cycles of CeO_2 ALD were applied on anatase TiO_2 NPs. After CeO_2 ALD, half amount of $80Ce/TiO_2$ sample was heated at 500 ºC for 4 hr in air and it was labeled as $80Ce/TiO_2$-500. 40 cycles of CeO_2 ALD was also deposited on ZrO_2 NPs (particle size of 10-15 nm) as a reference.

2.2. CHARACTERIZATIONS

A Quantachrome Autosorb-1 was used to obtain nitrogen adsorption and desorption isotherms of the uncoated and CeO_2-coated TiO_2 NPs at -196 ºC. The surface area of the particles was calculated using the BET method in a relative pressure range of 0.05 - 0.25. The crystal structure of TiO_2 was detected by XRD. The morphology of CeO_2 coated on TiO_2 was directly observed by FEI Tecnai F20 TEM/EDS. At least 200 particles were randomly measured to determine the average diameter of TiO_2 and CeO_2/TiO_2 samples. Raman spectra of TiO_2 and CeO_2/TiO_2 samples were collected using a Horiba-Jobin Yvon LabRam spectrometer. The PL spectra were recorded with a HORIBA FL3-22 spectrometer (HORIBA, Edison, NJ) to investigate the recombination of photo-generated e^-/h^+ pairs in the photocatalysts. UV–visible absorbance spectra and diffuse reflectance spectra (DRS) of CeO_2/TiO_2 samples were obtained with a UV–visible spectrophotometer (Varian Cary 5). $BaSO_4$ was used as an absorbance standard in the UV–visible reflectance experiments. The details of characterization are described in the SI.

2.3. PHOTOCATALYTIC ACTIVITY MEASUREMENT

MB solution was used to evaluate the photocatalytic activity of TiO_2 and CeO_2/TiO_2 samples. Typically, 0.1 g of catalyst was dispersed in a 100 mL, 10 ppm MB solution. Previous work indicated that all of the prepared samples in the solution could achieve the equilibrium of absorption-desorption in 60 minutes [27]. Thus, before irradiation, the suspension aqueous solution was first stirred in the dark for 60 min to ensure adsorption/desorption equilibrium. A100 W UV lamp was used for 360 nm UV

irradiation at a distance of 10 cm from the surface of the solution. This distance ensured that the UV light intensity would be ~10 mW/cm^2. At certain time intervals, 1.5 mL test samples were taken from the main solution and filtered through a Millipore filter to make it particle-free for analysis using an UV–vis spectrometer (Varian Cary 50-Bio) at a 664 nm wavelength [28]. The change in concentration of MB in the main solution was recorded over a period of irradiation time.

3. RESULTS AND DISCUSSION

3.1. PHOTOCATALYST CHARACTERIZATIONS

Figure 1 shows the typical morphology of uncoated TiO_2, 40Ce/TiO_2, and 80Ce/TiO_2 samples. Compared to the uncoated TiO_2 (Figure 1a), there is no obvious change observed for the 40Ce/TiO_2 sample (Figure 1b). With further increase in the number of ALD coating cycles, a uniform CeO_2 film was coated on TiO_2 NPs. For example, a thickness of around 1.3 nm was seen for the 80Ce/TiO_2 sample (Figure 1c), and the EDS spectrum verified the existence of Ce on TiO_2 (Figure S1). This growth rate is a bit lower than that of CeO_2 ALD on micro-sized lithium ion battery electrode particles in our previous studies [29]. The average particle sizes of uncoated TiO_2, 40Ce/TiO_2, and 80Ce/TiO_2 NPs were 20.4, 20.8 and 21.9 nm, respectively. The size of 80Ce/TiO_2 was slight larger than that of uncoated TiO_2 and 40Ce/TiO_2 samples, due to CeO_2 ALD films. Though there is no big difference in TEM images between uncoated TiO_2 and 40Ce/TiO_2 particles, the color of the samples changed significantly, and it changed from white to brown along with the increase of CeO_2 ALD cycles (Figure S2).

As it is well known, both CeO_2 and TiO_2 are white. However, the deposition of CeO_2 on TiO_2 could change the absorption edge of the samples in the UV-visible light region, so the color of the samples altered. This could be the unique phenomena between TiO_2 and CeO_2. In order to verify this, 40 cycles of CeO_2 ALD were also coated on ZrO_2 NPs, and the color of ZrO_2 NPs kept white and did not change (Figure S3). The surface area of the

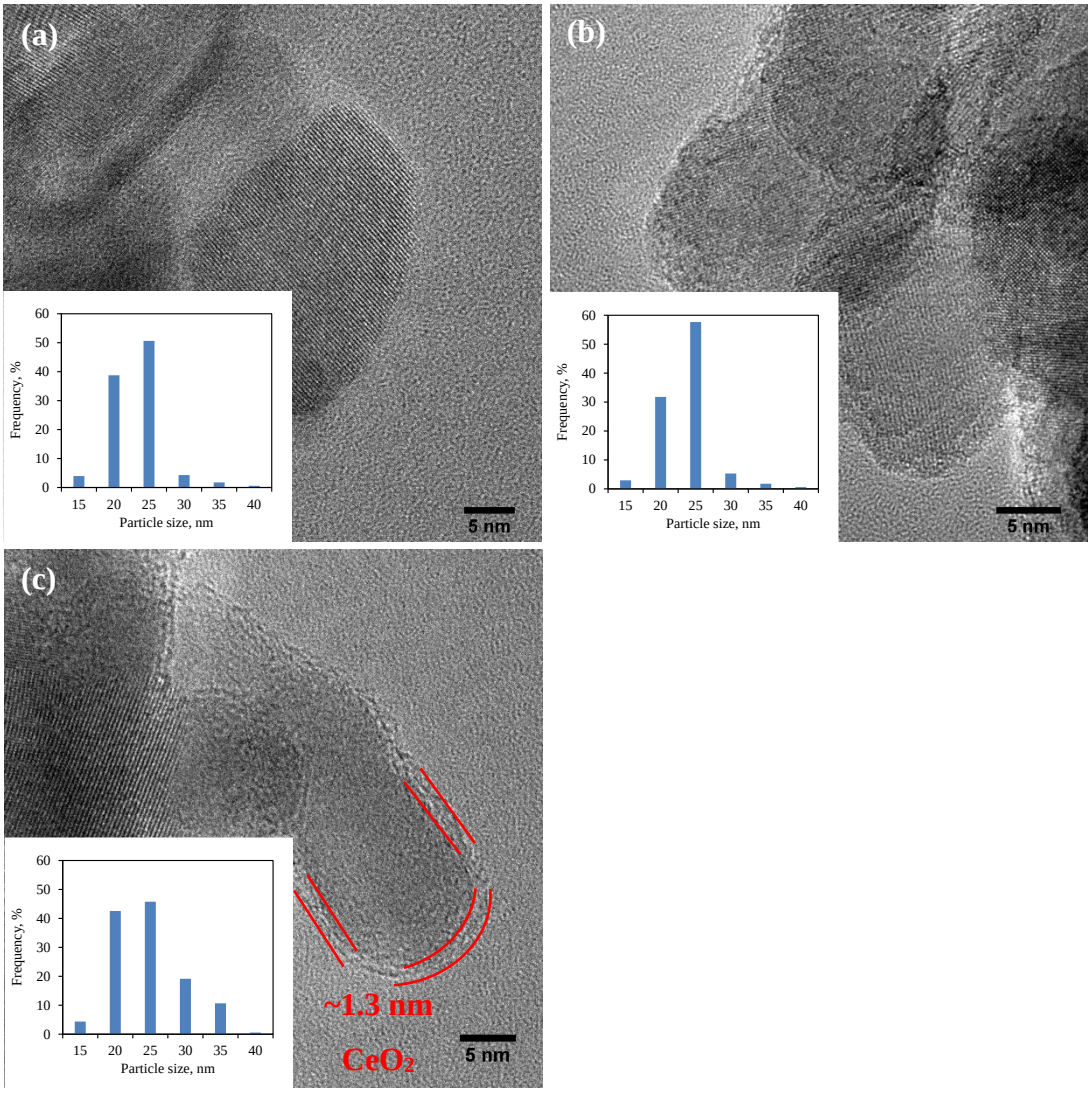

Figure 1. TEM images of (a) uncoated TiO_2, (b) 40Ce/TiO_2, and (c) 80Ce/TiO_2 samples. The *inset* figures show the size distributions of the samples.

CeO_2/TiO_2 sample almost kept the same after 80 cycles of CeO_2 ALD coating (Figure S4), since the film was so thin. It indicates that the CeO_2 films were coated on primary particle surface. There was no significant particle aggregation, and the structure of the TiO_2 NPs was not changed after the CeO_2 ALD process. Thus, the effect of the structure on the following photocatalytic activity tests was not considered when we studied the role of CeO_2 in the photocatalytic performance of the photocatalysts.

XRD was used to investigate the effect of CeO_2 deposition on the phase structure. Figure 2 displays the XRD patterns of CeO_2/TiO_2 samples with different number of CeO_2 ALD cycles. There is no significant difference for all photocatalysts. As shown, the peaks at 25.3º, 37.8º, 48.1º, 53.9º, 55.2º, 62.8º, and 75.2º correspond to the reflections from (101), (004), (200), (105), (211), (204), and (215) planes of TiO_2 in the anatase phase, respectively [30], and no rutile phase was detected for all samples. It indicates that the CeO_2 ALD did not modify the anatase phase of TiO_2 sample and the cell parameters of TiO_2 kept same for all samples (Table S1), as we expected. In addition, there is no peak correspond to the reflections from CeO_2, which could be due to the low loading and amorphous structure of CeO_2 on TiO_2. After heat treatment, 80Ce/TiO_2-500 sample remained anatase phase and there was still no peak from CeO_2 observed although the structure of CeO_2 had already transferred from amorphous to crystal, since 500 ºC was high enough based on previous reports [15, 17]. It indicates that the CeO_2 loading was very low even if 80 cycles of CeO_2 ALD were applied. According to the XRD analysis, the TiO_2 crystal size was around 19 nm for all samples, which is close to the actual particle size of TiO_2 (~20 nm).

Figure 3 shows the Raman spectra of the CeO_2/TiO_2 samples and the reference spectrum of uncoated anatase TiO_2 NPs. All samples showed three major Raman bands at 397, 517 and 640 cm^{-1}, which are ascribed to the Raman-active modes of TiO_2 anatase phase with the symmetries of B1g, A1g, and Eg, respectively [31]. Compared with the uncoated TiO_2 sample, all three bands of CeO_2/TiO_2 samples were weak due to the deposition of CeO_2. But there is no Raman band belonging to CeO_2 observed for all CeO_2/TiO_2 samples. Similar to the above XRD results, it should be attributed to the low amount and amorphous structure of CeO_2. It is also noted that the baseline of $10Ce/TiO_2$, $20Ce/TiO_2$ and $40Ce/TiO_2$ kept increasing from 300 to 1000 cm^{-1} and that of $60Ce/TiO_2$ and $80Ce/TiO_2$ increased slowly, which resulted from fluorescence effect after CeO_2 coating on TiO_2 NPs.

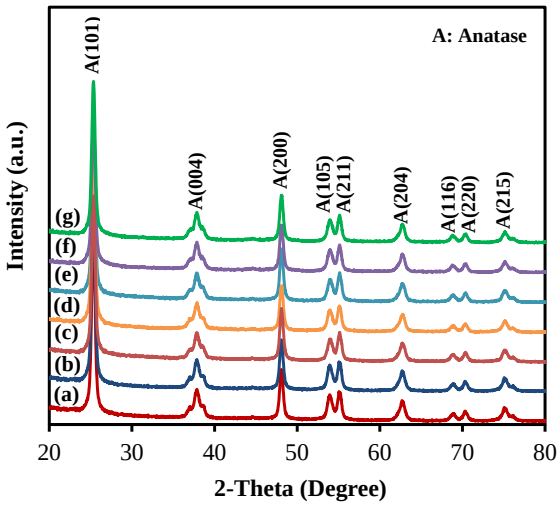

Figure 2. XRD patterns of (a) TiO_2, (b) $10Ce/TiO_2$, (c) $20Ce/TiO_2$, (d) $40Ce/TiO_2$, (e) $60Ce/TiO_2$, (f) $80Ce/TiO_2$, and (g) $80Ce/TiO_2$-500.

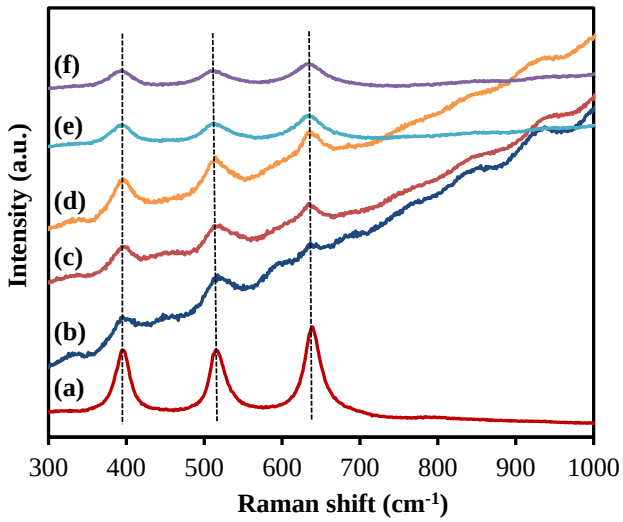

Figure 3. Raman spectra of (a) TiO_2, (b) 10Ce/TiO_2, (c) 20Ce/TiO_2, (d) 40Ce/TiO_2, (e) 60Ce/TiO_2, and (f) 80Ce/TiO_2.

In order to further investigate the fluorescence effect and evaluate separation rate of e^-/h^+ pairs, PL analysis was carried out. PL spectra of the all prepared TiO_2 and CeO_2/TiO_2 samples are shown in figure 4. The only one peak at 432 nm corresponds to the reflection from anatase phase of TiO_2, and no other peak was observed in the wavelength of 300-600 nm. So there is no signal from CeO_2, which is expected due to the low loading of CeO_2 in the samples. But with an increase in the number of CeO_2 ALD cycles, the PL intensity decreased greatly, which indicated that the separation efficiency of e^-/h^+ pairs enhanced for CeO_2/TiO_2 samples and it could result from the increase of the number of the oxygen vacancies and/or defects in the TiO_2 crystal [14]. In other words, more CeO_2 worked as trap centers to separate e^-/h^+ pairs and reduce the recombination rate. After heat treatment, the PL intensity of 80Ce/TiO_2-500 sample increased a lot in comparison to 80Ce/TiO_2. It implies that the concentration of the oxygen vacancies and/or defects decreased dramatically, and the heat treatment at 500 ºC modified the

crystal structure of CeO_2, removed oxygen vacancies and "healed" defects, which is consistent with previous studies [16, 32].

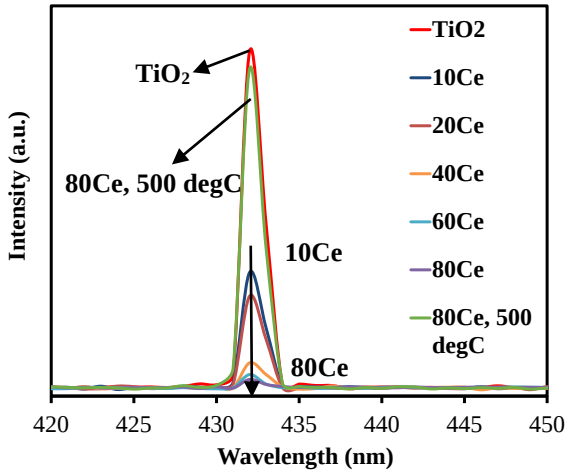

Figure 4. Photoluminescence spectra of TiO_2 and CeO_2/TiO_2 samples excited at 280 nm.

UV-visible DRS were recorded for uncoated TiO_2 and CeO_2/TiO_2 catalysts to demonstrate the lowering of the band gap energy after CeO_2 deposition. As presented in figure 5a, the uncoated TiO_2 sample showed strong photoabsorption only at wavelengths shorter than 400 nm, and the absorption edge increased with the increasing cycles of CeO_2 ALD. Figure 5b shows the subsequent Kubelka-Munk reflection plots derived from the UV-visible DRS (Figure S5). The band gap energy (E_g) values for uncoated TiO_2 and CeO_2/TiO_2 NPs ranged from 3.22 to 2.24 eV, which are similar to the reported values [17]. As it is well known, the band gap of bulk CeO_2 is around 3.2 eV, and the E_g values of CeO_2/TiO_2 samples are smaller than that of both TiO_2 and CeO_2. The narrowing in the band gap is associated with oxygen vacancies and formation of Ce^{3+} because oxygen vacancies and Ce^{3+} forms intermediate defect energy states in the band gap of CeO_2 [32] .

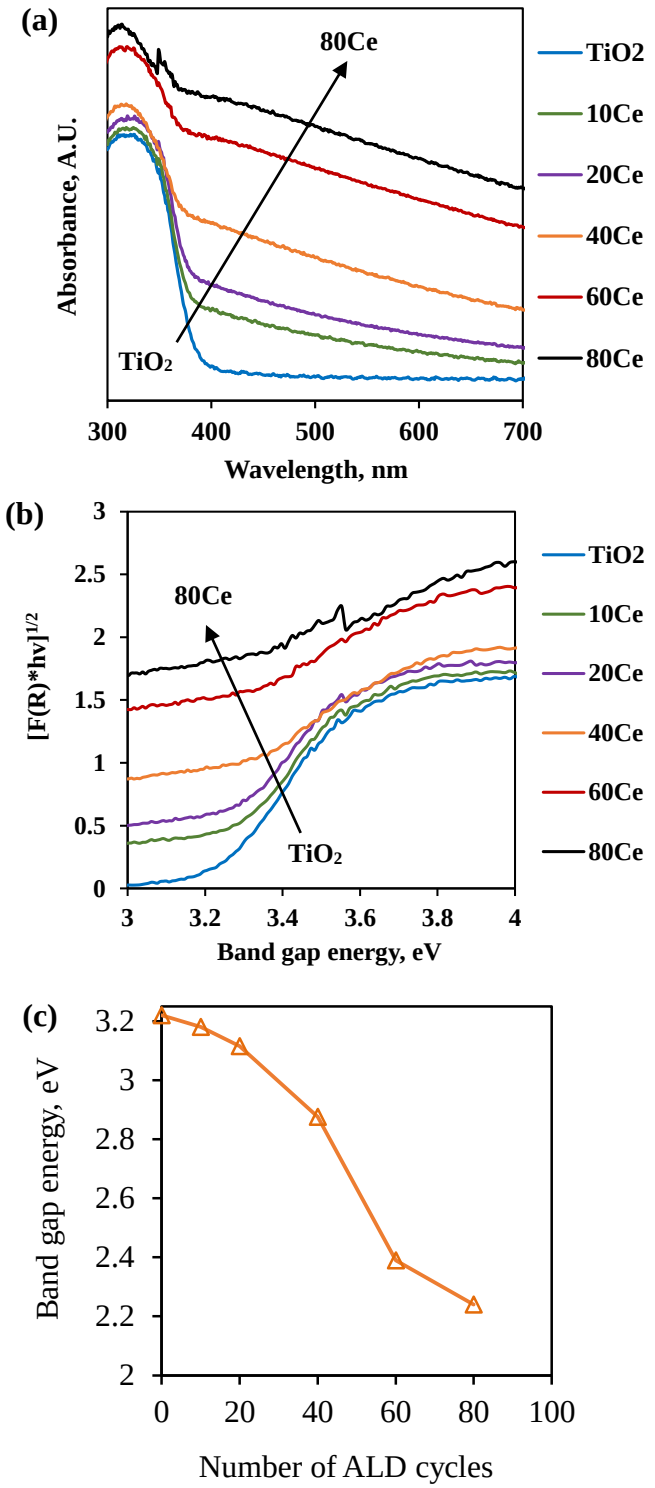

Figure 5. (a) UV-visible absorption spectra, (b) UV-visible spectroscopic measurements and subsequent Kubelka-Munk reflection plots, and (c) the band gap energy of TiO_2 and CeO_2/TiO_2 samples.

More cycles of CeO_2 ALD would provide more defects and thereby lead to lager reduction in the band gap, which is consistent with PL analysis. So increasing CeO_2 content in TiO_2 shifts the band gap energy toward longer wavelengths (Figures 5c and S6).

3.2. PHOTOCATALYTIC ACTIVITY

The photocatalytic activity of TiO_2 and CeO_2/TiO_2 catalysts were evaluated in terms of degradation of MB under irradiation of UV light. Figures 6a and S7 summarize

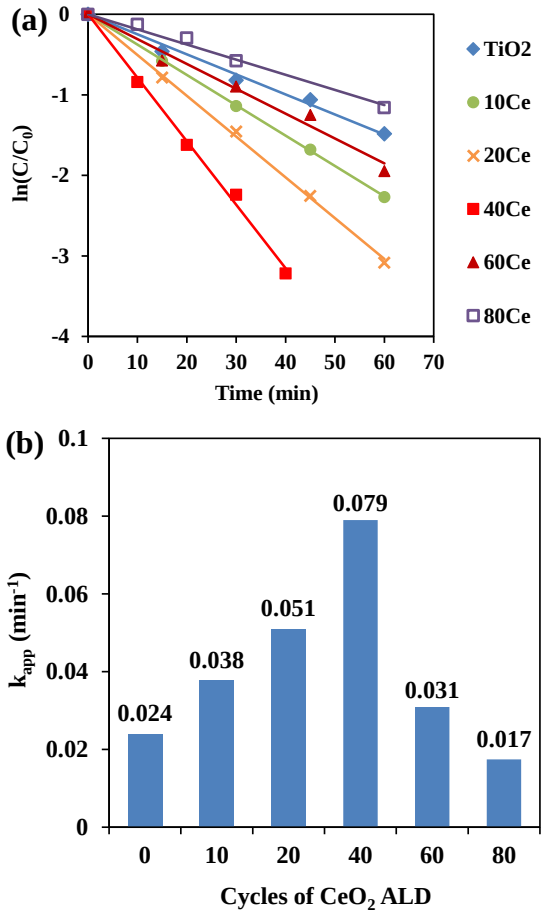

Figure 6. (a) Relative concentration of MB and (b) apparent kinetic constants (k_{app}, min^{-1}) as a function of CeO_2/TiO_2 catalysts with different number of CeO_2 ALD cycles.

the effect of CeO_2 ALD cycles on degradation efficiencies of MB solution. The results showed that the photodegradation efficiency of all CeO_2/TiO_2 samples was higher than that of the uncoated TiO_2 except for the $80Ce/TiO_2$ sample. With an increase in the number of ALD cycles, the photoactivity of samples kept increasing before 40 cycles of ALD, then it decreased with the further increase of the number of ALD cycles. Thus, 40 cycles was the optimal number of CeO_2 ALD cycles for the photocatalytic activity of TiO_2 in this study.

In order to compare the photocatalytic activity of the catalysts more intuitively, the Langmuir-Hinshelwood (L-H) kinetic equation was chosen. The photocatalytic degradation of MB follows roughly the pseudo-first-order reaction kinetics [33], as shown in Equation 1:

$$-\ln\left(\frac{C_t}{C_0}\right) = kKt = k_{app}t \quad (1)$$

where C_0 and C_t are the concentration of MB initially and at a given reaction time (min), respectively, k is the reaction rate constant, and K is adsorption constants associated with the substrate. k_{app} is the apparent first order rate constant (min^{-1}) and it is the slope of the plot.

As shown in figure 6b, with CeO_2 ALD deposition, all CeO_2/TiO_2 samples showed a higher photocatalytic efficiency than TiO_2 except for the $80Ce/TiO_2$ sample. The apparent kinetic constant of $40Ce/TiO_2$ sample reached a maximum value of 0.079 min^{-1}, and its activity exceeded that of uncoated TiO_2 (k_{app} = 0.024 min^{-1}) by a factor of more than three times. In comparison with other methods, CeO_2 ALD is one promising strategy to enhance the photocatalytic performance of CeO_2/TiO_2. For example, Li et al. [16] reported that the optimal CeO_2 loading (1.5 wt.%) increased the photocatalytic

activity of TiO_2 by 60% only. In addition, Pt ALD has been reported to be applied for improvement of TiO_2 photoactivity, and it showed three times increase of photocatalytic activity as compared to the pure TiO_2 at most [34]. Though Pt ALD and CeO_2 ALD showed similar enhancement for TiO_2 activity, CeO_2 is low-cost and much more economic for large-scale production compared to Pt. Thus, CeO_2 ALD is a prospective and effective way to enhance the photoactivity of TiO_2.

The much higher photoactivity of 40Ce/TiO_2 than that of TiO_2 in this work can be due to the following several factors. Firstly, CeO_2 improved the intensity of absorption in the UV-visible light region and made a red shift in the band gap transition of 40Ce/TiO_2 sample, as mentioned above (figure 5). This can induce more photo-generated e^- and h^+ to participate in the photocatalytic reactions. Moreover, CeO_2 can trap e^-/h^+ pairs at the interface as trap centers to suppress the recombination of e^-/h^+ pairs and enhance lifetimes of e^- and h^+, which can improve the photocatalytic activity of CeO_2/TiO_2 samples as well [15], according to the following reactions (figure 7):

$$TiO_2 + h\nu \rightarrow h^+ + e^- \quad \text{(charge pair generation)} \tag{2}$$

$$Ce^{4+} + e^- \rightarrow Ce^{3+} \quad \text{(electron trap)} \tag{3}$$

$$Ce^{3+} + h^+ \rightarrow Ce^{4+} \quad \text{(hole trap)} \tag{4}$$

Though more oxygen vacancies and defects can play a role as trap centers, capture e^-/h^+ pair, and inhibit their recombination effectively, the 60Ce/TiO_2 and 80Ce/TiO_2 samples did not show higher photoactivity than the 40Ce/TiO_2 sample. The reason could be that with more cycles of ALD coating, a conformal layer of CeO_2 film formed on the surface of TiO_2 NPs and it hindered the samples to utilize UV light and could not generate enough e^- and h^+ for MB degradation. In order to verify this, 80Ce/TiO_2 NPs were heated

at 500 ºC for 4 hr to form crystal CeO_2. Because the average size of CeO_2 single crystals is from 4 to 60 nm [35] and the CeO_2 film was only around 1.3 nm for the 80Ce/TiO_2 sample (Figure 1c) in this study, the CeO_2 would sinter and the film could crack during heat treatment. Therefore, 80Ce/TiO_2-500 sample can utilize more UV light than 80Ce/TiO_2 and such heat treatment could enhance its photoactivity although the amount of oxygen vacancies and defects decreased after heat treatment, as proved by PL analysis. As shown in figure S8, the 80Ce/TiO_2-500 catalyst was more active than the 80Ce/TiO_2 catalyst, which verified our hypothesis. Thus, the control of CeO_2 ALD cycles plays a key role affecting the photocatalytic activity of CeO_2/TiO_2 samples.

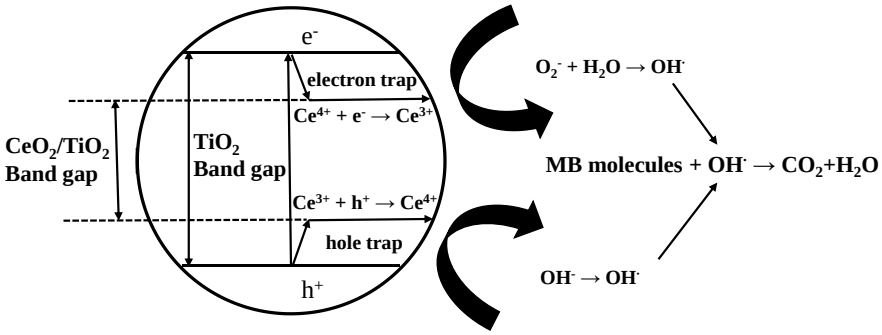

Figure 7. Proposed mechanism for the photoexcited electron–hole separation and transport processes at the CeO_2/TiO_2 interface under UV irradiation.

Moreover, the uniform dispersion of CeO_2 on TiO_2 surface by ALD is another important factor influencing the photocatalytic efficiency. CeO_2 ALD took full advantage of the high surface area of TiO_2 NPs and supplied more active sites for the degradation reaction of MB. The large surface area could effectively promote the separation efficiency of the e^-/h^+ pairs, resulting in a higher quantum efficiency of photocatalytic

reaction. All these factors mentioned above worked collectively and resulted in significantly improved photocatalytic activity of the 40Ce/TiO_2 catalyst.

4. CONCLUSION

Different cycles of CeO_2 were deposited on TiO_2 nanoparticles via ALD successfully. TEM images showed the thickness of CeO_2 ultrathin film was around 1.3 nm after 80 cycles of CeO_2 ALD. No continuous layer of CeO_2 films were seen after 40 cycles of CeO_2 ALD. Based on XRD analysis, the anatase structure of TiO_2 did not change after CeO_2 ALD. With an increase in the number of ALD coating cycles, the amount of trap center increased, which was verified by PL analysis and diffuse reflectance UV-vis measurement. The 40Ce/TiO_2 catalyst showed the highest photocatalytic activity and had a more than three-fold photocatalytic activity enhancement over pure TiO_2 for the degradation of MB due to the fact that CeO_2 played a role as e^-/h^+ pair trap centers and consequently reduced the recombination rate of e^-/h^+ pairs. The uniform dispersion of CeO_2 and high surface area of 40Ce/TiO_2 sample were another two factors to enhance the photocatalytic activity. The results proved that CeO_2 ALD is an effective and promising strategy to improve the photocatalytic activity of TiO_2 significantly.

ACKNOWLEDGEMENT

Acknowledgment is made to the donors of the American Chemical Society Petroleum Research Fund for partial support of this research. The authors thank Dr. Jingjing Qing at the Materials Research Center at Missouri University of Science and Technology for TEM analysis. The authors also thank Naveen K. Mahenderkar and Prof. Jay A. Switzer in the Department of Chemistry for the assistance with diffuse reflectance UV-vis measurement, and Jincheng Bai, Han Zhang, and Prof. Richard Brow in the Department of Materials Science and Engineering at Missouri University of Science and Technology for the assistance with Raman and photoluminescence analysis.

REFERENCES

1. Wang Y, Cheng H, Hao Y, Ma J, Li W, Cai S. Preparation, characterization and photoelectrochemical behaviors of Fe(III)-doped TiO_2 nanoparticles. Journal of Materials Science. 1999; 34 (15): 3721-9.

2. Linsebigler AL, Lu G, Yates Jr JT. Photocatalysis on TiO_2 surfaces: principles, mechanisms, and selected results. Chemical Reviews. 1995; 95 (3): 735-58.

3. Hoffmann MR, Martin ST, Choi W, Bahnemann DW. Environmental applications of semiconductor photocatalysis. Chemical Reviews. 1995; 95 (1): 69-96.

4. Shahmoradi B, Negahdary M, Maleki A. Hydrothermal synthesis of surface-modified, manganese-doped TiO_2 nanoparticles for photodegradation of methylene blue. Environmental Engineering Science. 2012; 29 (11): 1032-7.

5. Salehi K, Shahmoradi B, Bahmani A, Pirsaheb M, Shivaraju H. Optimization of reactive black 5 degradation using hydrothermally synthesized NiO/TiO_2 nanocomposite under natural sunlight irradiation. Desalination and Water Treatment. 2016; 57 (52): 25256-66.

6. Wong TJ, Lim FJ, Gao M, Lee GH, Ho GW. Photocatalytic H_2 production of composite one-dimensional TiO_2 nanostructures of different morphological structures and crystal phases with graphene. Catalysis Science & Technology. 2013; 3 (4): 1086-93.

7. Wang J, Ng YH, Lim Y-F, Ho GW. Vegetable-extracted carbon dots and their nanocomposites for enhanced photocatalytic H_2 production. RSC Advances. 2014; 4 (83): 44117-23.

8. Zhu L, Fu Tan C, Gao M, Ho GW. Design of a metal oxide-organic framework (MoOF) foam microreactor: solar-induced direct pollutant degradation and hydrogen generation. Advanced Materials. 2015; 27 (47): 7713-9.

9. Ye M, Gong J, Lai Y, Lin C, Lin Z. High-efficiency photoelectrocatalytic hydrogen generation enabled by palladium quantum dots-sensitized TiO_2 nanotube arrays. Journal of the American Chemical Society. 2012; 134 (38): 15720-3.

10. Sajan C, Shahmoradi B, Shivaraju H, Rai KL, Ananda S, Shayan M, et al. Photocatalytic degradation of textile effluent using hydrothermally synthesised titania supported molybdenum oxide photocatalyst. Materials Research Innovations. 2010; 14 (1): 89-94.

11. Shahmoradi B, Maleki A, Byrappa K. Photocatalytic degradation of Amaranth and Brilliant Blue FCF dyes using in situ modified tungsten doped TiO_2 hybrid nanoparticles. Catalysis Science & Technology. 2011; 1 (7): 1216-23.

12. Pirsaheb M, Shahmoradi B, Khosravi T, Karimi K, Zandsalimi Y. Solar degradation of malachite green using nickel-doped TiO_2 nanocatalysts. Desalination and Water Treatment. 2016; 57 (21): 9881-8.

13. Zhang X, Fujishima A, Jin M, Emeline AV, Murakami T. Double-layered TiO_2−SiO_2 nanostructured films with self-cleaning and antireflective properties. The Journal of Physical Chemistry B. 2006; 110 (50): 25142-8.

14. Li G, Zhang D, Jimmy CY. Thermally stable ordered mesoporous CeO_2/TiO_2 visible-light photocatalysts. Physical Chemistry Chemical Physics. 2009; 11 (19): 3775-82.

15. Yang H, Zhang K, Shi R, Tang A. Sol–gel synthesis and photocatalytic activity of CeO_2/TiO_2 nanocomposites. Journal of the American Ceramic Society. 2007; 90 (5): 1370-4.

16. Li Z, Sheng J, Zhang Y, Li X, Xu Y. Role of CeO_2 as oxygen promoter in the accelerated photocatalytic degradation of phenol over rutile TiO_2. Applied Catalysis B: Environmental. 2015; 166: 313-9.

17. Muñoz-Batista MJ, Gómez-Cerezo MN, Kubacka A, Tudela D, Fernández-García M. Role of interface contact in CeO_2–TiO_2 photocatalytic composite materials. ACS Catalysis. 2013; 4 (1): 63-72.

18. Tiejun C, Yuchao L, Zhenshan P, Yunfei L, Zongyuan W, Qian D. Photocatalytic performance of TiO_2 catalysts modified by $H_3PW_{12}O_{40}$, ZrO_2 and CeO_2. Journal of Environmental Sciences. 2009; 21 (7): 997-1004.

19. Jiang B, Zhang S, Guo X, Jin B, Tian Y. Preparation and photocatalytic activity of CeO_2/TiO_2 interface composite film. Applied Surface Science. 2009; 255 (11): 5975-8.

20. Xu A-W, Gao Y, Liu H-Q. The preparation, characterization, and their photocatalytic activities of rare-earth-doped TiO_2 nanoparticles. Journal of Catalysis. 2002; 207 (2): 151-7.

21. Tian J, Sang Y, Zhao Z, Zhou W, Wang D, Kang X, et al. Enhanced photocatalytic performances of CeO_2/TiO_2 nanobelt heterostructures. Small. 2013; 9 (22): 3864-72.

22. Puurunen RL. Surface chemistry of atomic layer deposition: a case study for the trimethylaluminum/water process. Journal of Applied Physics. 2005; 97 (12): Article No. 121301.

23. Patel RL, Palaparty SA, Liang X. Ultrathin conductive CeO_2 coating for significant improvement in electrochemical performance of $LiMn_{1.5}Ni_{0.5}O_4$ cathode materials. Journal of The Electrochemical Society. 2017; 164 (1): A6236-A43.

24. Liang X, Lynn AD, King DM, Bryant SJ, Weimer AW. Biocompatible interface films deposited within porous polymers by atomic layer deposition (ALD). ACS Applied Materials and Interfaces. 2009; 1 (9): 1988-95.

25. Patel RL, Jiang Y-B, Liang X. Highly porous titania films coated on sub-micron particles with tunable thickness by molecular layer deposition in a fluidized bed reactor. Ceramics International. 2015; 41 (2): 2240-6.

26. Wang X, Zhao H, Wu T, Liu Y, Liang X. Synthesis of highly dispersed and highly stable supported Au–Pt bimetallic catalysts by a two-step method. Catalysis Letters. 2016; 146 (12): 2606-13.

27. Liang X, King DM, Li P, Weimer AW. Low-temperature atomic layer-deposited TiO_2 films with low photoactivity. Journal of the American Ceramic Society. 2009; 92 (3): 649-54.

28. Wang X, Bayan M, Yu M, Ludlow D, Liang X. Atomic layer deposition surface functionalized biochar for adsorption of organic pollutants: improved hydrophilia and adsorption capacity. International Journal of Environmental Science and Technology. 2017; 14 (9): 1825-34.

29. Patel RL, Park J, Liang X. Ionic and electronic conductivities of atomic layer deposition thin film coated lithium ion battery cathode particles. RSC Advances. 2016; 6 (101): 98768-76.

30. Wang X, Donovan AR, Patel RL, Shi H, Liang X. Adsorption of metal and metalloid ions onto nanoporous microparticles functionalized by atomic layer deposition. Journal of Environmental Chemical Engineering. 2016; 4 (4): 3767-74.

31. Cao T, Li Y, Wang C, Wei L, Shao C, Liu Y. Fabrication, structure, and enhanced photocatalytic properties of hierarchical CeO_2 nanostructures/TiO_2 nanofibers heterostructures. Materials Research Bulletin. 2010; 45 (10): 1406-12.

32. Choudhury B, Chetri P, Choudhury A. Oxygen defects and formation of Ce^{3+} affecting the photocatalytic performance of CeO_2 nanoparticles. RSC Advances. 2014; 4 (9): 4663-71.

33. Naeem K, Ouyang F. Preparation of Fe^{3+}-doped TiO_2 nanoparticles and its photocatalytic activity under UV light. Physica B: Condensed Matter. 2010; 405 (1): 221-6.

34. Zhou Y, King DM, Liang X, Li J, Weimer AW. Optimal preparation of Pt/TiO_2 photocatalysts using atomic layer deposition. Applied Catalysis B: Environmental. 2010; 101 (1): 54-60.

35. Zhou X-D, Huebner W. Size-induced lattice relaxation in CeO_2 nanoparticles. Applied Physics Letters. 2001; 79 (21): 3512-4.

SUPPLEMENTARY INFORMATION

This file includes:

Characterization details

1. X-ray diffraction (XRD) analysis

2. Raman analysis

3. Band gap calculation

Figures. S1-S8.

Table S1.

*Corresponding authors:

E-mail: liangxin@mst.edu (Xinhua Liang)

Characterization details

1. *XRD analysis.*

The crystal structure of TiO_2 and CeO_2/TiO_2 samples was analyzed by X-ray diffraction (XRD) with filtered Cu Kα radiation (λ= 1.5406 Å). The scanning range was 2θ from 20º to 80º, with a scanning rate of 0.025 º/s. The Scherrer equation was applied to estimate the average crystallite sizes of TiO_2 and CeO_2/TiO_2 samples: $D = \frac{K\lambda}{B\cos\theta}$, where B is the half-height width of the diffraction peak of anatase, K=0.89 is a coefficient, θ is the diffraction angle, λ is the X-ray wavelength corresponding to the Cu Kα irradiation (1.5406 Å) and D is the average crystallite size of the powder sample. Cell parameters of TiO_2 were also obtained from the XRD data for the samples.

2. *Raman analysis.*

Raman spectra of TiO_2 and CeO_2/TiO_2 samples were recorded using a Horiba-Jobin Yvon LabRam spectrometer, equipped with a 17mW He-Ne laser. Spectra were collected using a 10× objective len over a wavenumber range of 200-1200 cm^{-1}. The reported spectra were generated from 10-20 scans of the respective wavenumber range, each taking ten seconds.

3. Band gap calculation.

The UV–visible diffuse reflectance spectra (DRS) were used to evaluate the band gap of TiO_2 and CeO_2/TiO_2 samples by plotting $[F(R)*hv]^{1/2}$ against *hv*, where *hv* is the energy of the incident photon and F(R) is the reflection in Kubelka-Munk function [1]. The linear part of the curve was extrapolated to zero reflectance and the band gap energy was derived.

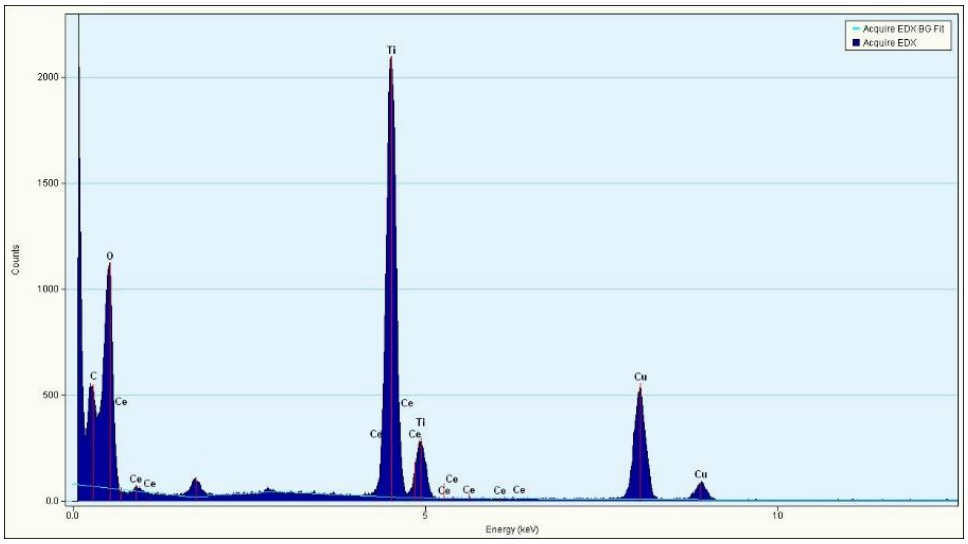

Figure S1. EDS spectrum of $80Ce/TiO_2$ sample.

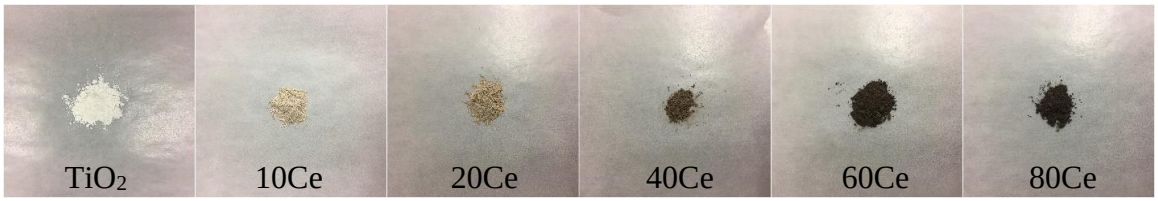

Figure S2. Images of TiO_2 nanoparticles coated with different cycles of CeO_2 ALD.

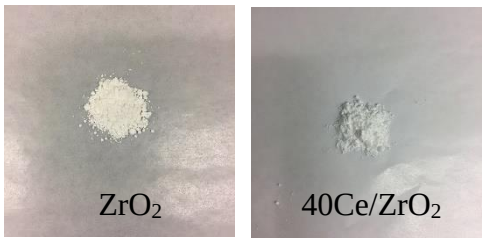

Figure S3. Images of uncoated ZrO_2 nanoparticles and ZrO_2 nanoparticles coated with 40 cycles of CeO_2 ALD.

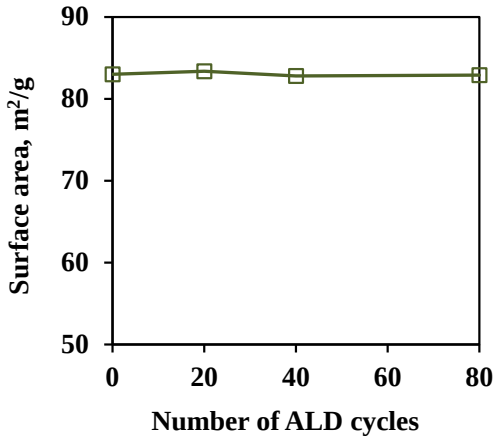

Figure S4. Surface area of uncoated TiO_2 nanoparticles and TiO_2 nanoparticles coated with different cycles of CeO_2 ALD.

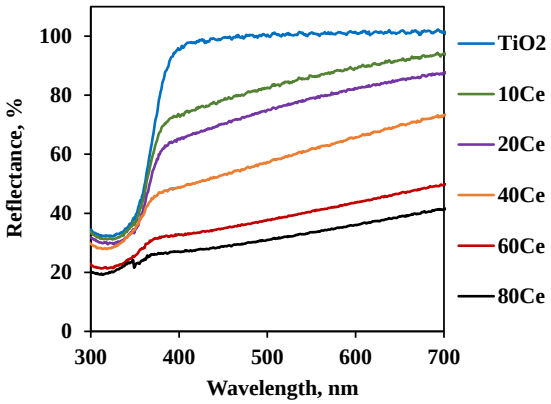

Figure S5. UV-visible diffuse reflectance spectra of TiO_2 and CeO_2/TiO_2 samples.

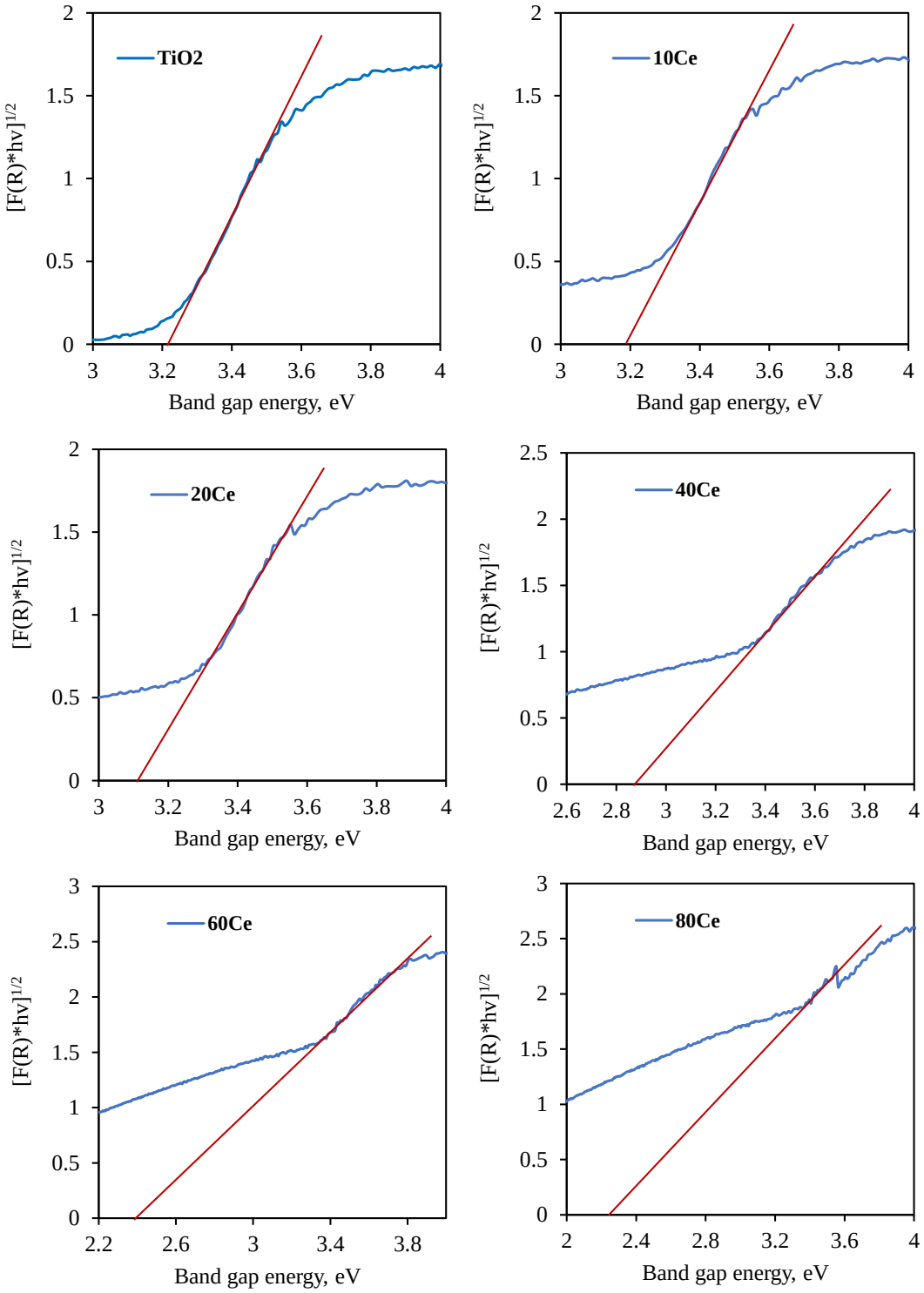

Figure S6. Band gap determination of uncoated TiO_2 nanoparticles and TiO_2 nanoparticles coated with different cycles of CeO_2 ALD. Blue and red lines represent experimental and extrapolated data, respectively.

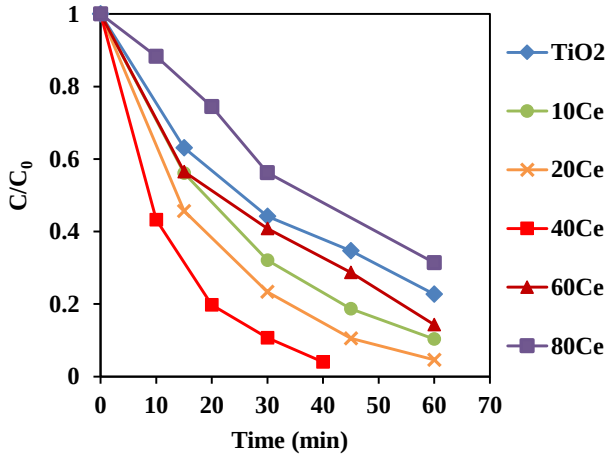

Figure S7. MB concentration as a function of UV irradiation time over different catalysts.

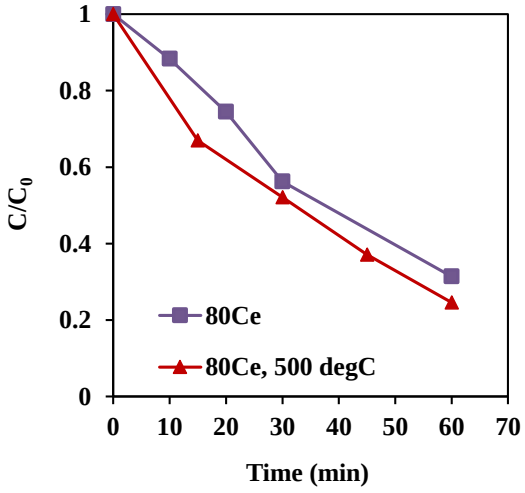

Figure S8. MB concentration as a function of UV irradiation time over 80Ce/TiO_2 sample before and after heat treatment (500 ºC for 4 hr in air).

Table S1. Cell parameters of TiO_2.

Sample	a/Å	c/Å	a:c ratio	V/Å^3
Uncoated TiO_2	3.78	9.51	0.3975	135.88
40Ce/TiO_2	3.78	9.51	0.3975	135.88
80Ce/TiO_2	3.78	9.51	0.3975	135.88
80Ce/TiO_2-500	3.78	9.51	0.3975	135.88

Reference

[1] S. George, S. Pokhrel, Z. Ji, B.L. Henderson, T. Xia, L. Li, J.I. Zink, A.E. Nel, L. Mädler, Role of Fe doping in tuning the band gap of TiO_2 for the photo-oxidation-induced cytotoxicity paradigm, Journal of the American Chemical Society, 133 (2011) 11270-11278.

VI. SIGNIFICANT IMPROVEMENT OF TIO_2 PHOTOCATALYTIC ACTIVITY THROUGH A CONTROLLABLE ZRO_2 DEPOSITION

Xiaofeng Wang, Rajankumar L. Patel and Xinhua Liang*

Department of Chemical and Biochemical Engineering, Missouri University of Science and Technology, Rolla, MO 65409, United States

ABSTRACT

5-80 cycles of ZrO_2 were deposited on TiO_2 nanoparticles by atomic layer deposition to improve their photocatalytic activity under UV light. 45 cycles of ZrO_2 deposited TiO_2 sample was proved to be the most efficient catalyst with degradation kinetic constant 10 times larger than that of the pure TiO_2 sample.

Nowadays, TiO_2 has been studied widely as an effective photocatalyst in degradation of organic pollutants due to its relatively high activity, chemical stability, nontoxicity, and low cost.[1] However, high recombination rate of photo-generated electrons (e^-) and holes (h^+) and slow reaction rate of pure TiO_2 have hindered its further applications. Thus, the photocatalytic efficiency of TiO_2 needs to be further improved from practical and commercial use.

It is well known that ZrO_2 is a *n*-type semiconductor with similar physico-chemical properties as those of TiO_2,[2] and thereby it has been used to prepare ZrO_2 doped TiO_2 photocatalysts because of these similar properties in order to improve the photocatalytic activity of TiO_2.[2-3] Through ZrO_2 doping, the band gap of photocatalysts increases and subsequently the recombination rate decreases, which leads to the

improvement of photocatalytic activity. But almost all studies adopted sol-gel and other similar methods to prepare ZrO_2/TiO_2, as shown in Table S1, and thereby the crystal structure and phase composition of samples were changed due to the mixture of Zr and Ti precursors. High ZrO_2 content would lead to poor anatase crystallinity and decrease the photocatalytic efficiency; in contrast, too low ZrO_2 loading does not ensure the obvious increase of the band gap and thereby the e^-/h^+ recombination rate cannot be reduced effectively. Thus, the enhancement of TiO_2 photocatalytic performances by ZrO_2 doping is restricted, and how to solve this dilemma is the key to further improve the activity of ZrO_2/TiO_2.

In this work, we deposited different cycles (5-80) of ZrO_2 on anatase TiO_2 nanoparticles (NPs) via atomic layer deposition (ALD) to investigate the effect of ZrO_2 in photocatalytic degradation of methylene blue (MB). The samples were labeled as *x*c-Zr/TiO_2, and *x* refers to the cycles of ZrO_2 ALD. ALD is a surface controlled layer-by-layer coating process based on self-limiting surface reactions, and it has been utilized to deposit uniform metal oxide films with nanometer-sized control of film thickness and well controlled film compositions.[4] Through making full use of the ALD advantages, the ZrO_2 content was controlled at a low level to remain the anatase crystallinity of TiO_2 and the e^-/h^+ recombination rate decreased due to the highly dispersion of ZrO_2 on the surface of TiO_2.

As shown in Figures 1 and S1, the photodegradation efficiency of all ZrO_2/TiO_2 samples was higher than that of the pure TiO_2, and with an increase in the number of ALD cycles, the photoactivity of samples kept increasing before 45 cycles of ZrO_2 ALD, then it decreased slightly with the further increase of the number of ALD cycles. The

apparent kinetic constants (k_{app}) of 45c-Zr/TiO_2 sample reached a maximum value (0.127 min^{-1}), and its activity exceeded that of pure TiO_2 (0.012 min^{-1}) by a factor of more than ten times. As shown in Table S1, Pt ALD and CeO_2 ALD have been reported to be applied for improvement of TiO_2 photoactivity, and it showed only 3.0 and 3.3 times increase of photocatalytic activity as compared to that of the pure TiO_2 at most, respectively.[5] More importantly, ZrO_2 is much cheaper and more economic for large-scale production compared to Pt. Compared to the reported ZrO_2/TiO_2 photocatalysts,[3] ALD prepared 45c-Zr/TiO_2 sample improved the photocatalytic activity of pure TiO_2 significantly, which proved that ZrO_2 ALD was one promising strategy to enhance ZrO_2/TiO_2 photocatalytic performance (Table S1). The reasons for the much higher photoactivity of 45c-Zr/TiO_2 than that of TiO_2 in this work were investigated.

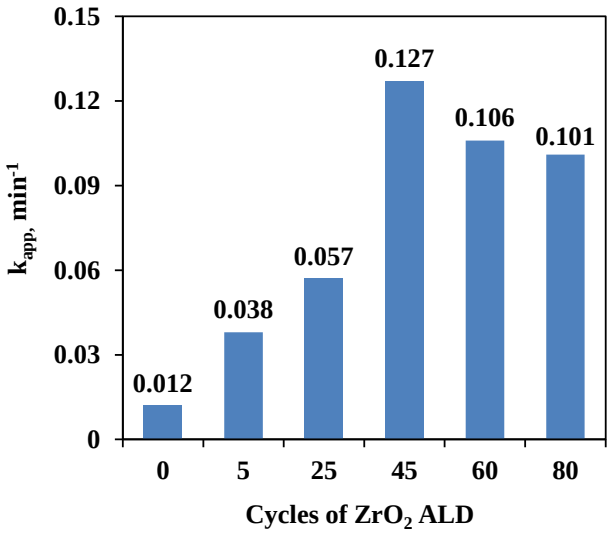

Figure 1. Apparent kinetic constants (k_{app}, min^{-1}) as a function of ZrO_2/TiO_2 catalysts with different number of ZrO_2 ALD cycles.

Firstly, the ZrO_2 ALD process did not affect the bulk properties of TiO_2 NPs (e.g., crystal structure and surface area). As shown in Figure 2, the ZrO_2 content of the samples increased steadily with an increase in the number of ALD cycles (from 0 to 1.5 wt.%). This is one characteristic of ALD process. This indicates the constant growth rate of ZrO_2. The ZrO_2 loading was 0.1, 0.5, 1.1, 1.2, 1.5 wt.% in 5c-Zr/TiO_2, 25c-Zr/TiO_2, 45c-Zr/TiO_2, 60c-Zr/TiO_2, and 80c-Zr/TiO_2 samples, respectively. Since the loading of ZrO_2 deposited on TiO_2 NPs was not high, it did not lead to increase of particle size (decrease of surface area) and poor anatase crystallinity, which would affect the photocatalytic efficiency of samples. In order to verify the hypothesis, the Brunauer–Emmett–Teller (BET) surface area, and crystal structure of all samples were analyzed. The BET surface area almost kept constant (~ 70 m^2/g) after 80 cycles of ZrO_2 ALD (Figure 2). The large surface area can provide more surface sites for the adsorption of reactants molecules.

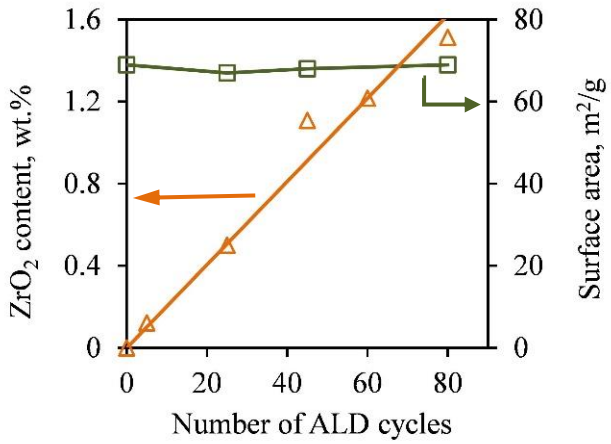

Figure 2. ZrO_2 content and BET surface area of pure TiO_2 nanoparticles and TiO_2 nanoparticles deposited with different cycles of ZrO_2 ALD.

Moreover, based on calculation, 1 g of 80c-Zr/TiO_2 contained 0.015 g ZrO_2 (5.68 g/cm^3) and the thickness of ZrO_2 should be around 0.038 nm (0.015/5.68/70*1000 nm) if ZrO_2 formed as a film on the TiO_2 NPs.[6] The thickness is much thinner than that of a real layer ZrO_2 (> 0.1 nm). Thus, ZrO_2 was highly dispersed on TiO_2 rather than formed a film. As shown in Figure 3, the TEM images of 45c-Zr/TiO_2 and 80c-Zr/TiO_2 were similar to that of pure anatase TiO_2 NPs, and the lattice fringes of 0.35 nm, 0.24 nm and 0.19 nm correspond to the (101), (004) and (200) planes of anatase, respectively.[7] No ZrO_2 film was observed, but the inductively coupled plasma–atomic emission spectroscopy (ICP-AES) and energy-dispersive X-ray spectroscopy (EDS) verified the existence of Zr on TiO_2 (Figure S2). It seems that ZrO_2 ALD follows an island growth mechanism (Volmer–Weber mechanism) during the initial stages of the ALD process, which is similar to that of some metal ALD.[8]

Figure S3 presents that X-ray diffraction (XRD) patterns of all samples show peaks appearing at 2θ: 25.3º, 37.8º, 48.1º, 53.9º, 55.2º, 62.8º, and 75.2º corresponding to the diffraction patterns of (101), (004), (200), (105), (211), (204), and (215), respectively, of the pure tetragonal phase of anatase TiO_2.[9] There was no significant difference for all samples. The TiO_2 in all samples remained anatase structure after ZrO_2 ALD and no peak corresponded to the reflections from ZrO_2, which could be due to the amorphous structure of ZrO_2 on TiO_2. According to the XRD analysis, the TiO_2 crystal size was around 19 nm for all samples, which is close to the actual particle size of TiO_2 (~20 nm). Raman analysis was also performed, and all samples showed three major Raman bands at 397, 517 and 640 cm^{-1} (Figure S4), which are attributed to the Raman-active modes of TiO_2 anatase phase with the symmetries of B1g, A1g, and Eg, respectively.[10] Thus, our

hypothesis was proved that the anatase crystallinity of samples were almost no change after ALD process.

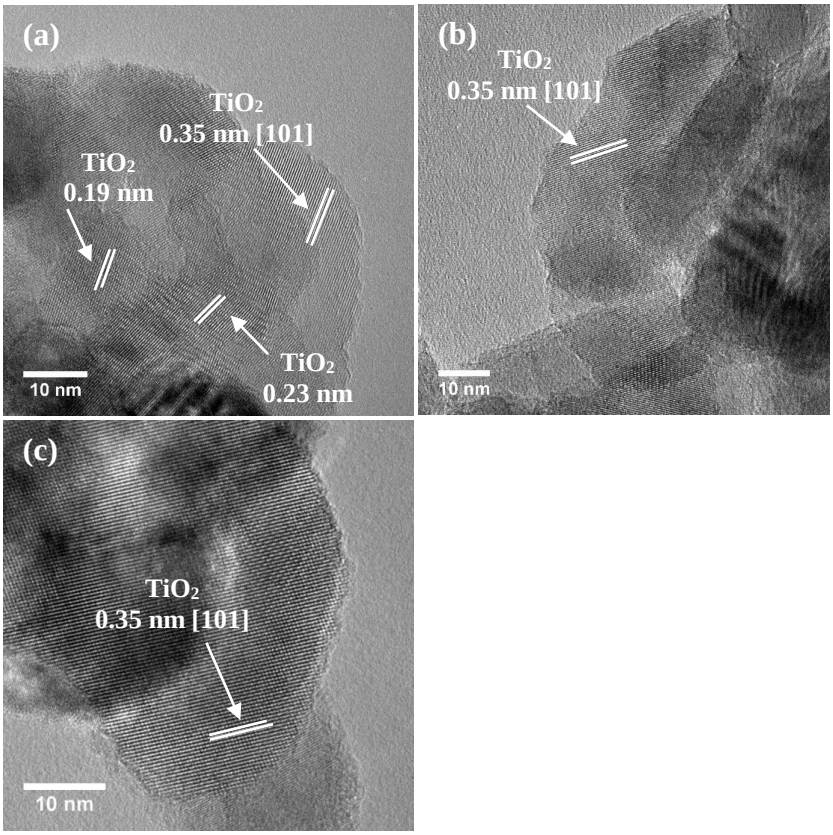

Figure 3. TEM images of (a) TiO_2, (b) 45c-Zr/TiO_2, and (c) 80c-Zr/TiO_2 nanoparticles.

Secondly, a larger band gap corresponds to stronger redox ability, which leads to reduction of e^-/h^+ recombination rate and improvement of photocatalytic activity. Since the band gap of ZrO_2 is around 4.6 eV and it is larger than that of anatase TiO_2 (3.2 eV),[11] the band gap of ZrO_2/TiO_2 samples enlarged after ZrO_2 ALD.[12] As shown in Figures 4 and S5-S6, the band gap of the samples kept increasing along with the increase of ALD cycles, which is consistent with previous reports.[3d, 13] Because the photocatalytic degradation process can be considered as an electrochemical cell, the increase in band

gap results in an enhanced oxidation-reduction potential.[14] However, the photocatalytic activity of 60c-Zr/TiO_2 and 80c-Zr/TiO_2 was lower than that of 45c-Zr/TiO_2, though the band gap of 60c-Zr/TiO_2 and 80c-Zr/TiO_2 were larger than that of 45c-Zr/TiO_2 sample. It can be explained that the samples with too large band gap cannot take full advantage of UV light and thereby they could not generate enough e^- and h^+ for MB degradation.

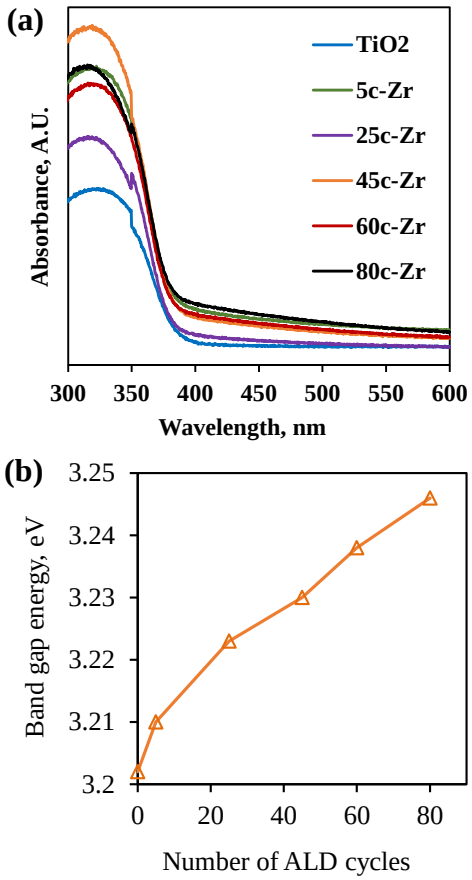

Figure 4. (a) UV-visible absorption spectra, and (b) the band gap energy of TiO_2 and ZrO_2/TiO_2 samples.

Thirdly, there is a fast transfer of the photo-formed electrons from the conduction band (CB) of ZrO_2 to that of TiO_2, when ZrO_2 was deposited on TiO_2 under UV

irradiation, since the bottom of the CB edge of ZrO_2 is about 1.3 eV, which is higher than that of TiO_2.[3d, 11] The electron transfer prevented radiative electron/holes recombination and thereby improved the photocatalytic activity of 45c-Zr/TiO_2 sample. In order to evaluate the separation rate of e^-/h^+ pairs, photoluminescence (PL) analysis was carried out. As shown in Figure 5, the only one peak at 433 nm corresponds to the reflection from anatase phase of TiO_2, and no other peak was observed in the wavelength of 300-600 nm. With an increase in the number of ZrO_2 ALD cycles, the PL intensity decreased greatly, which indicated that the separation efficiency of e^-/h^+ pairs enhanced for ZrO_2/TiO_2 samples. In other words, the existence of ZrO_2 helped trap the photo-generated charge carriers and inhibited the recombination of e^-/h^+ pairs (Figure 6). All factors mentioned above worked collectively and resulted in improved photocatalytic activity of 45c-Zr/TiO_2.

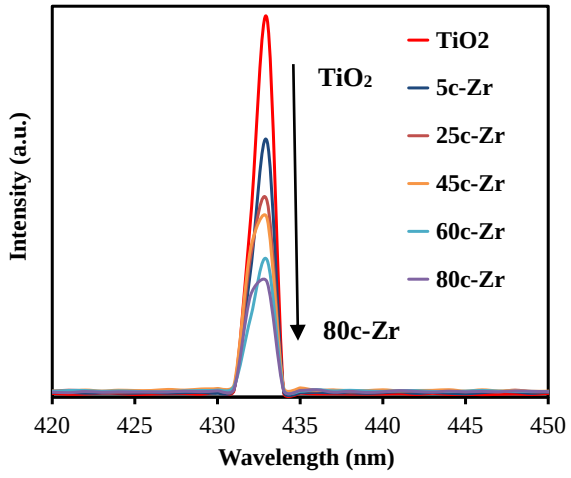

Figure 5. Photoluminescence spectra of TiO_2 and ZrO_2/TiO_2 samples excited at 280 nm.

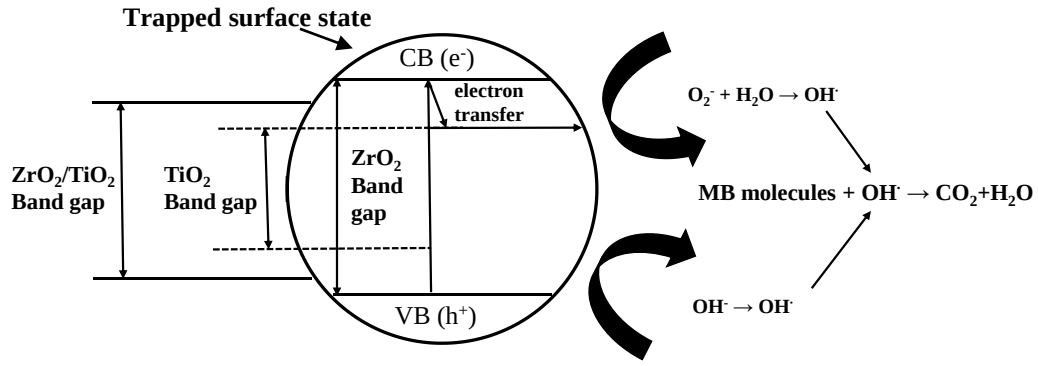

Figure 6. Proposed mechanism for the photoexcited electron–hole separation and transport processes at the ZrO_2/TiO_2 interface under UV irradiation.

It is also noted that the TiO_2 catalyst containing 1.1 wt.% ZrO_2 (45c-Zr/TiO_2) enhanced the photocatalytic activity at most and it was the optimal amount of deposition for degradation of MB in this study. However, the optimal ZrO_2 amount is not consistent with that in literatures, which reported that the optimal ZrO_2 loading was more than 5%. This could be due to the different preparation methods for ZrO_2/TiO_2 samples.[3a-c] Higher optimal ZrO_2 loading was needed via ZrO_2 doping method because some ZrO_2 inserted into the interior matrix of TiO_2 particles and cannot work with TiO_2 synergistically. Instead, in this study ZrO_2 was highly dispersed on the surface of TiO_2 NPs via ALD and thereby the ZrO_2 optimal content was significantly lower.

In summary, different cycles of ZrO_2 ALD were deposited on TiO_2 powders. The 45c-Zr/TiO_2 catalyst showed the highest photocatalytic activity and had a more than ten-fold photocatalytic activity enhancement over pure TiO_2 for the degradation of MB due to the fact that the fast electron transfer from the CB of ZrO_2 to that of TiO_2 prevented radiative electron/holes recombination. This factor worked collectively with another two factors, the relative high surface area and a larger band gap of ZrO_2/TiO_2, and thus

resulted in significantly improved photocatalytic activity of samples. ZrO_2 ALD is a novel and effective strategy to improve the photocatalytic activity of TiO_2 significantly, and it is a potential promising way to enhance the activity of other photocatalysts.

Acknowledgment is made to the donors of the American Chemical Society Petroleum Research Fund for partial support of this research. The authors thank Dr. Jingjing Qing at the Materials Research Center at Missouri University of Science and Technology for TEM analysis. The authors also thank Naveen K Mahenderkar and Prof. Jay A. Switzer in the Department of Chemistry for the assistance with diffuse reflectance UV-vis measurement, and Prof. Richard Brow in the Department of Materials Science and Engineering for the assistance with Raman and photoluminescence analysis.

NOTES AND REFERENCES

1. (a) M. R. Hoffmann, S. T. Martin, W. Choi and D. W. Bahnemann, *Chemical Reviews*, 1995, **95**, 69; (b) A. L. Linsebigler, G. Lu and J. T. Yates Jr, *Chemical Reviews*, 1995, **95**, 735; (c) Y. Wang, H. Cheng, Y. Hao, J. Ma, W. Li and S. Cai, *Journal of Materials Science*, 1999, **34**, 3721.

2. H. Liu, Y. Su, H. Hu, W. Cao and Z. Chen, *Advanced Powder Technology*, 2013, **24**, 683.

3. (a) Y. Gnatyuk, N. Smirnova, A. Eremenko and V. Ilyin, *Adsorption Science & Technology*, 2005, **23**, 497; (b) M. Li, X. Li, G. Jiang and G. He, *Ceramics International*, 2015, **41**, 5749; (c) B. Neppolian, Q. Wang, H. Yamashita and H. Choi, *Applied Catalysis A: General*, 2007, **333**, 264; (d) X. Qu, D. Xie, L. Cao and F. Du, *Ceramics International*, 2014, **40**, 12647; (e) C. Sun, L. Liu, L. Qi, H. Li, H. Zhang, C. Li, F. Gao and L. Dong, *Journal of colloid and interface science*, 2011, **364**, 288.

4. R. L. Puurunen, *Journal of Applied Physics*, 2005, **97**, Article No. 121301.

5. (a) Y. Zhou, D. M. King, X. Liang, J. Li and A. W. Weimer, *Applied Catalysis B: Environmental*, 2010, **101**, 54; (b) X. Wang, Y. Jin and X. Liang, *Nanotechnology*, 2017, **28**, Article No. 505709.

6. J. Cao, C. Rambo and H. Sieber, *Ceramics International*, 2004, **30**, 1967.

7. H. B. Wu, H. H. Hng and X. W. D. Lou, *Advanced Materials*, 2012, **24**, 2567.

8. S. M. George, *Chemical Reviews*, 2010, **110**, 111.

9. X. Wang, A. R. Donovan, R. L. Patel, H. Shi and X. Liang, *Journal of Environmental Chemical Engineering*, 2016, **4**, 3767.

10. T. Cao, Y. Li, C. Wang, L. Wei, C. Shao and Y. Liu, *Materials Research Bulletin*, 2010, **45**, 1406.

11. G. Ramakrishna, A. K. Singh, D. K. Palit and H. N. Ghosh, *The Journal of Physical Chemistry B*, 2004, **108**, 4775.

12. A. Kambur, G. S. Pozan and I. Boz, *Applied Catalysis B: Environmental*, 2012, **115**, 149.

13. B. M. Pirzada, N. A. Mir, N. Qutub, O. Mehraj, S. Sabir and M. Muneer, *Materials Science and Engineering: B*, 2015, **193**, 137.

14. C. Zuo, S. Dorris, U. Balachandran and M. Liu, *Chemistry of materials*, 2006, **18**, 4647.

SUPPLEMENTARY INFORMATION

This file includes:

Experimental section

1. *Preparation of ZrO_2/TiO_2 nanoparticles*
2. *Characterizations*
3. *Photocatalytic activity measurement*

Figures S1-S6.

Table S1.

Experimental section

1. Preparation of ZrO_2/TiO_2 nanoparticles

ZrO_2 were deposited on TiO_2 nanoparticles (NPs) by ALD using tetrakis(dimethylamido)zirconium(IV) (TDMAZ) (electronic grade, ≥ 99.99%, Sigma-Aldrich) and deionized water as precursors in a fluidized bed reactor, as described in detail elsewhere [1]. Anatase TiO_2 NPs with an average particle size of 20 nm were purchased from US Research Nanomaterials Inc. For a typical run, 5 g of TiO_2 NPs were loaded into the reactor. The reaction temperature was 250 °C. Before the reaction, the particles were first degassed at 250 °C for 3 hours. The particle substrates were fully fluidized with a gas flow rate controlled by mass flow controllers. N_2 was used as flush gas to remove unreacted precursors and any byproducts during the reaction. A typical half coating cycle used the following sequence: precursor dose, N_2 purge, and evacuation. This sequence was repeated alternatively for both precursors. 5 (5c-Zr/TiO_2), 25 (25c-Zr/TiO_2), 45 (45c-Zr/TiO_2), 60 (60c-Zr/TiO_2), and 80 (80c-Zr/TiO_2) cycles of ZrO_2 ALD were applied on anatase TiO_2 NPs.

2. Characterizations

Inductively coupled plasma–atomic emission spectroscopy (ICP-AES) was used to measure the Zr mass fraction in ZrO_2/TiO_2 samples. The surface area of the pure TiO_2 and ZrO_2-deposited TiO_2 NPs was calculated using the BET method in a relative pressure range (0.05-0.25) of nitrogen adsorption and desorption isotherms obtained by a Quantachrome Autosorb-1. The photoluminescence (PL) spectra were recorded with a HORIBA FL3-22 spectrometer (HORIBA, Edison, NJ) to evaluate the recombination rate of e^-/h^+ pairs in the samples. The morphology of ZrO_2 deposited on TiO_2 was directly

observed by FEI Tecnai F20 transmission electron microscopy/energy-dispersive X-ray spectroscopy (TEM/EDS).

The crystal structure of TiO_2 and ZrO_2/TiO_2 samples was analyzed by X-ray diffraction (XRD) with filtered Cu Kα radiation (λ= 1.5406 Å). The scanning range was 2θ from 20º to 80º, with a scanning rate of 0.025 º/s. The Scherrer equation was applied to calculate the average crystallite sizes of TiO_2 and ZrO_2/TiO_2 samples: $D = \frac{K\lambda}{B\cos\theta}$, where B is the half-height width of the diffraction peak of anatase, K=0.89 is a coefficient, θ is the diffraction angle, λ is the X-ray wavelength corresponding to the Cu Kα irradiation (1.5406 Å) and D is the average crystallite size of the powder sample [2].

Raman spectra of TiO_2 and ZrO_2/TiO_2 samples were recorded using a Horiba-Jobin Yvon LabRam spectrometer, equipped with a 17 mW He-Ne laser. Spectra were collected using a 10× objective lens over a wavenumber range of 200-1000 cm^{-1}. The reported spectra were generated from 10-20 scans of the respective wavenumber range, each taking ten seconds.

UV–visible absorbance and diffuse reflectance spectra (DRS) of TiO_2 and ZrO_2/TiO_2 samples were obtained with a UV–visible spectrophotometer (Varian Cary 5). $BaSO_4$ was used as an absorbance standard in the UV–visible reflectance experiments. The UV–DRS was used to evaluate the band gap of TiO_2 and ZrO_2/TiO_2 samples by plotting $[F(R)*h\nu]^{1/2}$ against $h\nu$, where $h\nu$ is the energy of the incident photon and F(R) is the reflection in Kubelka-Munk function [3]. The linear part of the curve was extrapolated to zero reflectance and the band gap energy was derived.

3. Photocatalytic activity measurement

Degradation of methylene blue (MB) was used to evaluate the photocatalytic performance of TiO_2 and ZrO_2/TiO_2 samples, as described in details previously [2]. Briefly, 0.1 g of sample was added in a 100 mL, 10 ppm MB solution. First, the solution was stirred in dark for 60 min to ensure adsorption/desorption equilibrium. Then the solution was irradiated using a UV lamp (360 nm UV light) and about 1 mL test samples were collected from the main solution at certain time intervals and filtered through a Millipore filter to make it particle-free for analysis using an UV–vis spectrometer (Varian Cary 50-Bio) at a 664 nm wavelength [4]. The change in concentration of MB in the main solution was recorded over a period of irradiation time.

Langmuir-Hinshelwood kinetic equation was used to evaluate the photocatalytic activity of catalysts intuitively. The photocatalytic degradation of MB follows the pseudo-first-order reaction kinetics [5], as shown in Equation 1:

$$-\ln\left(\frac{C_t}{C_0}\right) = kKt = k_{app}t \quad (1)$$

where C_0 and C_t are the concentration of MB initially and at a given reaction time (min), respectively, k is the reaction rate constant, and K is adsorption constants associated with the substrate. k_{app} is the apparent first order rate constant (min^{-1}) and it is the slope of the plot.

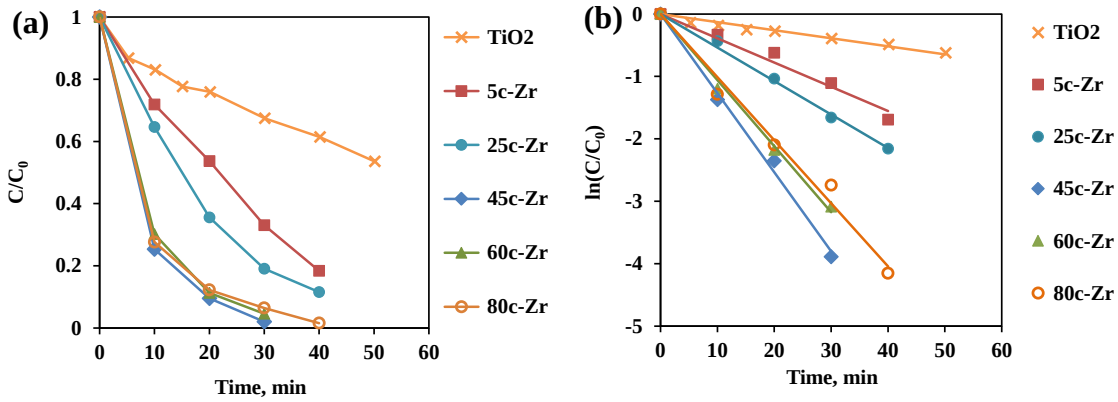

Figure S1. (a) MB concentration and (b) relative concentration of MB as a function of UV irradiation time over different catalysts.

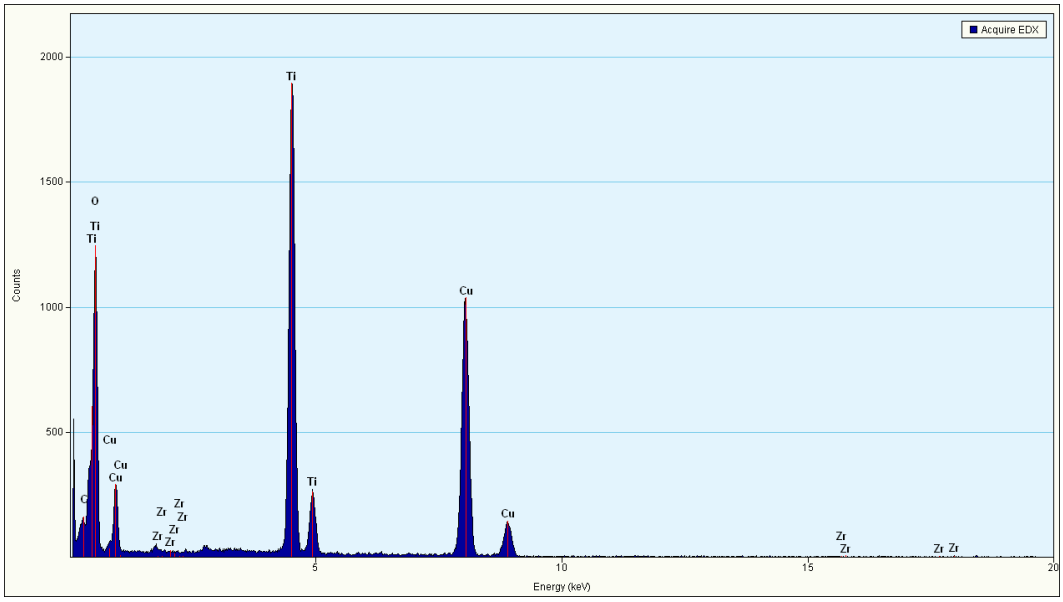

Figure S2. EDS spectrum of 80c-Zr/TiO_2 sample for Figure 3c.

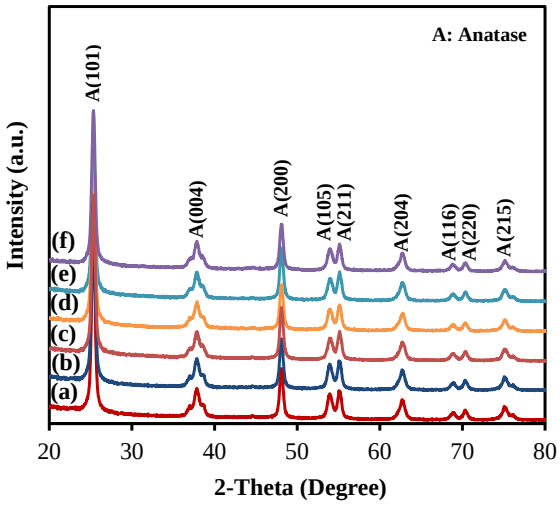

Figure S3. XRD patterns of (a) TiO_2, (b) 5c-Zr/TiO_2, (c) 25c-Zr/TiO_2, (d) 45c-Zr/TiO_2, (e) 60c-Zr/TiO_2, and (f) 80c-Zr/TiO_2.

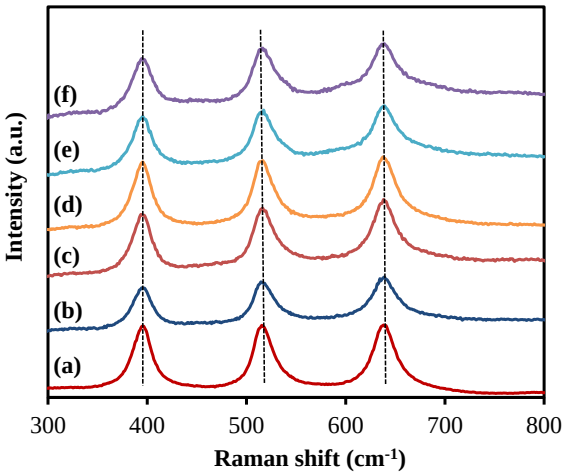

Figure S4. Raman spectra of (a) TiO_2, (b) 5c-Zr/TiO_2, (c) 25c-Zr/TiO_2, (d) 45c-Zr/TiO_2, (e) 60c-Zr/TiO_2, and (f) 80c-Zr/TiO_2.

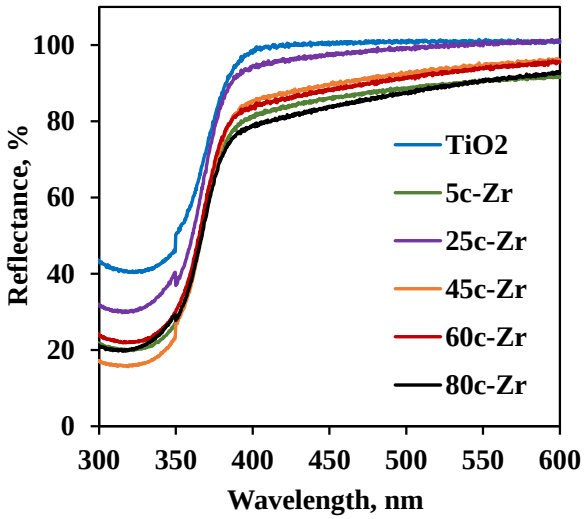

Figure S5. UV-visible diffuse reflectance spectra of TiO_2 and ZrO_2/TiO_2 samples.

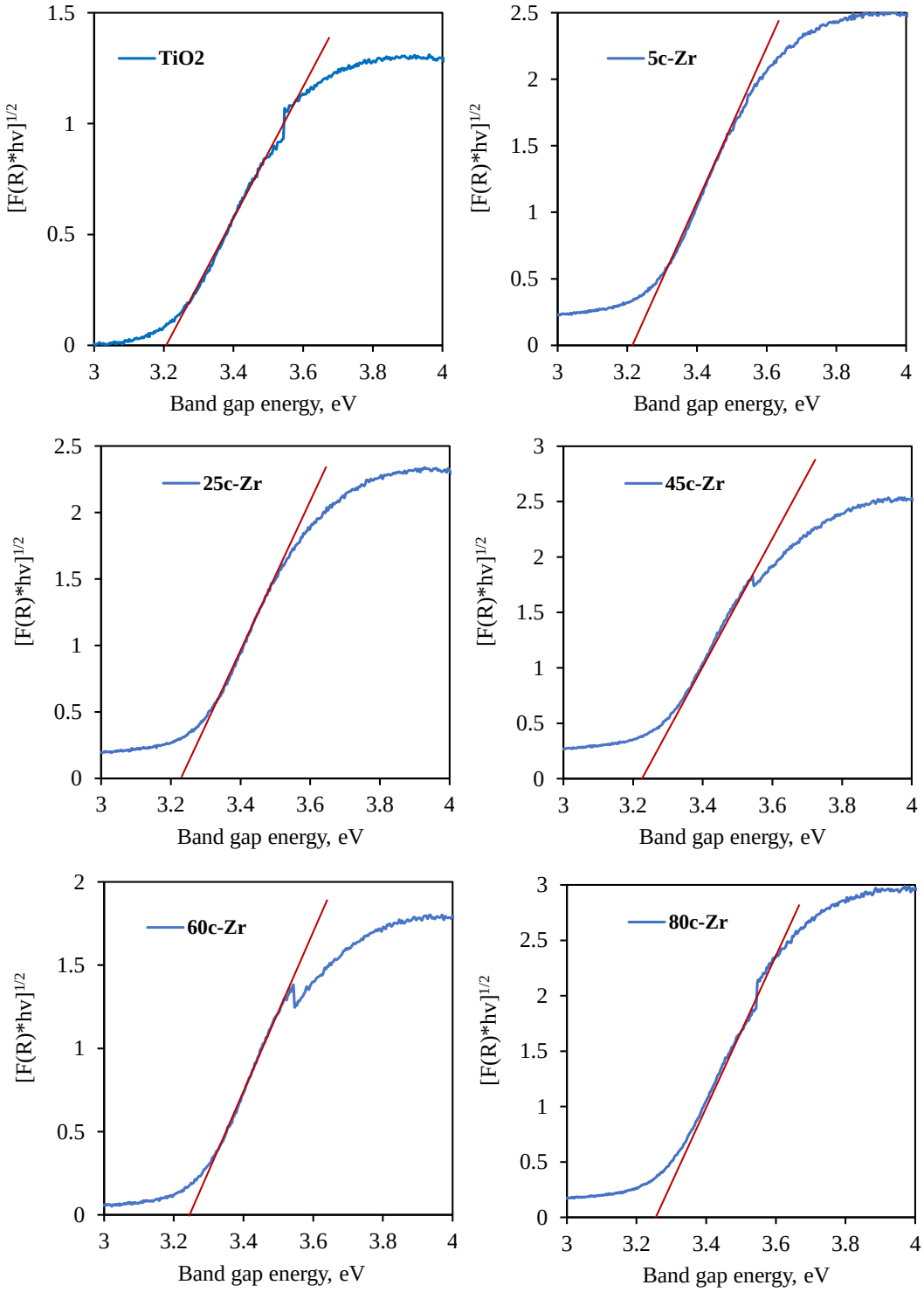

Figure S6. Band gap determination of pure TiO_2 nanoparticles and TiO_2 nanoparticles deposited with different cycles of ZrO_2 ALD. Blue and red lines represent experimental and extrapolated data, respectively.

Table S1. Comparison of photocatalytic activity of various photocatalysts.

Sample	Preparation method	Pollutant	k_{app}(sample):k_{app}(pure TiO_2)[a]	References
45c-Zr/TiO_2	**ALD**	**Methylene blue**	**10.6**	**This work**
40Ce/TiO_2	ALD	Methylene blue	3.3	[2]
Pt/TiO_2	ALD	Methylene blue	3.0	[6]
TZ(10:1)-HS	Functionalized polystyrene spheres	Rhodamine B	3.0	[7]
6.9% ZrO_2/TiO_2	Surfactant self-assembly method	Rhodamine B	2.0	[8]
TiO_2/ZrO_2	A two-step method	Methyl orange	1.8	[9]
10% ZrO_2/TiO_2	Sol-gel	Ethanol	1.5	[10]
12% ZrO_2/TiO_2	Sol-gel	4-chlorophenol	1.3	[11]

[a] k_{app} is the apparent first order constant.

References

[1] X. Liang, R.L. Patel, Porous titania microspheres with uniform wall thickness and high photoactivity, Ceramics International, 40 (2014) 3097-3103.

[2] X. Wang, Y. Jin, X. Liang, Significant photocatalytic performance enhancement of TiO_2 by CeO_2 atomic layer deposition, Nanotechnology, 28 (2017) Article No. 505709.

[3] S. George, S. Pokhrel, Z. Ji, B.L. Henderson, T. Xia, L. Li, J.I. Zink, A.E. Nel, L. Mädler, Role of Fe doping in tuning the band gap of TiO_2 for the photo-oxidation-induced cytotoxicity paradigm, Journal of the American Chemical Society, 133 (2011) 11270-11278.

[4] X. Wang, M. Bayan, M. Yu, D. Ludlow, X. Liang, Atomic layer deposition surface functionalized biochar for adsorption of organic pollutants: improved hydrophilia and adsorption capacity, International Journal of Environmental Science and Technology, 14 (2017) 1825-1834.

[5] K. Naeem, F. Ouyang, Preparation of Fe^{3+}-doped TiO_2 nanoparticles and its photocatalytic activity under UV light, Physica B: Condensed Matter, 405 (2010) 221-226.

[6] Y. Zhou, D.M. King, X. Liang, J. Li, A.W. Weimer, Optimal preparation of Pt/TiO_2 photocatalysts using atomic layer deposition, Applied Catalysis B: Environmental, 101 (2010) 54-60.

[7] C. Sun, L. Liu, L. Qi, H. Li, H. Zhang, C. Li, F. Gao, L. Dong, Efficient fabrication of ZrO_2-doped TiO_2 hollow nanospheres with enhanced photocatalytic activity of rhodamine B degradation, Journal of colloid and interface science, 364 (2011) 288-297.

[8] M. Li, X. Li, G. Jiang, G. He, Hierarchically macro–mesoporous ZrO_2–TiO_2 composites with enhanced photocatalytic activity, Ceramics International, 41 (2015) 5749-5757.

[9] X. Qu, D. Xie, L. Cao, F. Du, Synthesis and characterization of TiO_2/ZrO_2 coaxial core–shell composite nanotubes for photocatalytic applications, Ceramics International, 40 (2014) 12647-12653.

[10] Y. Gnatyuk, N. Smirnova, A. Eremenko, V. Ilyin, Design and photocatalytic activity of mesoporous TiO_2/ZrO_2 thin films, Adsorption Science & Technology, 23 (2005) 497-508.

[11] B. Neppolian, Q. Wang, H. Yamashita, H. Choi, Synthesis and characterization of ZrO_2–TiO_2 binary oxide semiconductor nanoparticles: application and interparticle electron transfer process, Applied Catalysis A: General, 333 (2007) 264-271.

VII. HIGHLY ACTIVE AND STABLE FE/SiO_2 CATALYST SYNTHESIZED BY ATOMIC LAYER DEPOSITION FOR CO OXIDATION

Xiaofeng Wang, [†] Xiaoqing He, [‡] Tommi A. White, [‡] and Xinhua Liang [†],*

[†] Department of Chemical and Biochemical Engineering, Missouri University of Science and Technology, Rolla, MO 65409, United States

[‡] Electron Microscopy Core Facility, University of Missouri, Columbia, MO 65211, United States

ABSTRACT

Highly dispersed Fe nanoparticles (NPs) were deposited on SiO_2 NPs by atomic layer deposition in a scalable fluidized bed reactor at 400 ºC. In CO oxidation reactions over the prepared Fe/SiO_2 catalyst, the temperatures for 100% conversion were 550 ºC, 470 ºC, and 410 ºC with the CO:O_2 molar ratio of 1:1, 1:5, and 1:10, respectively. Compared with reported iron oxide catalysts, the efficiency of Fe/SiO_2 for CO oxidation was more than two orders of magnitude higher than the reported values. Based on the results of cycling stability tests, Fe/SiO_2 was stable after four reaction cycles. In a long-term stability test, there was almost no activity decrease of Fe/SiO_2 at 550 ºC for more than 300 hrs of CO oxidation reaction.

KEYWORDS Iron nanoparticles, atomic layer deposition, CO oxidation, SiO_2, stability

Carbon monoxide (CO) is a strongly toxic gas. Vehicle emission is the largest anthropogenic source of CO in the United States.[1-2] Among numerous methods of CO

removal, catalytic oxidation is one of the most efficient approaches.[3] Since the temperature of exhaust gas produced in the vehicles is very high (400-800 ºC), a long-term thermally stable catalyst is needed for such applications. Many kinds of catalysts have been reported to remove CO, including noble metal catalysts (e.g., Au[4] and Pt[5]) and transition metal oxides (e.g., CeO_2[6] and Fe_2O_3 [7]). However, either high cost of noble metals or low stability limits their practical applications.[1, 8] Fe, an earth-abundant metal, is a potential and proper catalyst for CO oxidation reaction due to its unique properties. Several theoretical investigations have demonstrated that Fe was suitable as a catalyst in the CO oxidation,[9-11] however, few experimental studies were performed.

Herein, we report a novel atomic layer deposition (ALD) process to prepare a low-cost and long-term stable Fe/SiO_2 catalyst for CO oxidation reaction. ALD is a surface controlled process based on self-limiting reactions, and has been demonstrated to deposit highly dispersed metal nanoparticles (NPs) (e.g., Pt, Ni, and Pd) on various supports.[12-15] In this study, highly dispersed Fe NPs were deposited on SiO_2 NPs via ALD. The Fe/ SiO_2 catalyst was applied for CO oxidation and it showed a high catalytic activity and an excellent long-term stability. To the best of our knowledge, it is the first time to synthesize Fe NPs using ALD and utilize these Fe NPs for CO oxidation reactions.

The Fe mass fraction of Fe/SiO_2 NPs was 1.98 wt.% after 5 cycles of Fe ALD and the BET surface area was 95 m^2/g, which was lower than that of SiO_2 NPs (143 m^2/s, Table S1). Figure 1a shows the highly dispersed Fe NPs on the surface of SiO_2 NPs, with an average particle size of 1.5 nm. Based on XRD analysis, the sharp reflection located at the position $2\theta=22.1^\circ$ corresponded to the reflection from SiO_2 NPs, and no peaks from

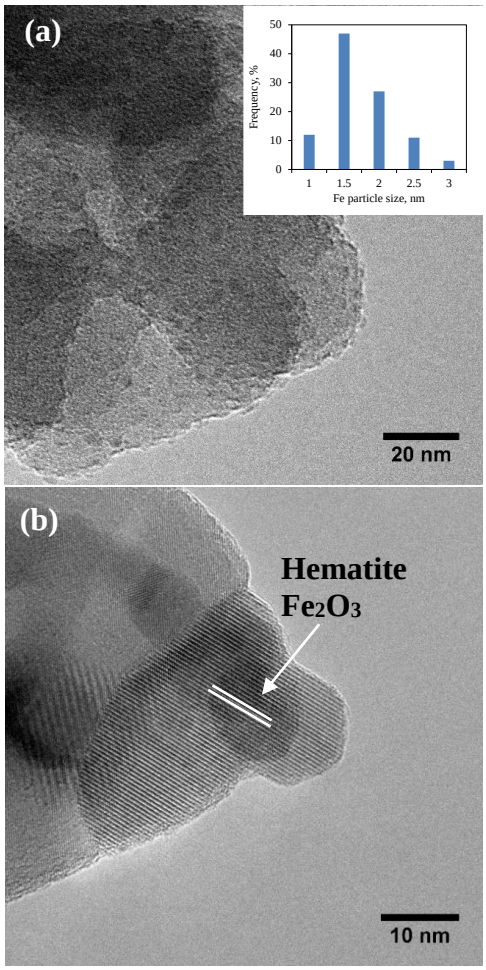

Figure 1. TEM images of (a) fresh Fe/SiO_2 catalyst (The *inset* figure shows the size distribution of Fe NPs), and (b) Fe/SiO_2 catalyst after 300 hr of CO oxidation reaction.

Fe, FeO, and Fe_2O_3 were observed (Figure 2a, line 1). It should be due to the ultrasmall size of Fe or amorphous structure of FeO and Fe_2O_3. The reduction property of Fe/SiO_2 was determined by H_2-TPR experiment. As shown in Figure 2b, the first peak at around 378 ºC should be attributed to the reduction of Fe_2O_3 to Fe_3O_4, and the second signal at around 625 ºC should be associated with the reduction of the subsequent multiple reduction of Fe_3O_4 to FeO and Fe.[16-17] It indicates that partial surface of some Fe NPs was oxidized in air due to its ultrasmall particle size. Thus, the color of Fe/SiO_2 was light

yellow instead of white (Figure S1). Similar phenomenon was observed in Pt NPs prepared by ALD.[18]

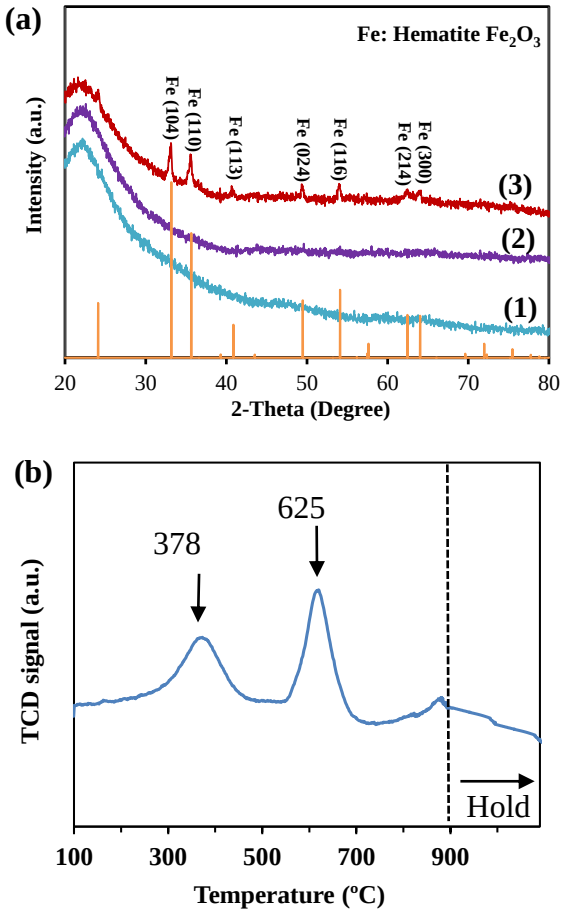

Figure 2. (a) XRD patterns of (1) as-prepared Fe/SiO_2 catalyst, (2) Fe/SiO_2 after four cycles of CO oxidation reaction, and (3) Fe/SiO_2 after 300 hr of CO oxidation reaction, and (b) H_2-TPR profile of Fe/SiO_2 sample.

Figure 3 compares the conversion curves of CO oxidation over Fe/SiO_2 NPs with different molar ratios of CO to O_2. It is clear that with the increase of O_2 to CO ratio, the conversion of CO oxidation reached 100% at a lower temperature. The temperatures for 100% conversion were 550 ºC, 470 ºC, and 410 ºC with the CO:O_2 ratio of 1:1, 1:5, and

1:10, respectively. It indicates that high concentration of O_2 in the gas stream is helpful for catalytic oxidation of CO over Fe/SiO_2 catalysts. Compared with previously reported iron oxide catalysts, though our Fe catalysts were not very active at low temperature, its specific rate was more than two orders of magnitude higher than the reported values (Table 1), and thereby our Fe/SiO_2 catalyst is more efficient in the reaction of CO oxidation and is more suitable in practical applications. It is also noted that the reaction temperature only increased 55 ºC (T_{100}-T_{10}) for the Fe/SiO_2 catalyst when the CO conversion increased from 10% to 100% and this number was much lower than those for other reported iron oxide catalysts, as shown in Table 1. It should be due to the high dispersion of Fe NPs on SiO_2, so the catalyst can offer more active sites. As a control, the activity of SiO_2 NPs was also evaluated by CO oxidation (Figure S2), and the SiO_2 support did not affect the performance of Fe/SiO_2 catalyst due to its low activity.

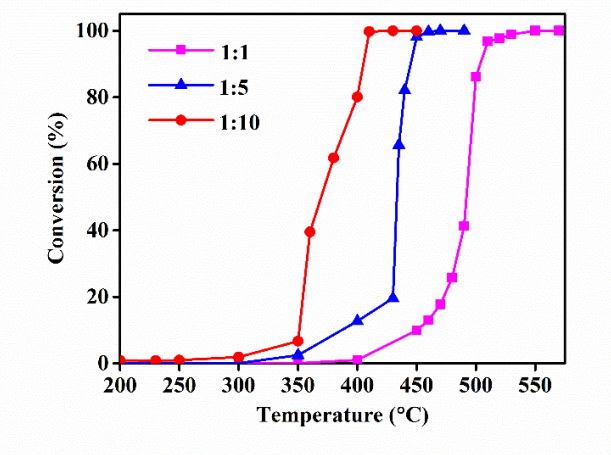

Figure 3. Effect of different molar ratios of CO to O_2 on CO conversion over Fe/SiO_2 catalysts. The flow rate of CO was kept at 2 sccm, and that of O_2 was 2 sccm, 10 sccm, and 20 sccm in each run.

Table 1. Comparison of catalytic activity for CO oxidation on different Fe-based catalysts.

Sample	$CO:O_2$	T_{10}[a], °C	T_{50}[b], °C	T_{100}[c], °C	Specific rate$_{T100}$[d], $mL_{CO}\ g_{Fe}^{-1}s^{-1}$
Fe/SiO_2	**1:10**	**355**	**370**	**410**	**33.67**
FeO_x-200 [7]	1:10	167	240	307	0.48
Fe_2O_3 [21]	1:10	210	290	420	0.48
Fe_2O_3 nanorods [22]	1:10	230	289	370	0.2
Fe_2O_3 nanocubes [22]	1:10	300	378	580	0.2
Fe_2O_3 nanotubes [22]	1:10	270	400	640	0.2
Fe_2O_3 large cube [23]	1:16	300	470	>500	0.12
Fe_2O_3 large rod [23]	1:16	190	240	280	0.12
Fe_2O_3-430 [24]	1:20	110	230	253	0.07

[a] Temperature (°C) for 10% CO conversion. [b] Temperature (°C) for 50% CO conversion. [c] Temperature (°C) for 100% CO conversion. [d] Volume per second of CO oxidized over per gram of Fe at the temperature for 100% CO conversion.

The recycle and reuse ability of catalysts is one of the key factors in practical applications. In order to evaluate the reproducibility of Fe catalysts, cycling tests were performed. As shown in Figure 4a, four cycles of reactions were applied for the Fe/SiO_2 catalyst and no noticeable difference in catalytic activity was observed with an increase in the number of reaction cycles. This demonstrates the excellent cycling stability of our

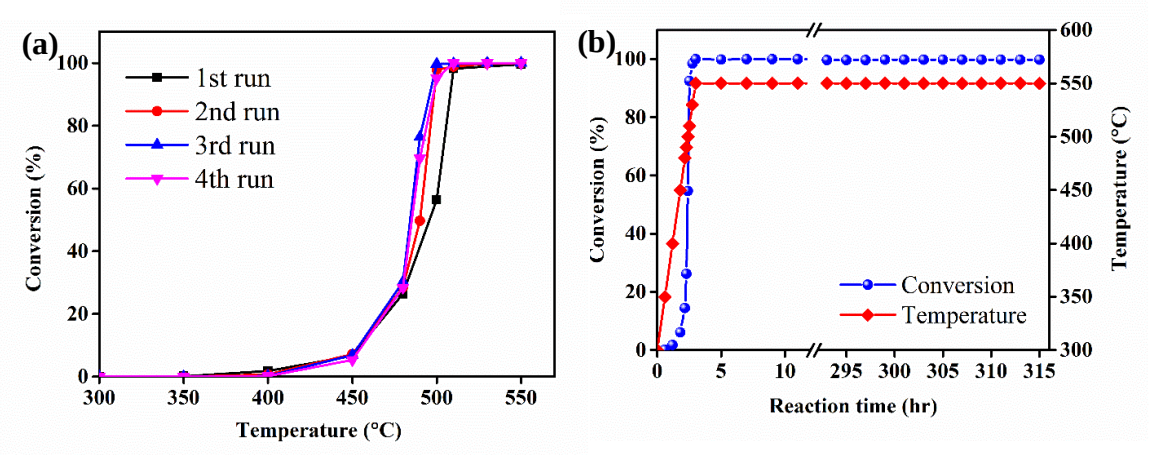

Figure 4. (a) Cycling stability test and (b) long-term stability test of Fe/SiO_2 catalyst for CO oxidation.

Fe/SiO_2 catalyst. In addition to cycling stability tests, a long-term stability test of Fe/SiO_2 catalyst was also performed. As shown in Figure 4b, after the CO conversion reached 100% at 550 ºC, the reaction was kept running for more than 300 hours and no decrease of CO conversion was observed. It indicates that the Fe/SiO_2 catalyst was extremely stable and durable under severe conditions, e.g., high temperature. Compared with other metal or metal oxide catalysts (e.g., Au, Pd and Co_3O_4), the Fe/SiO_2 catalyst kept stable in much longer time at higher temperature and it showed an excellent stability (Table S2). Generally, at low reaction temperature, metal nanoparticle catalysts can keep stable on the substrates and do not aggregate or sinter easily, but it is difficult to dissociate adsorbed O_2 due to lack of enough energy, which leads to deactivation of catalysts.[19] On the other hand, when the reaction temperature is high, the metal particles would tend to aggregate/sinter, which also results in deactivation, though the dissociate energy is enough.[20] In our current study, the Fe/SiO_2 catalyst prepared by ALD is very stable at

high temperature. So it is a potential and promising alternate for catalytic oxidation of CO exhausted from vehicles due to its high activity and outstanding stability.

Since both metallic and oxidized Fe (Fe, FeO, and Fe_2O_3) existed in the Fe/SiO_2 catalyst, it is important to figure out which one played a dominating role in the CO oxidation. As shown in Figure S1, the color of Fe/SiO_2 sample changed to dark yellow after 300 hr of reaction, which indicates that more Fe with metallic state was oxidized and changed to Fe_2O_3 during the long-term CO oxidation reaction. In order to verify this, XRD and Raman analysis for the Fe/SiO_2 samples before and after reaction were performed. The XRD pattern of Fe/SiO_2 after four cycles of reaction was similar to that of the as-prepared Fe/SiO_2 sample, and there was no peak corresponding to Fe, FeO, and Fe_2O_3 (line 2 in Figure 2a). In contrast, the sharp reflections located at the positions 2θ= 33.2º, 35.7º, 40.8º, 49.4º, 54.0º, 62.5º, and 64.2º corresponded to the reflections from (104), (110), (113), (024), (116), (214), and (300) planes of Fe_2O_3 in the hematite phase for Fe/SiO_2 after 300 hr of CO oxidation reaction (line 3 in Figure 2a), respectively. Peak assignments were made according to JCPDS (Cards No. 01-079-1741). Thus, the hypothesis was verified that more Fe was oxidized to Fe_2O_3 and the structure of Fe_2O_3 changed from amorphous to hematite due to the high reaction temperature (550 ºC) and long reaction time (300 hr). The structure of Fe_2O_3 still remained amorphous after four cycles of reaction (line 2 in Figure 2a), which could be attributed to the relatively short reaction time (~10 hr). In addition, as shown in Figure 1b, the particle size of Fe NPs became large after 300 hr of CO oxidation reaction and the lattice fringes were observed in the TEM image. The lattice fringe of 0.26 nm corresponded to the (110) planes of hematite Fe_2O_3.[25] Raman analysis was also performed and the Fe/SiO_2 sample after 300

hr reaction showed three major Raman bands at 225, 291, and 410 cm^{-1}, which are ascribed to the Raman-active modes of Fe_2O_3 hematite phase (Figure S3).[26] Both TEM and Raman analysis were consistent with XRD results.

Therefore, Fe_2O_3 was the dominate factor in the Fe/SiO_2 sample to oxidize CO to CO_2, since the conversion still kept 100% after 300 hr reaction, though more Fe changed to Fe_2O_3 during the long-term reaction. Generally, the catalytic CO oxidation over Fe_2O_3 can be divided into two steps. Firstly, Fe_2O_3 loses one oxygen atom and catalyzes CO to form CO_2; then the produced FeO is oxidized by O_2 soon.[8] In this study, when the concentration of O_2 in the gas stream was high, more O_2 could be used for FeO oxidation and more Fe_2O_3 would catalyze CO oxidation. Thus, 100% of CO conversion reached at a relatively low temperature with the $CO:O_2$ ratio of 1:10, as shown in Figure 3.

It is also noted that according to the XRD analysis, the Fe_2O_3 crystal size was around 30 nm for Fe/SiO_2 sample after 300 hr reaction, and it was much larger than that of as-prepared Fe NPs (1.5 nm). It indicates that Fe NPs aggregated during the long-term reaction process. In order to verify this, HRTEM and EDX mapping were applied for the Fe/SiO_2 catalyst after 300 hr of CO oxidation reaction. As shown in Figure 5, there were some large particles (> 30 nm), and they were aggregated Fe_2O_3 NPs, since only Fe and O were detected based on EELS results and no Si was detected. It is noted that the CO conversion was still 100%, though Fe NPs aggregated during the long-term CO oxidation process. This can be explained that at the beginning of the long-term stability test, only a limited number of Fe_2O_3 active sites were used to catalyze CO oxidation; as the reaction time went on, more Fe converted to Fe_2O_3 and involved in catalytic CO oxidation, though Fe NPs aggregated gradually. In addition, the BET surface area of Fe/SiO_2 after 300 hr of

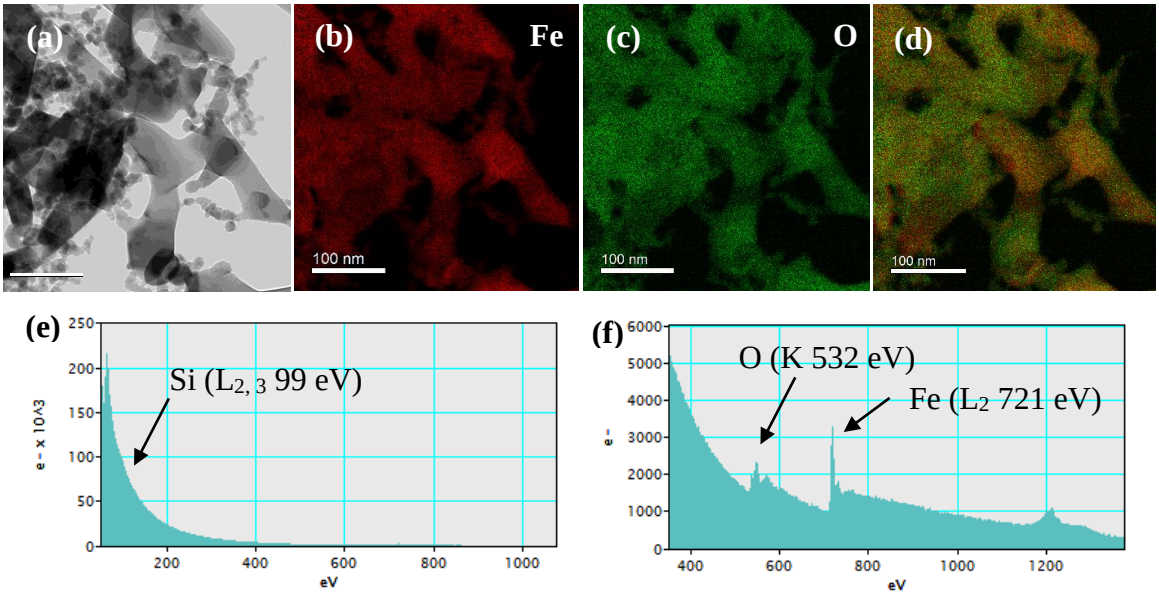

Figure 5. (a) HRTEM image, (b-d) EDX mappings and (e-f) electron energy loss spectra (EELS) of Fe/SiO_2 sample after 300 hr of CO oxidation reaction.

CO oxidation was higher than that of as-prepared Fe/SiO_2 sample (Table S1), which could be due to the fact that Fe NPs aggregated and became large NPs during the long-term stability test, and thereby some surface area of SiO_2 which were previously occupied by Fe NPs were released, as shown in Figure S4. So the surface area of the sample increased and the total number of Fe_2O_3 active sites would be enough for the catalytic reaction. Thus, the Fe/SiO_2 catalyst showed good stability of catalytic performance. As we know, a mix of precious metal (Pd, Pt, and Rh) is the most widely used catalyst in catalytic convertor of vehicles that converts toxic gases and pollutants in exhaust gas to less toxic pollutants by catalyzing a redox reaction (an oxidation and a reduction reaction). Among them, Pd and Pt are mainly applied for catalytic oxidization of CO and unburnt hydrocarbons. Based on the results in this study, our Fe/SiO_2 catalyst has potential to substitute Pd and Pt to catalyze CO oxidation. Since Fe is an earth-abundant

element and is much cheaper than noble metals (i.e., Pd and Pt), it will significantly reduce the cost, if Fe catalyst can be used in emissions control and auto industry in the future.

In conclusion, highly dispersed Fe NPs were deposited on SiO_2 NPs by ALD successfully, and the average size of the Fe NPs was 1.5 nm. The Fe/SiO_2 catalyst showed a high activity and an excellent long-term stability at high temperature in the reaction of CO oxidation. Fe_2O_3 played a vital role in catalytic CO oxidation. Due to their high efficiency, excellent stability, and low cost, it is a potential catalyst for CO removal in large-scale applications, such as treatment of exhaust gas.

AUTHOR CONTRIBUTIONS

X. L. and X. W. proposed the concept of Fe/SiO_2 catalyst prepared by ALD for CO oxidation reaction and designed the experiments. X. W. conducted the experiments. X. W. and X.L. analyzed the results and drafted the manuscript. X. H. and T. W. performed HRTEM, EDX mapping, and EELS analysis of Fe/SiO_2 and analyzed the related results. All authors reviewed the manuscript.

ACKNOWLEDGMENT

The authors thank Dr. Jessica TerBush at the Materials Research Center at Missouri University of Science and Technology for TEM analysis. The authors also

thank Electron Microscopy Core Facility (EMC) and the Office of Research at University of Missouri for supporting the TEM work at EMC.

REFERENCES

(1) Biabani-Ravandi, A.; Rezaei, M.; Fattah, Z. Low-temperature CO oxidation over nanosized Fe–Co mixed oxide catalysts: effect of calcination temperature and operational conditions. *Chemical Engineering Science* **2013,** *94*, 237-244.

(2) Council, N. R. *The ongoing challenge of managing carbon monoxide pollution in fairbanks, Alaska*. National Academies Press: 2002.

(3) Gac, W. The influence of silver on the structural, redox and catalytic properties of the cryptomelane-type manganese oxides in the low-temperature CO oxidation reaction. *Applied Catalysis B: Environmental* **2007,** *75*, 107-117.

(4) Li, X.-N.; Yuan, Z.; He, S.-G. CO oxidation promoted by gold atoms supported on titanium oxide cluster anions. *Journal of the American Chemical Society* **2014,** *136*, 3617-3623.

(5) Qiao, B.; Wang, A.; Yang, X.; Allard, L. F.; Jiang, Z.; Cui, Y.; Liu, J.; Li, J.; Zhang, T. Single-atom catalysis of CO oxidation using Pt_1/FeOx. *Nature Chemistry* **2011,** *3*, 634-641.

(6) Mock, S. A.; Sharp, S. E.; Stoner, T. R.; Radetic, M. J.; Zell, E. T.; Wang, R. CeO_2 nanorods-supported transition metal catalysts for CO oxidation. *Journal of Colloid and Interface Science* **2016,** *466*, 261-267.

(7) Šmit, G.; Zrnčević, S.; Lázár, K. Adsorption and low-temperature oxidation of CO over iron oxides. *Journal of Molecular Catalysis A: Chemical* **2006,** *252*, 103-106.

(8) Li, P.; Miser, D. E.; Rabiei, S.; Yadav, R. T.; Hajaligol, M. R. The removal of carbon monoxide by iron oxide nanoparticles. *Applied Catalysis B: Environmental* **2003,** *43*, 151-162.

(9) Li, F.; Zhao, J.; Chen, Z. Fe-anchored graphene oxide: a low-cost and easily accessible catalyst for low-temperature CO oxidation. *The Journal of Physical Chemistry C* **2012,** *116*, 2507-2514.

(10) Wu, P.; Du, P.; Zhang, H.; Cai, C. Graphyne-supported single Fe atom catalysts for CO oxidation. *Physical Chemistry Chemical Physics* **2015,** *17*, 1441-1449.

(11) Tang, Y.; Zhou, J.; Shen, Z.; Chen, W.; Li, C.; Dai, X. High catalytic activity for CO oxidation on single Fe atom stabilized in graphene vacancies. *RSC Advances* **2016,** *6*, 93985-93996.

(12) Shang, Z.; Patel, R. L.; Evanko, B. W.; Liang, X. Encapsulation of supported metal nanoparticles with an ultra-thin porous shell for size-selective reactions. *Chemical Communications* **2013,** *49*, 10067-10069.

(13) Gould, T. D.; Lubers, A. M.; Neltner, B. T.; Carrier, J. V.; Weimer, A. W.; Falconer, J. L.; Will Medlin, J. Synthesis of supported Ni catalysts by atomic layer deposition. *Journal of Catalysis* **2013,** *303*, 9-15.

(14) Wang, X.; Hu, W.; Deng, B.; Liang, X. Selective hydrogenation of citral over supported Pt catalysts: insight into support effects. *Journal of Nanoparticle Research* **2017,** *19*, Article No. 153.

(15) Yan, H.; Cheng, H.; Yi, H.; Lin, Y.; Yao, T.; Wang, C.; Li, J.; Wei, S.; Lu, J. Single-atom Pd_1/graphene catalyst achieved by atomic layer deposition: remarkable performance in selective hydrogenation of 1, 3-butadiene. *Journal of the American Chemical Society* **2015,** *137*, 10484-10487.

(16) Khoudiakov, M.; Gupta, M. C.; Deevi, S. Au/Fe_2O_3 nanocatalysts for CO oxidation: a comparative study of deposition–precipitation and coprecipitation techniques. *Applied Catalysis A: General* **2005,** *291*, 151-161.

(17) Xi, X.; Ma, S.; Chen, J.-F.; Zhang, Y. Promotional effects of Ce, Mn and Fe oxides on CuO/SiO_2 catalysts for CO oxidation. *Journal of Environmental Chemical Engineering* **2014,** *2*, 1011-1017.

(18) Wang, X.; Zhao, H.; Wu, T.; Liu, Y.; Liang, X. Synthesis of highly dispersed and highly stable supported Au–Pt bimetallic catalysts by a two-step method. *Catalysis Letters* **2016,** *146*, 2606-2613.

(19) Li, Y.; Yu, Y.; Wang, J.-G.; Song, J.; Li, Q.; Dong, M.; Liu, C.-J. CO oxidation over graphene supported palladium catalyst. *Applied Catalysis B: Environmental* **2012,** *125*, 189-196.

(20) Qi, J.; Chen, J.; Li, G.; Li, S.; Gao, Y.; Tang, Z. Facile synthesis of core–shell $Au@CeO_2$ nanocomposites with remarkably enhanced catalytic activity for CO oxidation. *Energy & Environmental Science* **2012,** *5*, 8937-8941.

(21) Biabani-Ravandi, A.; Rezaei, M.; Fattah, Z. Catalytic performance of Ag/Fe_2O_3 for the low temperature oxidation of carbon monoxide. *Chemical Engineering Journal* **2013,** *219*, 124-130.

(22) Gao, Q.-X.; Wang, X.-F.; Di, J.-L.; Wu, X.-C.; Tao, Y.-R. Enhanced catalytic activity of α-Fe_2O_3 nanorods enclosed with {110} and {001} planes for methane combustion and CO oxidation. *Catalysis Science & Technology* **2011,** *1*, 574-577.

(23) Liu, X.; Liu, J.; Chang, Z.; Sun, X.; Li, Y. Crystal plane effect of Fe_2O_3 with various morphologies on CO catalytic oxidation. *Catalysis Communications* **2011,** *12*, 530-534.

(24) Cui, L.; Zhao, D.; Yang, Y.; Wang, Y.; Zhang, X. Synthesis of highly efficient α-Fe_2O_3 catalysts for CO oxidation derived from MIL-100 (Fe). *Journal of Solid State Chemistry* **2017**.

(25) Wang, W.-W.; Zhu, Y.-J.; Ruan, M.-L. Microwave-assisted synthesis and magnetic property of magnetite and hematite nanoparticles. *Journal of Nanoparticle Research* **2007,** *9*, 419-426.

(26) De Faria, D.; Venâncio Silva, S.; De Oliveira, M. Raman microspectroscopy of some iron oxides and oxyhydroxides. *Journal of Raman spectroscopy* **1997,** *28*, 873-878.

SUPPORTING INFORMATION

This file includes experimental section, images of Fe/SiO_2 samples before and after CO oxidation, CO oxidation data of Fe/SiO_2 and SiO_2, Raman spectra and BET surface areas of SiO_2 support and Fe/SiO_2 samples, scheme of Fe nanoparticles aggregation during long term stability test, and comparison of long-term stability of different catalysts for CO oxidation.

Experimental section

1. Preparation of Fe/TiO_2

Fe ALD was carried out using ferrocene (99% purity, Alfa Aesar) and hydrogen (H_2, 99.9%, Airgas) as precursors in a fluidized bed reactor. All of the chemicals were

used as received without any treatment. Total five cycles of Fe ALD were applied on SiO_2 nanoparticles (NPs) (20-30 nm). For a typical run, 3 g SiO_2 NPs was loaded into the reactor. The reaction temperature was 400 ºC. During the ALD process, the solid ferrocene was loaded into a heated bubbler and carried by nitrogen (N_2, 99.9%, Airgas) into the reactor. Ferrocene and H_2 were fed separately. The particle substrates were fully fluidized and gas flow rates were controlled by mass flow controllers. The reactor was also subjected to vibration from vibrators to improve the quality of particle fluidization during the ALD process.[1-2] N_2 was used as a flush gas to remove unreacted precursors and any byproducts during the reaction. A typical coating cycle involved the following steps: ferrocene dose (900 s), N_2 purge (900 s), evacuation (10 s); H_2 dose (1200 s), N_2 purge (900 s), evacuation (10 s).

2. Characterizations

The Fe mass fractions of Fe/SiO_2 NPs were measured by inductively coupled plasma atomic emission spectroscopy (ICP-AES). Raman spectra of SiO_2 NPs and Fe/SiO_2 samples were obtained using a Horiba-Jobin Yvon LabRam spectrometer. A Quantachrome Autosorb-1 was used to obtain nitrogen adsorption and desorption isotherms of SiO_2 NPs at -196 ºC. The BET surface areas of the SiO_2 NPs and Fe/SiO_2 samples before and after CO oxidation tests were calculated using the BET method in a relative pressure range of 0.05 - 0.25. TEM image of the Fe/SiO_2 catalyst was characterized by a FEI Tecnai F20 TEM operated at 200 kV. Samples were directly supported on holey-carbon Cu grids. At least 200 particles were randomly measured to determine the average diameter of Fe NPs.

H_2-temperature programmed reduction (H_2-TPR) was applied to analyze the Fe/SiO_2 catalyst. TPR experiments were performed using a Micromeritics AutoChem 2920 instrument. For a typical run, 50 mg of sample was loaded in a U-tube quartz reactor. Then, the sample was reduced in a flow of H_2-Ar mixture (containing 10 vol.% H_2), and the sample temperature increased to 900 ºC at a rate of 10 ºC/min and held at 900 ºC for 30 min. TPR patterns were obtained by recording the thermal conductivity detector (TCD) signal with respect to temperature.

The crystal structure of Fe/SiO_2 sample before and after CO oxidation was detected by XRD with filtered Cu Ka radiation (λ= 1.5406 Å). The scanning range was 2θ from 20º to 80º, with a scanning rate of 0.025 º/s. The Scherrer equation was applied to estimate the average crystallite sizes of Fe/SiO_2 samples: $D = \frac{K\lambda}{B\cos\theta}$, where B is the half-height width of the diffraction peak of anatase, K=0.89 is a coefficient, θ is the diffraction angle, λ is the X-ray wavelength corresponding to the Cu Kα irradiation (1.5406 Å) and D is the average crystallite size of the powder sample.

3. General procedure for CO oxidation

The CO oxidation reactions were carried out in a fixed bed quartz reactor with quartz wool supporting the catalysts. In a typical run, 50 mg Fe/SiO_2 or SiO_2 NPs was used for the reactions. A gas mixture, with 4% CO, 4% O_2, and 92% N_2 of a total flow rate of 50 mL/min (sccm), was introduced into the reactor for CO oxidation reaction. MKS® mass flow controllers were used to control the gas flow rate. Reaction temperature ranged from 200 °C to a temperature at which the CO conversion reached 100%. Reaction products were analyzed by an online gas chromatograph (SRI 8610C) equipped with a 6 feet HAYESEP D column, a 6 feet MOLECULAR SIEVE 13X column, and a

FID detector. After reaction, the Fe/SiO_2 catalyst was directly used for the following cycling tests when applicable. In addition, CO oxidation reactions over the Fe/SiO_2 catalyst were performed with different molar ratios of CO to O_2 (1:1, 1:5, and 1:10) to investigate the effect of oxygen amount on the reaction. Moreover, in order to verify the long-term stability of the Fe/SiO_2 sample, the CO oxidation reaction over Fe/SiO_2 (50 mg) was performed for more than 300 hrs at 550 ºC.

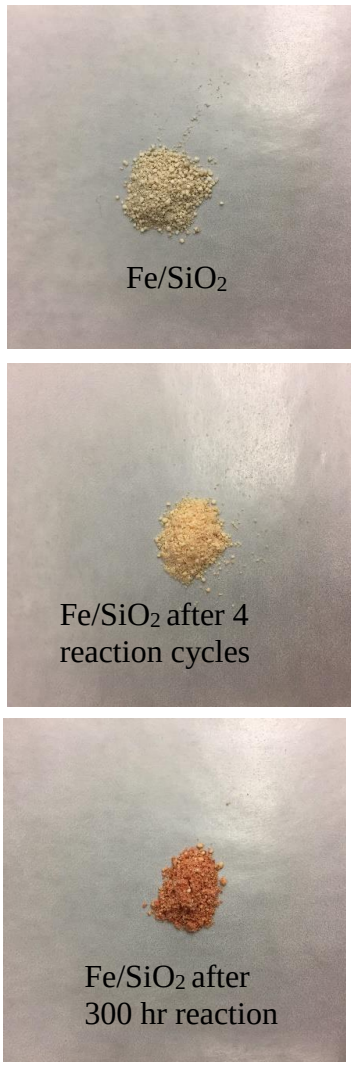

Figure S1. Images of Fe/SiO_2 samples before and after CO oxidation reaction.

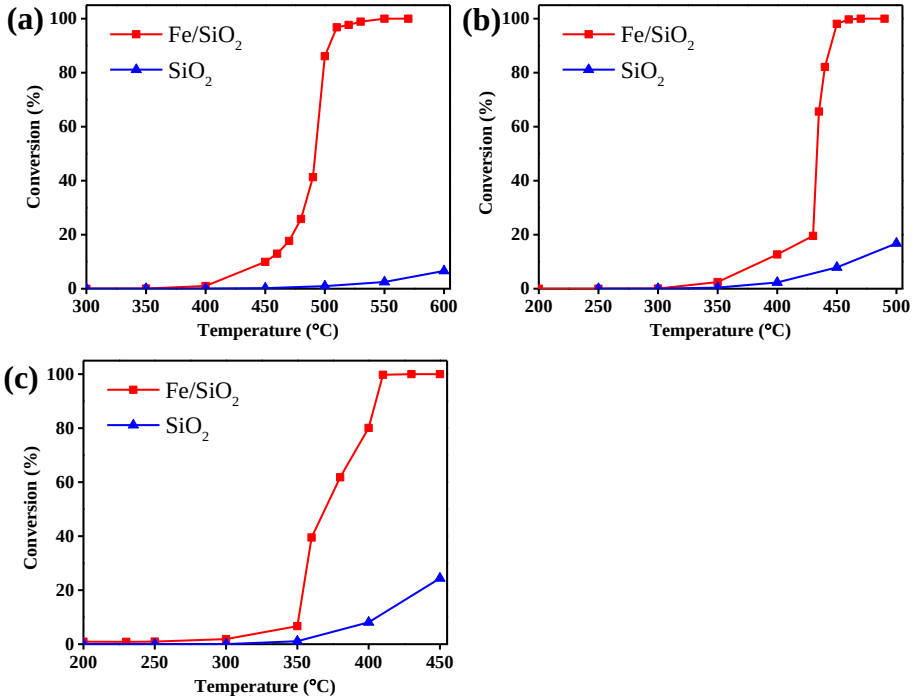

Figure S2. Comparison of Fe/SiO_2 and SiO_2 activity on CO oxidation with different $CO:O_2$ molar ratios of (a) 1:1, (b) 1:5, and (c) 1:10.

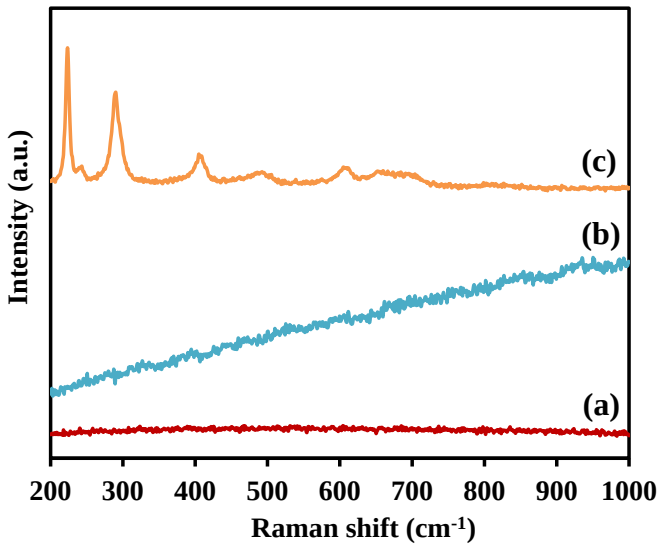

Figure S3. Raman spectra of (a) SiO_2, (b) as-prepared Fe/SiO_2, and (c) Fe/TiO_2 catalyst after 300 hr reaction.

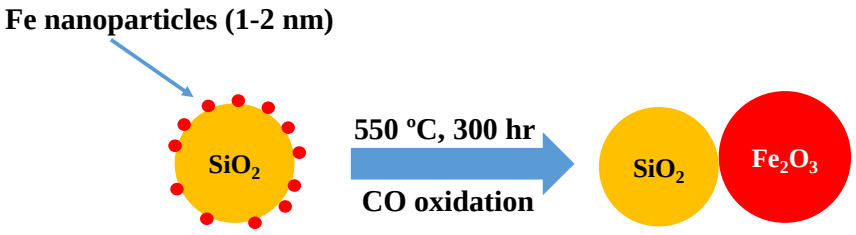

Figure S4. Scheme of Fe nanoparticles aggregation during CO oxidation long-term stability test over Fe/SiO_2 catalyst.

Table S1. BET surface areas of SiO_2 NPs and Fe/SiO_2 samples.

Sample	Surface area, m^2/g
SiO_2	143
As-prepared Fe/SiO_2	95
Fe/SiO_2 after 4 cycles of CO oxidation reaction	97
Fe/SiO_2 after 300 hr of CO oxidation reaction	122

Table S2. Comparison of long-term stability of different catalysts for CO oxidation.

Sample	Temperature, °C	Time, hr	Decrease of CO conversion, %	References
Fe/SiO_2	**550**	**>300**	**0**	**This work**
Pd/graphene	120	24	0	Li et al.[3]
$Au@CeO_2$	120	70	0	Qi et al.[4]
Pd-Au alloy	80	10	2	Xu et al.[5]
Nanoporous Au	30	24	4	Xu et al.[6]
$Au-Cu/TiO_2$	20	24	10	Sandoval et al.[7]
Co_3O_4 (LCP-300)	25	9	20	Wang et al.[8]
Au/Zeolite Y	25	70	27	Chen et al.[9]
$Au-Ir/TiO_2$-S	23	20	60	Gómez-Cortés et al.[10]

References

(1) Patel, R. L.; Jiang, Y.-B.; Liang, X. Highly porous titania films coated on sub-micron particles with tunable thickness by molecular layer deposition in a fluidized bed reactor. *Ceramics International* **2015,** *41*, 2240-2246.

(2) Wang, X.; Zhao, H.; Wu, T.; Liu, Y.; Liang, X. Synthesis of highly dispersed and highly stable supported Au–Pt bimetallic catalysts by a two-step method. *Catalysis Letters* **2016,** *146*, 2606-2613.

(3) Li, Y.; Yu, Y.; Wang, J.-G.; Song, J.; Li, Q.; Dong, M.; Liu, C.-J. CO oxidation over graphene supported palladium catalyst. *Applied Catalysis B: Environmental* **2012,** *125*, 189-196.

(4) Qi, J.; Chen, J.; Li, G.; Li, S.; Gao, Y.; Tang, Z. Facile synthesis of core–shell Au@CeO_2 nanocomposites with remarkably enhanced catalytic activity for CO oxidation. *Energy & Environmental Science* **2012,** *5*, 8937-8941.

(5) Xu, J.; White, T.; Li, P.; He, C.; Yu, J.; Yuan, W.; Han, Y.-F. Biphasic Pd−Au alloy catalyst for low-temperature CO oxidation. *Journal of the American Chemical Society* **2010,** *132*, 10398-10406.

(6) Xu, C.; Su, J.; Xu, X.; Liu, P.; Zhao, H.; Tian, F.; Ding, Y. Low temperature CO oxidation over unsupported nanoporous gold. *Journal of the American Chemical Society* **2007,** *129*, 42-43.

(7) Sandoval, A.; Louis, C.; Zanella, R. Improved activity and stability in CO oxidation of bimetallic Au–Cu/TiO_2 catalysts prepared by deposition–precipitation with urea. *Applied Catalysis B: Environmental* **2013,** *140*, 363-377.

(8) Wang, Y.-Z.; Zhao, Y.-X.; Gao, C.-G.; Liu, D.-S. Origin of the high activity and stability of Co_3O_4 in low-temperature CO oxidation. *Catalysis Letters* **2008,** *125*, 134-138.

(9) Chen, Y.-H.; Mou, C.-Y.; Wan, B.-Z. Ultrasmall Gold Nanoparticles Confined in Zeolite Y: Preparation and Activity in CO Oxidation. *Applied Catalysis B: Environmental* **2017**.

(10) Gómez-Cortés, A.; Díaz, G.; Zanella, R.; Ramírez, H.; Santiago, P.; Saniger, J. M. Au−Ir/TiO_2 prepared by deposition precipitation with urea: improved activity and stability in CO oxidation. *The Journal of Physical Chemistry C* **2009,** *113*, 9710-9720.

VIII. SUPPORTED IRON SINGLE ATOMS SYNTHESIZED VIA ATOMIC LAYER DEPOSITION

Xiaofeng Wang,[1] Tianpin Wu,[2] Lu Ma,[2] Ye Jin,[1] and Xinhua Liang,[1,*]

[1] Department of Chemical and Biochemical Engineering, Missouri University of Science and Technology, Rolla, MO 65409, United States

[2] X-Ray Science Division, Advanced Photon Source, Argonne National Laboratory, 9700 S. Cass Ave., Argonne, Illinois, 60439, United States

ABSTRACT

Recently, supported single-atom materials attracted increasing attention due to their unique properties, but the limitation of supports is a main challenge to restrict their applications. Here, we report a general strategy to synthesize Fe single-atom materials on various substrates (e.g., multi-walled carbon nanotubes, SiO_2, and TiO_2) by atomic layer deposition (ALD) through optimization of ferrocene (Fe precursor) dose time and the number of ALD cycles. The formation of Fe single atoms was verified by HAADF-STEM and XAS analysis. One application of Fe single atoms is used as catalysts. The photocatalytic activity of Fe/TiO_2 catalysts was evaluated based on the degradation of methylene blue (MB) solution under UV light. The photocatalysis experiment demonstrates that TiO_2 nanoparticles deposited with 2 cycles of Fe ALD showed the highest activity and had a more than six-fold photocatalytic activity enhancement over pure TiO_2 for the degradation of MB. This universal method, optimized Fe ALD, expands the potential applications of Fe single atoms on different substrates.

1. INTRODUCTION

Recently, metal single-atom materials have become the forefront of international scientific research within the field of a new hot spot due to their unique properties and great potential in a variety of applications, especially in catalysis [1-7]. However, single atoms are too mobile on supports, since the surface free energy of metal increases dramatically when the metal particle size reduces to single-atom level [1]. Thus, the metal single atoms are easy to sinter and aggregate during drying or calcination in the synthesis process. It is a main challenge to prepare single-atom materials by traditional methods, including sol-gel and coprecipitation methods.

During the past few years, some studies have focused on synthesis of single-atom materials, and several new methods have been reported; these include taking advantage of the unique properties of supports (e.g., photocatalysis of TiO_2 and defects of graphene) [5, 7-10], and enhancing the metal-support interactions (e.g., Pt-CeO_2, Pd-C_3N_4, and Au-zeolite) [6, 11, 12]. In these methods, specific substrates are needed to be chosen, since strong interaction between metal single atoms and substrates is needed to prevent moving of single atoms on the substrates during preparation. Thereby, though most of these single-atom catalysts presented excellent catalytic performance in various applications, the specific supports used in these methods become a limitation to expand their applications. Moreover, although some reports have been published, few of them focused on synthesis and applications of transition metal (e.g., Fe, Co and Ni) single-atom materials [3, 10, 13, 14].

Herein, we report a general atomic layer deposition (ALD) strategy to deposit well dispersed Fe single atoms on various substrates (e.g., multi-walled carbon nanotubes (MWCNTs), SiO_2, and TiO_2). ALD is a surface controlled layer-by-layer gas phase coating process based on self-limiting surface reactions [15]. Pt and Pd single-atom catalysts have been deposited on graphene successfully using ALD [8, 9]. In this study, through optimizing dose time of ferrocene ($Fe(Cp)_2$, precursor of Fe) and the number of Fe ALD cycles, we deposited Fe single atoms on different supports via Fe ALD. All prepared Fe samples are named and listed in Table S1. The formation of Fe single atoms was verified by X-ray absorption spectroscopy (XAS) and high-angle annular dark-field scanning transmission electron microscopy (HAADF-STEM). The photocatalytic activity of Fe/TiO_2 catalysts was evaluated by photocatalytic degradation of methylene blue (MB), as one application example of Fe/TiO_2. The results showed that 2 cycles of Fe ALD deposited TiO_2 catalyst presented the highest activity and had a more than six-fold enhancement of photocatalytic activity over pure anatase TiO_2 nanoparticles (NPs).

2. RESULTS

2.1. PREPARATION OF FE SINGLE ATOMS

Firstly, different cycles (2-8 cycles) of Fe ALD were deposited on 3 g of MWCNTs in a fluidized bed reactor (Figure S1) using ferrocene ($Fe(Cp)_2$) and H_2 as precursors (all samples labeled in Table S1). The dose time of $Fe(Cp)_2$ was 300 s. As shown in Figure 1a, there is no Fe NPs observed through high resolution transmission electron microscopy (HRTEM) for 8c-Fe/MWCNTs with 0.36 wt.% Fe loading

determined by ICP-AES (Figure S2a). However, HAADF-STEM image presented that some bright dots of atomic size scattered on MWCNTs, highlighted by the red circles in Figure 1b. Each dot represented an individual Fe atom, which proved that Fe single atoms were deposited on MWCNTs successfully. Then, 3 and 10 cycles of Fe ALD were applied on 3 g of SiO_2 NPs, respectively, using the same dose time (300 s) of $Fe(Cp)_2$. The Fe content was 0.14 wt.% and 0.57 wt.% in 3c-Fe/SiO_2 and 10c-Fe/SiO_2 samples, respectively (Figure S2b). As presented in Figure 1c, there is also no Fe NPs observed on SiO_2 NPs after 10 cycles of Fe ALD, which indicated the formation of Fe single atoms on SiO_2 NPs. In contrast, when the $Fe(Cp)_2$ dose time increased to 600 s, Fe NPs were formed on SiO_2 NPs after only 5 cycles of Fe ALD, and the average particle size of Fe NPs was around 1.5 nm, as shown in Figure 1d. These results indicated that Fe single atoms would form with short $Fe(Cp)_2$ dose time, but if the dose time was extended, Fe NPs would form on the substrates instead of single atoms. This could be explained that when more $Fe(Cp)_2$ molecules entered the ALD reactor with longer Fe precursor dose time, there was a higher possibility of the formation of Fe NPs in each Fe ALD cycle, which could be changed from Fe single atoms. So $Fe(Cp)_2$ dose time played an important role in the formation of Fe single atoms during the ALD process.

Fe single atoms were also deposited on TiO_2 via ALD to prove that Fe ALD is a universal method to synthesize Fe single-atom materials on various substrates. 1-25 cycles of Fe ALD were applied on TiO_2 NPs with 300 s of $Fe(Cp)_2$ dose time. As shown in Figure S3, no Fe NPs on TiO_2 was observed in HRTEM image for 5c-Fe/TiO_2 sample with 0.49 wt.% of Fe loading (Figure S2c). In order to verify the Fe single-atom structure of Fe/TiO_2 samples, XAS analysis was applied. As shown in Figure 2a, the Fe K-edge of

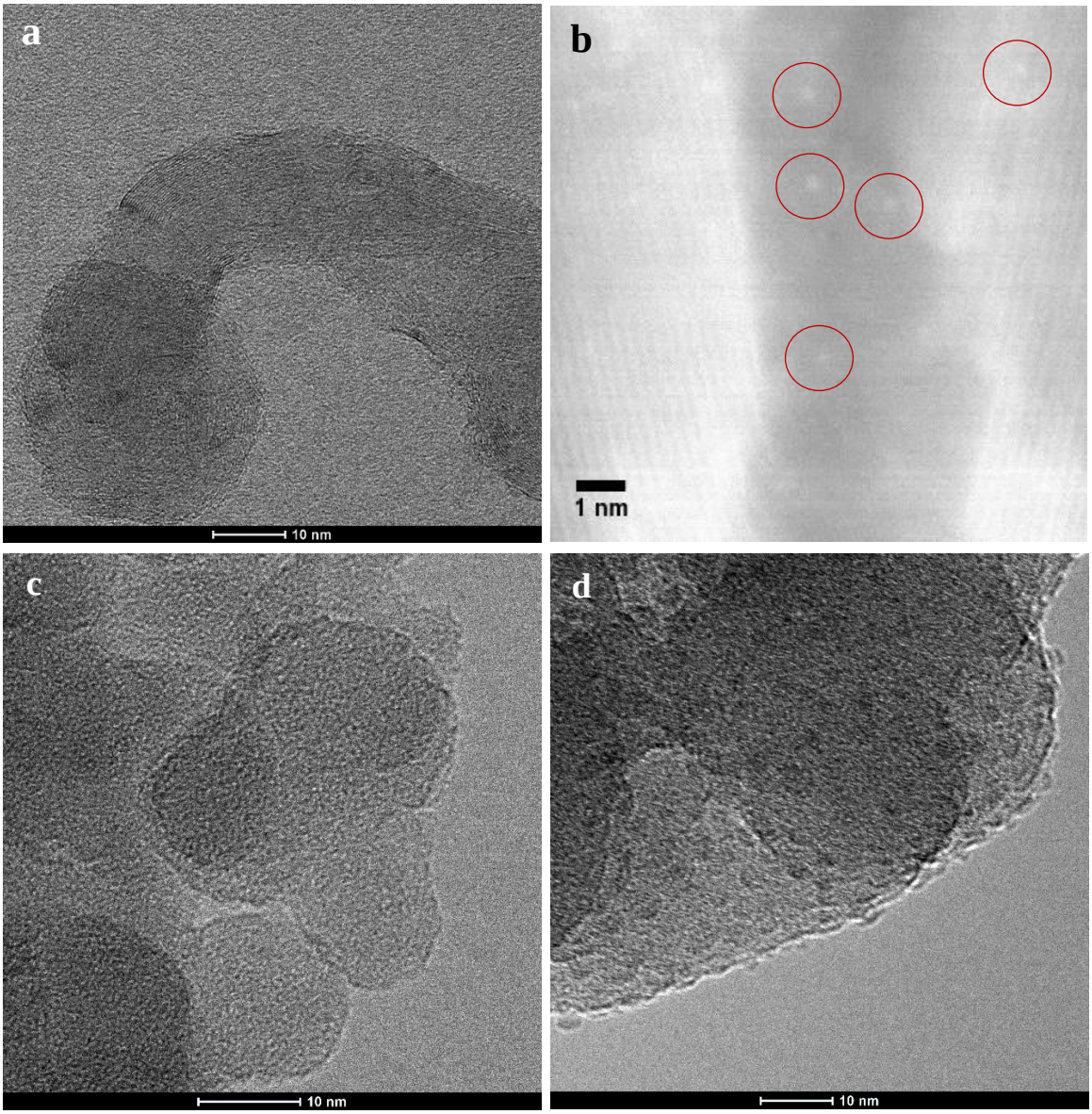

Figure 1. TEM/STEM analysis for Fe/MWCNTs and Fe/SiO_2 samples. (a) HRTEM image and (b) HAADF-STEM image of 8c-Fe/MWCNTs sample, and HRTEM images of (c) 10c-Fe/TiO_2 and (d) 5c-Fe/TiO_2-600s samples.

X-ray absorption near edge structure spectroscopy (XANES) in 2c-Fe/TiO_2 and 5c-Fe/TiO_2 samples exhibited a near-edge structure similar to that of the Fe_2O_3, but it was very different from those of Fe foil and FeO, indicating that Fe were single atoms and oxidized upon air exposure. After fitting and calculating, both two samples were oxidized

to the extent of a mixture of 90% Fe^{3+} and 10% Fe^{2+} (Table S2). Extended X-ray absorption fine structure spectroscopy (EXAFS) of the Fe K-edge shows that there was only one notable peak in the region of 1 to 2 Å from the Fe-O contribution, and no peak in the region of 2 to 3 Å from the Fe-Fe contribution, confirming the sole presence of dispersed Fe atoms in both 2c-Fe/TiO_2 and 5c-Fe/TiO_2 samples (Figure 2b). We believe that the Fe in 1c-Fe/TiO_2 sample, with lower Fe loading, should also be single atoms.

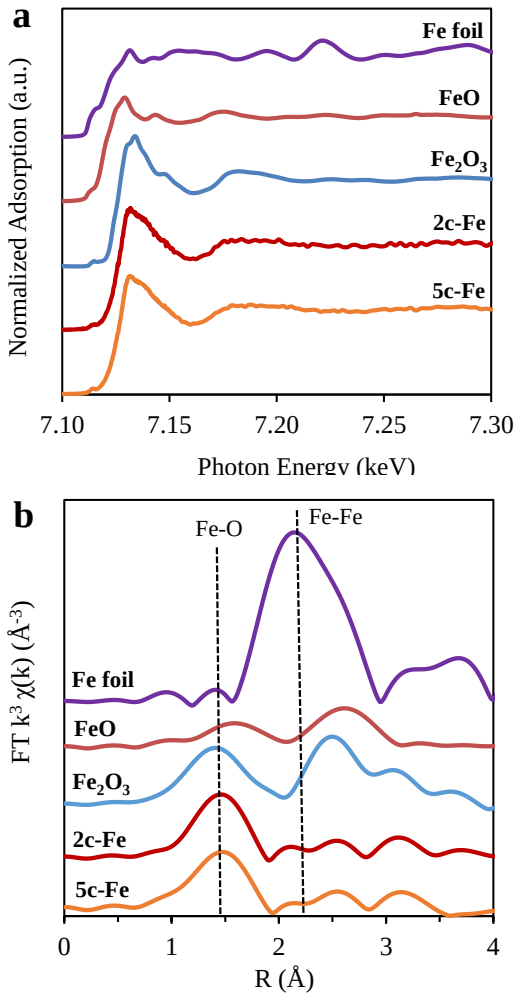

Figure 2. XAS analysis for Fe/TiO_2. (a) Fe K-edge XANES (7.0-7.7 keV) and (b) Fourier transformed (FT) k^3-weighted χ(k)-function of EXAFS spectra of 2c-Fe/TiO_2 and 5c-Fe/TiO_2 samples in comparison to Fe foil, FeO, and Fe_2O_3.

Figures 3a-b present that there is still no Fe NPs showed for 25c-Fe/TiO_2 samples even the Fe loading was as high as 3.5 wt.% (Figure S2c). However, based on element mapping (Figures 3c-e), the signal of Fe was very strong, which indicates that Fe formed clusters or films, instead of single atoms, on the TiO_2 NPs after 25 cycles of Fe ALD. No Fe observed from HRTEM images could be due to the fact that the contrast between Fe and Ti was not obvious in TEM analysis, since they have very close molecular weights. It indicates that Fe formed single atoms on TiO_2 NPs first, and then they became clusters or films gradually with the increase of the number of Fe ALD cycles. In the first few ALD cycles, $Fe(Cp)_2$ entered the ALD reactor, reacted with hydroxide groups on the TiO_2 and formed single atoms; then in the subsequent Fe ALD cycles, more $Fe(Cp)_2$ molecules reacted with hydroxide groups on TiO_2, and NPs or clusters formed. Thus, except for $Fe(Cp)_2$ dose time, controlling the number of Fe ALD cycles is another important factor to prepare Fe single atoms. It is also noted that the Fe content in the Fe/TiO_2 particles increased almost linearly with an increase in the number of ALD cycles after 25 cycles of Fe ALD, which indicated that the Fe deposition was uniform in every cycle (Figure S2c).

ALD is a surface controlled process based on self-limiting surface reactions. Through making use of the unique advantage of ALD, Fe single atoms deposited on MWCNTs, SiO_2, and TiO_2 by controlling the $Fe(Cp)_2$ dose time and the number of ALD cycles. Therefore, Fe ALD has been demonstrated to be a general method and can be used in preparation of Fe single-atom materials on various supports, including inorganic non-metallic materials, metal oxides, and carbon materials. Moreover, ALD is a potential way to be used in preparation of other metal single-atom materials (e.g., Ni and Co) on various substrates.

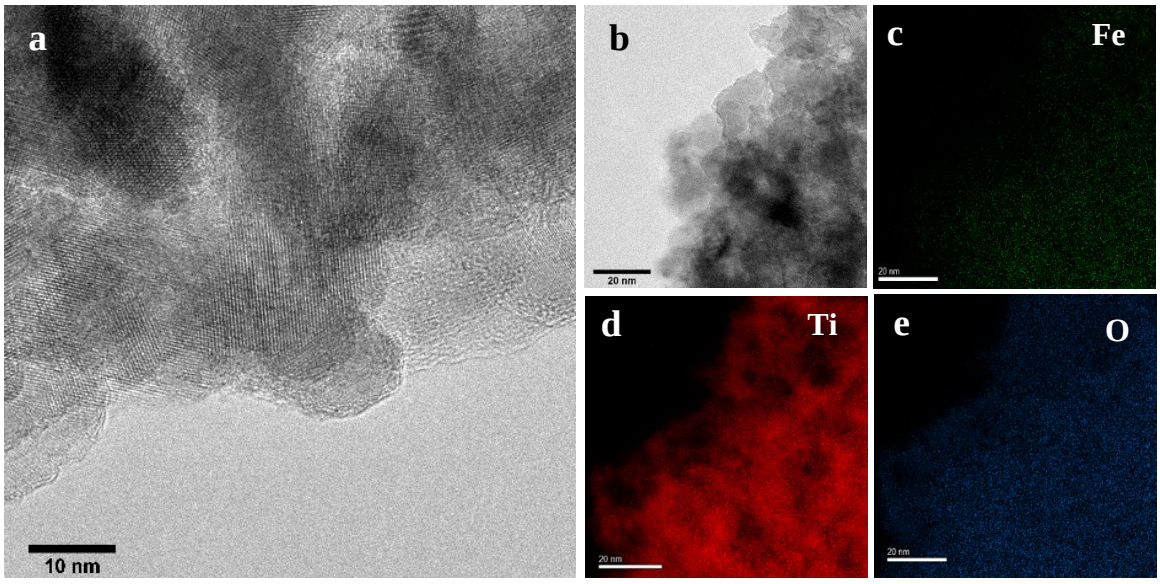

Figure 3. Electron microscopy analysis of Fe/TiO_2 sample. HRTEM images of 25c-Fe/TiO_2 sample at (a) high and (b) low magnifications, (c-e) EDX mappings of 25c-Fe/TiO_2 sample.

2.2. PHOTOCATALYTIC PERFORMANCE OF FE/TIO_2

The photocatalytic activity of TiO_2 and Fe/TiO_2 catalysts were evaluated in terms of degradation of MB under irradiation of UV light. Figures 4 and S4 summarize the effect of Fe ALD cycles on degradation efficiencies of MB solution as a function of irradiation. The results showed that the concentration of MB decreased by 78% over pure TiO_2 for 1 hr of UV irradiation, and the photodegradation efficiency of Fe decorated TiO_2 is higher than that of untreated TiO_2. 2c-Fe/TiO_2 was higher than that of 1c-Fe/TiO_2, but the efficiency of Fe/TiO_2 catalysts with more Fe ALD cycles (5-25) decreased dramatically and was lower than that of 1c-Fe/TiO_2 and 2c-Fe/TiO_2 catalysts. It was found that the TiO_2 catalyst containing 0.16 wt.% Fe (0.21 at.%) enhanced the photocatalytic activity at most and it was the optimal amount of Fe for degradation of MB in this study. However, the optimal Fe amount in this study is not consistent with

that in literatures, which reported that the optimal Fe loading was around 0.5 at.% [16, 17], which could be due to the different preparation methods for Fe/TiO_2 samples. Higher optimal Fe loading (0.5 at.%) was needed via Fe doping method because some Fe ions inserted into the matrix interior of TiO_2 particles and cannot work as e^-/h^+ pair traps. Instead, isolated Fe atoms were only deposited on the surface of TiO_2 particles via ALD and thereby the Fe optimal content was much lower in this study.

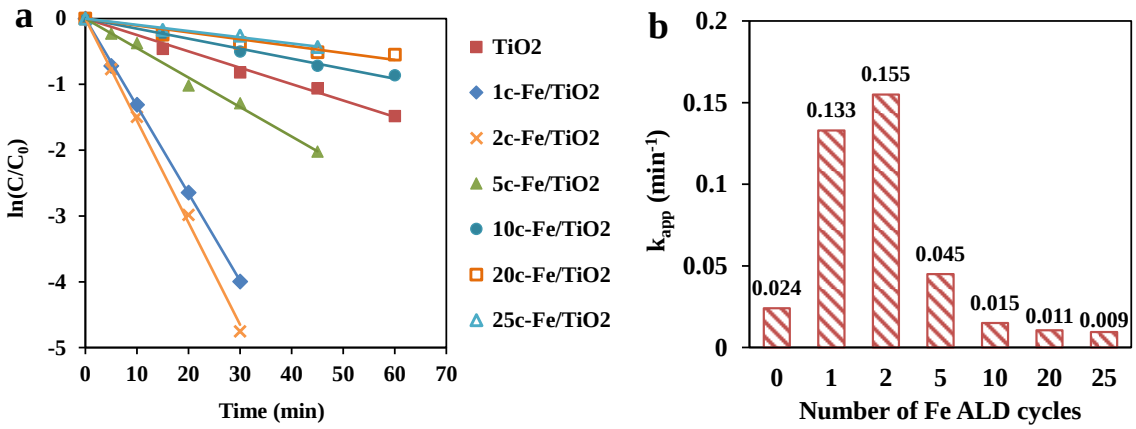

Figure 4. Photocatalytic performance of TiO_2 and Fe/TiO_2 catalysts. (a) Relative concentration of MB and (b) apparent kinetic constants (k_{app}, min^{-1}) as a function of Fe/TiO_2 catalysts with different number of Fe ALD cycles.

As shown in Figure 4, after Fe ALD deposition, the Fe/TiO_2 samples with 1-5 Fe ALD cycles showed higher photocatalytic efficiency than TiO_2, and the apparent kinetic constants (k_{app}) of 2c-Fe/TiO_2 sample reached a maximum value (0.155 min^{-1}), and its activity exceeded that of pure TiO_2 by a factor of more than six times. Liu and Chen [18] has reported only 1.62 times increase of photocatalytic activity as compared to the undoped TiO_2 for a similar system. In addition, Pt ALD and CeO_2 ALD have been reported to be applied for improvement of TiO_2 photoactivity, and it showed only 3 and

3.3 times increase of photocatalytic activity as compared to the pure TiO_2 at most, respectively [19, 20]. More importantly, Fe is much cheaper and more economic for large-scale production compared to Pt. Thus, in comparison with other methods, Fe ALD is one promising strategy to enhance Fe/TiO_2 photocatalytic performance (Table S3). The much higher photoactivity of 2c-Fe/TiO_2 than that of TiO_2 in this work can be due to the following several factors.

Firstly, Fe^{3+} ions could improve the intensity of absorption in the UV-visible light region and made a red shift in the band gap transition of 2c-Fe/TiO_2 sample. This can induce more photo-generated e^- and h^+ to participate in the photocatalytic reactions [21]. In order to verify the hypothesis, UV-visible diffuse reflectance spectra (DRS) for pure TiO_2 and Fe/TiO_2 catalysts were recorded and the band gap was calculated. As presented in Figure 5a, the pure TiO_2 sample showed strong photoabsorption only at wavelengths shorter than 400 nm, and the absorption edge increased with the increasing cycles of Fe ALD. The UV-visible spectroscopic measurements and subsequent Kubelka-Munk reflection plots for TiO_2 and Fe-TiO_2 samples are shown in Figures S5 and S6. Figures 5b show that the band gap energy values decreased from 3.22 to 3.03 eV along with the increase of the number of Fe ALD cycles from 0 to 5. Increasing the Fe content in TiO_2 shifts the band gap energy toward longer wavelengths due to the creation of trap levels between the conduction band and valence band of TiO_2 [22, 23]. More cycles of Fe ALD would provide more e^-/h^+ pair trap centers and thereby lead to a lager reduction in the band gap. At the same time, the color of the samples changed from white to black along with the increase of Fe ALD cycles (Figure S7). It could be explained that the deposition of Fe on TiO_2 changed the absorption edge of the Fe/TiO_2 samples in the UV-visible light

region, so the color of the samples altered, which is consistent with UV-vis DRS results. Similar phenomenon was observed in CeO_2-coated TiO_2 samples prepared by CeO_2 ALD [20].

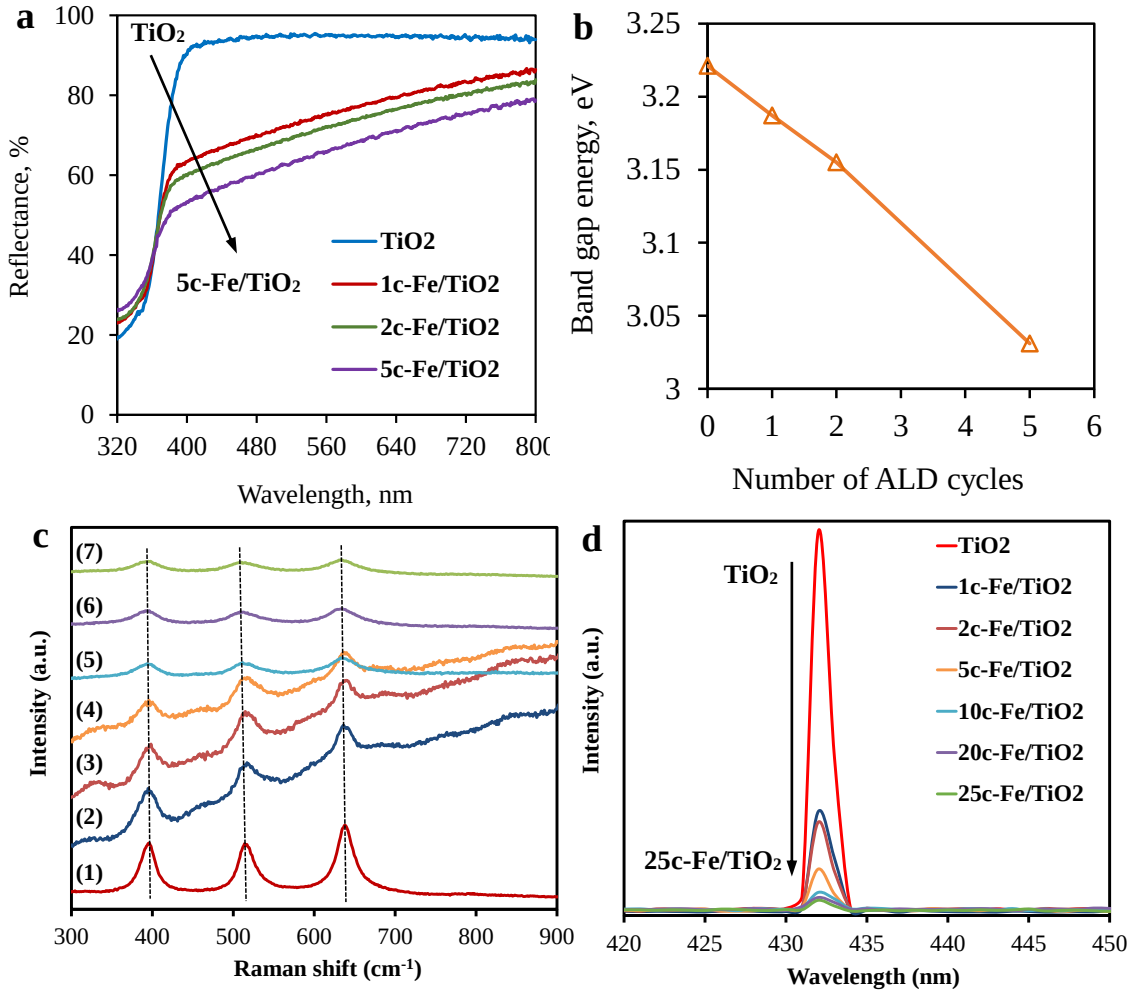

Figure 5. Characterizations of Fe/TiO_2 photocatalysts. (a) UV-visible reflectance spectra and (b) the band gap energy of TiO_2 and Fe/TiO_2 samples. (c) Raman spectra of (1) TiO_2, (2) 1c-Fe/TiO_2, (3) 2c-Fe/TiO_2, (4) 5c-Fe/TiO_2, (5) 10c-Fe/TiO_2, (6) 20c-Fe/TiO_2, and (7) 25c-Fe/TiO_2. (d) Photoluminescence spectra of TiO_2 and Fe/TiO_2 samples excited at 280 nm.

Secondly, Fe^{3+} can work as an e^-/h^+ pair traps to suppress the recombination of e^-/h^+ pairs and thus enhance lifetimes of e^- and h^+, which can improve the photocatalytic activity of Fe/TiO_2 samples as well. In order to investigate the recombination rate of e^-/h^+ pairs in all catalysts, Raman and photoluminescence (PL) were performed. As shown in Figure 5c, all samples showed three major Raman bands at 397, 517 and 640 cm^{-1}, which are attributed to the Raman-active modes of TiO_2 anatase phase with the symmetries of B1g, A1g, and Eg, respectively [24]. Compared with the uncoated TiO_2 sample, all these three bands of Fe/TiO_2 samples were weak due to the deposition of Fe. But there is no band corresponding to Fe observed for all Fe/TiO_2 samples. It should be attributed to the low content of Fe. It is also noted that the baseline of 1c-Fe/TiO_2, 2c-Fe/TiO_2, and 5c-Fe/TiO_2 kept increasing from 300 to 1000 cm^{-1}, which resulted from fluorescence effect after Fe deposition on TiO_2 NPs. In contrast, the baseline of 10c-Fe/TiO_2, 20c-Fe/TiO_2, and 25c-Fe/TiO_2 did not increase, and it could be due to the fact that Fe formed clusters or films and prevented fluorescence phenomenon with a large number of Fe ALD coating cycles, which is consistent with element mapping analysis (Figure 3). PL analysis of all prepared TiO_2 and Fe/TiO_2 samples was carried out to further study the fluorescence effect and recombination rate of e^-/h^+ pairs (Figure 5d). The only peak at 432 nm corresponds to the reflection from anatase phase of TiO_2, and no other peak was presented corresponding to Fe in the wavelength of 300-600 nm, which could be due to the amorphous structure of Fe in the samples. But with an increase in the number of Fe ALD cycles, the PL intensity decreased greatly, which indicated that the separation efficiency of e^-/h^+ pairs improved for Fe/TiO_2 samples and it could result from the increase of the number of trap centers [25]. In other words, more Fe^{3+} ions played an

important role to separate e^-/h^+ pairs and reduce the recombination rate. However, with the increase of Fe content in samples, Fe^{3+} ions can serve not only as the e^-/h^+ traps but also as a recombination center. In this study, compared to 2c-Fe/TiO_2 catalyst, the photocatalytic activity decreased greatly when the Fe concentration increased. It could be attributed to the fact that more Fe^{3+} ions played a role as e^-/h^+ recombination centers and improved the e^-/h^+ recombination rate, which led to the reduction of the k_{app} values. In addition, with more Fe ALD cycles applied on TiO_2, Fe formed clusters or films, as shown in Figure 3, and they hindered the samples to utilize UV light and could not generate enough e^- and h^+ for MB degradation. Thus, the control of Fe loading plays a key role to affect the properties of Fe/TiO_2 samples.

Moreover, the atomic size and uniform dispersion of Fe on TiO_2 surface is another important factor influencing photocatalytic efficiency. Fe ALD took full advantage of the high surface area of TiO_2 and Fe single atoms (~0.2 nm) were highly dispersed on TiO_2. Thus, Fe^{3+} ions worked as e^-/h^+ traps as many as possible in Fe/TiO_2 samples, which led to the fact that the recombination of e^- and h^+ decreased and the photocatalytic activity improved drastically. In addition, according to XRD analysis, the TiO_2 in all samples remained anatase structure after Fe ALD and no peak corresponded to the reflections from Fe, which indicates that the crystal structure did not affect the photocatalytic activity for 2c-TiO_2 sample (Figure S8).

At last, the defect sites on the surface of TiO_2 would be decorated by Fe single atoms because Fe atoms preferred to deposit and grow on defect sites during the ALD process based on ALD mechanism [26], which can be called “defect healing”. As reported before [27], a large surface area can enhance the photocatalytic performance of

samples. However, powders with a large surface area are usually associated with large amounts of crystalline defects, which favor the recombination of photo-generated e^- and h^+ leading to a poor photoactivity [28, 29]. In the Fe ALD process, Fe was deposited on defect sites preferentially and overcame this problem. All factors mentioned above worked collectively and resulted in improved photocatalytic activity of 2c-Fe/TiO_2.

3. DISCUSSION

Fe single atoms were deposited on MWCNTs, SiO_2, and TiO_2 NPs by Fe ALD. HAADF-STEM and XAS analysis proved the existence of Fe single atoms on MWCNTs and TiO_2 NPs, respectively. Ferrocene dose time and the number of ALD cycles are two dominating factors in the preparation of Fe single atoms on substrates. 2c-Fe/TiO_2 catalyst showed the highest photocatalytic activity and had a more than six-fold photocatalytic activity enhancement over pure TiO_2 for the degradation of MB due to the fact that Fe^{3+} ions played a role as e^-/h^+ pair traps and consequently reduced e^-/h^+ pair recombination rate. The uniform dispersion of Fe and the effect of “defect healing” were another two factors to enhance the activity of samples. Moreover, the ALD method can be expanded to synthesize other metal single-atom materials without supports limitation through optimization of corresponding precursor dose time and the number of ALD cycles.

4. METHODS

4.1. CATALYSTS PREPARATION

Fe single atoms were deposited on MWCNTs (US Nano Inc), SiO_2 NPs (20-30 nm, US Nano Inc), and TiO_2 NPs (DT 51, 100% anatase, ~80 m^2/g, Cristal Inc) by ALD using ferrocene and hydrogen (H_2, 99.9%, Airgas) as precursors in a fluidized bed reactor, as schematically shown in Figure S1. The reactor was described in detail elsewhere [30, 31]. All of the chemicals were used as received without any treatment. For a typical cycle, 5 g of substrate were loaded into the reactor. The reaction temperature was 400 ºC. Before a reaction, the substrates were degassed at 150 °C for 10 hr. During the ALD process, the solid ferrocene (~ 0.2 g) was loaded into a heated bubbler (115 ºC) and carried by nitrogen (N_2, 99.9% Airgas) into the reactor. $Fe(Cp)_2$ and H_2 were fed separately through a distributor plate. The particle substrates were fully fluidized with the gas flow rate controlled by mass flow controllers. The reactor was also subjected to vibration from vibrators to improve the quality of particle fluidization during the ALD coating process [32, 33]. N_2 was used as flush gas to remove unreacted precursors and any byproducts during the reaction. A typical coating cycle involved the following steps: ferrocene dose, N_2 purge, evacuation; H_2 dose, N_2 purge, evacuation.

4.2. CHARACTERIZATIONS

The Fe mass fractions of prepared Fe samples with different Fe ALD cycles were measured by ICP-AES. The crystal structure of TiO_2 was detected by XRD. The Fe supported on MWCNTs, SiO_2, and TiO_2 NPs were directly observed by FEI Tecnai F30

HRTEM. HAADF-STEM analysis was performed by Nion UltraSTEM 100. XAS was applied to verify the composition of Fe on the TiO_2 nanoparticles. Raman spectra of TiO_2 and Fe/TiO_2 samples were obtained using a Horiba-Jobin Yvon LabRam spectrometer. The PL spectra were recorded with a HORIBA FL3-22 spectrometer (HORIBA, Edison, NJ) to investigate the recombination of photo-generated e^-/h^+ pairs in the samples. UV–visible DRS of Fe/TiO_2 samples were obtained with a UV–visible spectrophotometer (Varian Cary 5) and $BaSO_4$ was used as an absorbance standard in the UV–visible absorbance experiment. The details of characterization are described in Supplementary Information (SI).

4.3. PHOTOCATALYTIC ACTIVITY MEASURMENT

Methylene blue (MB) solution was used to evaluate the photocatalytic activity of TiO_2 and Fe/TiO_2 particles, as described in detail previously [20]. Briefly, 0.1 g of sample was added in a 100 mL, 10 ppm MB solution. First, the suspension solution was stirred in the dark for 60 min to achieve adsorption/desorption equilibrium. Then a UV lamp was used for 360 nm UV irradiation, and ~1 mL test samples were taken from the main solution for analysis at a 664 nm wavelength at certain time intervals. The change in concentration of MB in the main solution was recorded over a period of reaction time.

ACKNOWLEDGEMENT

The authors thank Dr. Jingjing Qing at the Materials Research Center at Missouri University of Science and Technology for TEM analysis, and Katia March at LeRoy

Eyring Centerfor Solid State Science at Arizona State University for HAADF-STEM analysis. The authors also thank Naveen K. Mahenderkar and Prof. Jay A. Switzer in the Department of Chemistry for the assistance with diffuse reflectance UV-vis measurement, and Jincheng Bai and Prof. Richard Brow in the Department of Materials Science and Engineering at Missouri University of Science and Technology for the assistance with Raman and photoluminescence analysis.

REFERENCES

[1] Qiao, B., et al., Single-atom catalysis of CO oxidation using Pt_1/FeOx. *Nature Chemistry*, 2011. **3**(8): p. 634-641.

[2] Kyriakou, G., et al., Isolated metal atom geometries as a strategy for selective heterogeneous hydrogenations. *Science(Washington)*, 2012. **335**(6073): p. 1209-1212.

[3] Deng, D., et al., A single iron site confined in a graphene matrix for the catalytic oxidation of benzene at room temperature. *Science advances*, 2015. **1**(11): p. e1500462.

[4] Ding, K., et al., Identification of active sites in CO oxidation and water-gas shift over supported Pt catalysts. *Science*, 2015. **350**(6257): p. 189-192.

[5] Liu, P., et al., Photochemical route for synthesizing atomically dispersed palladium catalysts. *Science*, 2016. **352**(6287): p. 797-800.

[6] Jones, J., et al., Thermally stable single-atom platinum-on-ceria catalysts via atom trapping. *Science*, 2016. **353**(6295): p. 150-154.

[7] Cheng, N., et al., Platinum single-atom and cluster catalysis of the hydrogen evolution reaction. *Nature Communications*, 2016. **7**.

[8] Sun, S., et al., Single-atom catalysis using Pt/graphene achieved through atomic layer deposition. *Scientific reports*, 2013. **3**.

[9] Yan, H., et al., Single-atom Pd1/graphene catalyst achieved by atomic layer deposition: remarkable performance in selective hydrogenation of 1, 3-butadiene. *Journal of the American Chemical Society*, 2015. **137**(33): p. 10484-10487.

[10] Chen, X., et al., Highly active and stable single iron site confined in graphene nanosheets for oxygen reduction reaction. *Nano Energy*, 2017. **32**: p. 353-358.

[11] Vilé, G., et al., A stable single‐site palladium catalyst for hydrogenations. *Angewandte Chemie International Edition*, 2015. **54**(38): p. 11265-11269.

[12] Yang, M., et al., Catalytically active Au-O (OH) x-species stabilized by alkali ions on zeolites and mesoporous oxides. *Science*, 2014. **346**(6216): p. 1498-1501.

[13] Fei, H., et al., Atomic cobalt on nitrogen-doped graphene for hydrogen generation. *Nature communications*, 2015. **6**.

[14] Qiu, H.J., et al., Nanoporous graphene with single‐atom nickel dopants: An efficient and stable catalyst for electrochemical hydrogen production. *Angewandte Chemie*, 2015. **127**(47): p. 14237-14241.

[15] Puurunen, R.L., Surface chemistry of atomic layer deposition: a case study for the trimethylaluminum/water process. *Journal of Applied Physics*, 2005. **97**(12): p. Article No. 121301.

[16] Li, Z., et al., Effect of Fe-doped TiO_2 nanoparticle derived from modified hydrothermal process on the photocatalytic degradation performance on methylene blue. *Journal of Hazardous Materials*, 2008. **155**(3): p. 590-594.

[17] Dukes, F.M., et al., Differing photo-oxidation mechanisms: electron transfer in TiO_2 versus iron-doped TiO_2. *Langmuir*, 2012. **28**(49): p. 16933-16940.

[18] Liu, S. and Y. Chen, Enhanced photocatalytic activity of TiO_2 powders doped by Fe unevenly. *Catalysis Communications*, 2009. **10**(6): p. 894-899.

[19] Zhou, Y., et al., Optimal preparation of Pt/TiO_2 photocatalysts using atomic layer deposition. *Applied Catalysis B: Environmental*, 2010. **101**(1): p. 54-60.

[20] Wang, X., Y. Jin, and X. Liang, Significant photocatalytic performance enhancement of TiO_2 by CeO_2 atomic layer deposition. *Nanotechnology*, 2017. **28**(50): p. Article No. 505709.

[21] Zhou, M., J. Yu, and B. Cheng, Effects of Fe-doping on the photocatalytic activity of mesoporous TiO_2 powders prepared by an ultrasonic method. *Journal of Hazardous Materials*, 2006. **137**(3): p. 1838-1847.

[22] George, S., et al., Role of Fe doping in tuning the band gap of TiO_2 for the photo-oxidation-induced cytotoxicity paradigm. *Journal of the American Chemical Society*, 2011. **133**(29): p. 11270-11278.

[23] Serpone, N., et al., Spectroscopic, photoconductivity, and photocatalytic studies of TiO_2 colloids: naked and with the lattice doped with Cr^{3+}, Fe^{3+}, and V^{5+} cations. *Langmuir*, 1994. **10**(3): p. 643-652.

[24] Cao, T., et al., Fabrication, structure, and enhanced photocatalytic properties of hierarchical CeO_2 nanostructures/TiO_2 nanofibers heterostructures. *Materials Research Bulletin*, 2010. **45**(10): p. 1406-1412.

[25] Li, G., D. Zhang, and C.Y. Jimmy, Thermally stable ordered mesoporous CeO_2/TiO_2 visible-light photocatalysts. *Physical Chemistry Chemical Physics*, 2009. **11**(19): p. 3775-3782.

[26] George, S.M., Atomic layer deposition: An overview. *Chemical Reviews*, 2010. **110**(1): p. 111-131.

[27] Zhang, D., Enhanced photocatalytic activity for titanium dioxide by co-modification with copper and iron. *Transition Metal Chemistry*, 2010. **35**(8): p. 933-938.

[28] Carp, O., C.L. Huisman, and A. Reller, Photoinduced reactivity of titanium dioxide. *Progress in solid state chemistry*, 2004. **32**(1): p. 33-177.

[29] Ohtani, B., Y. Ogawa, and S.-i. Nishimoto, Photocatalytic activity of amorphous−anatase mixture of titanium (IV) oxide particles suspended in aqueous solutions. *The Journal of Physical Chemistry B*, 1997. **101**(19): p. 3746-3752.

[30] Liang, X., et al., Biocompatible interface films deposited within porous polymers by atomic layer deposition (ALD). *ACS Applied Materials and Interfaces*, 2009. **1**(9): p. 1988-1995.

[31] Wang, X., et al., Adsorption of metal and metalloid ions onto nanoporous microparticles functionalized by atomic layer deposition. *Journal of Environmental Chemical Engineering*, 2016. **4**(4): p. 3767-3774.

[32] Patel, R.L., Y.-B. Jiang, and X. Liang, Highly porous titania films coated on sub-micron particles with tunable thickness by molecular layer deposition in a fluidized bed reactor. *Ceramics International*, 2015. **41**(2): p. 2240-2246.

[33] Wang, X., et al., Synthesis of highly dispersed and highly stable supported Au–Pt bimetallic catalysts by a two-step method. *Catalysis Letters*, 2016. **146**(12): p. 2606-2613.

SUPPLEMENTARY MATERIAL

This file includes:

1. Raman analysis
2. XRD analysis
3. Band gap calculation
4. XAS analysis

Figures S1–S8

Tables S1-S3

*Corresponding author:

E-mail: liangxin@mst.edu (Xinhua Liang)

1. Raman analysis

Raman spectra of TiO_2 and Fe/TiO_2 samples were recorded using a Horiba-Jobin Yvon LabRam spectrometer, equipped with a 17 mW He-Ne laser. Spectra were collected using a 10× objective lens over a wavenumber range of 200-1200 cm^{-1}. The reported spectra were generated from 10-20 scans of the respective wavenumber range, each taking ten seconds.

2. XRD analysis

The crystal structure of TiO_2 and Fe/TiO_2 samples was detected by X-ray diffraction (XRD) with filtered Cu Kα radiation (λ= 1.5406 Å). The scanning range was 2θ from 20º to 80º, with a scanning rate of 0.025 º/s. The Scherrer equation was applied

to estimate the average crystallite sizes of TiO_2 and Fe/TiO_2 samples: $D = \frac{K\lambda}{B\cos\theta}$, where B is the half-height width of the diffraction peak of anatase, K=0.89 is a coefficient, θ is the diffraction angle, λ is the X-ray wavelength corresponding to the Cu Kα irradiation (1.5406 Å) and D is the average crystallite size of the powder sample.

3. Band gap calculation

The UV–visible diffuse reflectance spectra (DRS) were used to evaluate the band gap of TiO_2 and Fe/TiO_2 samples by plotting $[F(R)*hv]^{1/2}$ against *hv*, where *hv* is the energy of the incident photon and F(R) is the reflection in Kubelka-Munk function [1]. The linear part of the curve was extrapolated to zero reflectance and the band gap energy was derived.

4. XAS analysis

XAS, including extended X-ray absorption fine structure spectroscopy (EXAFS) and X-ray absorption near edge structure spectroscopy (XANES), was conducted at bending magnet beamline 9-BM at the Advanced Photon Source (APS), Argonne National Laboratory. The XAS spectra were recorded in transmission mode with the ionization chamber optimized for maximum current with a linear response [2]. Spectra at the Fe K edge (7.0-7.7 keV) were acquired for the 2c-Fe/TiO_2 and 5c-Fe/TiO_2 samples. Fe foil was used to calibrate the monochromator. Standard procedures based on Athena software were used to fit the XAS data.

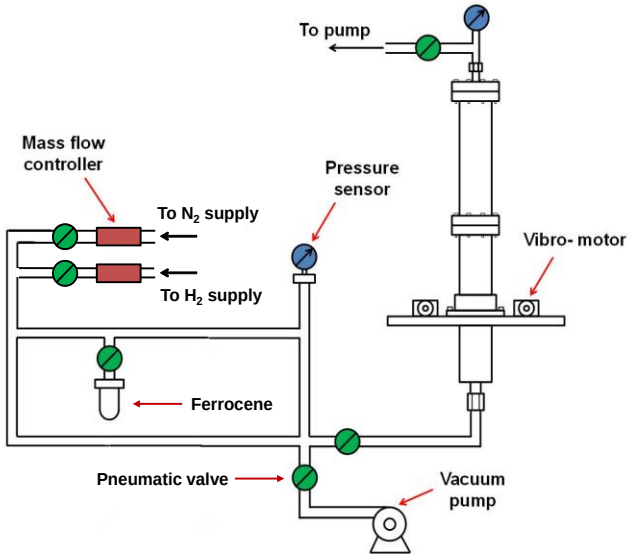

Figure S1. Schematic diagram of ALD fluidized bed reactor.

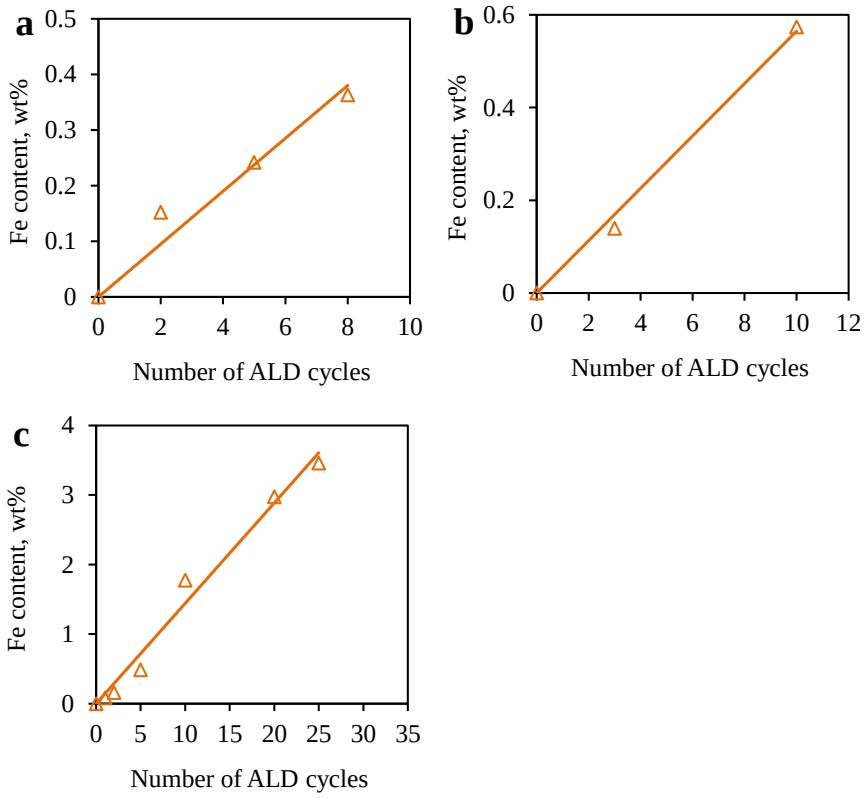

Figure S2. Fe content of (a) Fe/MWCNTs, (b) Fe/SiO_2, and (c) Fe/TiO_2 samples versus the number of Fe ALD cycles.

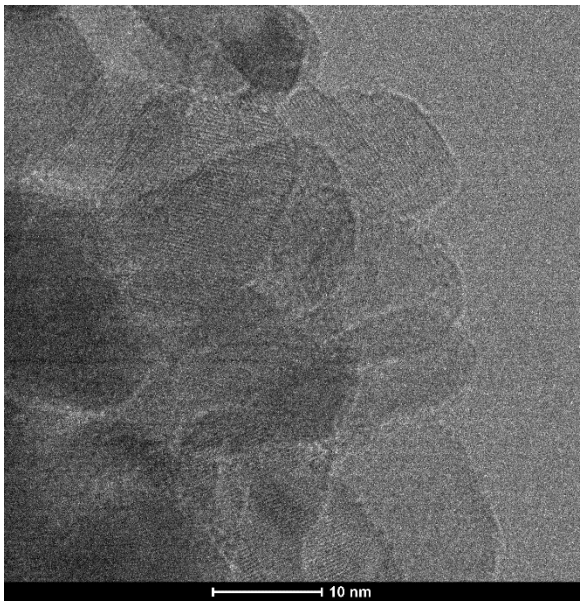

Figure S3. TEM image of 5c-Fe/TiO_2 sample.

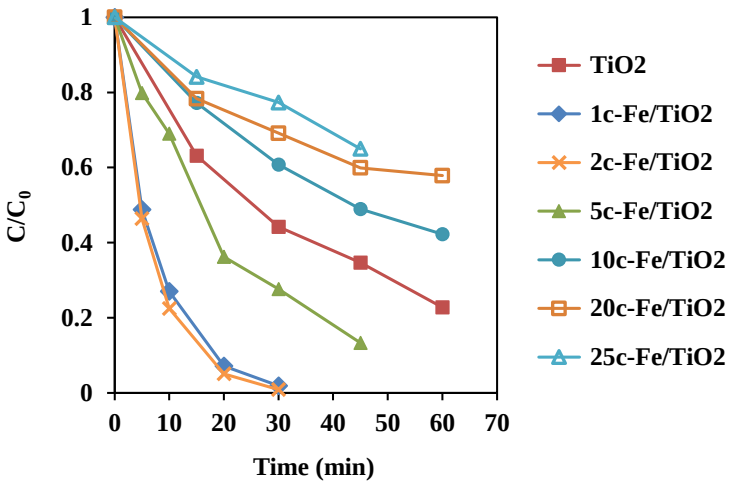

Figure S4. Methylene blue concentration as a function of UV irradiation time over different samples.

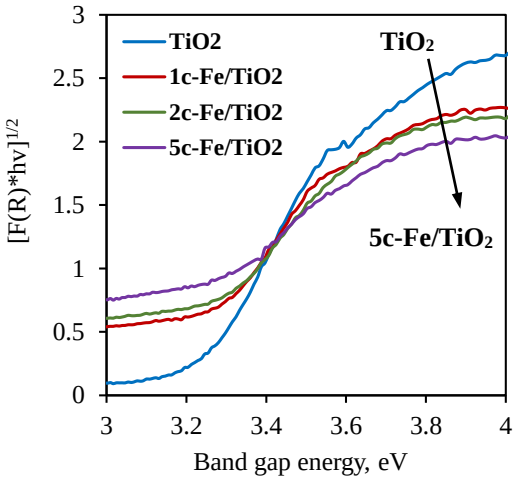

Figure S5. UV-visible spectroscopic measurements and subsequent Kubelka-Munk reflection plots for TiO_2 and Fe-TiO_2 samples.

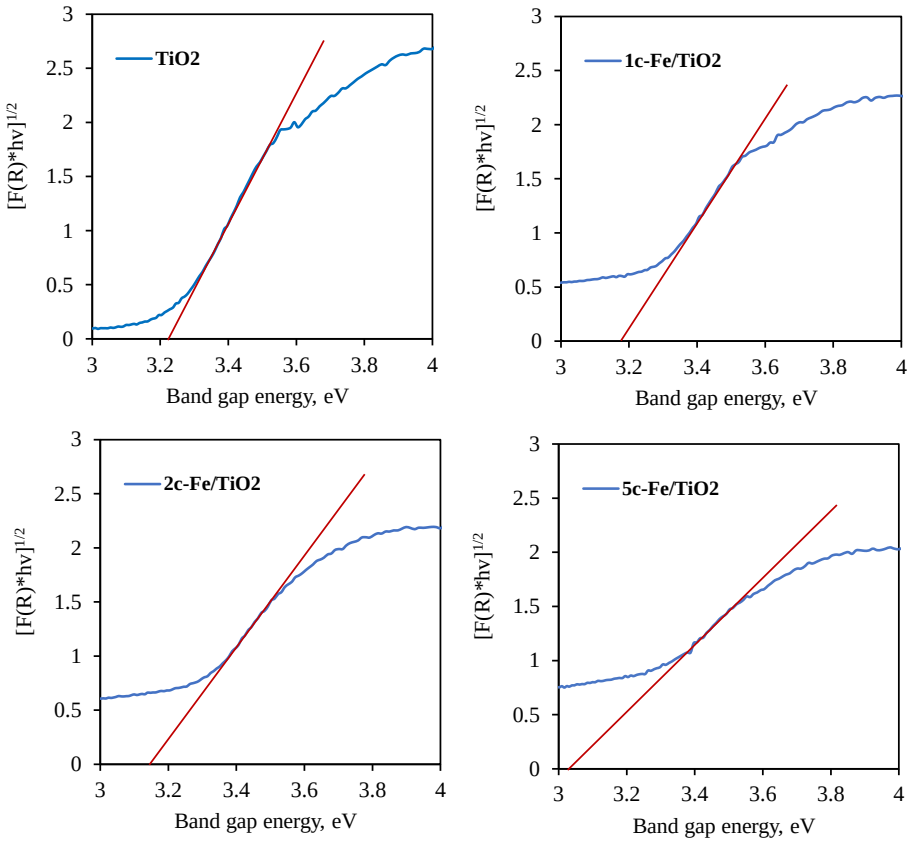

Figure S6. Band gap determination of uncoated TiO_2 nanoparticles and TiO_2 nanoparticles coated with different cycles of Fe ALD. Curved blue and red linear lines represent experimental and extrapolated data, respectively.

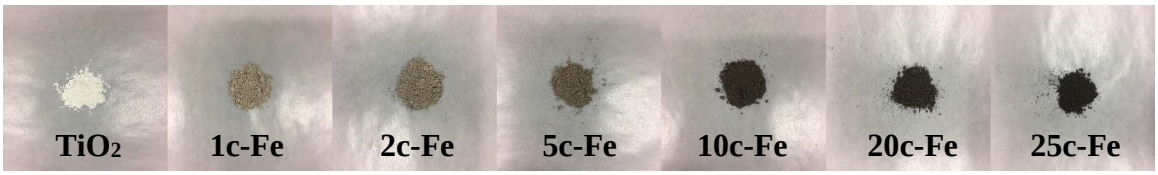

Figure S7. Images of TiO_2 and Fe/TiO_2 samples.

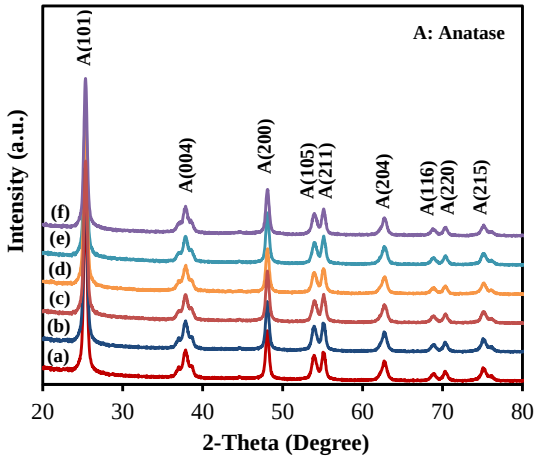

Figure S8. XRD patterns of (a) TiO_2, (b) 2c-Fe/TiO_2, (c) 5c-Fe/TiO_2, (d) 10c-Fe/TiO_2, (e) 20c-Fe/TiO_2, and (f) 25c-Fe/TiO_2.

X-ray diffraction (XRD) was used to investigate the effect of Fe deposition on the phase structure. Figure S8 displays the XRD patterns of Fe/TiO_2 samples with different number of Fe ALD cycles. There was no significant difference for all samples. The peaks at 25.3º, 37.8º, 48.1º, 53.9º, 55.2º, 62.8º, and 75.2º corresponded to the reflections from (101), (004), (200), (105), (211), (204), and (215) planes of TiO_2 in the anatase phase, respectively [3], and no rutile phase was detected for all samples. It indicates that the Fe ALD deposition did not modify the anatase phase of TiO_2 sample. In addition, there was no peak correspond to the reflections from Fe, which could be due to the ultrasmall size

of Fe on TiO_2. According to the XRD analysis, the TiO_2 crystal size was around 19 nm for all samples, which is close to the actual particle size of TiO_2 (~20 nm).

Table S1. Label of samples and sample description.

	Label of Sample	Sample description	Ferrocene dose time (s)
1	2c-Fe/MWCNTs	2 cycles of Fe ALD on MWCNTs	300
2	5c-Fe/MWCNTs	5 cycles of Fe ALD on MWCNTs	300
3	8c-Fe/MWCNTs	8 cycles of Fe ALD on MWCNTs	300
4	3c-Fe/SiO_2	3 cycles of Fe ALD on SiO_2	300
5	10c-Fe/SiO_2	10 cycles of Fe ALD on SiO_2	300
6	5c-Fe/SiO_2-600s	5 cycles of Fe ALD on SiO_2	600
7	1c-Fe/TiO_2	1 cycle of Fe ALD on TiO_2	300
8	2c-Fe/TiO_2	2 cycles of Fe ALD on TiO_2	300
9	5c-Fe/TiO_2	5 cycles of Fe ALD on TiO_2	300
10	10c-Fe/TiO_2	10 cycles of Fe ALD on TiO_2	300
11	20c-Fe/TiO_2	20 cycles of Fe ALD on TiO_2	300
12	25c-Fe/TiO_2	25 cycles of Fe ALD on TiO_2	300

Table S2. Valence state of Fe in 2c-Fe/TiO_2 and 5c-Fe/TiO_2 samples.

	Fe^0	Fe^{2+}	Fe^{3+}
2c-Fe/TiO_2	0	12.8%	87.2%
5c-Fe/TiO_2	0	14.6%	85.4%

Table S3. Comparison of the photocatalytic activity of various Fe/TiO_2 samples.

Sample	Preparation method	Pollutant	k_{app}(sample):k_{app}(pure TiO_2)[a]	References
2c-Fe/TiO_2	**ALD**	**Methylene blue**	**6.46**	**This work**
0.5% Fe/TiO_2	Wang et al. [4]	Formaldehyde	3	[5]
4% Fe/TiO_2	Sol-gel method	Methyl orange	2.0-2.5	[6]
0.25 at.% Fe/TiO_2	Ultrasonic method	Acetone	1.75	[7]
0.002 % Fe/TiO_2	Sol-gel method	Methyl orange	1.62	[8]
1.8 at.% Fe/TiO_2	Sol-gel method	Salicylic acid	1.18	[9]
0.1% Fe/TiO_2	Hydrothermal method	Methylene blue	<1	[10]

[a] k_{app} is the apparent first order constant.

References

[1] George, S., et al., Role of Fe doping in tuning the band gap of TiO_2 for the photo-oxidation-induced cytotoxicity paradigm. *Journal of the American Chemical Society*, 2011. **133**(29): p. 11270-11278.

[2] Lei, Y., et al., Synthesis of Pt–Pd core–shell nanostructures by atomic layer deposition: application in propane oxidative dehydrogenation to propylene. *Chemistry of Materials*, 2012. **24**(18): p. 3525-3533.

[3] Wang, X., et al., Adsorption of metal and metalloid ions onto nanoporous microparticles functionalized by atomic layer deposition. *Journal of Environmental Chemical Engineering*, 2016. **4**(4): p. 3767-3774.

[4] Wang, C.-y., D.W. Bahnemann, and J.K. Dohrmann, A novel preparation of iron-doped TiO_2 nanoparticles with enhanced photocatalytic activity. *Chemical Communications*, 2000(16): p. 1539-1540.

[5] Dukes, F.M., et al., Differing photo-oxidation mechanisms: electron transfer in TiO_2 versus iron-doped TiO_2. *Langmuir*, 2012. **28**(49): p. 16933-16940.

[6] Sonawane, R., B. Kale, and M. Dongare, Preparation and photo-catalytic activity of Fe TiO_2 thin films prepared by sol–gel dip coating. *Materials Chemistry and Physics*, 2004. **85**(1): p. 52-57.

[7] Zhou, M., J. Yu, and B. Cheng, Effects of Fe-doping on the photocatalytic activity of mesoporous TiO_2 powders prepared by an ultrasonic method. *Journal of Hazardous Materials*, 2006. **137**(3): p. 1838-1847.

[8] Liu, S. and Y. Chen, Enhanced photocatalytic activity of TiO_2 powders doped by Fe unevenly. *Catalysis Communications*, 2009. **10**(6): p. 894-899.

[9] Popa, M., et al., Synthesis, structural characterization, and photocatalytic properties of iron-doped TiO_2 aerogels. *Journal of materials science*, 2009. **44**(2): p. 358.

[10] Li, Z., et al., Effect of Fe-doped TiO_2 nanoparticle derived from modified hydrothermal process on the photocatalytic degradation performance on methylene blue. *Journal of Hazardous Materials*, 2008. **155**(3): p. 590-594.

SECTION

2. CONCLUSIONS AND FUTURE WORK

2.1. CONCLUSIONS

In this dissertation, ALD was employed to synthesize nanostructured materials for catalysis. Pt NPs were deposited on MWCNTs, silica gel, γ-Al_2O_3, and porous ALD-Al_2O_3 supports with similar Pt particle sizes and uniform Pt dispersion by ALD, and they were used in selective hydrogenation of citral to UA. Pt/SiO_2 showed the highest activity, with 82% conversion of citral and a selectivity of 58%. Pt/MWCNTs showed the highest selectivity, with 65% selectivity to UA. The acid-base property of supports was the dominating factor that determined the activity of all catalysts. On the other hand, the electronic effect and geometric structure influenced the product distribution of citral hydrogenation greatly for Pt/MWCNTs.

Then, highly dispersed Pt-Co bimetallic NPs were deposited on MWCNTs for selective hydrogenation of α, β-unsaturated aldehydes to unsaturated alcohols. The optimized Pt-Co/MWCNTs catalyst showed high selectivity to unsaturated alcohols (> 90%), with high conversion in various selective hydrogenation reactions due to the synergistic effect between Pt, Co, and MWCNTs, and proved its universality. A series of experiments revealed that the interaction between Pt and Co NPs improved the selectivity in C=O activation of the selective hydrogenation reactions, and the synergistic effect between Pt-Co bimetallic NPs and MWCNTs dramatically enhanced the activity of the catalysts.

Pt-Co/MWCNTs bimetallic catalysts were also used in hydrogenolysis of HMF to DMF. High yield of DMF (> 90%) was achieved in hydrogenolysis of HMF over the optimized Pt-Co/MWCNTs catalyst after 8 hr of reaction time under mild conditions. More importantly, through a series of experiments, it is revealed that the synergistic effect between Pt-Co bimetallic NPs and MWCNTs dramatically improved the yield of DMF in the HMF hydrogenolysis reactions, since MWCNTs with excellent electrical conductivity enhanced the electronic transfer and thereby enhanced the charge density on Pt-Co NPs.

Highly dispersed Au-Pt bimetallic NPs were deposited on porous γ-Al_2O_3 particles by a two-step approach. Pt NPs were first deposited on γ-Al_2O_3 particles by ALD, and Au NPs were stabilized on ALD Pt/γ-Al_2O_3 particles from a hydrosol of gold clusters. Au-Pt bimetallic catalysts showed much higher activity and stability than those of Au catalyst. The Au-Pt bimetallic catalysts were synthesized in this work by using the two-step method to overcome the leaching problem and to maintain high activity and stability. The strategy of combining ALD and a conventional method to fabricate a bimetallic catalyst with a long-term stability provides an alternative way for preparing other highly dispersed, stable, and recyclable bimetallic catalysts.

Different cycles of CeO_2 and ZrO_2 were deposited on TiO_2 NPs via ALD to improve the photocatalytic activity of TiO_2 under UV light. The optimized 40Ce/TiO_2 catalyst showed the highest photocatalytic activity among TiO_2 samples with different cycles of CeO_2 ALD, and had a more than three-fold photocatalytic activity enhancement over pure TiO_2 for the degradation of MB due to the fact that CeO_2 played a role as e^-/h^+ pair trap centers and consequently reduced the recombination rate of e^-/h^+ pairs. The 45c-

Zr/TiO_2 catalyst showed the highest photocatalytic activity among TiO_2 samples with different cycles of ZrO_2 ALD, and had a more than ten-fold photocatalytic activity enhancement over pure TiO_2 for the degradation of MB due to the fact that the fast electron transfer from the conduction band of ZrO_2 to that of TiO_2 prevented radiative electron/holes recombination. This factor worked collectively with another two factors, the relatively high surface area and a larger band gap of ZrO_2/TiO_2, and thus resulted in significantly improved photocatalytic activity of TiO_2.

Highly dispersed Fe NPs were deposited on SiO_2 NPs by ALD. The Fe/SiO_2 catalyst showed a high activity and an excellent long-term stability at high temperature in the reaction of CO oxidation. Fe_2O_3 played a vital role in catalytic CO oxidation. In a long-term stability test, there was almost no activity decrease of Fe/SiO_2 at 550 ºC for more than 300 hours of CO oxidation reaction. Due to their high efficiency, excellent stability, and low cost, it is a potential catalyst for CO removal in large-scale applications, such as treatment of exhaust gas.

Fe single atoms were deposited on MWCNTs, SiO_2, and TiO_2 NPs by Fe ALD. HAADF-STEM and XAS analysis proved the existence of Fe single atoms on MWCNTs and TiO_2 NPs, respectively. 2c-Fe/TiO_2 catalyst showed the highest photocatalytic activity and had a more than six-fold photocatalytic activity enhancement over pure TiO_2 for the degradation of MB, due to the fact that Fe^{3+} ions played a role as e^-/h^+ pair traps and consequently reduced e^-/h^+ pair recombination rate. The uniform dispersion of Fe and the effect of “defect healing” were another two factors to enhance the activity of samples. Fe ALD could be a universal strategy to prepare Fe single-atom materials on various kinds of substrates.

2.2. FUTURE WORK

For the Pt-Co/MWCNTs bimetallic catalysts, we noticed there was some catalytic activity loss for selective hydrogenation reactions of α, β-unsaturated aldehydes to unsaturated alcohols and hydrogenolysis of HMF to DMF. The stability problem of the Pt-Co catalysts needs to be solved, though very high yield of target products was achieved. Some other substrates should also be evaluated as the supports for Pt-Co bimetallic catalysts, so that we can have a better understanding for the effects of supports on the stability of the catalysts.

In addition, the ALD applications in catalysis field will be expanded. Firstly, Ni NPs will be deposited on various substrates via ALD and the Ni catalysts will be used in chemoselective transfer hydrogenation of nitroarenes reactions. Since the size of Ni NPs prepared by ALD is ultrasmall (<3 nm), it should show high activity, which is very important for chemoselective transfer hydrogenation of nitroarenes. Secondly, Pt-based bimetallic catalysts will also be synthesized by ALD besides Pt-Co bimetallic NPs, such as Pt-Ni and Pt-Fe NPs. These catalysts will be used in gas phase (e.g., CO oxidation) and liquid phase (e.g., hydrogenolysis of HMF to DMF) reactions. The mechanism of the synergistic effect between Pt and other metals will also be investigated.

Supported Fe single-atom catalysts have been prepared by ALD successfully, and Fe/TiO_2 showed high photocatalytic activity under UV light. Thus, supported Co and Ni single-atom catalysts will be synthesized using similar method (ALD) and they will be used in catalytic gas phase reactions, photocatalysis and electrocatalysis applications. Compared with traditional catalysts, single-atom catalysts should show high activity and efficiency due to their unique properties, and these hypothesis will be investigated.

BIBLIOGRAPHY

[1] Liang, X.; Weimer, A. W. An overview of highly porous oxide films with tunable thickness prepared by molecular layer deposition. *Current Opinion in Solid State and Materials Science* 2015, 19, 115-125.

[2] Liang, X.; Patel, R. L. Porous titania microspheres with uniform wall thickness and high photoactivity. *Ceramics International* 2014, 40, 3097-3103.

[3] Liang, X.; Lynn, A. D.; King, D. M.; Bryant, S. J.; Weimer, A. W. Biocompatible interface films deposited within porous polymers by atomic layer deposition (ALD). *ACS Applied Materials and Interfaces* 2009, 1, 1988-1995.

[4] Liang, X.; King, D. M.; Li, P.; George, S. M.; Weimer, A. W. Nanocoating hybrid polymer films on large quantities of cohesive nanoparticles by molecular layer deposition. *AIChE journal* 2009, 55, 1030-1039.

[5] George, S. M. Atomic layer deposition: An overview. *Chemical Reviews* 2010, 110, 111-131.

[6] Ohkuma, T.; Ooka, H.; Ikariya, T.; Noyori, R. Preferential hydrogenation of aldehydes and ketones. *Journal of the American Chemical Society* 1995, 117, 10417-10418.

[7] Gallezot, P.; Richard, D. Selective hydrogenation of α,β-unsaturated aldehydes. *Catalysis Reviews - Science and Engineering* 1998, 40, 81-126.

[8] Subash Babu, P.; Prabuseenivasan, S.; Ignacimuthu, S. Cinnamaldehyde—A potential antidiabetic agent. *Phytomedicine* 2007, 14, 15-22.

[9] Anand, P.; Murali, K. Y.; Tandon, V.; Murthy, P. S.; Chandra, R. Insulinotropic effect of cinnamaldehyde on transcriptional regulation of pyruvate kinase, phosphoenolpyruvate carboxykinase, and GLUT4 translocation in experimental diabetic rats. *Chemico-Biological Interactions* 2010, 186, 72-81.

[10] Gerberick, G. F.; Troutman, J. A.; Foertsch, L. M.; Vassallo, J. D.; Quijano, M.; Dobson, R. L. M.; Goebel, C.; Lepoittevin, J.-P. Investigation of Peptide Reactivity of Pro-hapten Skin Sensitizers Using a Peroxidase-Peroxide Oxidation System. *Toxicological Sciences* 2009, 112, 164-174.

[11] Troutman, J. A.; Foertsch, L. M.; Kern, P. S.; Dai, H. J.; Quijano, M.; Dobson, R. L. M.; Lalko, J. F.; Lepoittevin, J.-P.; Gerberick, G. F. The Incorporation of Lysine into the Peroxidase Peptide Reactivity Assay for Skin Sensitization Assessments. *Toxicological Sciences* 2011, 122, 422-436.

[12] Giroir-Fendler, A.; Richard, D.; Gallezot, P. Chemioselectivity in the catalytic hydrogenation of cinnamaldehyde. Effect of metal particle morphology. *Catal Lett* 1990, 5, 175-181.

[13] Grosselin, J. M.; Mercier, C.; Allmang, G.; Grass, F. Selective hydrogenation of .alpha.,.beta.-unsaturated aldehydes in aqueous organic two-phase solvent systems using ruthenium or rhodium complexes of sulfonated phosphines. *Organometallics* 1991, 10, 2126-2133.

[14] Mercadante, L.; Neri, G.; Milone, C.; Donato, A.; Galvagno, S. Hydrogenation of α,β-unsaturated aldehydes over Ru/Al2O3 catalysts. *Journal of Molecular Catalysis A: Chemical* 1996, 105, 93-101.

[15] Schroder, U.; Deverdier, L. Influence of Oxygen and Iron in the Liquid-Phase Hydrogenation of α,β-Unsaturated Aldehydes. *Journal of Catalysis* 1993, 142, 490-498.

[16] Mahata, N.; Gonçalves, F.; Pereira, M. F. R.; Figueiredo, J. L. Selective hydrogenation of cinnamaldehyde to cinnamyl alcohol over mesoporous carbon supported Fe and Zn promoted Pt catalyst. *Applied Catalysis A: General* 2008, 339, 159-168.

[17] Plomp, A.; Van Asten, D.; Van der Eerden, A.; Mäki-Arvela, P.; Murzin, D. Y.; de Jong, K.; Bitter, J. Catalysts based on platinum–tin and platinum–gallium in close contact for the selective hydrogenation of cinnamaldehyde. *Journal of Catalysis* 2009, 263, 146-154.

[18] Zgolicz, P. D.; Stassi, J. P.; Yañez, M. J.; Scelza, O. A.; de Miguel, S. R. Influence of the support and the preparation methods on the performance in citral hydrogenation of Pt-based catalysts supported on carbon nanotubes. *Journal of Catalysis* 2012, 290, 37-54.

[19] Tsang, S. C.; Cailuo, N.; Oduro, W.; Kong, A. T.; Clifton, L.; Yu, K. K.; Thiebaut, B.; Cookson, J.; Bishop, P. Engineering preformed cobalt-doped platinum nanocatalysts for ultraselective hydrogenation. *ACS Nano* 2008, 2, 2547-2553.

[20] Wu, B.; Huang, H.; Yang, J.; Zheng, N.; Fu, G. Selective hydrogenation of α, β-unsaturated aldehydes catalyzed by amine‐capped platinum‐cobalt nanocrystals. *Angewandte Chemie International Edition* 2012, 51, 3496-3499.

[21] Li, Y.; Li, Z.-G.; Zhou, R.-X. Bimetallic Pt-Co catalysis on carbon nanotubes for the selective hydrogenation of cinnamaldehyde to cinnamyl alcohol: Preparation and characterization. *Journal of Molecular Catalysis A: Chemical* 2008, 279, 140-146.

[22] Bertero, N. M.; Trasarti, A. F.; Moraweck, B.; Borgna, A.; Marchi, A. J. Selective liquid-phase hydrogenation of citral over supported bimetallic Pt–Co catalysts. *Applied Catalysis A: General* 2009, 358, 32-41.

[23] Zu, Y.; Yang, P.; Wang, J.; Liu, X.; Ren, J.; Lu, G.; Wang, Y. Efficient production of the liquid fuel 2,5-dimethylfuran from 5-hydroxymethylfurfural over Ru/Co3O4 catalyst. *Applied Catalysis B: Environmental* 2014, 146, 244-248.

[24] Saha, B.; Bohn, C. M.; Abu-Omar, M. M. Zinc-assisted hydrodeoxygenation of biomass-derived 5-hydroxymethylfurfural to 2,5-dimethylfuran. *ChemSusChem* 2014.

[25] Huber, G. W.; Iborra, S.; Corma, A. Synthesis of transportation fuels from biomass: Chemistry, catalysts, and engineering. *Chemical Reviews* 2006, 106, 4044-4098.

[26] Metzger, J. O. Production of liquid hydrocarbons from biomass. *Angewandte Chemie - International Edition* 2006, 45, 696-698.

[27] Román-Leshkov, Y.; Barrett, C. J.; Liu, Z. Y.; Dumesic, J. A. Production of dimethylfuran for liquid fuels from biomass-derived carbohydrates. *Nature* 2007, 447, 982-985.

[28] Deng, L.; Li, J.; Lai, D. M.; Fu, Y.; Guo, Q. X. Catalytic conversion of biomass-derived carbohydrates into γ-valerolactone without using an external h2 supply. *Angewandte Chemie - International Edition* 2009, 48, 6529-6532.

[29] Bond, J. Q.; Alonso, D. M.; Wang, D.; West, R. M.; Dumesic, J. A. Integrated catalytic conversion of γ-valerolactone to liquid alkenes for transportation fuels. *Science* 2010, 327, 1110-1114.

[30] Horváth, I. T.; Mehdi, H.; Fábos, V.; Boda, L.; Mika, L. T. γ-Valerolactone-a sustainable liquid for energy and carbon-based chemicals. *Green Chemistry* 2008, 10, 238-242.

[31] Lange, J. P.; van de Graaf, W. D.; Haan, R. J. Conversion of furfuryl alcohol into ethyl levulinate using solid acid catalysts. *ChemSusChem* 2009, 2, 437-441.

[32] Wang, H.; Deng, T.; Wang, Y.; Cui, X.; Qi, Y.; Mu, X.; Hou, X.; Zhu, Y. Graphene oxide as a facile acid catalyst for the one-pot conversion of carbohydrates into 5-ethoxymethylfurfural. *Green Chemistry* 2013, 15, 2379-2383.

[33] Yadav, G. D.; Sharma, R. V. Biomass derived chemicals: Environmentally benign process for oxidation of 5-hydroxymethylfurfural to 2,5-diformylfuran by using nano-fibrous Ag-OMS-2-catalyst. *Applied Catalysis B: Environmental* 2014, 147, 293-301.

[34] Nishimura, S.; Ikeda, N.; Ebitani, K. Selective hydrogenation of biomass-derived 5-hydroxymethylfurfural (HMF) to 2,5-dimethylfuran (DMF) under atmospheric hydrogen pressure over carbon supported PdAu bimetallic catalyst. *Catalysis Today* 2014, 232, 89-98.

[35] Nakagawa, Y.; Tamura, M.; Tomishige, K. Catalytic reduction of biomass-derived furanic compounds with hydrogen. *ACS Catalysis* 2013, 3, 2655-2668.

[36] Chatterjee, M.; Ishizaka, T.; Kawanami, H. Hydrogenation of 5-hydroxymethylfurfural in supercritical carbon dioxide-water: A tunable approach to dimethylfuran selectivity. *Green Chemistry* 2014, 16, 1543-1551.

[37] Zhang, J.; Lin, L.; Liu, S. Efficient production of furan derivatives from a sugar mixture by catalytic process. *Energy and Fuels* 2012, 26, 4560-4567.

[38] Hu, L.; Tang, X.; Xu, J.; Wu, Z.; Lin, L.; Liu, S. Selective transformation of 5-hydroxymethylfurfural into the liquid fuel 2,5-dimethylfuran over carbon-supported ruthenium. *Industrial and Engineering Chemistry Research* 2014, 53, 3056-3064.

[39] Chidambaram, M.; Bell, A. T. A two-step approach for the catalytic conversion of glucose to 2,5-dimethylfuran in ionic liquids. *Green Chemistry* 2010, 12, 1253-1262.

[40] Thananatthanachon, T.; Rauchfuss, T. B. Efficient production of the liquid fuel 2,5-dimethylfuran from fructose using formic acid as a reagent. *Angewandte Chemie - International Edition* 2010, 49, 6616-6618.

[41] Jae, J.; Zheng, W.; Lobo, R. F.; Vlachos, D. G. Production of dimethylfuran from hydroxymethylfurfural through catalytic transfer hydrogenation with ruthenium supported on carbon. *ChemSusChem* 2013, 6, 1158-1162.

[42] De, S.; Dutta, S.; Saha, B. One-pot conversions of lignocellulosic and algal biomass into liquid fuels. *ChemSusChem* 2012, 5, 1826-1833.

[43] Hu, L.; Lin, L.; Liu, S. Chemoselective hydrogenation of biomass-derived 5-hydroxymethylfurfural into the liquid biofuel 2,5-dimethylfuran. *Industrial and Engineering Chemistry Research* 2014, 53, 9969-9978.

[44] Wang, G. H.; Hilgert, J.; Richter, F. H.; Wang, F.; Bongard, H. J.; Spliethoff, B.; Weidenthaler, C.; Schüth, F. Platinum-cobalt bimetallic nanoparticles in hollow carbon nanospheres for hydrogenolysis of 5-hydroxymethylfurfural. *Nature Materials* 2014, 13, 293-300.

[45] Luo, J.; Arroyo-Ramírez, L.; Gorte, R. J.; Tzoulaki, D.; Vlachos, D. G. Hydrodeoxygenation of HMF over Pt/C in a continuous flow reactor. *AIChE Journal* 2015, 61, 590-597.

[46] Binder, J. B.; Raines, R. T. Simple chemical transformation of lignocellulosic biomass into furans for fuels and chemicals. *Journal of the American Chemical Society* 2009, 131, 1979-1985.

[47] Scholz, D.; Aellig, C.; Hermans, I. Catalytic transfer hydrogenation/hydrogenolysis for reductive upgrading of furfural and 5-(hydroxymethyl)furfural. *ChemSusChem* 2014, 7, 268-275.

[48] Wang, Y.; Cheng, H.; Hao, Y.; Ma, J.; Li, W.; Cai, S. Preparation, characterization and photoelectrochemical behaviors of Fe(III)-doped TiO_2 nanoparticles. *Journal of Materials Science* 1999, 34, 3721-3729.

[49] Linsebigler, A. L.; Lu, G.; Yates Jr, J. T. Photocatalysis on TiO_2 surfaces: principles, mechanisms, and selected results. *Chemical Reviews* 1995, 95, 735-758.

[50] Hoffmann, M. R.; Martin, S. T.; Choi, W.; Bahnemann, D. W. Environmental applications of semiconductor photocatalysis. *Chemical Reviews* 1995, 95, 69-96.

[51] Zhang, X.; Fujishima, A.; Jin, M.; Emeline, A. V.; Murakami, T. Double-layered TiO_2−SiO_2 nanostructured films with self-cleaning and antireflective properties. *The Journal of Physical Chemistry B* 2006, 110, 25142-25148.

[52] Yang, H.; Zhang, K.; Shi, R.; Tang, A. Sol–gel synthesis and photocatalytic activity of CeO_2/TiO_2 nanocomposites. *Journal of the American Ceramic Society* 2007, 90, 1370-1374.

[53] Li, Z.; Sheng, J.; Zhang, Y.; Li, X.; Xu, Y. Role of CeO_2 as oxygen promoter in the accelerated photocatalytic degradation of phenol over rutile TiO_2. *Applied Catalysis B: Environmental* 2015, 166, 313-319.

[54] Muñoz-Batista, M. J.; Gómez-Cerezo, M. N.; Kubacka, A.; Tudela, D.; Fernández-García, M. Role of interface contact in CeO_2–TiO_2 photocatalytic composite materials. *ACS Catalysis* 2013, 4, 63-72.

[55] Tiejun, C.; Yuchao, L.; Zhenshan, P.; Yunfei, L.; Zongyuan, W.; Qian, D. Photocatalytic performance of TiO_2 catalysts modified by $H_3PW_{12}O_{40}$, ZrO_2 and CeO_2. *Journal of Environmental Sciences* 2009, 21, 997-1004.

[56] Jiang, B.; Zhang, S.; Guo, X.; Jin, B.; Tian, Y. Preparation and photocatalytic activity of CeO_2/TiO_2 interface composite film. *Applied Surface Science* 2009, 255, 5975-5978.

[57] Xu, A.-W.; Gao, Y.; Liu, H.-Q. The preparation, characterization, and their photocatalytic activities of rare-earth-doped TiO_2 nanoparticles. *Journal of Catalysis* 2002, 207, 151-157.

[58] Tian, J.; Sang, Y.; Zhao, Z.; Zhou, W.; Wang, D.; Kang, X.; Liu, H.; Wang, J.; Chen, S.; Cai, H. Enhanced photocatalytic performances of CeO_2/TiO_2 nanobelt heterostructures. *Small* 2013, 9, 3864-3872.

[59] Qiao, B.; Wang, A.; Yang, X.; Allard, L. F.; Jiang, Z.; Cui, Y.; Liu, J.; Li, J.; Zhang, T. Single-atom catalysis of CO oxidation using Pt_1/FeOx. *Nature Chemistry* 2011, 3, 634-641.

[60] Kyriakou, G.; Boucher, M. B.; Jewell, A. D.; Lewis, E. A.; Lawton, T. J.; Baber, A. E.; Tierney, H. L.; Flytzani-Stephanopoulos, M.; Sykes, E. H. Isolated metal atom geometries as a strategy for selective heterogeneous hydrogenations. *Science(Washington)* 2012, 335, 1209-1212.

[61] Deng, D.; Chen, X.; Yu, L.; Wu, X.; Liu, Q.; Liu, Y.; Yang, H.; Tian, H.; Hu, Y.; Du, P. A single iron site confined in a graphene matrix for the catalytic oxidation of benzene at room temperature. *Science advances* 2015, 1, e1500462.

[62] Ding, K.; Gulec, A.; Johnson, A. M.; Schweitzer, N. M.; Stucky, G. D.; Marks, L. D.; Stair, P. C. Identification of active sites in CO oxidation and water-gas shift over supported Pt catalysts. *Science* 2015, 350, 189-192.

[63] Liu, P.; Zhao, Y.; Qin, R.; Mo, S.; Chen, G.; Gu, L.; Chevrier, D. M.; Zhang, P.; Guo, Q.; Zang, D. Photochemical route for synthesizing atomically dispersed palladium catalysts. *Science* 2016, 352, 797-800.

[64] Jones, J.; Xiong, H.; DeLaRiva, A. T.; Peterson, E. J.; Pham, H.; Challa, S. R.; Qi, G.; Oh, S.; Wiebenga, M. H.; Hernández, X. I. P. Thermally stable single-atom platinum-on-ceria catalysts via atom trapping. *Science* 2016, 353, 150-154.

[65] Cheng, N.; Stambula, S.; Wang, D.; Banis, M. N.; Liu, J.; Riese, A.; Xiao, B.; Li, R.; Sham, T.-K.; Liu, L.-M. Platinum single-atom and cluster catalysis of the hydrogen evolution reaction. *Nature Communications* 2016, 7.

[66] Sun, S.; Zhang, G.; Gauquelin, N.; Chen, N.; Zhou, J.; Yang, S.; Chen, W.; Meng, X.; Geng, D.; Banis, M. N. Single-atom catalysis using Pt/graphene achieved through atomic layer deposition. *Scientific reports* 2013, 3.

[67] Yan, H.; Cheng, H.; Yi, H.; Lin, Y.; Yao, T.; Wang, C.; Li, J.; Wei, S.; Lu, J. Single-atom Pd1/graphene catalyst achieved by atomic layer deposition: remarkable performance in selective hydrogenation of 1, 3-butadiene. *Journal of the American Chemical Society* 2015, 137, 10484-10487.

[68] Chen, X.; Yu, L.; Wang, S.; Deng, D.; Bao, X. Highly active and stable single iron site confined in graphene nanosheets for oxygen reduction reaction. *Nano Energy* 2017, 32, 353-358.

[69] Vilé, G.; Albani, D.; Nachtegaal, M.; Chen, Z.; Dontsova, D.; Antonietti, M.; López, N.; Pérez‐Ramírez, J. A stable single‐site palladium catalyst for hydrogenations. *Angewandte Chemie International Edition* 2015, 54, 11265-11269.

[70] Yang, M.; Li, S.; Wang, Y.; Herron, J. A.; Xu, Y.; Allard, L. F.; Lee, S.; Huang, J.; Mavrikakis, M.; Flytzani-Stephanopoulos, M. Catalytically active Au-O (OH) x-species stabilized by alkali ions on zeolites and mesoporous oxides. *Science* 2014, 346, 1498-1501.

[71] Fei, H.; Dong, J.; Arellano-Jiménez, M. J.; Ye, G.; Kim, N. D.; Samuel, E. L.; Peng, Z.; Zhu, Z.; Qin, F.; Bao, J. Atomic cobalt on nitrogen-doped graphene for hydrogen generation. *Nature communications* 2015, 6.

[72] Qiu, H. J.; Ito, Y.; Cong, W.; Tan, Y.; Liu, P.; Hirata, A.; Fujita, T.; Tang, Z.; Chen, M. Nanoporous graphene with single‐atom nickel dopants: An efficient and stable catalyst for electrochemical hydrogen production. *Angewandte Chemie* 2015, 127, 14237-14241.

APPENDIX

Xiaofeng Wang's List of Publications during Ph.D. Studies

I. Papers published:

1. Xiaofeng Wang, Haiyan Zhao, Tianpin Wu, Yuzi Liu, and Xinhua Liang*, Synthesis of highly dispersed and highly stable supported Au–Pt bimetallic catalysts by a two-step method, ***Catalysis Letters***, 146 (12), 2606-2613, 2016.

2. Xiaofeng Wang, Ariel R. Donovan, Rajankumar L. Patel, Honglan Shi, and Xinhua Liang*, Adsorption of metal and metalloid ions onto nanoporous microparticles functionalized by atomic layer deposition, ***Journal of Environmental Chemical Engineering***, 4 (4), 3767-3774, 2016.

3. Xiaofeng Wang, Ye Jin, Xinhua Liang*, Significant photocatalytic performance enhancement of TiO_2 by CeO_2 atomic layer deposition, ***Nanotechnology***, 28 (50), article No. 505709, 2017.

4. Xiaofeng Wang, Weiming Hu, Baolin Deng, and Xinhua Liang*, Selective hydrogenation of citral over supported Pt catalysts: insight into support effects, ***Journal of Nanoparticle Research***, 19 (4), article No. 153, 2017.

5. Xiaofeng Wang, Raimund Bayan, Miao Yu, Douglas Ludlow, and Xinhua Liang*, Atomic layer deposition surface functionalized biochar for adsorption of organic pollutants: Improved hydrophilia and adsorption capacity, ***International Journal of Environmental Science and Technology***, 14 (9), 1825–1834, 2017.

6. Yan Gao, Rajankumar Petel, Kuan-Yu Shen, Xiaofeng Wang, Richard Axelbaum, Xinhua Liang*, Boosting electrochemical performance of $Li_{1.2}Mn_{0.54}Ni_{0.13}Co_{0.13}O_2$ by atomic layer deposited CeO_2 coating, ***ACS Omega***, 3 (1), 906-916, 2018

II. Manuscripts in progress:

1. Xiaofeng Wang, Yuzi Liu, Xinhua Liang*, Atomic layer deposited Pt-Co bimetallic catalysts for selective hydrogenation of α, β-unsaturated aldehydes to unsaturated alcohols, *revision submitted to* ***ACS Catalysis***.

2. Xiaofeng Wang, Yuzi Liu, Xinhua Liang*, Hydrogenolysis of 5-hydroxymethylfurfural to 2,5-dimethylfuran over supported Pt-Co bimetallic catalyst under mild conditions, *submitted to* ***Green Chemistry***.

3. Xiaofeng Wang, Xinhua Liang*, Significant improvement of TiO_2 photocatalytic activity through a controllable ZrO_2 deposition, *submitted to* ***ChemCatChem***.

4. Xiaofeng Wang, Xinhua Liang*, Highly active and stable Fe/SiO_2 catalyst synthesized by atomic layer deposition for CO oxidation, to be submitted to ***ACS Catalysis***.

5. Xiaofeng Wang, Ye Jin, Xinhua Liang*, Supported iron single atoms synthesized via atomic layer deposition, to be submitted to ***Nano Letters***.

VITA

The author, Xiaofeng Wang, was born in Shandong, China. He entered East China University of Science and Technology, China in 2009 and received B.S. degree with a major in Polymer Material Science and Technology from East China University of Science and Technology in July 2013. Then he obtained M.S. degree with a major in Chemical Engineering from University of Missouri-Columbia in July 2014. Xiaofeng Wang received a Doctor of Philosophy degree in Chemical Engineering from Missouri University of Science and Technology in May 2018.